Title
Liquefaction and Post-Liquefaction Behavior of Coarse-Grained Soils

Author
Humire Guarachi, Francisco Alejandro

Publication Date
2022

Liquefaction and Post-Liquefaction Behavior of Coarse-Grained Soils

By

FRANCISCO ALEJANDRO HUMIRE GUARACHI

DISSERTATION

Submitted in partial satisfaction of the requirements for the degree of

DOCTOR OF PHILOSOPHY

in

Civil and Environmental Engineering

in the

OFFICE OF GRADUATE STUDIES

of the

UNIVERSITY OF CALIFORNIA

DAVIS

Approved:

Katerina Ziotopoulou, Chair

Jason T. DeJong

Ross W. Boulanger

Committee in Charge

2022

Liquefaction and Post-Liquefaction Behavior of Coarse-Grained Soils

Abstract

Liquefaction assessments require the ability to estimate triggering potential and possible consequences across a range of seismic hazard levels and in-situ soil conditions. This Dissertation aims to advance the fundamental understanding of the element level response of coarse-grained soils prior and after liquefaction triggering, and to evaluate tools currently used in engineering practice for the estimation of liquefaction effects on geosystems. This is achieved by (1) resolving experimental issues pertaining to performing Direct Simple Shear (DSS) testing, (2) establishing framework that facilitates the comparison of both triggering and post-triggering responses, and (3) performing extensive DSS investigations of coarse-grained materials encompassing a range of properties and conditions.

A series of constant-volume (CV) DSS tests show that applying a pre-conditioning sequence improves the engagement at the soil-platen interface when textured platens are used. Given the efficacy of these protocols to enhance the shear stress transfer to sand specimens, all the CV-DSS tests presented in this Dissertation consider a pre-conditioning sequence prior to constant-volume shearing. Although the pre-conditioning protocol presented herein is specific to the testing equipment and materials considered, recommendations are provided to develop pre-conditioning protocols for other soils, platens, and testing devices.

The factors and mechanisms controlling the accumulation of shear strains of clean uniform sands exhibiting cyclic mobility behavior under level-ground conditions are investigated from CV-DSS tests on Ottawa F-65 sand subjected to uniform and irregular cyclic loading conditions. Experimental data show that the rate of shear strain accumulation per loading cycle depends on the relative density, cyclic stress amplitude, and overburden stress. Mechanisms of shear strain accumulation are investigated by decoupling the shear strain developed in each loading cycle in two components: γ_0, developed at near-zero effective stress, and γ_d, developed during dilation. Results show that γ_0 mostly depends on the shear strain history, while γ_d depends on the cyclic stress amplitude and relative density.

The role of gradation and grain size on the liquefaction behavior of coarse-grained soils is investigated from a series of CV-DSS tests performed on seven soil mixtures with different coefficients of uniformity (C_u) and median grain sizes (D_{50}). Empirical observations of liquefaction triggering, post-triggering shear strain accumulation, and post-liquefaction reconsolidation strains are synthesized to evaluate functional trends with C_u and D_{50}. Results show that the effects of C_u and D_{50} on the liquefaction triggering resistance depend on the relative density (D_R) at which they are compared, while the post-triggering shear strain accumulation decrease while increasing both C_u and D_{50}. Results also show that an increase in C_u leads to smaller post-liquefaction reconsolidation volumetric strains, while changes in D_{50} have little effect on such strains.

The combined effect of gradation and sloping ground conditions on soil liquefaction is investigated from monotonic and cyclic CV-DSS tests performed on two sands with different gradations. Monotonic test results show that an increase in gradation slightly reduces the degree of strain-softening and peak shear stresses. Results from cyclic tests are synthesized to examine the effect of gradation on patterns of pore pressure generation, liquefaction triggering resistance, and sloping ground correction factors (K_α). Additional cyclic tests under irregular loading conditions are analyzed to evaluate the role of gradation in the post-triggering shear strain accumulation.

Finally, this Dissertation examines the capabilities and limitations of the PM4Sand constitutive model in capturing key features of the liquefaction behavior of two sands with different gradations under sloping ground conditions. Simulations with PM4sand successfully captured the monotonic response and liquefaction triggering resistance for both soils. Still, the calibration process required activating some of the secondary parameters of the model, and using alternative parameter sets depending on the target responses prioritized during calibration.

Acknowledgements

The work presented herein would not have been possible without the help of many people and organizations for whom I am very thankful.

I want to thank Professor Katerina Ziotopoulou for her constant support and guidance throughout my PhD research. I appreciate her willingness to discuss new research ideas, passion for teaching and mentoring, and encouragement to sharpen my communication skills. I am also thankful to Professor Jason DeJong for his support and guidance inside and out of the lab. I appreciate him for constantly pushing me to think from multiple perspectives and find practical and pragmatic solutions. I also would like to thank Professors Alejandro Martinez and Michael Gomez for providing thoughtful discussions and guidance that brought my research to a higher level, Professors Ross Boulanger and James McLain for serving on my Dissertation and qualifying exam committees and the advising provided in those instances, and Professor Idriss for generously sharing his wisdom and unique experience that inspired and motivated me to be better researcher every day.

I want to express my gratitude to all the people that helped me with the experimental work presented in this Dissertation. I want to thank Rachel Reardon for her collaboration to perform hundreds of DSS tests within the gravels project, Minyong Lee for helping me with the development of DSS testing procedures, and Brian Morales for introducing me to the DSS world. I also want to thank Daret Kehlet and Victor Jones for their patience and support in troubleshooting any issues during my testing plans.

I am grateful to many fellow students that contributed to my research and brightened my days in the darkness of Bainer Hall. I am thankful for the help of Renmin Pretell in many aspects of my research, but also for his friendship, generosity, and unconditional support. I also want to thank Sumeet Kumar Sinha, Patrick Bassal, Dr. Barry Zheng, Maya El Kortbawi, Matt Burrall, Hyunsoo Seol, Sophia Palumbo, Brian Morales, Casey Phradichith, and Mandeep Basson for all the good moments in and out of Bainer and, of course, for the rewarding conversations about soils, research, and non-engineering topics.

I want to thank the National Science Foundation (NSF) for funding this research under the grant CMMI #1916152, and the United States Society on Dams (USSD) for providing additional support through their student scholarship award. I am also grateful to the UC Davis College of Engineering for the funding provided during my first year of graduate studies through the PEGS-21 and TOPS awards.

Finally, I would like to thank my family for their unconditional support over these years. I want to thank my wife, Cori Ritter, for her support, infinite love, and patience during these years, and for brightening every day of my life. I am also thankful for my loving parents, Lucia and Francisco, and siblings, Francis, Marisol, and Alvaro, for their support that transcends all physical and spiritual boundaries.

Table of contents

Chapter 1

Introduction

1.1 Background

Liquefaction assessments for geosystems require the ability to estimate triggering potential and possible consequences across a range of seismic hazard levels and in-situ soil conditions. Among other liquefaction-related phenomena, sands exhibiting cyclic mobility behavior can result in significant lateral deformations as a result of the progressive accumulation of shear strains after liquefaction is triggered. Our current understanding of this phenomenon has been made possible predominantly through element level laboratory tests (e.g., direct simple shear, triaxial, torsional tests), which have shown that the process of shear strain accumulation depends on factors such as the relative density, shear stress amplitude, and intrinsic properties of the sand tested (Tasiopoulou et al. 2020). Still, the stress-strain response of sands undergoing cyclic mobility at large shear deformation levels remains not fully understood (NASEM 2016) and further research is needed to clarify the physics-based mechanisms and factors controlling the shear strain accumulation.

Most of the current understanding about liquefaction is based on empirical observations of clean uniform sands. This poses an additional challenge for liquefaction assessments of geosystems founded upon or comprised by well-graded coarse-grained soils. Few studies have systematically investigated the role of soil gradation on the behavior prior to and after liquefaction triggering (Vaid et al. 1990; Kokusho et al. 2004; Doygun et al. 2019). However, those studies have led to contradictory and ambiguous findings regarding the effects of a coarse-grained soil's gradation on its liquefaction and post-liquefaction behavior. Due to these limitations, the current standard of practice typically assumes that liquefaction effects can be assessed with engineering correlations developed for clean uniform sands without accounting for the effects of soil gradation. Recent experimental and numerical research efforts (e.g., Sturm 2019; Kuei 2019) have shown that disregarding the effect of gradation on liquefaction assessments may lead to overestimations of the anticipated damage in system level analyses.

Advanced constitutive models capable of capturing the response of liquefiable sands at the element level (e.g., Beaty and Byrne 1998; Boulanger and Ziotopoulou 2017; Khosravifar et al. 2018) have led to increasingly reliable estimations of liquefaction effects in system level analyses. Still, the simulation of liquefaction effects lacks a quantitative framework to guide the prediction of cyclic mobility-induced shear deformations. This limitation is particularly important at sites subjected to long duration motions where several loading cycles may occur after liquefaction triggering (Tasiopoulou et al. 2020). Also, current constitutive models are mostly based on theoretical frameworks and empirical observations of clean uniform sands, and as such do not explicitly accommodate the effect of gradation in their formulations. The systematic calibration and validation of constitutive models against the stress-strain behavior of sands observed in laboratory tests (e.g., Ziotopoulou et al. 2014; Wichtmann et al. 2019) can inform about their capabilities and limitations for this particular behavior. Identified limitations can in turn lead to refinements of the said constitutive formulations, as well as well-formulated calibration protocols for their use in engineering practice.

1.2 Scope of Research

This dissertation aims to advance the fundamental understanding of the element level response of coarse-grained soils prior and after liquefaction triggering, and to evaluate tools currently used in engineering practice for the estimation of liquefaction effects on geosystems.

The first part of this dissertation (Chapters 2-4) builds upon the work of Tasiopoulou et al. (2020) in order to investigate the mechanisms and factors controlling the shear strain accumulation of clean sands exhibiting cyclic mobility behavior. This part provides a basis for the interpretation and performance of cyclic constant-volume direct simple shear (CV-DSS) tests on clean sands that is used in the following chapters of the dissertation.

The second part of this dissertation (Chapters 5-7) falls under a broader research project aimed to investigate the characterization and cyclic response of well-graded coarse-grained soils. The focus of this part is to investigate systematically with CV-DSS tests the combined effects of relative density, soil gradation, and sloping ground conditions on the liquefaction triggering resistance and the mechanism of shear strain accumulation. Additionally, test results are synthetized to: (1) reassess engineering correlations typically used in practice for assessing liquefaction triggering and liquefaction-induced deformations, and (2) evaluate the capabilities of the PM4Sand constitutive model (Boulanger and Ziotopoulou 2017) to capture key features of the cyclic response of well-graded coarse-grained soils. Findings from these chapters provide a basis to perform liquefaction assessments considering the effects of soil gradation, which will help to reduce the uncertainty of those assessments in the engineering practice.

1.3 Dissertation Organization

This dissertation is organized into eight chapters and two appendices. Chapters 2 to 7 are based on journal and conference papers that are published or under consideration for publication. Summaries of the content of each chapter are provided below.

Chapter 2 introduces a framework for tracking the accumulation of shear strains in laboratory experiments on sands exhibiting cyclic mobility behavior, which is implemented in cyclic undrained tests available in the literature.

Chapter 3 presents a methodology to develop pre-conditioning protocols for CV-DSS tests aimed to ensure the compliance between textured top platens and sand specimens. Given the efficacy of these protocols to improve the shear stress transfer to sand specimens, all the CV-DSS tests presented in the following chapters consider a pre-conditioning sequence prior to constant-volume cyclic shearing.

Chapter 4 examines the process of shear strain accumulation observed in cyclic CV-DSS tests performed on a clean uniform sand under level-ground conditions. The framework proposed by Tasiopoulou et al. (2020) is implemented to quantify the combined effects of relative density, cyclic stress amplitude, loading device, and overburden stress on the rate of shear strain accumulation. Based on the approach and previous insights from Shamoto et al. (1997), a revised interpretation is provided regarding the role of shear strain history, cyclic stress amplitude, and dilation on the process of shear strain accumulation under uniform and irregular cyclic loading conditions.

Chapter 5 presents an experimental investigation about the role of gradation and grain size on the liquefaction and post-liquefaction behavior of coarse-grained soils. Empirical observations of liquefaction triggering, shear strain accumulation, and post-liquefaction reconsolidation are synthetized in order to identify functional trends with the coefficient of uniformity (C_u) and the median grain size (D_{50}). Tests results are also used to discuss the appropriateness of empirical correlations based on clean uniform sands (e.g., Ishihara and Yoshimine 1992) for the assessment of liquefaction effects on well-graded soils.

Chapter 6 extends the work presented in Chapter 5 by assessing the combined effect of gradation and sloping ground conditions on the monotonic and cyclic response of coarse-grained soils. Test results are used to reevaluate empirical correlations for liquefaction analyses under sloping ground conditions, such as cyclic strength correction factors (K_α) and pore pressure generation charts (Idriss and Boulanger 2008).

Chapter 7 evaluates the capabilities and limitations of the PM4Sand constitutive model in capturing key features of the liquefaction behavior of well-graded coarse-grained soils under sloping ground conditions. Empirical data and correlations obtained in Chapter 5 and 6 are used to calibrate the PM4Sand model using single-element simulations to approximate the stress-strain response of well-graded soils.

Chapter 8 summarizes the main conclusions of this dissertation and presents ideas for further research.

Appendix A presents the procedures followed to perform the CV-DSS tests presented in this dissertation.

Appendix B summarizes all the CV-DSS tests presented in this work and their specifications.

1.4 References

Beaty, M. and Byrne, P. M. 1998. An effective stress model for predicting liquefaction behavior of sand. In *Geotechnical Earthquake Engineering and Soil Dynamics III. ASCE Geotechnical Special Publication. Vol. 1*, pp. 766–777.

Boulanger, R. W. and Ziotopoulou, K. 2017. *PM4Sand (version 3.1): A sand plasticity model for earthquake engineering applications*. Report No. UCD/CGM-17/01. Center for Geotechnical Modeling, Department of Civil and Environmental Engineering, University of California, Davis, CA.

Doygun, O., Brandes, H. G., and Roy, T. T. 2019. Effect of gradation and non-plastic fines on monotonic and cyclic simple shear strength of silica sand. *Geotechnical and Geological Engineering* 37(4): 3221–3240.

Idriss, I. M. and Boulanger, R. W. 2008. *Soil liquefaction during earthquakes*. Monograph MNO-12. Earthquake Engineering Research Institute, Oakland, CA.

Ishihara, K. and Yoshimine, M. 1992. Evaluation of settlements in sand deposits following liquefaction during earthquakes. *Soils and Foundations* 32(1): 173–188.

Khosravifar, A., Elgamal, A., Lu, J., and Li, J. 2018. A 3D model for earthquake-induced liquefaction triggering and post-liquefaction response. *Soil Dynamics and Earthquake Engineering* 110: 43–52.

Kokusho, T., Hara, T., and Hiraoka, R. 2004. Undrained shear strength of granular soils with different particle gradations. *Journal of Geotechnical and Geoenvironmental Engineering* 130(6): 621–629.

Kuei, K. 2019. *Pile Dynamics and Shearing Behavior of Granular Soils*. Ph.D. dissertation, University of California, Davis.

National Academies of Sciences, Engineering, and Medicine. 2016. *State of the art and practice in the assessment of earthquake-induced soil liquefaction and its consequences*. The National Academies Press, Washington, DC. https://doi.org/10.17226/23474

Shamoto, Y., Zhang, J.-M., and Goto, S. 1997. Mechanism of large post-liquefaction deformation in saturated sand. *Soils and Foundations* 37(2): 71–80.

Sturm, A. P. 2019. *On the Liquefaction Potential of Gravelly Soils: Characterization, Triggering and Performance*. Ph.D. dissertation, University of California, Davis.

Tasiopoulou, P., Ziotopoulou, K., Humire, F., Giannakou, A., Chacko, J., and Travasarou, T. 2020. Development and implementation of semiempirical framework for modeling postliquefaction shear deformation accumulation in sands. *Journal of Geotechnical and Geoenvironmental Engineering* 146(1): 4019120.

Vaid, Y. P., Fisher, J. M., Kuerbis, R. H., and Negussey, D. 1990. Particle gradation and liquefaction. *Journal of Geotechnical Engineering* 116(4): 698–703.

Wichtmann, T., Fuentes, W., and Triantafyllidis, T. 2019. Inspection of three sophisticated constitutive models based on monotonic and cyclic tests on fine sand: Hypoplasticity vs. Sanisand vs. ISA. *Soil Dynamics and Earthquake Engineering* 124(May): 172–183.

Ziotopoulou, K., Maharjan, M., Boulanger, R. W., Beaty, M. H., Armstrong, R. J., and Takahashi, A. 2014. Constitutive modeling of liquefaction effects in sloping ground. In *Proceedings of the 10th National Conference on Earthquake Engineering, July 21-25, Anchorage, AK.*

Chapter 2

Framework for tracking the accumulation of shear strains during cyclic mobility

Original publication: Humire, F., Ziotopoulou, K., Basson, M. S., and Martinez, A. 2019. Framework for tracking the accumulation of shear strains during cyclic mobility. In Earthquake Geotechnical Engineering for Protection and Development of Environment and Constructions – Proceedings of the 7th International Conference on Earthquake Geotechnical Engineering, (ICEGE 2019), June 17-20, 2019, Rome, Italy. Edited by F. Silvestri and N. Moraci. CRC Press, Taylor and Francis, London. pp. 2906–2914.

Author's note: This chapter presents the original publication with minor modifications for consistency with the other Chapters of this Dissertation and to reflect data curation that took place between the original publication and the time of this Dissertation. The methodology presented in the original publication proposed a critical value of the pore pressure ratio (r_u) to decouple the shear strains occurring during cyclic mobility. Later efforts in this investigation showed that establishing a certain value of effective vertical stresses (σ'_v) is more appropriate for that purpose. This Chapter presents a criterion based on σ'_v to improve consistency with the other chapters of the Dissertation. However, the use of either r_u or σ'_v does not alter the results presented in the original publication.

Abstract

A framework for tracking the accumulation of shear strains in experiments exhibiting cyclic mobility behavior of liquefiable sands is implemented in order to evaluate its applicability. Shear strains are decoupled in two components: γ_0, developed at near-zero effective stress, and γ_d, developed while the soil dilates. Results show that the development of γ_d is triggered after the specimen exhibits dilative behavior, and increases up to a saturation value after liquefaction triggering. Conversely, γ_0 initiates at liquefaction triggering and its evolution per loading cycle follows an almost linear trend. These results suggest that the linear increase of post-liquefaction shear strains is related to the strains developed at near-zero effective stress, which are closely linked to the evolution of fabric at the particle scale. Further experimental work and DEM simulations are proposed to study the behavior under large deformations, and to understand the mechanism controlling strain accumulation during cyclic mobility.

2.1 Introduction

The evaluation of liquefaction effects on geotechnical structures requires, amongst others, the ability to estimate deformations across a range of seismic hazard levels and in-situ stress conditions. Lateral deformations developed when soils exhibit cyclic mobility behavior, wherein soil progressively accumulates shear strains after liquefaction has been triggered, can result in significant damages to structures built on or in sandy soils. On the basis of macroscopic observations of soil behavior, different constitutive models have been formulated capable of capturing the response at the element level. Still, simulation of cyclic mobility effects remains a challenging task, lacking a fundamental understanding of the mechanisms controlling the accumulation of shear strains. Evidence from Discrete Element Method (DEM) simulations, as well as from the examination of experimental data collected on sands, indicate that shear strain accumulation is controlled by particle-level mechanisms such as fabric evolution. However, the physical mechanisms controlling this phenomenon have not been fully resolved thus limiting our ability to capture it at the macroscopic level.

The present paper is part of an integrated research plan involving laboratory tests and DEM simulations, with the objective of providing information regarding the mechanisms controlling accumulation of shear strains during cyclic mobility. The first step towards taking a closer look at this behavior is to define strategies for quantitatively assessing the development of post-liquefaction shear strains. In this context, this paper focuses on the implementation of a framework for interpretation of cyclic mobility data and, in particular, for tracking the accumulation of shear strains. This is achieved by reviewing approaches available in the literature together with previous works on DEM (particularly in regard to fabric descriptors that have been shown to be closely related to the accumulation of shear strains within the cyclic mobility regime) and implementing a framework on sets of cyclic mobility data. The specific objectives of this paper are to: (1) implement a framework to study the post-liquefaction shear strain accumulation, (2) apply the framework in two laboratory undrained cyclic tests, and closely study the development of shear strains during cyclic mobility, and (3) complement the framework with insights at the particle level observed on previous works on DEM.

2.2 Literature review

2.2.1 Available frameworks for quantifying cyclic shear strain accumulation in experiments

Shear strain accumulation in undrained cyclic experiments can be assessed by plotting the maximum strain achieved at each loading cycle versus the number of cycles (Figure 2.1). This plot allows recognizing important features of experiments exhibiting cyclic mobility behavior. For example, the accumulation of shear strains per loading cycle follows an almost linear trend after initial liquefaction, as illustrated in Figure 2.1b. Based on this observation, Tasiopoulou et al. (2020) evaluated the shear strain increment rate per loading cycle in the post-liquefaction regime for a large body of cyclic experiments, and found a dependency of this rate on the relative density, the shear stress amplitude, and the laboratory sand used in the tests.

Shamoto et al. (1997) proposed another approach for assessing the accumulation of shear strains during cyclic mobility. Based on experimental observations of undrained monotonic and cyclic torsional tests, Shamoto et al. (1997) proposed decoupling the post-liquefaction shear strains in two components: (1) a strain component developed at near-zero effective stress, denoted by γ_0, and (2) a strain component developed during dilation at non-zero effective stress, denoted by γ_d. Their results showed that γ_0 governs the development of shear strains during cyclic mobility, and suggested a dependence of γ_0 on the maximum shear strain achieved in the previous loading cycle (i.e., loading history). Later, Zhang and Wang (2012) decoupled γ_0 and γ_d for a series of undrained cyclic torsional experiments and named each strain component "fluid-like shear strain" and "solid-like shear strain", respectively. They noticed that the evolution of γ_0 versus the number of cycles follows a monotonically increasing trend. Their analysis also revealed that γ_d is almost the same for all loading cycles in the post-liquefaction regime, thus implying that γ_d depends exclusively on the current effective stress and possibly other properties of the sand.

Alternative methods for investigating cyclic mobility-related behaviors have also been presented in the literature. The development of shear strains during cyclic mobility has been captured by quantifying the shear modulus reduction at different strain levels (Zhuang et al. 2018), or by assessing the dilative tendency along the experiment (Ziotopoulou and Boulanger 2016). However, these methods are considered as being outside the scope of this paper.

2.2.2 Available fabric descriptors for DEM simulations

Particle level mechanisms, such as evolution of fabric (i.e., the spatial arrangement of solid particles, contacts, and pores in a soil matrix), control the global-scale behavior of soils (e.g., Oda et al. 1985, O'Sullivan and Cui 2009). Destructive and non-destructive techniques, such as optical microscopy, X-Ray computed tomography, and acoustic wave velocity (e.g., Wiebicke et al. 2017) have been employed to understand the evolution of fabric during laboratory tests. DEM codes have the additional ability of tracking micromechanical interactions between the particles of a granular assembly due to a multitude of contact-detection algorithms and the capability to model complex grain shapes and different soil gradations. This section summarizes the different fabric metrics currently available for quantifying effects related to cyclic mobility.

Contact-based descriptors are commonly used to quantify soil fabric during cyclic mobility since the number and orientation of inter-particle contacts evolve during cyclic loading. Out of these, the coordination number (C_N – mean number of contacts per particle in the assembly) has been shown via studies based on 2D and 3D DEM simulations of cyclic undrained tests to be oscillating around a value that corresponds to the minimum required to maintain a stable fabric before liquefaction triggering (e.g., Wei and Wang 2015, Wang et al. 2016).

Void-based and distance-based fabric descriptors have been introduced in recent years to describe post-liquefaction behavior. Wei et al. (2018) showed a good correlation between post-liquefaction strains and void-based metrics to define fabric anisotropy, such as the evolution of average elongation of void space (E_d) and principal direction of void space (A_d). Descriptors of the distance between particles are also appropriate to describe the cyclic mobility response. Amongst them we can find: (1) the Centroid Number (Wang and Wei 2016), which is the normalized distance between a particle centroid and the centroid of the Voronoi cell enclosing the particles, and (2) the Mean Neighboring Particle Distance (MNPD – Wang et al. 2016), which is a scalar that depicts the average surface-to-surface distance between all particles and the neighboring particles needed to create a stable load-bearing structure.

2.3 Implementation on experimental data

2.3.1 Procedure of the selected framework

The accumulation of shear strains during cyclic mobility is assessed following the approach of Shamoto et al. (1997). The procedure to compute γ_0 and γ_d in each loading cycle is as follows:

1) Define a critical effective vertical stress ($\sigma'_{v,crit}$) determining the limit between "solid-like" and "fluid-like" behavior;
2) Compute γ_0 as the cumulative shear strain developed with an effective vertical stress σ'_v below $\sigma'_{v,crit}$. As illustrated in Figure 2.2, this leads to the calculation of two values of γ_0 (γ_0^+ and γ_0^-), one for each loading direction;
3) Compute γ_d as the cumulative shear strain developed during dilation with an effective vertical stress σ'_v above $\sigma'_{v,crit}$ (Figure 2.3). In consequence, only the shear strain experienced after crossing the dilatancy (or phase transformation) line and with an increasing shear stress level is considered in γ_d. Again, two values of γ_d are computed, one for each loading direction (γ_d^+ and γ_d^-);
4) Plot the values of γ_0 and γ_d versus the number of loading cycles.

2.3.2 Application on two undrained cyclic experiments

The selected framework was applied on one experiment from each of the following two sets of experiment series: (1) a series of undrained cyclic direct simple shear (DSS) tests conducted on Ottawa F-50 sand at UC Davis (Morales et al. 2021), and (2) a series of isotropically consolidated undrained cyclic triaxial (TXC) tests conducted on Karlsruhe fine sand (Wichtmann and Triantafyllidis 2016). Relevant features of both selected experiments are summarized in Table 2.1. Both DSS and TXC tests demonstrated similar patterns of evolution of γ_0 and γ_d, whose values were computed considering a $\sigma'_{v,crit}$ of 5 kPa. Sensitivity of the results regarding the selection of $\sigma'_{v,crit}$ is discussed in Section 2.3.3.

2.3.2.1 Direct simple shear test

Figure 2.4 summarizes results obtained for the DSS experiment illustrated in Figure 2.1 using a $\sigma'_{v,crit}$ of 5 kPa. From Figure 2.4a, γ_d is triggered at the 5th loading cycle when the specimen starts exhibiting dilative behavior. After liquefaction triggering, γ_0 starts increasing and following an almost linear trend (Figure 2.4b), while γ_d tends to stabilize to a saturation value (defined as γ_d^{sat}). The evolution of γ_0 suggests that the linear increase of post-liquefaction shear strains (Figure 2.1b) is mostly related to the strains developed at near-zero effective stress. It is however not possible to evaluate if the rate of γ_0 decreases at higher shear strains due to limitations of the DSS device. Negligible differences are noticed between both directions of loading.

2.3.2.2 Triaxial test

Figure 2.5 summarizes results obtained for the triaxial test using a $\sigma'_{v,crit}$ of 5 kPa. In this case, $\varepsilon_{1,0}$ and $\varepsilon_{1,d}$ are defined as the “solid-like axial strain” and “fluid-like axial strain”, respectively. In general, the evolution of $\varepsilon_{1,0}$ and $\varepsilon_{1,d}$ follows a similar pattern to the one observed for the DSS test. However, the saturation value of $\varepsilon_{1,d}$ (defined as $\varepsilon_{1,d}^{sat}$) obtained in extension is about 50% larger than the one obtained in compression. Since the evolutions of $\varepsilon_{1,0}$ in compression and extension are parallel to each other, the larger development of deviatoric strains in extension loading is mostly related to the development of strains during dilation.

2.3.3 Sensitivity on the selection of $\sigma'_{v,crit}$

Selecting a transition criterion between γ_0 and γ_d is critical for the implemented framework. Herein $\sigma'_{v,crit}$ was chosen as the threshold delineating the transition from the one to the other and results showed that it is a viable criterion. However, in order to assess the sensitivity of the evolution of γ_0 and γ_d subject to this selection, the DSS experiment was re-analyzed considering four different values of $\sigma'_{v,crit}$ (Figure 2.6). Smaller values of γ_0 and larger values of γ_d are obtained when considering a smaller $\sigma'_{v,crit}$, but the evolution patterns are very similar to each other. The main implication regarding the selection of $\sigma'_{v,crit}$ is related to the stabilization of γ_d, which is not as distinct when using a value of $\sigma'_{v,crit}$ smaller than 5 kPa. This lack of clarity could however be attributed to the limited shear strain level achieved in the DSS experiment and, in consequence, to the few loading cycles with effective vertical stresses below $\sigma'_{v,crit}$. Thus, although results show that effective vertical stresses can be used as the transition from solid-like to fluid-like behavior, further experimental work is required in order to reach final conclusions regarding the definition of a specific $\sigma'_{v,crit}$ and the uniqueness of this parameter as a threshold. Therefore, further experimental work is needed to fully understand the physical meaning of this transition and to define a less iterative selection of $\sigma'_{v,crit}$.

2.4 Insights from DEM simulations

This section explores the relationship between shear strain accumulation and the particle level mechanisms taking place during cyclic mobility. The evolution of the fabric descriptors introduced in Section 2.2.2 and obtained from DEM simulations available in the literature, is compared to the evolution of γ_0 and γ_d observed in the experimental data.

The evolution of contact-based fabric descriptors was assessed using a 2D DEM simulation of an undrained cyclic test (Figure 2.7a) available by Wang et al. (2016). This simulation shows an overall decrease of C_N from the beginning of the cyclic loading, followed by a sudden decrease upon liquefaction triggering (Figure 2.7b). For the pre-liquefaction regime, the gradual increase of γ_d in the experimental data is consistent with the loss of the interparticle contacts reflected by the decreasing trend of C_N. After liquefaction triggering, the range where C_N oscillates in each loading cycle stabilizes, in such a way that γ_d develops when C_N oscillates between 2.0 and 2.7, while γ_0 when C_N oscillates between 1.1 and 2.0. Therefore, the stabilization of γ_d in the post-liquefaction regime observed in the experimental data could be explained by a stabilization of the range where C_N oscillates in each loading cycle. However, the increasing trend of γ_0 in the post-liquefaction regime cannot be explained by that stabilization. This observation is consistent with other studies (Wei and Wang 2016, 2017) that suggest fabric descriptors based on orientations of interparticle contacts are not closely related to the fluid-like behavior during cyclic mobility. Thus, contact-based metrics may not be appropriate to characterize fluid-like behavior, but they may be able to characterize the pre-liquefaction regime as well as the solid-like behavior during cyclic mobility.

A better correlation can be found between the post-liquefaction behavior and void-based and distance-based fabric descriptors. Wei et al. (2018) concluded that void-based metrics, such as E_d and A_d, evolve along with γ_0 during cyclic mobility. The same authors found a linear relationship between A_d and γ_0 (Figure 2.7c), which indicates that the evolution of γ_0 in the post-liquefaction regime is associated to changes in the particle-void distribution of the grain assembly and defined a relationship between E_d and A_d (Hardening State Line) delineating regions of fluid-like and solid-like behavior. Using the distance-based descriptor MNPD, Wang et al. (2016) observed a relationship between γ_0 and the maximum MNPD achieved in each post-liquefaction loading cycle ($MNDP_{max}$). $MNPD_{max}$ and γ_0 exhibited a similar increase in magnitude while increasing the number of loading cycles (Figure 2.7d). Therefore, A_d and $MNPD_{max}$ are good candidates to quantifying the fabric evolution during cyclic mobility, given the good correlation between them and γ_0.

2.5 Conclusions and future work

Based on the approach of Shamoto et al. (1997), a framework for tracking the accumulation of post-liquefaction shear strains in laboratory tests was presented. The shear strain generated within each loading cycle is decoupled in two components: the shear strain at near-zero effective stress, denoted by γ_0, and the shear strain that occurs during dilation, denoted by γ_d. A critical effective vertical stress $\sigma'_{v,crit}$ is considered as the limit between γ_0 and γ_d. The framework was successfully applied in two undrained cyclic experiments (direct simple shear and triaxial tests). According to the analysis results, γ_d is triggered when the specimen starts exhibiting dilative behavior, and monotonically increases until it reaches a saturation value (γ_d^{sat}) at liquefaction triggering or few cycles after that. On the other hand, γ_0 initiates at liquefaction triggering and its evolution per loading cycle follows an almost linear trend. These results suggest that the linear increase of post-liquefaction shear strains is mostly related to shear strains developed at near-zero effective stress. Further experimental work is needed to elucidate if γ_0 decreases or arrests at higher strain levels.

The sensitivity of the results to the selection of $\sigma'_{v,crit}$ was investigated. It was found that the values of γ_0 and γ_d depend on the selected $\sigma'_{v,crit}$, but their overall evolutions follow similar patterns independently of the selected $\sigma'_{v,crit}$. The main implication regarding the selection of $\sigma'_{v,crit}$

is that the stabilization of γ_d is not as clear when using a smaller value of $\sigma'_{v,crit}$, which is probably related to the limited shear strain level achieved in the experiment.

The evolution of different fabric descriptors in previous DEM works was compared to the evolution of γ_0 and γ_d observed in the experimental data. Despite contact-based descriptors being the most straightforward to work with, they provide limited information during the post-liquefaction stage. For example, the coordination number shows no correlation with the accumulation of γ_0 during cyclic mobility. Conversely, void-based and distance-based descriptors, such as A_d and $MNPD_{max}$, seem to have better relationship with post-liquefaction shear strains.

The implemented framework and the associated fabric-based descriptors were shown to be promising, however further experimental work and DEM simulations are proposed to study the cyclic mobility behavior at large deformations. More specifically, future work will focus on: (1) investigating the possibility of achieving a saturation value for γ_0 at large strain levels, (2) evaluating the factors influencing the evolution of γ_0 and γ_d, and (3) elucidating the relationship between the particle level response and the development of γ_0 and γ_d. Results of this work are expected to provide insights regarding the fundamental mechanism controlling the post-liquefaction shear strain accumulation towards future improvements in constitutive models for liquefaction analysis.

The proposed framework will be applied in undrained cyclic DSS tests to be performed at UC Davis in a recently acquired device able to achieve large shear strain levels (γ_{SA} up to 10%). The testing plan considers experiments on sands with different particle properties (e.g., grain shape, mean grain size, gradation) and subjected to different loading conditions (e.g., sloping-ground conditions, non-uniform cyclic loading). These experiments will allow the study of the evolution of γ_0 and γ_d at large strain levels, and to explore correlations of γ_d^{sat} and the rate of γ_0 per loading cycle with relative density, loading conditions, and grain properties.

2.6 References

Morales, B., Humire, F., and Ziotopoulou, K. 2021. Direct Simple Shear Testing on Ottawa F50 and F65 Sand. DesignSafe-CI [publisher], Dataset.

Oda, M., Nemat-Nasser, S., and Konishi, J. 1985. Stress-induced anisotropy in granular masses. *Soils and Foundations* 25(3): 85-97.

O'Sullivan, C. and Cui, L. 2009. Micromechanics of granular material response during load reversals: Combined DEM and experimental study. *Powered Technology* 139: 289-302.

Shamoto, Y., Zhang, J.-M., and Goto, S. 1997. Mechanism of large post-liquefaction deformation in saturated sand. *Soils and Foundations* 37(2): 71-80.

Tasiopoulou, P., Ziotopoulou, K., Humire, F., Giannakou, A., Chacko, J., and Travasarou, T. 2020. Development and implementation of a semi- empirical framework for modeling post-liquefaction deformation accumulation of sands. *Journal of Geotechnical and Geoenvironmental Engineering* 146(1): 4019120.

Thornton, C. 2000. Numerical simulations of deviatoric shear deformation of granular media. *Géotechnique* 50(1): 43-53.

Wang, G. and Wei, J. 2016. Microstructure evolution of granular soils in cyclic mobility and post-liquefaction process. *Granular Matter* 18(3): 51.

Wang, R., Fu, P., Zhang, J.-M., and Dafalias, Y. F. 2016. DEM study of fabric features governing undrained post-liquefaction shear deformation of sand. *Acta Geotechnica* 11(6): 1321-1337.

Wei, J. and Wang, G. 2015. Microstructure evolution of granular soils during liquefaction process. In Kenichi Soga (ed.). *Proc. Intern. Symp. on Geomechanics from Micro to Macro, Cambridge 1-3 September 2014*.

Wei, J. and Wang, G. 2017. Discrete-element method analysis of initial fabric effects on pre- and post-liquefaction behavior of sands. *Géotechnique Letters* 7(2): 61-166.

Wei, J., Huang, D., and Wang, G. 2018. Microscale descriptors for particle-void distribution and jamming transition in pre- and post-liquefaction of granular soils. *Journal of Engineering Mechanics* 144(8): 4018067.

Wichtmann, T. and Triantafyllidis, T. 2016. An experimental database for the development, calibration and verification of constitutive models for sand with focus to cyclic loading: Part I - tests with monotonic loading and stress cycles. *Acta Geotechnica* 11(4): 739-761.

Wiebicke, M., Andò, E., Herle, I., and Viggiani, G. 2017. On the metrology of interparticle contacts in sand from x-ray tomography images. *Measurement Science and Technology* 28(12): 124007.

Zhang, J.-M. and Wang, G. 2012. Large post-liquefaction deformation of sand, part I: Physical mechanism, constitutive description and numerical algorithm. *Acta Geotechnica* 7(2): 69-113.

Zhuang, H., Wang, R., Chen, G., Miao, Y., and Zhao, K. 2018. Shear modulus reduction of saturated sand under large liquefaction-induced deformation in cyclic torsional shear tests. *Engineering Geology* 240: 110-122.

Ziotopoulou, K. and Boulanger, R. W. 2016. Plasticity modeling of liquefaction effects under sloping ground and irregular cyclic loading conditions. *Soil Dynamics and Earthquake Engineering* 84: 269-283.

2.7 Tables and figures

Table 1. Summary of the experimental data.

Test	**DSS**	**Triaxial**
Relative Density, D_R (%)	63	79
Initial Effective Stress, σ'_{vo}* (kPa)	100	100
Cyclic Stress Ratio, CSR	0.16	0.25
Material	Ottawa F-50	Karlsruhe fine sand
Grain Shape	Sub-rounded	Sub-angular
Reference	Morales et al. (2021)	Wichtmann and Triantafyllidis (2016)

*Vertical consolidation stress for the DSS test and isotropic effective stress for the triaxial test.

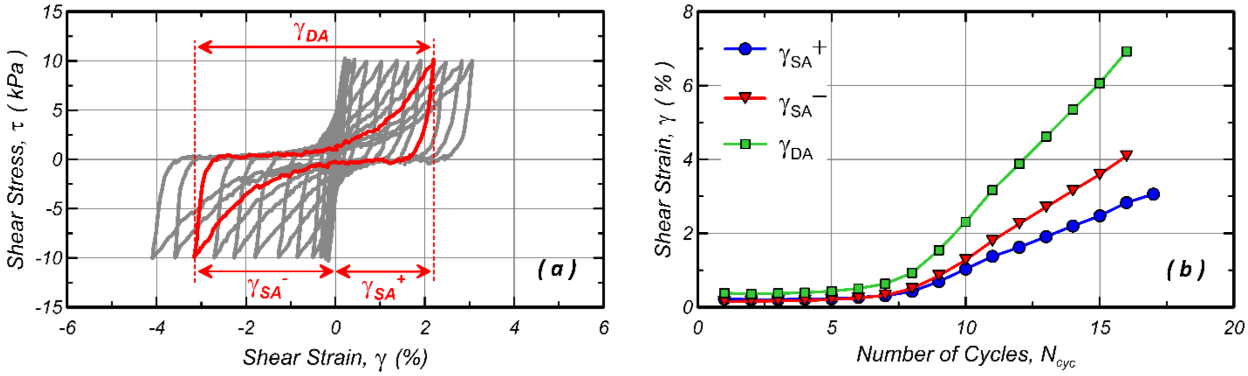

Figure 2.1. Results of an undrained cyclic direct simple shear test on Ottawa F-50 sand (Morales et al. 2021): (a) definition of single amplitude shear strains (γ_{SA}^{+} and γ_{SA}^{-}) and double amplitude shear strain (γ_{DA}), nd (b) evolution of γ_{SA}^{+}, γ_{SA}^{-} and γ_{DA} per loading cycle (after Tasiopoulou et al. 2020).

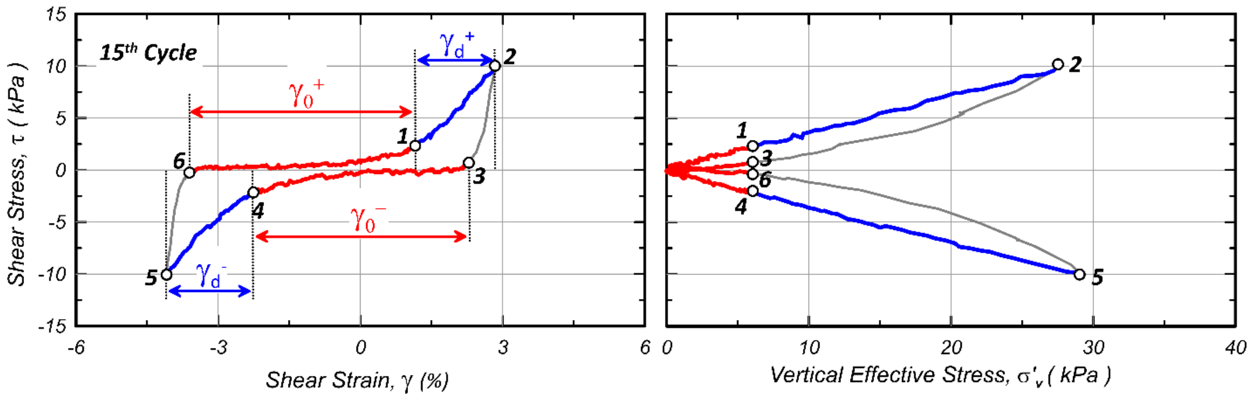

Figure 2.2. Near-zero effective shear strain (γ_0) and shear strain during dilation (γ_d) for the 15th loading cycle of the test illustrated in Figure 2.1 (modified after Tasiopoulou et al. 2020).

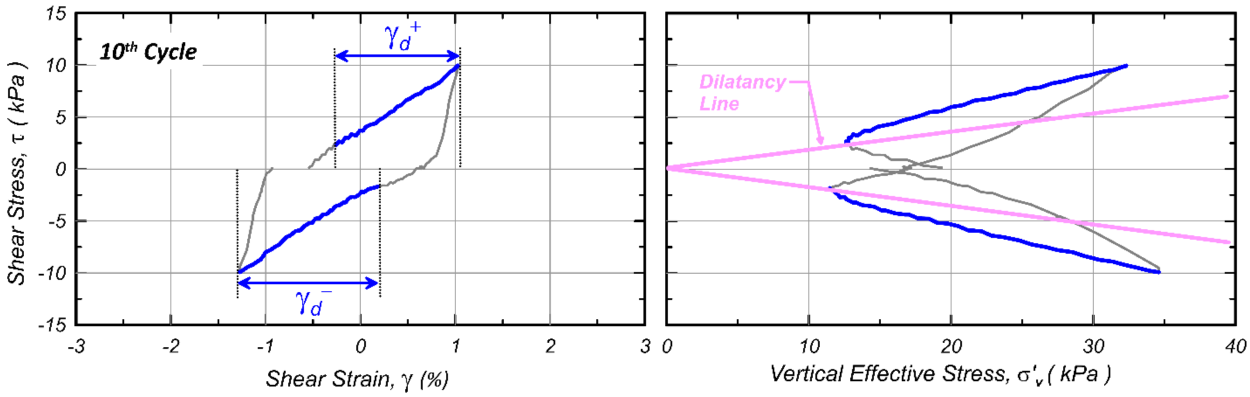

Figure 2.3. Estimation of γ_d before liquefaction triggering (in blue). Example for the 10th loading cycle of the test illustrated in Figure 2.1 using $\sigma'_{v,crit}$ = 5 kPa.

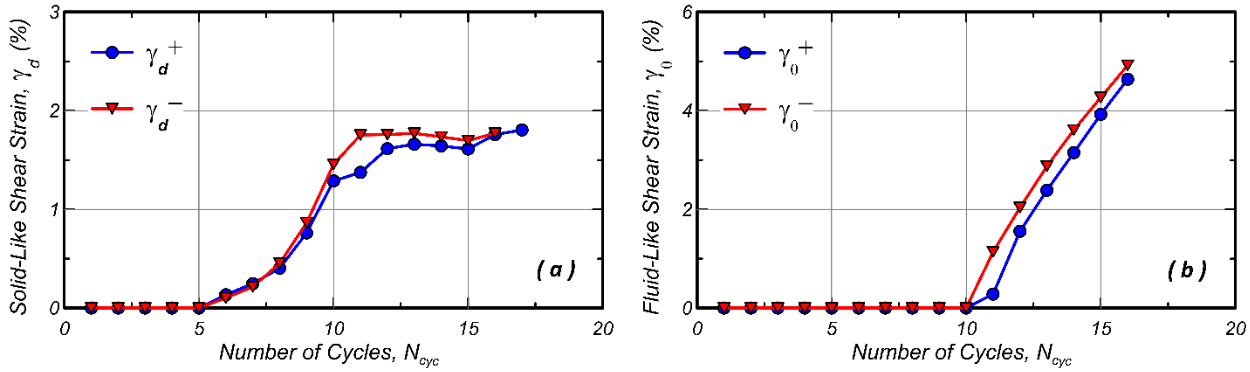

Figure 2.4. Shear strain accumulation for the cyclic DSS test of Morales et al. (2021): (a) evolution of γ_d, and (b) evolution of γ_0.

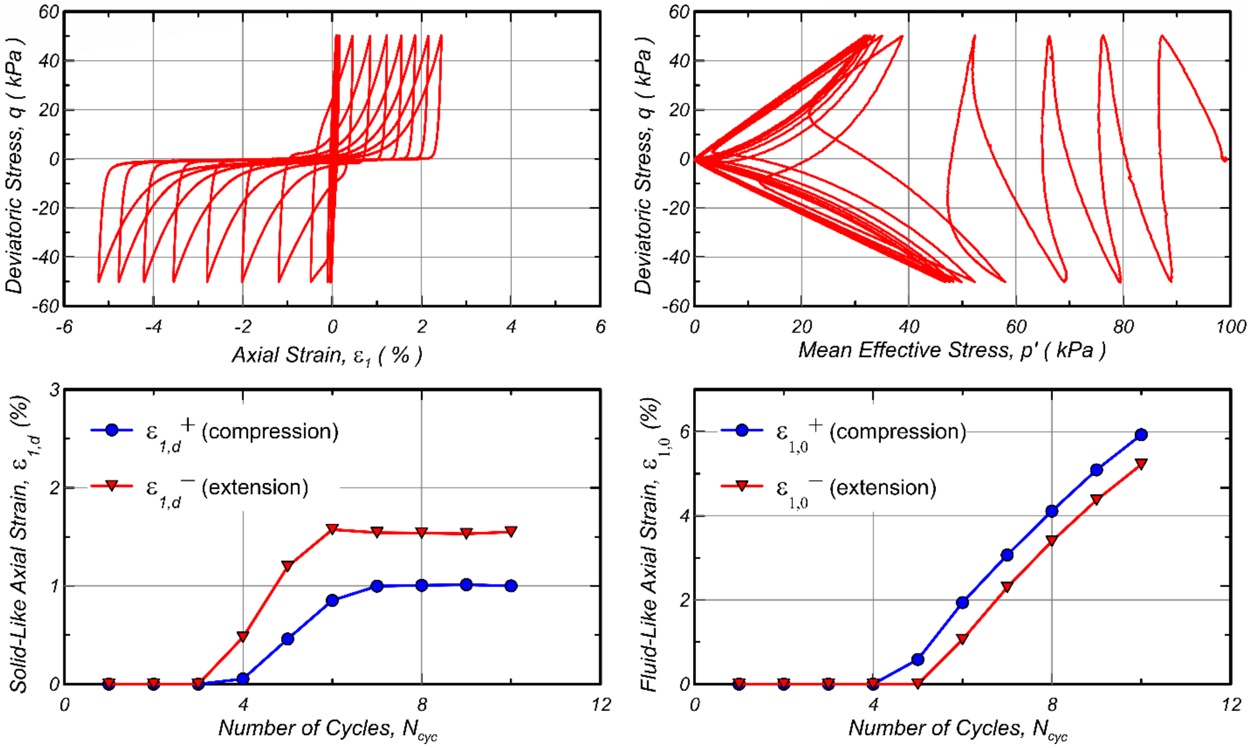

Figure 2.5. Evolution of $\varepsilon_{1,0}$ and $\varepsilon_{1,d}$ for the cyclic triaxial test of Wichtmann and Triantafyllidis (2016).

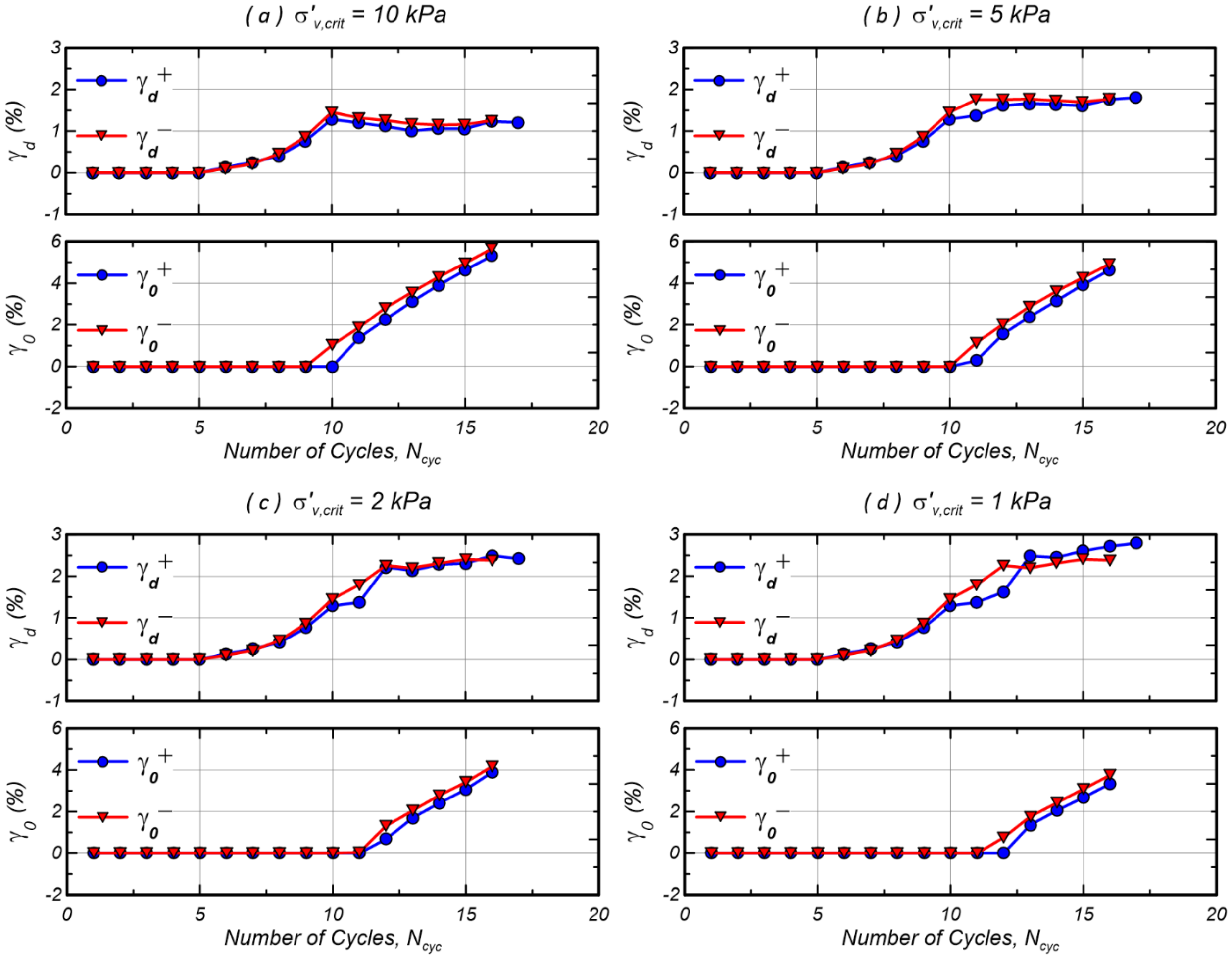

Figure 2.6. Evolution of γ_0 and γ_d in the DSS experiment for different values of $\sigma'_{v,crit}$: (a) $\sigma'_{v,crit}$ = 10 kPa, (b) $\sigma'_{v,crit}$ = 5 kPa, (c) $\sigma'_{v,crit}$ = 2 kPa, and (d) $\sigma'_{v,crit}$ = 1 kPa.

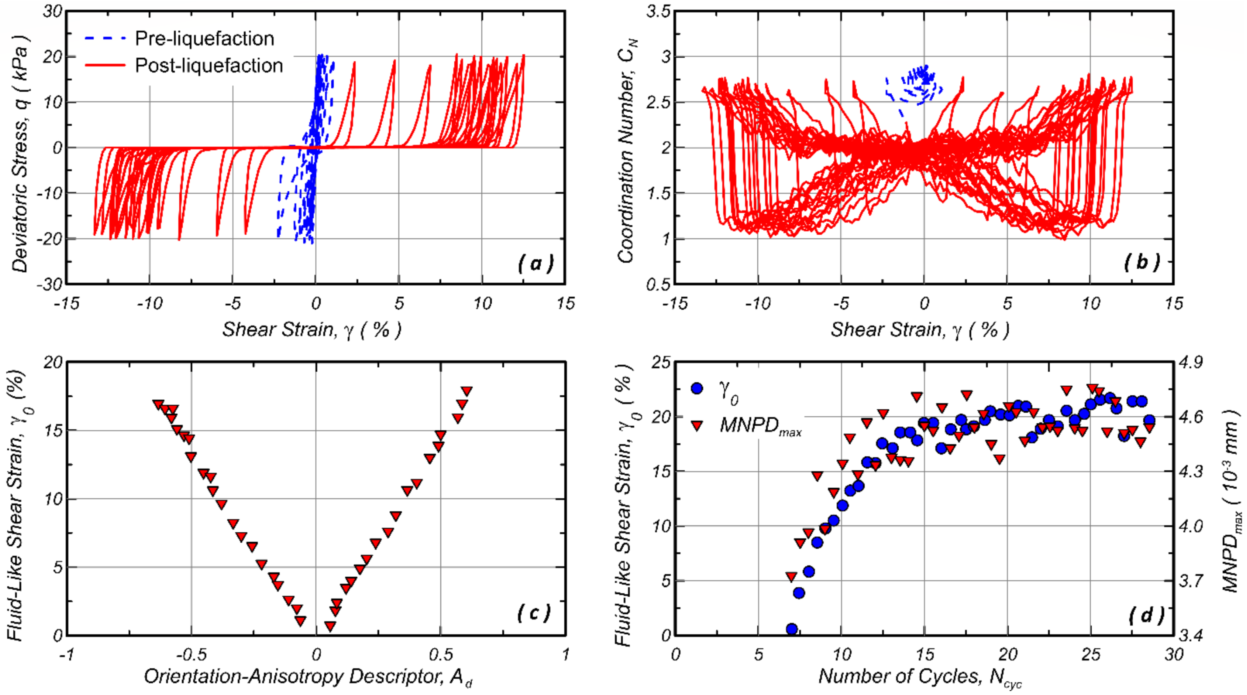

Figure 2.7. (a) Example of cyclic mobility 2D DEM simulation (data from Wang et al. 2016), (b) evolution of coordination number with shear strain (data from Wang, et al. 2016), (c) correlation between void orientation anisotropy, A_d, and fluid-like strain, γ_0, (after Wei et al. 2018), and (d) correlation between maximum mean neighboring particle distance $MNPD_{max}$, and γ_0 (replotted data after Wang et al. 2016).

Chapter 3

Development and evaluation of pre-conditioning protocols for sand specimens in constant-volume cyclic direct simple shear tests

Author's note: This Chapter was submitted as a technical note authored by Francisco Humire, Minyong Lee, Katerina Ziotopoulou, Michael G. Gomez, and Jason T. DeJong to the ASTM Geotechnical Testing Journal. The technical note is currently under review and is presented herein with some minor edits for consistency with the other chapters of this Dissertation.

Abstract

Textured platens are often used to improve the transfer of shear stresses from the platens to the soil specimen during direct simple shear (DSS) tests. However, constant-volume DSS tests when textured platens are used can be affected by inadequate engagement of the soil at the platen-soil interface leading to large reductions in the vertical stress at the start of shearing. The application of a pre-conditioning sequence involving small-strain drained cycles prior to constant-volume shearing can improve engagement at the soil-platen interface, but when excessively implemented, it can also have adverse effects on the measured soil behavior (e.g., strength, stiffness). A series of constant-volume cyclic DSS tests preceded by different pre-conditioning sequences were

performed to evaluate the effect of pre-conditioning on: (1) the engagement of sand specimens at the platen-soil interface, and (2) the stress-strain response of these specimens. Results showed that textured platens that are properly engaged with sand specimens can reduce slippage at the platen-soil interface. This engagement can be achieved by applying a limited number of small-strain drained cycles at a low vertical stress, while still obtaining representative soil behavior during the subsequent equivalent undrained constant-volume cyclic loading. Although the pre-conditioning protocol presented herein is specific to the testing equipment and materials considered, similar procedures may be adopted to develop pre-conditioning protocols for other soils, platens, and testing devices.

3.1 Introduction

ASTM (2019) specifies that constant-volume cyclic direct simple shear (DSS) tests should be performed using flat porous platens, which should have pores that are fine enough to prevent soil intrusion, and should provide enough roughness to effectively transmit shear stresses to specimens. Porous ceramic, sintered brass, or sintered steel flat platens of different porosities have been commonly used for this purpose, in all cases demonstrating the ability to provide stiff boundaries in the top and bottom surfaces. The ability of such platens to properly transfer shear stresses to specimens depends on their surface roughness, defined by the surface finishing process during manufacturing. Figure 3.1 presents examples of flat platens available for DSS testing, including measurements of their surface roughness. Flat platens with appropriate surface roughness (e.g., Figure 3.1b) have been shown to effectively transfer shear stresses to both fine-grained soils (e.g., Price et al. 2017) and fine sands (e.g., Morales et al. 2021). However, some flat platens (e.g., smooth sintered stainless steel platens) may not be sufficiently rough (e.g., Figure 3.1d) to prevent slippage at the top platen and soil specimen interface. Prevost and Høeg (1976) concluded that the shear stress distribution in the sample can be severely affected as a consequence of slippage along this platen-soil interface. Previous experimental works suggest that such slippages can be reduced by using textured platens, such as platens with embedded pins (e.g., Porcino and Diano 2016; Robinson et al. 2019) or protruding ridges (e.g., Kovacs and Leo 1981; Milatz and Grabe 2015).

Despite their ability to limit slippage, the use of textured platens can also lead to improper engagement of soil specimens at the end of the consolidation phase, resulting in excessive voids at the platen-soil interface. If the presence of such voids is not mitigated prior to constant-volume cyclic loading, large and non-representative reductions in vertical stresses can take place early on during shearing. This can result in both erroneous stress-strain behavior and localization of shear strains at the top platen-soil interface.

Previous research (Andersen 2009; Rees 2016) indicates that engagement of soil specimens at the top platen-soil interface can be improved through the application of a pre-conditioning sequence consisting of low amplitude drained cycles prior to shearing. Pre-conditioning drained cycles are intended to fully engage the top platen with the soil specimen prior to shearing events.

The application of pre-conditioning sequences may also improve the mobilization of lateral stresses within specimens, therefore creating near K_0 conditions in the specimen prior to shearing (Dyvik 2019). These near K_0 conditions were demonstrated by measurements of lateral stresses in DSS specimens by Dyvik (2019), which showed that lateral stresses may not be fully mobilized when only vertical stresses (seating and consolidation) are applied due to soil arching effects and the shedding of a portion of the applied vertical stress to specimen sidewalls. The application of pre-conditioning sequences, however, have been shown to mitigate such stress localizations while increasing the horizontal stresses mobilized in specimens (Finn 1981; Andersen 2009), therefore allowing for more representative and repeatable K_0 conditions to be established prior to undrained cyclic shearing.

Previous research has shown that the application of low amplitude cycles prior to undrained cyclic shearing can also lead to significant increases in liquefaction resistance (Finn et al. 1970; Seed et al. 1977; Finn 1981; Andersen 2009; Nelson and Okamura 2019). This increase not only results from an improved engagement of specimens at end platen interfaces and increases in K_0 coefficients, but also due to changes in the soil fabric due to pre-straining effects (Finn 1981; Andersen 2009). These past studies have also shown that changes in specimen liquefaction resistances depend on both the number and amplitude of the loading cycles applied before shearing. Therefore, the number and amplitude of pre-conditioning cycles must be carefully selected to minimize excessive changes in subsequent soil responses.

Although pre-conditioning sequences are commonly used, procedures to determine the number of drained cycles needed to engage specimens without excessively altering their soil behaviors (e.g., strength, stiffness) remain non-standardized. The objectives of this work are to: (1) confirm that textured platens can be used as a viable method to prevent slippage at the top platen-sand interface, when the sand is incompatible with the flat platens' available roughness, (2) assess the effects of pre-conditioning loading sequences on the initial relative density (D_R) and stress-strain response of sand specimens, and (3) present a testing plan that can be used to develop lab-specific pre-conditioning protocols for constant-volume cyclic DSS tests on reconstituted sand specimens. This is achieved by conducting DSS tests with different top platen geometries and pre-conditioning loading sequences using a fixed cyclic strain amplitude, and comparing test results with experimental information available in the literature for the same sand and stress conditions. Although pre-conditioning is expected to improve both the initial establishment of K_0 conditions within DSS specimens and the transfer of shear stresses during cyclic shearing, only the latter effect was evaluated in this study as it reflects the collective impacts of both factors on specimen behaviors. The engagement issues at the top platen-soil interface presented in this work, as well as the pre-conditioning protocol identified through this study, are specific to the testing equipment and type of materials considered in this investigation. Recommendations are provided regarding the development of pre-conditioning procedures for other testing conditions; however, further research is recommended given the numerous factors affecting the engagement at the top-platen interface (e.g., platen geometry, platen roughness). In addition to the specific objectives of this paper, the present study is intended to highlight the sensitivity of results to lab-specific testing protocols and to broadly encourage the dissemination of thorough and complete testing procedures.

3.2 Experimental setup and procedures

3.2.1 Equipment

An Electromechanical Dynamic Cyclic Simple Shear (EMDCSS) device manufactured by GDS Instruments was used to perform all the constant-volume cyclic direct simple shear (DSS) tests presented herein. Constant-volume conditions were enforced with the active height control system implemented in the EMDCSS device, which achieved vertical strain fluctuations of less than 0.01% in all tests, which met the 0.05% criterion recommended by ASTM (2019) and the 0.025% threshold recommended by Zekkos et al. (2018). Cylindrical samples near 22 mm in height and 70 mm in diameter were laterally enclosed within stacked Teflon-coated steel rings and a latex membrane of about 0.3 mm in thickness. Three types of sintered stainless steel porous platens were used to transmit the shear forces to the sand specimens: flat platens (Figure 3.1c), platens with protruding ridges of 1 mm in height, 2 mm in width and with a spacing of about 6 mm between the tip of ridges (Figure 3.2a), and platens with embedded pins of 2 mm in height with a spacing of about 7 mm between pins (Figure 3.2b). During tests involving platens with protruding ridges, platen ridges were oriented perpendicular to the direction of shearing. Gypsum was applied to fill all voids in exposed head screws that secured porous platens to end caps in order to eliminate the potential for soil migration into screw voids during shearing.

3.2.2 Material and previous testing

Experiments were conducted on specimens of Ottawa F-65 sand, which was the primary soil used in the Liquefaction Experiments and Analysis Projects or LEAP (Kutter et al. 2020). In the context of the LEAP project, this soil was classified as a poorly-graded sand (SP), with a mean grain size (D_{50}) of 0.20 mm, a coefficient of uniformity (C_u) of 1.47, and no fines (Carey et al. 2020). A range of values for the maximum and minimum void ratios (e_{max} and e_{min}) have been reported for Ottawa F-65 by different LEAP researchers (Vasko 2015; Parra Bastidas 2016; Carey et al. 2020). Carey, Stone, and Kutter (2020) concluded that the index properties of the Ottawa F-65 sand used in different research facilities are relatively consistent, and that the variability in the index dry densities are associated with operator variability. They recommended the use of an e_{max} of 0.78 and an e_{min} of 0.51 for future analyses on Ottawa F-65 sand for the LEAP project. These values were used for the calculation of relative densities for all tests presented in this study.

The development of pre-conditioning protocols was guided using two experimental datasets developed through the LEAP project for the same material, including hollow cylinder tests performed by Ueda et al. (2018) and DSS tests performed by Morales et al. (2021). The high quality and reliability of these datasets is reflected in the detailed documentation of experimental procedures, observations which confirm specimens did not experience slippage and/or shear localization prior to liquefaction triggering, compliance with ASTM specifications (e.g., vertical strains below ±0.05% for constant-volume DSS tests), and other procedures followed to maintain a high level of consistency and repeatability in the produced data (El Ghoraiby et al. 2020). All tests presented in these datasets were performed using reconstituted (via air pluviation) Ottawa F-65 specimens, and shear stresses were applied to sand specimens using flat porous ceramic platens (Figure 3.1a) but without pre-conditioning. Cyclic stress ratios from hollow cylinder tests ($\mathrm{CSR_{HC}}$) were converted using Equation 3.1 to estimate CSR values expected during simple shear conditions ($\mathrm{CSR_{DSS}}$) while assuming a coefficient of earth pressure at rest (K_0) of 0.5 (Ishihara 1996).

$$CSR_{DSS} = \frac{1 + 2K_0}{3} CSR_{HC} \tag{3.1}$$

3.2.3 Procedures and testing plan

All samples were prepared using air pluviation, which involved raining oven dried sand from a constant fall height to create soil specimens. The performed testing plan aimed to evaluate the effect of top platen geometries and seating loads during the pre-conditioning process (Table 3.1). Prior to pre-conditioning, samples were subjected to a seating vertical stress of either 25 or 100 kPa, and were either saturated with de-ionized water or remained dry as indicated in Table 3.1. Then, samples were subjected to a pre-conditioning protocol wherein identical strain-controlled drained cycles with an amplitude of 0.01 mm (about 0.045% shear strain) were applied at a frequency of 0.1 Hz (Figure 3.3a). The number of pre-conditioning cycles ($N_{\text{pre-cond}}$) varied between 0 and 200 cycles and induced changes in both the measured vertical strains and the secant shear moduli (Figure 3.3b). After completing the pre-conditioning protocol, the vertical stress was either maintained or increased to the target initial consolidation stress (100 kPa) for all specimens.

Finally, all samples were subjected to constant-volume cyclic shearing wherein stress-controlled cycles were applied at a frequency of 0.05 Hz.

3.3 Test results and discussion

3.3.1 Effect of pre-conditioning and platen geometry

Figure 3.4 presents the results of three DSS tests prepared to the same relative density (D_R = 60%) and subjected to the same initial consolidation stress (σ'_{vc} = 100 kPa) and cyclic stress ratio (CSR = 0.10), but with different top platens and pre-conditioning sequences including: (1) sintered stainless steel flat platens without pre-conditioning, (2) ridged platens without pre-conditioning, and (3) ridged platens with 115 pre-conditioning drained cycles with an amplitude of about 0.045% shear strain. As shown in Figure 3.5, past tests by Ueda et al. (2018) and Morales et al. (2021) suggested that approximately 40 loading cycles were needed to trigger liquefaction (defined with a double amplitude strain criterion of γ_{DA}=6%) for similar conditions. For tests conducted with sintered stainless steel flat platens (Figure 3.4a) liquefaction triggering occurred after only 4 loading cycles and large shear strains developed immediately post-triggering. These behaviors can be associated with slippage observed at the top platen and soil interface during the application of the undrained cyclic loading, which occurred due to the inadequate roughness of the sintered stainless steel flat platens (Figure 3.1d) and resulted in shear stresses not being properly mobilized through the sand specimen. When ridged platens were used instead (Figure 3.4b), a slight increase in the number of cycles required to trigger liquefaction as well as reductions in post-triggering shear strains occurred. Despite some improvement in the transfer of shear stresses when using the ridged platens, the number of cycles needed to trigger liquefaction remained significantly less than similar tests from the literature (Figure 3.5), suggesting that the soil specimen remained poorly engaged at the top platen interface. Observations of arching in the corners of sheared specimens also suggested a poor engagement at the top platen interface. In contrast, when tests were performed using ridged platens and 115 pre-conditioning drained cycles (Figure 3.4c), both pre- and post-triggering behaviors agreed well with similar tests from the literature. This result was attributed to the rearrangement of soil particles at the platen-soil interface, which improved contact between the textured porous platen and soil specimen. The improvement of engagement at the platen-soil interface was also supported by observations of more uniform shear deformations along the height of the sheared specimens.

3.3.2 Development of lab-specific pre-conditioning protocols

A lab-specific pre-conditioning protocol was developed for specimens with ridged platens by performing tests at identical D_R, σ'_{vc}, and CSR values, but with different numbers of drained pre-conditioning strain-controlled cycles ($N_{pre\text{-}cond}$) applied at a vertical effective stress of 25 kPa (Test Group 3a in Table 3.1). The application of drained pre-conditioning cycles induced minor changes in specimen heights and, therefore, gradually increased specimen D_R values. Figure 3.6a presents changes in specimen D_R values resulting from pre-conditioning as a function of the number of drained pre-conditioning cycles applied. As shown, large increases in D_R values resulted from the application of the first 100 drained pre-conditioning cycles, which was primarily attributed to the elimination of voids present initially at the top platen-soil interface. Figure 3.6a also presents changes in D_R values which resulted from increasing vertical stresses from 25 kPa (after pre-conditioning) to 100 kPa. Such changes were larger for tests with smaller $N_{pre\text{-}cond}$ due to the existence of voids at the platen-sand interface, which became partially filled when increasing the vertical stress.

Figure 3.6b presents increases in the number of cycles required to trigger liquefaction as a function of the number of drained pre-conditioning cycles applied. Apparent increases in specimen triggering resistances again resulted from the improved engagement of specimens at the top platen-soil interface, but may have also resulted from an increase in K_0 coefficients and changes in soil fabrics (Finn 1981; Andersen 2009). Large and progressive increases in the number of loading cycles required to trigger liquefaction were observed for specimens receiving over 100 pre-conditioning cycles. For these specimens, progressive increases in measured secant moduli and relative densities with increasing drained cycles suggested that the majority of voids present at the top platen-soil interface were eliminated during the first 100 pre-conditioning cycles. Subsequent cycles were found to dramatically increase cyclic resistances, which can be likely attributed to progressive changes in initial soil fabrics resulting from pre-straining effects (Finn 1981; Andersen 2009). Therefore, pre-conditioning protocols must be developed in order to ensure the engagement of specimens at the top platen-soil interface, while minimizing adverse effects on initial soil fabrics and subsequent soil responses.

Independent experimental data from previous studies suggested that for similar conditions, air-pluviated specimens of Ottawa F-65 sand should require near 40 loading cycles to trigger liquefaction for a CSR of 0.10 (Figure 3.5). For the materials, equipment, and procedures used during this testing, it was therefore identified that 115 strain-controlled drained cycles, with an amplitude of about 0.045% shear strain, should be applied under a vertical effective stress of 25 kPa during pre-conditioning to prepare specimens that achieve liquefaction triggering after 40 undrained cycles (CSR = 0.10, σ'_{vc} = 100 kPa) consistent with similar past studies.

This pre-conditioning protocol was used to develop liquefaction triggering plots for specimens with identical D_R and σ'_{vc} values but with different applied cyclic stress ratios (Test

Group 3b, Table 3.1). Liquefaction triggering curves were determined for specimens with ridged platens using both the identified pre-conditioning protocol as well as no pre-conditioning (Figure 3.5). Triggering curve data obtained using the identified pre-conditioning protocol agreed well with data from similar past studies and exhibited higher liquefaction resistances when compared to similar tests without pre-conditioning.

3.3.3 Changes in subsequent undrained behaviors due to pre-conditioning

In the previous section, it was shown that the application of more than 100 pre-conditioning cycles can lead to a large increase in liquefaction triggering resistances, which was associated with progressive changes in soil fabrics due to pre-shearing effects. However, the precise number of cycles after which pre-shearing effects begin to alter soil fabrics and subsequent soil behaviors cannot be definitively identified. It is therefore necessary to acknowledge that some changes in soil fabrics may occur during pre-conditioning sequences, which may alter subsequent soil behaviors. The experimental data presented herein is solely representative of reconstituted specimens subjected to a pre-conditioning sequence prior to shearing. Still, the described approach for improving platen-soil engagement may be useful for parametric investigations using reconstituted specimens wherein all samples are prepared and pre-conditioned in identical manners. Although undisturbed sand samples are not commonly used for laboratory testing, the application of pre-conditioning sequences to such samples is not recommended as this may induce unknown disturbances and changes in in-situ soil fabrics, all of which were not examined in this study.

Changes in subsequent soil behaviors not only depend on the number of drained pre-conditioning cycles, but also on the loading conditions at which pre-conditioning is performed. Following the identification of a pre-conditioning protocol, a series of DSS tests were performed to investigate the effect of changes in the vertical effective stress present during pre-conditioning. Collectively, the results of these tests suggested that when the vertical effective stress present during pre-conditioning cycles was larger, a smaller number of drained cycles was required to effectively engage specimens. As shown in Figure 3.5, when pre-conditioning cycles were applied at a vertical effective stress of 100 kPa (rather than 25 kPa used in the previously discussed protocol), only 50 drained cycles were required for specimens to obtain similar liquefaction resistances. While consistency of liquefaction resistances with past studies could be achieved with either protocol, the presence of a vertical effective stress during pre-conditioning that was identical to the final consolidation stress (i.e., 100 kPa) appeared to significantly affect specimen contractive tendencies during the onset of undrained cyclic loading. As shown in Figure 3.7, much smaller reductions in vertical effective stresses were observed during the first cycle for specimens pre-conditioned at 100 kPa when compared to similar specimens pre-conditioned at 25 kPa despite having similar triggering resistances. The greater initial contraction observed in specimens pre-conditioned at lower vertical effective stresses is more representative of behaviors expected for normally-consolidated specimens, which suggests that over-consolidation of specimens may result from pre-conditioning at a vertical effective stress that is identical to the target consolidation stress. It is recommended that pre-conditioning therefore be performed at a vertical effective stress level of no more than 25% of the target consolidation vertical effective stress in order to reset the stress history of specimens prior to undrained shearing.

3.3.4 Recommendations for developing lab-specific pre-conditioning protocols

While this study presents the rationale and testing processes needed to develop lab-specific pre-conditioning protocols for constant-volume DSS tests, details regarding applied stresses and cycle numbers are specific to the equipment, materials, and procedures used. Therefore, it is recommended that researchers perform similar experiments involving the application of different numbers of pre-conditioning cycles to evaluate the appropriate level of pre-conditioning required for other platen geometries, soil gradations/angularities, preparation procedures, and equipment. For example, Figure 3.8 compares results obtained for loose Ottawa F-65 sand specimens pre-conditioned under a vertical effective stress of 100 kPa using either ridged or pinned platens with varying numbers of applied pre-conditioning cycles. As shown, when 0 to 80 pre-conditioning cycles are applied prior to shearing, specimens with pinned platens exhibited similar liquefaction resistances compared to similar specimens with ridged platens. However, triggering resistances are quite different when 150 pre-conditioning cycles are applied, suggesting further investigation of the effect of platen geometries is needed. While both platen types can be used, lab-specific testing can help identify the effect of such variables and adjust pre-conditioning protocols to maintain consistency of testing data with reliable benchmarks from the literature and/or other testing devices.

The lab-specific protocol identified in this study was guided by past experimental data available for Ottawa F-65 sand. In the absence of such reference tests, it is recommended to perform a testing plan similar to that presented herein in order to examine the effect of the number of pre-conditioning cycles ($N_{\text{pre-cond}}$) on changes in specimen D_R, secant moduli values, and numbers of loading cycles required to trigger liquefaction. The stabilization of changes in D_R (Figure 3.6a) and the sudden increase in N_{liq} (Figure 3.6b) may be used as criteria to define an appropriate $N_{\text{pre-cond}}$ for which engagement at the top platen-soil interface is improved without excessively altering soil responses. Using similar criteria for the tests shown in Figure 3.6, the value of $N_{\text{pre-cond}}$ would be approximately 100, which is very close to the value determined by comparison with reference tests ($N_{\text{pre-cond}} = 115$). Lastly, additional geotechnical testing of similar specimens using alternative testing devices (e.g., triaxial, hollow cylinder) can provide importance reference data needed to develop and verify lab-specific pre-conditioning protocols.

3.4 Conclusions

Ensuring the effective transfer of shear stresses to soil specimens is a key requirement for all DSS tests. This transfer can be accomplished using flat platens as recommended by ASTM (2019), but care must be taken to ensure that platens have a roughness compatible with the tested soil to avoid slippage at the top platen-soil interface (e.g., Morales et al. 2021). If in a given equipment the flat platens are found to not be adequate, the use of porous platens with protrusions (e.g., ridges, pins) can provide the ability to effectively transfer shear stresses within sand specimens without slippage at the top-platen soil interface. Although textured platens alone offer improved engagement, pre-conditioning consisting of the application of small-strain drained cyclic loading is needed to ensure that voids are removed from the top platen-soil interface.

The pre-conditioning protocol developed in this study consists of the application of strain-controlled drained cycles prior to consolidation to the target overburden stress. The number of pre-conditioning drained cycles ($N_{pre\text{-}cond}$) required to ensure specimen engagement was determined by: (1) analyzing changes in D_R resulting from the application of drained cycles, and (2) comparing the number of loading cycles required to trigger liquefaction (N_{liq}) to past experimental data available for the same tested material. A pre-conditioning phase consisting of the application of 115 strain-controlled drained cycles (0.045% shear strain amplitude) under a vertical effective stress of 25 kPa was found to effectively engage sand specimens at the top platen-sand interface, without significantly affecting the stress-strain response of reconstituted Ottawa F-65 sand specimens as suggested by the consistency between the achieved data and the results of similar past studies. Although the identified pre-conditioning protocol is specific to the materials, equipment, and procedures used in this study, recommendations are provided which can be used to develop similar procedures for tests involving other conditions including textured platens with varying geometries, other equipment and preparation procedures, and different sandy soil types.

While pre-conditioning sequences can improve specimen engagement at platen-sand interfaces, pre-conditioning can also result in significant changes in subsequent soil responses. These effects can include changes in specimen volumetric tendencies during the onset of undrained cyclic loading, such as the case when pre-conditioning is applied at a vertical stress similar to the target consolidation stress, as well as dramatic increases in triggering resistances, such as the case when an excessive number of pre-conditioning drained cycles is applied. The selection of pre-conditioning procedures should always be evaluated with reference to a testing plan's primary objectives and scope in order to ensure that its effects on the soil behaviors of interest (e.g., liquefaction resistance) are more fully understood. Although not considered in this study given the complexity of the engagement issues at the platen-soil interface, further work is required to investigate the importance of other variables (e.g., drained pre-conditioning cycle strain amplitudes, soil grain size, platen geometry and roughness, loading frequency) on pre-conditioning sequences, and their collective effects on behaviors of interest. The sensitivity of tests characterizing liquefaction resistances to both sand-platen engagement and pre-conditioning sequences also highlights remaining concerns regarding the repeatability of DSS results across different laboratories and research facilities. For that reason, the authors encourage the performance of a collaborative round robin testing program to assess the repeatability of DSS testing results on sandy soils which have no existing reference test data.

Finally, the presented DSS tests were aimed at evaluating the liquefaction behavior of sands, and responses of interest (e.g., cycles required for liquefaction triggering) were shown to depend strongly on the pre-conditioning protocols followed. Thus, the utility of similar laboratory testing results will strongly rely on the thorough documentation and dissemination of all testing procedures (e.g., pre-conditioning). This information is valuable for evaluating uncertainties, providing more robust experimental databases, supporting future reexaminations of published data, and promoting progressive improvements in both laboratory equipment and testing protocols.

3.5 References

Andersen, K. H. 2009. Bearing Capacity Under Cyclic Loading – Offshore, Along the Coast, and on Land. The 21st Bjerrum Lecture Presented in Oslo, 23 November 2007. *Canadian Geotechnical Journal* 46(5): 513–535. https://doi.org/10.1139/T09-003

ASTM International. 2019. *Standard Test Method for Consolidated Undrained Cyclic Direct Simple Shear Test under Constant Volume with Load Control or Displacement Control*. ASTM D8296-19. West Conshohocken, PA: ASTM International, approved November 1, 2019. https://doi.org/10.1520/D8296-19

Carey, T. J., Stone, N., and Kutter, B. L. 2020. Grain Size Analysis and Maximum and Minimum Dry Density Testing of Ottawa F-65 Sand for LEAP-UCD-2017. In *Model Tests and Numerical Simulations of Liquefaction and Lateral Spreading*, edited by B. L. Kutter, M. T. Manzari, and M. Zeghal, 31–44. Cham, Switzerland: Springer. https://doi.org/10.1007/978-3-030-22818-7

Dyvik, R. 2019. Personal communication. January 17th, 2019.

El Ghoraiby, M., Park, H., and Manzari, M. T. 2020. Physical and Mechanical Properties of Ottawa F65 Sand. In *Model Tests and Numerical Simulations of Liquefaction and Lateral Spreading*, edited by B. L. Kutter, M. T. Manzari, and M. Zeghal, 45–67. Cham, Switzerland: Springer. https://doi.org/10.1007/978-3-030-22818-7

Finn, W. D. L. 1981. Liquefaction Potential: Developments Since 1976. In *Proceedings: First International Conference on Recent Advances in Geotechnical Earthquake Engineering and Soil Dynamics*, 655–681. Rolla, MO: University of Missouri-Rolla.

Finn, W. D. L., Bransby, P. L., and Pickering, D. J. 1970. Effect of Strain History on Liquefaction of Sand. *Journal of the Soil Mechanics and Foundations Division* 96(6): 1917–1934. https://doi.org/10.1061/JSFEAQ.0001478

Ishihara, K. 1996. *Soil behaviour in earthquake geotechnics*. Oxford, UK: Clarendon Press.

Kovacs, W. D. and Leo, E. 1981. Cyclic Simple Shear of Large Scale Sand Samples: Effects of Diameter to Height Ratio. In *Proceedings: First International Conference on Recent Advances in Geotechnical Earthquake Engineering and Soil Dynamics*, 897–904. Rolla, MO: University of Missouri-Rolla.

Kutter, B. L., Manzari, M. T., and Zeghal, M. 2020. *Model Tests and Numerical Simulations of Liquefaction and Lateral Spreading*. Cham, Switzerland: Springer. https://doi.org/https://doi.org/10.1007/978-3-030-22818-7

Milatz, M. and Grabe, J. 2015. A New Simple Shear Apparatus and Testing Method for Unsaturated Sands. *Geotechnical Testing Journal* 38(1): 9–22. https://doi.org/10.1520/GTJ20140035

Morales, B., Humire, F., and Ziotopoulou, K. 2021. Direct Simple Shear Testing on Ottawa F50 and F65 Sand. DesignSafe-CI [publisher], Dataset. https://doi.org/10.17603/ds2-eahz-9466

Nelson, F. and Okamura, M. 2019. Influence of Strain Histories on Liquefaction Resistance of Sand. *Soils and Foundations* 59(5): 1481–1495. https://doi.org/10.1016/j.sandf.2019.06.011

Parra Bastidas, A. M. 2016. Ottawa F-65 Sand Characterization. PhD dissertation, University of California, Davis.

Porcino, D. and Diano, V. 2016. Laboratory Study on Pore Pressure Generation and Liquefaction of Low-Plasticity Silty Sandy Soils During the 2012 Earthquake in Italy. *Journal of Geotechnical and Geoenvironmental Engineering* 142(10): 04016048. https://doi.org/10.1061/(ASCE)GT.1943-5606.0001518

Prevost, J.-H. and Høeg, K. 1976. Reanalysis of Simple Shear Soil Testing. *Canadian Geotechnical Journal* 13(4): 418–429. https://doi.org/10.1139/t76-042

Price, A. B., DeJong, J. T., and Boulanger, R. W. 2017. Cyclic Loading Response of Silt with Multiple Loading Events. *Journal of Geotechnical and Geoenvironmental Engineering* 143(10): 4017080. https://doi.org/10.1061/(ASCE)GT.1943-5606.0001759

Rees, S. D. 2016. Effect of Pre-Shearing During Cyclic Simple Shear Testing of Clean Sand for Liquefaction Analyses. In *Proceedings of the 11th Australia and New Zealand Young Geotechnical Professionals Conference – 11YGPC,* 57–62. Wellington, New Zealand: The New Zealand Geotechnical Society.

Robinson, S., Brennan, A. J., Knappett, J. A., Wang, K., and Bengough, A. G. 2019. Cyclic Simple Shear Testing for Assessing Liquefaction Mitigation by Fibre Reinforcement. In *Earthquake Geotechnical Engineering for Protection and Development of Environment and Constructions: Proceedings of the 7th International Conference on Earthquake Geotechnical Engineering, (ICEGE 2019), June 17-20, 2019, Rome, Italy*, edited by F. Silvestri, and N. Moraci, 4728–4735. London, UK: CRC Press.

Seed, H. B., Mori, K., and Chan, C. K. 1977. Influence of Seismic History on Liquefaction of Sands. *Journal of the Geotechnical Engineering Division* 103(4): 257–270. https://doi.org/10.1061/AJGEB6.0000399

Ueda, K., Vargas, R., and Uemura K. 2018. LEAP-Asia-2018: Stress-Strain Response of Ottawa Sand in Cyclic Torsional Shear Tests. DesignSafe-CI [publisher], Dataset. https://doi.org/10.17603/DS2D40H

Vasko, A. 2015. An Investigation into the Behavior of Ottawa Sand through Monotonic and Cyclic Shear Tests. Master's thesis, George Washington University.

Zekkos, D., Athanasopoulos-Zekkos, A., Hubler, J., Fei, X., Zehtab, K. H., and Marr, W. A. 2018. Development of a Large-Size Cyclic Direct Simple Shear Device for Characterization of Ground Materials with Oversized Particles. *Geotechnical Testing Journal* 41(2): 263–279. https://doi.org/10.1520/GTJ20160271

3.6 Tables and figures

Table 3.1. Summary of direct simple shear (DSS) tests performed to evaluate the effect of pre-conditioning protocols.

Test Group	Number of Tests	Type of Platens	D_R (%)	σ'_{vc} (kPa)	CSR	$\sigma'_{v\ \text{pre-conditioning}}$ (kPa)	Number of drained pre-conditioning strain-controlled cycles, $N_{\text{pre-cond}}$	Testing Sequence
1	2	Flat	60	100	0.1	25	0	(1) Applied vertical effective stress of 25 kPa; (2) Increased vertical effective stress to 100 kPa; (3) Applied undrained cyclic shearing.
2	3	Ridged	60	100	0.05, 0.10, 0.15	25	0	
3a	12	Ridged	60	100	0.1	25	25, 50 75, 100, 110, 115, 120, 125, 130, 141, 150, 200	(1) Applied vertical effective stress of 25 kPa; (2) Applied drained cycles to pre-condition specimens; (3) Increased vertical effective stress to 100 kPa; (4) Applied undrained cyclic shearing.
3b	3	Ridged	60	100	0.10, 0.12, 0.15	25	115	
4a	4	Ridged	60	100	0.10, 0.12, 0.15, 0.18	100	50	(1) Applied vertical effective stress of 100 kPa; (2) Applied drained cycles to pre-condition specimens; (3) Applied undrained cyclic shearing.
4b [1]	8	Ridged	40	100	0.1	100	0, 10, 20, 30, 40, 50, 75, 150	
5 [1]	10	Pinned	40	100	0.1	100	0, 10, 30, 40, 50, 60, 70, 75, 80, 150	

[1] Denotes tests performed on dry sand specimens.

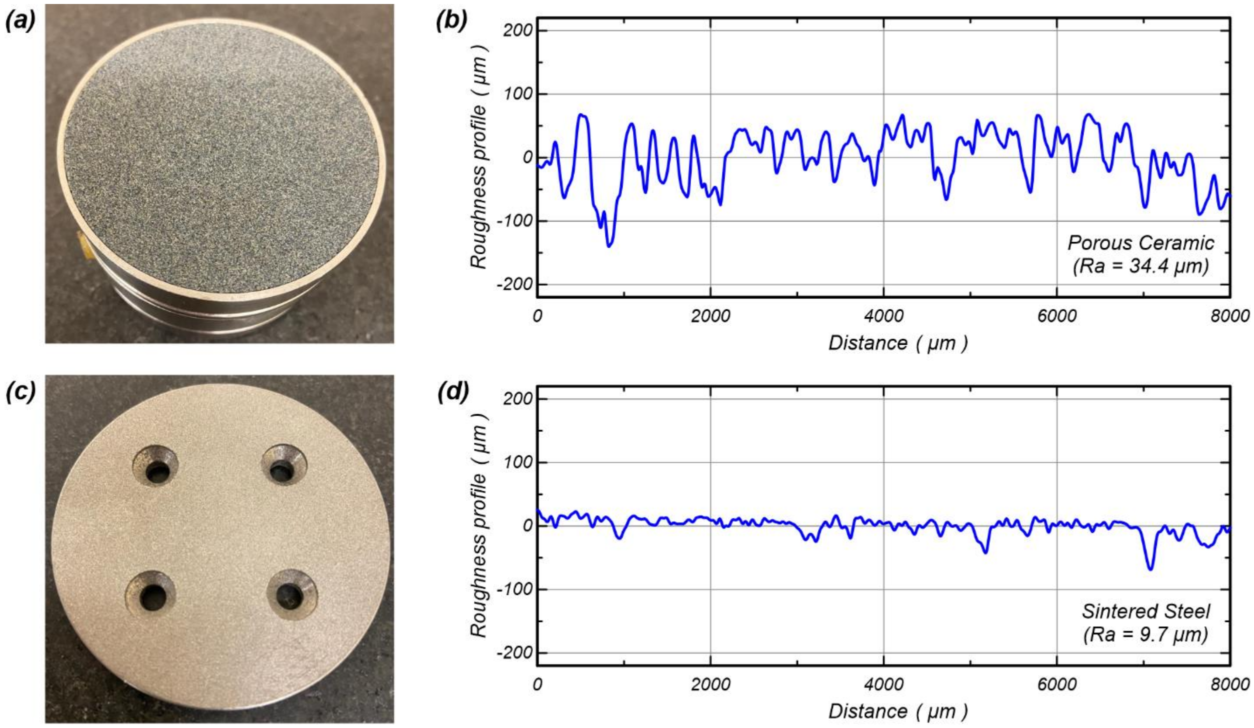

Figure 3.1. Examples of direct simple shear (DSS) flat porous platens and measurements of their average roughness (Ra) with a 3D optical profiling system: (a) porous ceramic platens used by Morales et al. (2021), (b) representative surface roughness profile of the platen shown in (a), (c) flat sintered stainless steel porous platens used in this study, and (d) representative surface roughness profile of the platen shown in (c).

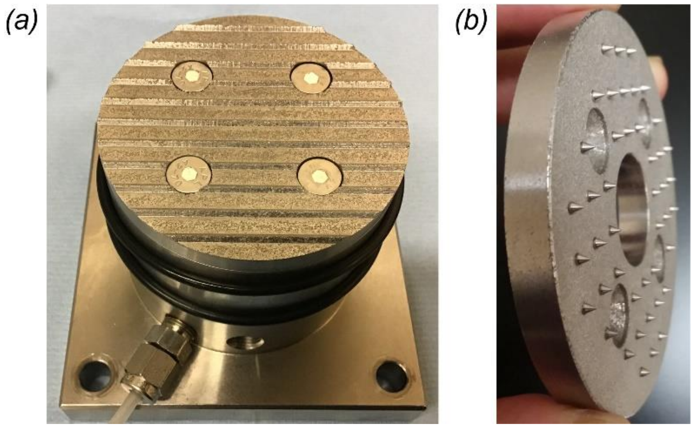

Figure 3.2. DSS sintered stainless steel porous platens of 70 mm in diameter with (a) protruding ridges and (b) embedded pins that were used in this study.

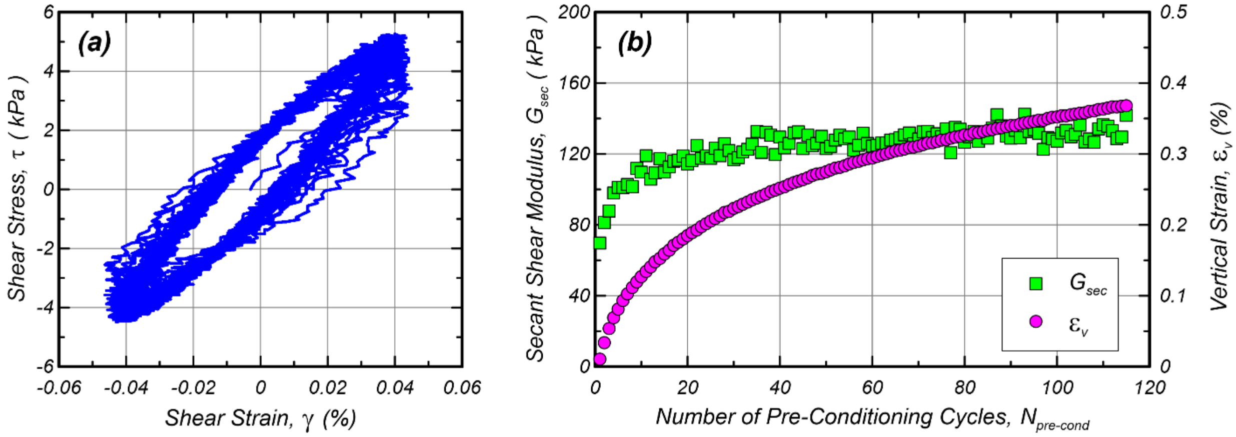

Figure 3.3. Pre-conditioning stage with 115 drained loading cycles of 0.01 mm in amplitude (about 0.045% shear strain) applied under a seating load of 25 kPa: (a) shear stress-strain loops, and (b) changes in the secant shear modulus and vertical strain for each drained cycle.

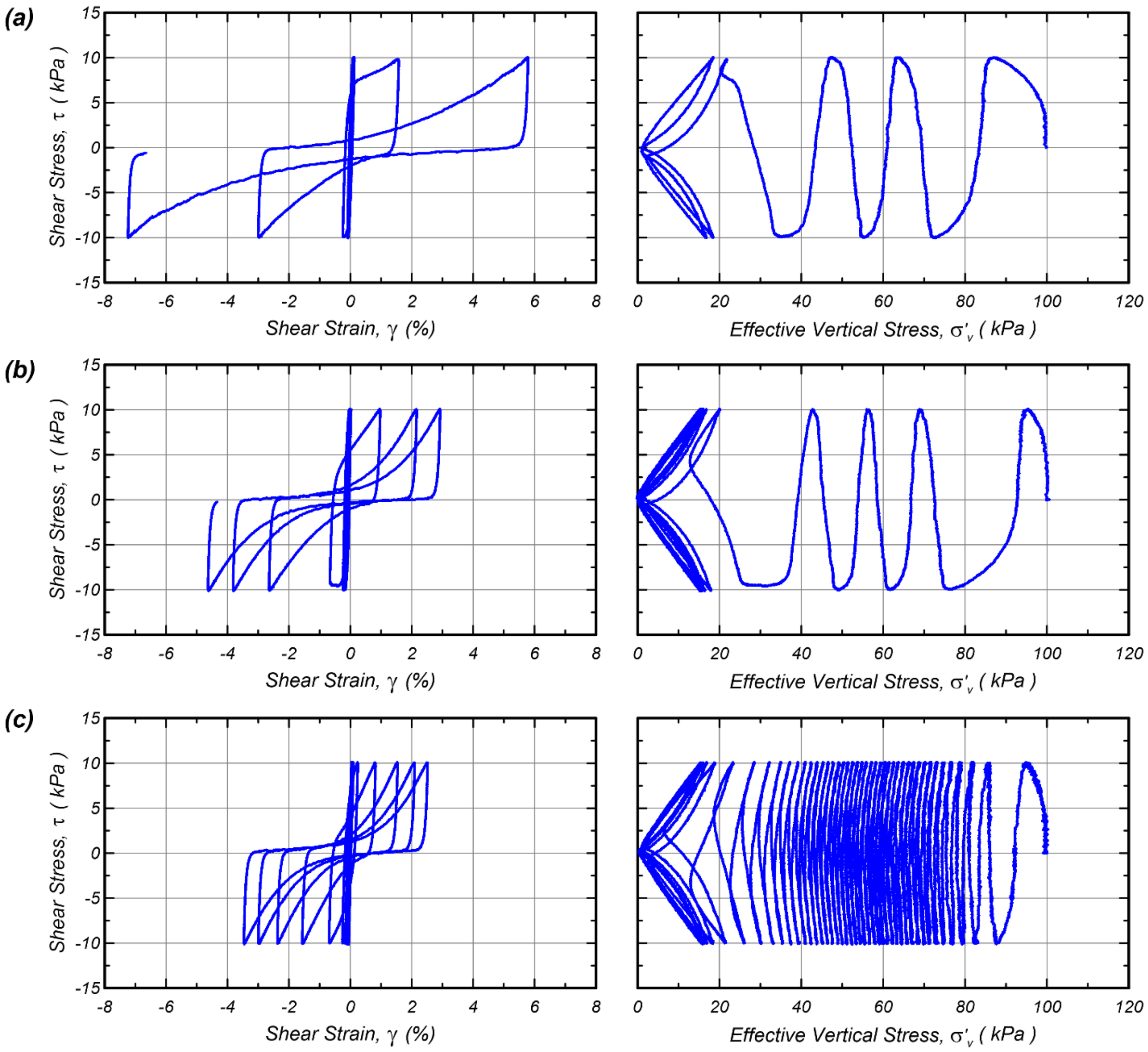

Figure 3.4. Results from DSS tests performed on specimens of Ottawa F-65 sand (D_R = 60%) with: (a) sintered steel flat platens and no pre-conditioning, (b) ridged platens and no pre-conditioning, and (c) ridged platens with pre-conditioning consisting of 115 drained cycles.

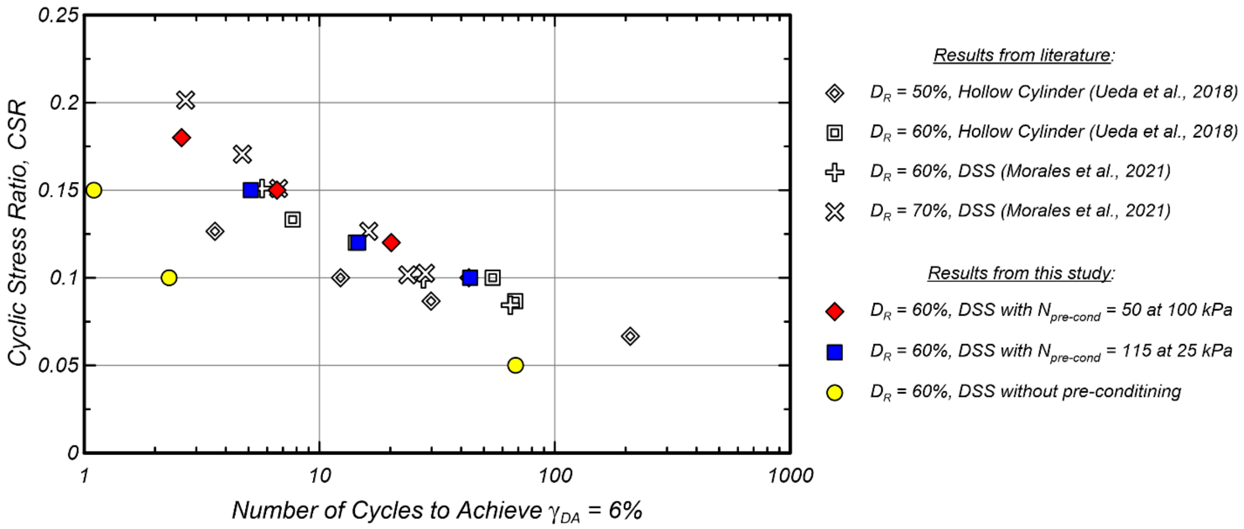

Figure 3.5. Liquefaction resistance data for Ottawa F-65 sand (D_R = 50-70%, σ'_{vc} = 100 kPa) including experimental data from Ueda et al. (2018) and Morales et al. (2021) as well as data obtained in this study using different pre-conditioning sequences.

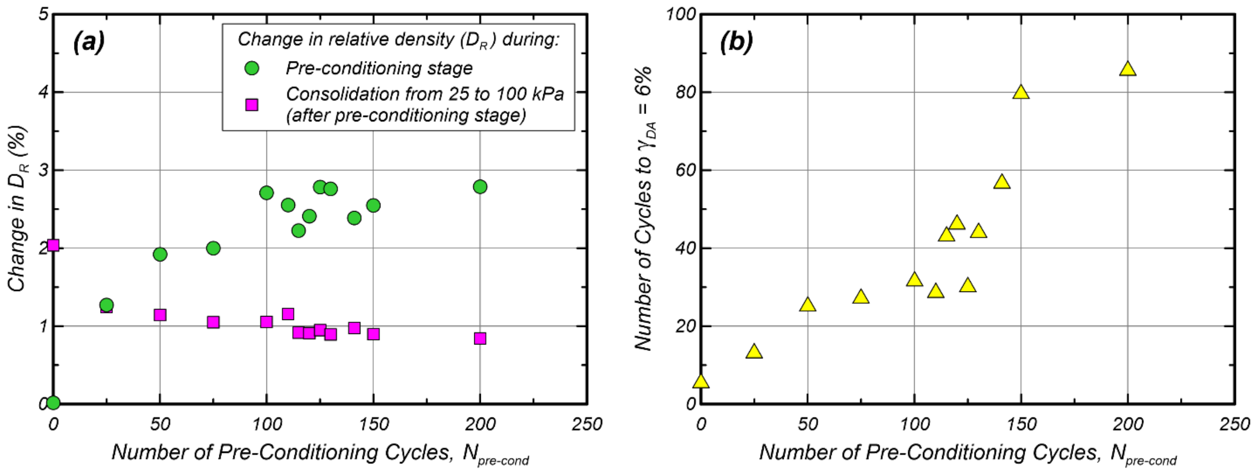

Figure 3.6. Effect of the number of pre-conditioning cycles ($N_{pre\text{-}cond}$) with an amplitude of 0.045% shear strain on: (a) changes in specimen relative densities (D_R) resulting from pre-conditioning and consolidation, and (b) the number of cycles required to trigger liquefaction (γ_{DA}=6%).

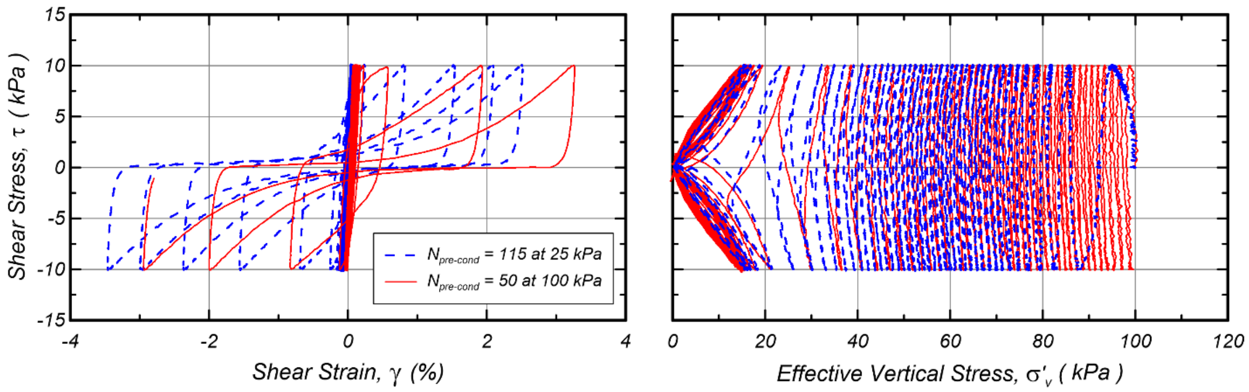

Figure 3.7. Comparison of DSS tests performed on specimens of Ottawa F-65 sand (D_R = 60%) with pre-conditioning cycles applied at different vertical stress levels.

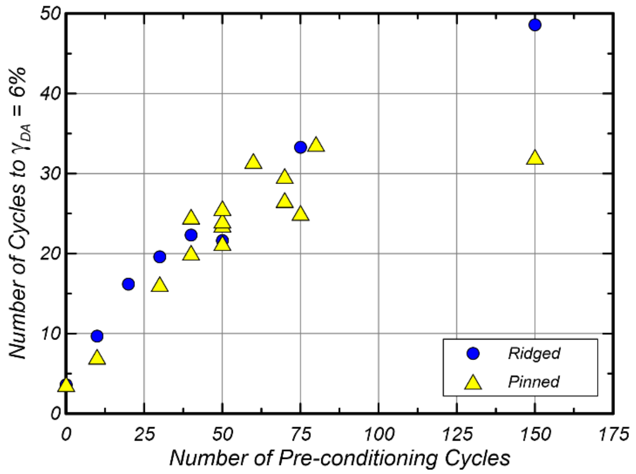

Figure 3.8. Number of undrained cycles required to trigger liquefaction (γ_{DA}=6%) for similar specimens involving pinned and ridged porous platens and varying numbers of applied pre-conditioning cycles.

Chapter 4

Mechanisms of shear strain accumulation in laboratory experiments on sands exhibiting cyclic mobility behavior

Author's note: This Chapter was submitted as a journal paper for publication authored by Francisco Humire and Katerina Ziotopoulou to the Canadian Geotechnical Journal. The paper is currently under review and is presented herein with some minor edits for consistency with the other chapters of this Dissertation.

Abstract

The factors and mechanisms controlling the accumulation of shear strains of clean uniform sands exhibiting cyclic mobility behavior under level-ground conditions are examined. This phenomenon is investigated through a series of constant-volume cyclic direct simple shear (DSS) tests subjected to uniform and irregular loading conditions, and undrained cyclic element tests collected from the literature. Experimental data show that the rate of shear strain accumulation per loading cycle depends on the relative density, cyclic stress amplitude, and effective overburden stress. Mechanisms of shear strain accumulation are investigated by decoupling the shear strain developed in each loading cycle in two components: γ_0, developed at near-zero effective stress, and γ_d, developed during dilation. Results show that γ_0 mostly depends on the shear strain history, while γ_d depends on the cyclic stress amplitude and relative density. These dependencies of γ_d and

γ_0 are used to provide an explanation for the gradual decrease of the rate of shear strain accumulation that is observed while increasing the number of post-triggering loading cycles in tests performed on dense specimens.

4.1 Introduction

Lateral deformations developed when soils exhibit cyclic mobility behavior, wherein soil progressively accumulates shear strains after liquefaction triggering, can result in significant damages to structures built on or in liquefiable sandy soils. In the context of performance-based evaluations, more reliable estimations of liquefaction-induced shear deformations are needed for the seismic design of geosystems. Progress towards more reliable estimations of such deformations in boundary value problems has been possible through the development of constitutive models capable of capturing the cyclic mobility response at the element level (e.g., Beaty and Byrne 1998; Boulanger and Ziotopoulou 2017; Khosravifar et al. 2018). Even though such constitutive models can replicate the process of shear strain accumulation, there is a very limited development of physics-based frameworks or empirical/semi-empirical correlations to guide their calibration and to better constrain predicted liquefaction-induced deformations. This is due to the lack of a fundamental understanding of the physical mechanisms and factors controlling the process of shear strain accumulation associated with the lack of experimental data that can serve as a baseline to guide such developments. As such, and before upscaling the problem to the system level and accounting for the uncertainties of the field (e.g., boundary conditions, spatial variability of soils), it is key to understand element level mechanisms and the factors that control the process of shear strain accumulation.

The cyclic mobility response of sands in stress-controlled element experiments is initially characterized by a gradual decrease in the effective vertical stresses (Figure 4.1a), followed by a progressive accumulation of limited shear strains in each loading cycle (Figure 4.1b). In this work, triggering is defined as the soil reaching 6% double amplitude shear strain. From that point onward, the post-triggering shear strain accumulation is typically assessed by tracking the evolution of the double and single amplitude maximum shear strains (γ_{DA} and γ_{SA}) in each loading cycle (Figures 4.1c and 4.1d). This approach quantifies the rate of shear strain accumulation per loading cycle or $\Delta\gamma$, which is defined by Tasiopoulou et al. (2020) as the difference in γ_{DA} or γ_{SA} between two consecutive loading cycles. Several available experimental databases (e.g., Kammerer et al. 2000; Sriskandakumar 2004) show that the post-triggering response in clean sands is characterized by an almost linear accumulation of shear strains while increasing the number of loading cycles. However, experiments performed on dense specimens of clean sands (Zhang and Wang 2012; Wichtmann and Triantafyllidis 2016) show that $\Delta\gamma$ can gradually decrease while increasing the number of post-triggering cycles, and eventually saturating at large deformations. Experiments performed to up to 50% shear strains showed that this gradual decrease of $\Delta\gamma$ can also occur on loose and medium dense specimens (Kiyota et al. 2008; Chiaro et al. 2012; Chiaro et al. 2013), but these large deformations are not typically explored with conventional laboratory devices. For example, the hollow cylinder tests performed by Kiyota et al. (2008) on medium dense specimens of Toyoura sand showed a progressive decrease in the rate of strain accumulation after achieving 15% shear strain. In parallel, discrete element model (DEM) simulations of cyclic undrained tests (Wang et al. 2016; Wang and Wei 2016; Wei et al. 2018) have also exhibited the gradual decrease of $\Delta\gamma$ at large strain levels. More importantly, those works have shown that the shear strain accumulation per loading cycle saturates after reaching a certain strain threshold. The gradual decrease and the subsequent saturation in the shear strain accumulation observed by those works were associated with the progressive saturation of changes in the fabric of liquefied soils, as reflected by the evolution of metrics of particle-void anisotropy (Wei et al. 2018) and distances among neighboring particles (Wang et al. 2016). Despite the significant progress achieved through the aforementioned experimental and numerical efforts, the stress-strain response of sands exhibiting cyclic mobility behavior at large deformations levels remains not fully understood, and further research is needed to clarify the physics-based mechanisms (e.g., fabric evolution, dilatancy) and factors (e.g., loading conditions) controlling the post-triggering response (NASEM 2016).

The undrained cyclic response of sands largely depends on the relative density D_R and effective overburden stress σ'_{vo} (Seed and Lee 1966; Idriss and Boulanger 2008) which combined through the state or relative state parameter (Been and Jefferies 1985; Konrad 1988; Boulanger 2003) have facilitated the interpretation of sand responses within the broader framework of critical state soil mechanics. Other factors like the grain properties (Kokusho et al. 2004), static shear bias (Sivathayalan and Ha 2011; Chiaro et al. 2012), testing device (Bhatia et al. 1985), or the initial soil fabric as determined by the sample preparation method (Vaid and Sivathayalan 2000; Sze and Yang 2014) have also been found to play a role in experimentally-obtained sand responses. The effect of these factors is typically captured through frameworks that allow for the quantification of key aspects of the soil response like the pore pressure generation (e.g., Seed et al. 1976) and liquefaction triggering resistance (e.g., Seed and Lee 1966; Wijewickreme and Soysa 2016). However, few frameworks are available in the literature for quantitative evaluations of the post-triggering response and the accumulation of shear strains of sands undergoing cyclic mobility. On the basis of the almost linear accumulation of post-triggering shear strains per loading cycle observed in a large body of experimental data available in the literature, Tasiopoulou et al. (2020) quantified the rate of shear strain accumulation per loading cycle ($\Delta\gamma$) in those experiments, and found a dependency of $\Delta\gamma$ on D_R and cyclic stress amplitude τ_{cyc}. Based on that dependency, Tasiopoulou et al. (2020) proposed to quantify the shear strain accumulation through a metric called "compliance rate", defined as $\Delta\gamma$ normalized by τ_{cyc}, which physically represents the increase of compliance (i.e., inverse of stiffness) while increasing the number of post-triggering loading cycles. This framework allowed for developing an empirical relationship of the compliance rate as a function of D_R for five laboratory sands, which was used towards the calibration of constitutive models to capture the development of post-liquefaction deformations in system-level numerical simulations. Although this framework initially located the differences in the rate of shear strain accumulation for sands in their different grain properties, the effects of other important factors like σ'_{vo} or the static shear bias were not studied given the limited experimental data collected from the literature.

Several efforts to provide a conclusive explanation of the fundamental mechanisms controlling the post-triggering response are available in the literature, including investigations based on empirical observations of sand behavior (Shamoto et al. 1997; Zhang et al. 1997; Zhang and Wang 2012) and results of DEM simulations (Wang et al. 2016; Wang and Wei 2016; Wei et al. 2018; Yang et al. 2021). Amongst these, Shamoto et al. (1997) provided a basis to interpret the mechanisms controlling the shear strain accumulation in undrained cyclic laboratory tests. Shamoto et al. (1997) proposed to characterize the shear strain accumulation by decoupling the shear strain component that develops during dilation (γ_d) and the shear strain component that develops at near-zero effective stress (γ_0) in each loading cycle (Figure 4.2). Using this approach for torsional tests subjected to uniform and irregular cyclic loading conditions, Shamoto et al.

(1997) showed that the accumulation of shear strains is governed by the development of γ_0, and that those strains are directly proportional to the maximum shear deformations achieved in the preceding loading cycle, thus hinting at the importance of previously accumulated damage in the ensuing response. The implementation of this approach on laboratory data allowed to identify that shear strains developed during dilation in each loading cycle tend to stabilize after liquefaction triggering (Zhang and Wang 2012; Humire et al. 2019). This approach has also been useful for the interpretation of DEM works aimed at finding the particle-level mechanisms controlling the development of post-triggering shear deformations. For example, the DEM results of Wang et al. (2016) and Wei et al. (2018) suggest that (i) the evolution of γ_d is mostly related to changes in the load-bearing stability of the grain assembly as reflected by the evolution of contact-based fabric metrics (e.g., coordination number), while (ii) the evolution of γ_0 is associated with changes in the particle-void distribution and distances between neighboring particles. Similar DEM analyses performed by Yang et al. (2021) suggest that the transition from γ_0 to γ_d occurs at a critical value of the coordination number, which is needed to reach in order to rebuild the load-bearing network within the grain assembly.

To better understand and characterize the post-triggering behavior of sands, this work examines the factors and mechanisms controlling the process of shear strain accumulation of clean uniform sands exhibiting cyclic mobility behavior under level-ground conditions. This is achieved by developing an extensive experimental database to characterize the post-triggering response at large shear strain levels for a broad range of different D_R's and loading conditions. First, the post-triggering response for uniform and irregular cyclic loading conditions is assessed through the evolution of γ_{DA}, with the rate of shear strain accumulation being defined as the difference in γ_{DA} between two consecutive loading cycles ($\Delta\gamma = \Delta\gamma_{DA}$). Then, the framework proposed by

Tasiopoulou et al. (2020) is implemented to quantify the combined effects of relative density D_R, cyclic stress amplitude τ_{cyc}, loading device, and effective overburden stress σ'_{vo} on the rate of shear strain accumulation. Finally, and based on the approach and previous insights from Shamoto et al. (1997), a revised interpretation is provided regarding the role of strain history, τ_{cyc}, and dilation on the process of shear strain accumulation under uniform and irregular loading conditions. Tests under irregular cyclic loading conditions allow the validation of empirical observations from uniform loading tests. The results presented herein are expected to form a physics-based basis for the validation and calibration of constitutive models to capture cyclic mobility-induced deformations, as well as more broadly guide the liquefaction evaluations in geosystems comprised of soils undergoing cyclic mobility.

4.2 Experimental data

4.2.1 Material

Experiments were conducted on reconstituted specimens of Ottawa F-65 sand, which was the primary soil used in the Liquefaction Experiments and Analysis Projects or LEAP (Kutter et al. 2020 amongst many). In the context of the LEAP project, Ottawa F-65 sand was classified as a poorly-graded sand (SP), with a median grain size (D_{50}) of 0.20 mm, a coefficient of uniformity (C_u) of 1.47, a coefficient of curvature (C_c) of 0.88, and no fines (Carey et al. 2020). However, different values of minimum and maximum void ratios (e_{min} and e_{max}) were reported for this material by different researchers that participated in the LEAP project and beyond (Vasko 2015; Parra Bastidas 2016; Carey et al. 2020). The variability of these parameters may be associated with the use of different laboratory methods for the determination of maximum and minimum densities, as well as with issues in the repeatability of each method (Lunne et al. 2019). Given the impact of these parameters in the evaluation of D_R, the values of e_{min} and e_{max} must be carefully selected. In this investigation, values of e_{min} and e_{max} of 0.51 and 0.78 were selected as more reliable based on the statistical analysis of the properties of Ottawa F-65 sand by Carey et al. (2020).

4.2.2 Testing equipment and procedures

An Electromechanical Dynamic Cyclic Simple Shear (EMDCSS) device manufactured by GDS Instruments was utilized to perform constant-volume (equivalent undrained) cyclic direct simple shear (DSS) tests. The active height control system implemented in the EMDCSS device allowed to perform constant-volume DSS tests with vertical strains below the threshold of 0.05% recommended by ASTM (2019). Samples of about 70 mm in diameter and 22 mm in height were laterally enclosed within stacked Teflon-coated steel rings and a latex membrane of about 0.35 mm (±0.05 mm) in thickness. Sintered steel porous discs with protruding ridges with a height of about 1 mm were placed on the end caps to optimize the shear stress transfer to the samples.

Specimens were prepared with the air pluviation method, which involved raining oven-dried sand from a constant height into the soil container. For this investigation, the specimens were prepared to target post-consolidation D_R's ranging between 37 and 80%. After applying a seating load of 10 kPa, specimens were saturated by slowly flushing deionized water from bottom to top of specimens. Saturation was ensured by monitoring air bubbles in the outgoing water as described in Parra Bastidas (2016). Following saturation, all samples were subjected to a series of pre-conditioning strain-controlled drained cycles with an amplitude of 0.01 mm (about 0.045% shear strain) to ensure the engagement of the textured top platen with the specimen (Humire et al. 2021). This pre-conditioning stage consisted of 50 drained cycles applied under a vertical stress of 100 kPa for tests with a σ'_{vo} of 100 or 400 kPa, and 115 drained cycles at a vertical stress of 25 kPa for tests with a σ'_{vo} of 50 kPa. Both pre-conditioning sequences were found to lead to similar results in terms of stress-strain response and liquefaction resistance (Humire et al. 2021). Following pre-conditioning, the vertical stress was raised to the target initial consolidation stress if the target value was larger than the vertical stress during pre-conditioning. Finally, specimens were subjected to a stress-controlled constant-volume cyclic shearing with a frequency of 0.05 Hz until a single amplitude shear strain of 10% was achieved or more than 100 loading cycles were applied in the post-triggering regime.

4.2.3 Testing program

The testing program comprised a series of DSS tests subjected to uniform loading conditions to evaluate the effect of cyclic stress amplitude (τ_{cyc}) and effective overburden stress (σ'_{vo}) on the process of shear strain accumulation (Table 4.1). Additionally, a series of experiments were performed to evaluate the effect of irregular cyclic loading conditions on the post-triggering response. Similar to the tests presented in Ziotopoulou and Boulanger (2016), irregular loading tests involved varying the τ_{cyc} along the course of the post-triggering regime in three loading stages (Table 4.2). The first loading stage of these tests ended after exceeding a shear strain of 4%, while the second stage ended after achieving a shear strain of 5-7%. Results presented in this work were complemented with datasets available in the literature for the same material, which included triaxial (El Ghoraiby et al. 2017), DSS (El Ghoraiby and Manzari 2018; Morales et al. 2021; Lee at al. 2022), and hollow cylinder torsional shear tests (Ueda et al. 2020).

4.3 Test results and discussion

4.3.1 Liquefaction triggering

Before focusing on the process of shear strain accumulation, the liquefaction triggering resistance of the experiments performed within this work were assessed to confirm expected trends on sands undergoing cyclic mobility. Considering a triggering criterion of γ_{DA}=6%, DSS results for relative densities around 60% were grouped to define liquefaction resistance curves for different σ'_{vo} values (Figure 4.3). Results were in good agreement with: (1) liquefaction triggering data available in the literature for the same material, (2) previous works that show a decrease in the cyclic resistance when increasing σ'_{vo} (Vaid et al. 2001; Idriss and Boulanger 2008), and (3) critical state theory wherein the increase of effective overburden stress increases contraction and suppresses dilation, and thus reduces the overall liquefaction resistance (Vaid and Chern 1985).

4.3.2 Post-triggering shear strain accumulation per loading cycle

4.3.2.1 Uniform loading conditions

Figure 4.4 illustrates the effect of σ'_{vo} and D_R on the shear strain accumulation for a series of DSS tests sheared with the same uniform cyclic stress ratio (CSR = τ_{cyc}/σ'_{vo}). As shown in Figure 4.4a, the shear strain accumulation per loading cycle was much faster for tests under higher σ'_{vo} values. Since the main difference between these tests was the stress level, the results confirm and strengthen the observations by Tasiopoulou et al. (2020) regarding the dependency of the rate of shear strain accumulation per loading cycle on τ_{cyc} and not on the CSR. On the other hand, the accumulation of shear strains per loading cycle was much faster for looser specimens than for denser specimens subjected to the same loading conditions (Figure 4.4b), which confirms the strong dependency of the rate of shear strain accumulation per loading cycle on the D_R value, as previously shown by Tasiopoulou et al. (2020). Also, the accumulation of shear strains for loose and medium dense specimens followed an almost linearly increasing trend, while for dense specimens the rate of shear strain accumulation tended to gradually decrease while increasing the number of cycles. This gradual decrease in the accumulation of strains was observed in all tests performed on dense specimens of Ottawa F-65 sand, including two tests that exhibited an almost full arrest (UL-14 and 23) on the rate of shear strain accumulation with no signs of having been affected by strain non-uniformities. Due to device limitations, for most of the tests presented herein, measurements of shear deformations were affected by the development of non-uniformities (e.g., rotation of confining rings) at large strain levels (γ_{DA} > 12-18%), which can be visualized as a sudden increase in the slope of the plots of γ_{DA} versus the number of loading cycles. Therefore, it is interpreted that the gradual arrest might have occurred in looser specimens at much higher strain levels; however, that eventual gradual arrest could not be explored due to the development of non-uniform deformations at large strain levels.

4.3.2.2 Irregular loading conditions

Figure 4.5 presents an indicative stress-strain response exhibited by one of the tests conducted under irregular loading conditions, and Figure 4.6 summarizes the process of shear strain accumulation exhibited by all the irregular loading DSS tests listed in Table 4.2. The accumulation of γ_{DA} per loading cycle for all tests was characterized by a progressively increasing trend after liquefaction triggering with evident discontinuities (drops of 1-3% in the vertical γ_{DA} axis) when transitioning from one loading stage to another. Setting those discontinuities aside, it is evident that the rate of shear strain accumulation ($\Delta\gamma_{DA}$) varied in each stage accordingly to the changes on τ_{cyc} along the tests. For example, test IL-01 (Figure 4.6a) showed a decrease of $\Delta\gamma_{DA}$ of about 1.5-2.5% in the first loading stage ($\tau_{cyc,1}$ =15 kPa) to a $\Delta\gamma_{DA}$ of about 0.6-1.0% in the second loading stage ($\tau_{cyc,2}$ =7.5 kPa), and later to a $\Delta\gamma_{DA}$ closer to zero in the third loading stage ($\tau_{cyc,3}$ =3.75 kPa). Similar observations hold for tests IL-02 to IL-04 (Figures 4.6b to 4.6d) which showed a decrease in $\Delta\gamma_{DA}$ when transitioning from the first to the second stage ($\tau_{cyc,1} > \tau_{cyc,2}$), and then a slight increase in $\Delta\gamma_{DA}$ when passing to the third stage ($\tau_{cyc,2} < \tau_{cyc,3}$).

The shear strains obtained after transitioning from one loading stage to another suggest that the strains developed in each cycle depend on the maximum shear strain developed in the previous loading stage. For example, the first loading cycle of the second loading stage of all irregular loading tests exhibited similar shear strains to those developed in the last loading cycle of the first stage despite the reduction in τ_{cyc}. This observation is consistent with previous works that showed that the shear deformations measured in the post-triggering regime depend on the maximum deformations achieved in previous loading cycles (Shamoto et al. 1997; Zhang and Wang 2012). On the other hand, the dependency of $\Delta\gamma_{DA}$ on the τ_{cyc} on the current loading stage agrees with observations previously made for tests under uniform loading conditions (Section 4.3.2.1).

4.3.3 Factors controlling the rate of shear strain accumulation

4.3.3.1 Compliance rate

The compliance rate defined in Tasiopoulou et al. (2020) was used to quantify the differences in the process of shear strain accumulation for different loading and testing conditions. The compliance rate was evaluated for all the experiments that were subjected to uniform loading conditions by following the procedure described by Tasiopoulou et al. (2020). First, the shear strains developed only in the post-triggering regime ($\gamma_{post\text{-}trigg}$) were isolated from the double amplitude shear strains as illustrated in Figure 4.1d. Then, the values of $\gamma_{post\text{-}trigg}$ were normalized by τ_{cyc} and plotted versus the number of post-triggering loading cycles ($N_{post\text{-}trigg}$) as shown in Figure 4.7. The appropriateness of the normalization of the rate of shear strain accumulation with τ_{cyc} was confirmed by the good agreement of the evolution of $\gamma_{post\text{-}trigg}/\tau_{cyc}$ for tests performed with the same D_R and σ'_{vo} but different τ_{cyc}. Then, the compliance rate for each experiment was computed as half of the slope of the linear fit of the $\gamma_{post\text{-}trigg}/\tau_{cyc}$ versus $N_{post\text{-}trigg}$ curve, but only considering the data between 6 and 10% double amplitude shear strain. This range was selected following the recommendation of Tasiopoulou et al. (2020) about defining an upper bound for the compliance rate of tests exhibiting a gradual decrease in the rate of shear strain accumulation per loading cycle. In this range, the evolution of $\gamma_{post\text{-}trigg}/\tau_{cyc}$ per loading cycle followed an almost linear trend for almost all the experiments, except for two experiments performed on dense specimens ($D_R \approx 80\%$) that exhibited an early arrest on the accumulation of shear strains (tests UL-14 and UL-23).

The compliance rates obtained for all the DSS tests subjected to uniform loading conditions were plotted against D_R as shown in Figure 4.8. This plot confirmed the good correlation between the compliance rate and D_R, and allowed to recognize differences between the datasets with different σ'_{vo}. Similar to Tasiopoulou et al. (2020), power trends were fitted to each dataset using the linear least square fitting method:

$$Compliance\ Rate = B\ \cdot\ e^{A \cdot D_R} \tag{4.1}$$

where D_R corresponded to the percentage values indicated in Table 1, A was -0.098 for all datasets, while B was varied for each dataset. The coefficients of determination (R^2) of the power fits presented in Figure 4.8 ranged between 0.95 and 0.97.

4.3.3.2 Comparison with other testing devices and procedures

Figure 4.9 presents a comparison between the compliance rates obtained in this work and the compliance rates obtained using experimental data available in the literature for the same tested sand, but obtained using other testing devices and procedures. All the tests presented in Figure 4.9 were performed on air-pluviated specimens of Ottawa F-65 sand that were subjected to an initial effective vertical stress of 100 kPa. For the triaxial tests performed by El Ghoraiby et al. (2017), the compliance rate was evaluated for a range of 4 to 7% double amplitude vertical strain ($\varepsilon_{v,DA}$), and shear strains were estimated as $\gamma_{DA} = 1.5\ \varepsilon_{v,DA}$. In general, good agreement was observed between the compliance rates estimated for the different experimental databases presented in Figure 4.9. These results suggest that specimens prepared to the same D_R with the same sample preparation method and subjected to the same loading conditions (τ_{cyc} and σ'_{vo}), should exhibit a similar rate of shear strain accumulation per loading cycle despite differences in the mode of shearing (e.g., simple shear, torsional, triaxial). Also, almost no differences in terms of compliance rates were noticed between cyclic DSS tests performed on saturated and dry specimens, which is in agreement with previous works that have shown a negligible effect of saturation on the constant-volume response of clean sands for this type of test (Finn and Vaid 1977; Monkul et al. 2015).

4.3.3.3 Effect of effective overburden stress

The results presented in Figure 4.8 showed that the compliance rates for the DSS tests performed with σ'_{vo}'s of 50 and 100 kPa were very similar to each other. Conversely, the DSS tests performed under 400 kPa led to compliance rates smaller than those exhibited by DSS tests performed at 50 and 100 kPa. Given the normalization of the rate of shear strain accumulation by τ_{cyc} to obtain the compliance rate, its reduction while increasing σ'_{vo} is not equivalent to less strains per loading cycle with larger effective overburden stresses. To isolate and examine the effect of σ'_{vo} on the post-triggering shear strain accumulation and the compliance rate, Figure 4.10 presents a comparison of the stress-strain response obtained between triggering (γ_{DA}>6%) and up until γ_{DA} = 12% for three experiments with the same D_R and loaded with the same CSR but under different σ'_{vo}. For the test with higher σ'_{vo}, larger shear strains developed in each loading cycle, but most of those strains occurred when the soil was dilating (i.e., regaining stiffness). On the other hand, the tests with lower σ'_{vo} exhibited smaller rates of shear strain accumulation per loading cycle, but most of the shear strains occurred when the soil was at liquefied state (i.e., near-zero stiffness).

Therefore, on average, the shear strains developed in tests performed at 400 kPa occurred at higher stiffness levels than the tests at lower σ'_{vo}'s, which explains the reduction of the compliance rate (i.e., inverse of stiffness). Conversely, the minimal effect of σ'_{vo} on the compliance rate when comparing tests at 50 and 100 kPa (Figure 4.8) can be explained by considering that: (1) shear strains in these tests are being controlled by strains developed at near-zero stiffness, and (2) the impact of friction within the testing apparatus on the development of shear strains is larger for DSS tests performed under smaller σ'_{vo}'s.

4.3.4 Mechanisms controlling the shear strain accumulation

4.3.4.1 Decomposition of shear strain at near-zero effective stress and at dilation

Previous DSS results under different σ'_{vo}'s showed that the process of shear strain accumulation depends to a great extent on the changes in stiffness along each loading cycle. To take a closer look at this phenomenon, the approach presented by Shamoto et al. (1997) was implemented to examine the differences between shear strains developed at dilation (γ_d) and strains developed at near-zero stiffness or near-zero effective stress (γ_0) on the process of shear strain accumulation. Both strain components for all the DSS tests performed in this work were decoupled according to the procedure defined by Humire et al. (2019), and considering 2 kPa as the threshold between γ_d and γ_0. As previously shown in Figure 4.2c, the post-triggering response was characterized by a quasi-stabilization of γ_d accompanied by a progressive increase of γ_0, which is in agreement with results presented in previous works (Zhang and Wang 2012; Humire et al. 2019). In general, γ_d exhibited a slight increase at large deformation levels (γ_{DA} >12-18%), which was associated to the development of strain non-uniformities at those levels of deformations. These empirical observations were similar for all the DSS tests performed in this work under uniform loading conditions.

4.3.4.2 Role of the shear strain history

To extend and further validate previous observations by Shamoto et al. (1997) regarding the dependency of γ_0 on the shear strain history, Figure 4.11 summarizes and correlates the values of γ_0 for all the experiments performed under uniform loading conditions versus the γ_{DA} obtained in the respective preceding loading cycle ($\gamma_{DA,pre}$). These results confirm the linear relationship between γ_0 and $\gamma_{DA,pre}$ as previously shown by Shamoto et al. (1997). The comparison of tests on samples with different D_R values but same σ'_{vo} shows a slightly decreasing trend of γ_0 while increasing D_R (Figure 4.11a). On the other hand, results for different σ'_{vo} values but similar D_R values show a decreasing trend of γ_0 while increasing σ'_{vo} (Figure 4.11b). The larger scattering of γ_0 observed for tests with a σ'_{vo} of 400 kPa is attributed to the smaller sampling used to capture the stress-strain response in the region where γ_0 is evaluated. Since all the tests were performed with a loading frequency of 0.05 Hz and sampling frequency of 500 Hz, each stress-strain loop consisted of 10,000 recording points. However, only 10 of those points were in the region where γ_0 was evaluated for tests at 400 kPa, while more than 100 points were in that region for tests at 50 and 100 kPa.

A similar relationship between γ_0 and $\gamma_{DA,pre}$ was observed for the experiments performed under irregular loading conditions. Despite the changes in τ_{cyc} amongst these tests, γ_0 and $\gamma_{DA,pre}$ presented an almost linear relationship that is similar to that exhibited by tests under uniform loading conditions with similar densities (Figure 4.12). The good agreement between uniform and irregular loading tests confirms observations by Shamoto et al. (1997) regarding γ_0 being independent from τ_{cyc}, and that its value mostly depends on the shear strain history.

4.3.4.3 Role of cyclic stress amplitude and dilation

Previous works have concluded that the evolution of γ_d per loading cycle stabilizes towards a saturation value after liquefaction triggering (Zhang and Wang 2012; Humire et al. 2019). For the purpose of this work, the saturation values of γ_d (herein defined as γ_d^{sat}) were estimated as the average value of γ_d within a range of $\gamma_{DA,pre}$ of 6 to 10%, which was the range where those strains remained almost stable. Following a rationale similar to Tasiopoulou et al. (2020) to develop the compliance rate, the values of γ_d^{sat} estimated for all the DSS tests performed under uniform loading conditions were normalized by τ_{cyc} and plotted against D_R (Figure 4.13). The results show a good correlation between $\gamma_d^{sat}/\tau_{cyc}$ and D_R by following trends that are very similar to those determined for the compliance rate for different values of σ'_{vo} (Figure 4.8). This suggests that the rate of shear strain accumulation per loading cycle is mostly controlled by the development of strains during dilation.

The dependency of γ_d on τ_{cyc} was also confirmed by tests conducted under irregular loading conditions, as noticed when comparing the evolution of γ_d and γ_d/τ_{cyc} per loading cycle obtained from these tests (Figure 4.14). In general, the evolution of γ_d/τ_{cyc} per loading cycle followed a monotonically increasing trend that tended to stabilize around $\gamma_d/\tau_{cyc} = 0.20 – 0.25$. However, a sudden increase in γ_d/τ_{cyc} was observed in the third loading stage of tests IL-02 to IL-04, which occurred after exceeding $\gamma_{DA} = 12 – 15\%$ and strain non-uniformities started to affect measurements of shear deformations. More importantly, these tests exhibited a continuity in the values of γ_d/τ_{cyc} between loading stages with different CSRs, which confirms that the γ_d's developed in each loading stage are proportional to the τ_{cyc} of the current stage.

4.3.4.4 Plausible explanation for the gradual decrease of the shear strain accumulation

The quasi-stabilization of γ_d and the dependency of γ_0 on the strains developed in the previous half loading cycle ($\gamma_{DA,pre}$) can explain the gradual decrease of the shear strain accumulation per loading cycle observed in tests performed on dense specimens (D_R = 65-80%). The rationale to support this statement is explained as follows:

- Once the specimen begins to exhibit dilative behavior, γ_d increases in each loading cycle until it stabilizes to a γ_d value that remains constant with additional cycling within a few cycles after liquefaction is triggered. On the other hand, γ_0 begins to increase with continued cycling after liquefaction is triggered.
- Before the quasi-stabilization of γ_d, the values of $\Delta\gamma_{DA}$ in each cycle are defined as the sum of the increments in γ_d and γ_0 ($\Delta\gamma_{DA} \approx \Delta\gamma_d + \Delta\gamma_0$). However, once the evolution of γ_d stabilizes ($\Delta\gamma_d \approx 0$), $\Delta\gamma_{DA}$ only continues increasing due to increases in γ_0 ($\Delta\gamma_{DA} \approx \Delta\gamma_0$).
- Since $\Delta\gamma_{DA}$ decreases as cycling continues, the next increment of γ_0 decreases due to the proportionality between γ_0 and γ_{DA} (Figure 4.11).
- This produces a progressive decrease in both γ_{DA} and γ_0 with cycling, which explains the gradual decrease on the rate of shear strain accumulation.

The evolution of γ_d and γ_0 described above is inherently related to changes in the soil fabric during the post-triggering regime. Following the interpretation presented in Humire et al. (2019), the quasi-stabilization of γ_d is attributed to a stabilization of changes on the particle-scale coordination number and inter-particle force chains, while the evolution of γ_0 is attributed to a stabilization of changes in the particle-void distribution of the grain assembly and distances between neighboring particles. As found by Wang et al. (2016) and Wei et al. (2018), fabric metrics associated with γ_0 tend to saturate at large strain levels, which leads to a gradual arrest on the development of shear strains after achieving a certain strain threshold. This was not the case for the tests performed on loose and medium dense specimens; however, their γ_d and γ_0 values exhibited similar dependencies than those observed in dense samples (Figures 4.11a and 4.13). Therefore, it is expected that the gradual decrease in the shear strain accumulation may occur at larger strain levels for loose and medium dense specimens. It is noted that higher shear strain levels (e.g., $\gamma > 10\%$) are difficult to investigate in a DSS device due to increasing boundary effects at those strain levels. However, other devices such as hollow cylinder could be used to extend the findings and evaluating the applicability of the framework up to shear strains of 50% and even higher (Chiaro et al. 2013). In that sense, further work is needed to experimentally capture the cyclic mobility behavior at large strain levels across the broader spectrum of relative densities.

4.4 Summary and conclusions

A series of constant-volume cyclic direct simple shear (DSS) tests were performed to investigate the accumulation of shear strains in clean uniform sands undergoing cyclic mobility for a broad range of relative densities and loading conditions. In the majority of the experiments under uniform loading, the accumulation of shear strains per loading cycle was characterized by a monotonically increasing trend following initial liquefaction with an almost constant rate of shear strain accumulation in the post-triggering regime (γ_{DA}>6%). In experiments performed on denser specimens (D_R = 65-80%), the rate of shear strain accumulation per loading cycle was found to be gradually decreasing. Experiments under irregular loading comprised of uniform loading stages of a varying amplitude each, showed that shear strains developed in each loading stage depend on: (1) the cyclic stress amplitude τ_{cyc} of the current stage, and (2) the shear strains developed in previous loading stages.

The framework proposed by Tasiopoulou et al. (2020) was implemented to investigate the effect of different factors on the shear strain accumulation for tests conducted under uniform loading conditions. The results confirmed the observations of Tasiopoulou et al. (2020) regarding the dependency of the rate of post-triggering shear strain accumulation on the D_R of the specimen and τ_{cyc}. Compliance rates (i.e., rate of shear strain accumulation normalized by τ_{cyc}) evaluated in this work exhibited trends similar to those obtained from other experimental databases available in the literature for the same tested material but with other testing devices. Testing results also showed that increasing the effective overburden stress σ'_{vo} can affect the rate of shear strain accumulation, as shown by the series of tests performed under 400 kPa, which resulted in smaller compliance rates compared to those obtained under lower σ'_{vo} values (50 and 100 kPa). The decrease in compliance rate observed for tests at 400 kPa was explained by the shear strains in those tests being controlled by strains developed when the soil is dilating (i.e., regaining stiffness).

Based on the approach of Shamoto et al. (1997), the process of shear strain accumulation was characterized by decoupling the shear strains in two components: a shear strain component developed during dilation (γ_d) that tends to stabilize after liquefaction triggering, and a shear strain component developed at near-zero effective stress (γ_0) that follows a monotonically increasing trend after triggering. Similar to the experimental results presented in Shamoto et al. (1997), the tests performed in this work showed that the process of shear strain accumulation is governed by the development of γ_0, whose magnitude depends on the maximum shear strain developed in the previous half loading cycle ($\gamma_{DA,prev}$). The results also showed that γ_d depends on the cyclic stress amplitude τ_{cyc} and the relative density D_R of the specimen with similar functional dependencies to those obtained for the compliance rate. Combined, the quasi-stabilization of γ_d and the dependency of γ_0 on $\gamma_{DA,prev}$ explain the gradual decrease and eventual saturation of the rate of shear strain accumulation per loading cycle observed on dense specimens.

Results of this work experimentally confirm that, independent of relative density, the accumulation of shear strains in tests on clean sands subjected to uniform loading patterns gradually decrease after exceeding a certain strain threshold. This finding is experimentally proving the previous observations of DEM simulations of undrained cyclic tests (Wang et al. 2016; Wei et al. 2018), which have shown that the development of shear strains gradually arrests as a result of a saturation of changes of the soil fabric in the post-triggering regime and, in particular, of changes in void-based fabric metrics. Still, further investigations are needed to evaluate the extent to which this gradual decrease on the shear strain accumulation occurs in the field, and how it depends on the features of geosystems being analyzed (i.e., sloping ground conditions, spatial variability and/or continuity of liquefiable soils). Also, further work and developments in testing devices are needed to more reliably experimentally capture large shear deformations, as the gradual decrease of the rate of shear strain accumulation and stabilization of both γ_d and γ_0 at large strain levels may be affected by the development of strain non-uniformities or other boundary effects. The use of other testing devices (e.g., hollow cylinder tests, ring shear tests) could resolve these issues and complete the picture of shear strain accumulation in the cyclic mobility regime across the broader spectrum of relative densities. Such developments will later facilitate the evaluation of the progressive arrest of the shear strain accumulation for loose and medium dense specimens, and the formulation of relationships between saturation shear strains and other properties (e.g., state properties, grain properties).

Lastly, the results presented in this work provide a basis for the validation and calibration of constitutive models to capture cyclic mobility-induced shear strain accumulation and, therefore, to improve the estimation of liquefaction-induced deformations required for the performance-based design of geosystems. Capturing this phenomenon is particularly important for the design of geosystems at potentially liquefiable sites that can be subjected to long-duration earthquakes and, therefore, where several loading cycles can occur after liquefaction triggering. The results also highlight the need for using experimental data representative of the expected in-situ soil and loading conditions given their impact on the resulting deformations, as well as the importance of prioritizing behaviors of interest given those conditions. As such, capturing the shear strains developed during dilation should be prioritized when calibrating data for high effective overburden stresses, while capturing near-zero stiffness features should be prioritized when modeling the response under small effective overburden stresses. Even though the experimental database presented in this work already covers a broad range of conditions (e.g., relative density, effective overburden stresses, irregular loading patterns) and extends prior datasets, further research is needed to similarly quantify the effect of other factors such as initial static shear bias (i.e., sloping ground conditions) and grain properties (e.g., grain size, gradation, grain shape) on the mechanisms of shear strain accumulation.

4.5 References

ASTM International. 2019. *Standard Test Method for Consolidated Undrained Cyclic Direct Simple Shear Test under Constant Volume with Load Control or Displacement Control*. ASTM D8296-19. West Conshohocken, PA: ASTM International, approved November 1, 2019. https://doi.org/10.1520/D8296-19

Beaty, M. and Byrne, P. M. 1998. An effective stress model for predicting liquefaction behavior of sand. In *Geotechnical Earthquake Engineering and Soil Dynamics III*. ASCE Geotechnical Special Publication. Vol. 1, pp. 766–777.

Been, K. and Jefferies, M. G. 1985. A state parameter for sands. *Geotechnique* 35(2): 99–112. https://doi.org/10.1680/geot.1985.35.2.99.

Bhatia, S. K., Schwab, J., and Ishibashi, I. 1985. Cyclic simple shear, torsional shear and triaxial - A comparative study. In *Advances in the Art of Testing Soils Under Cyclic Conditions*, edited by V. Khosla. ASCE, New York, NY. pp. 232–254.

Boulanger, R. W. and Ziotopoulou, K. 2017. *PM4Sand (version 3.1): A sand plasticity model for earthquake engineering applications*. Report No. UCD/CGM-17/01. Center for Geotechnical Modeling, Department of Civil and Environmental Engineering, University of California, Davis, CA.

Boulanger, R. W. 2003. Relating Kα to relative state parameter index. *Journal of Geotechnical and Geoenvironmental Engineering* 129(8): 770–773. https://doi.org/10.1061/(ASCE)1090-0241(2003)129:8(770)

Carey, T. J., Stone, N., and Kutter, B. L. 2020. Grain Size Analysis and Maximum and Minimum Dry Density Testing of Ottawa F-65 Sand for LEAP-UCD-2017. In *Model Tests and Numerical Simulations of Liquefaction and Lateral Spreading*, edited by B. L. Kutter, M. T. Manzari, and M. Zeghal, 31–44. Cham, Switzerland: Springer. https://doi.org/10.1007/978-3-030-22818-7

Chiaro, G., Kiyota, T., and Koseki, J. 2013. Strain localization characteristics of loose saturated Toyoura sand in undrained cyclic torsional shear tests with initial static shear. *Soils and Foundations* 53(1): 23–34. https://doi.org/10.1016/j.sandf.2012.07.016

Chiaro, G., Koseki, J., and Sato, T. 2012. Effects of initial static shear on liquefaction and large deformation properties of loose saturated Toyoura sand in undrained cyclic torsional shear tests. *Soils and Foundations* 52(3): 498–510. https://doi.org/10.1016/j.sandf.2012.05.008

El Ghoraiby, M. A. and Manzari, M. T. 2018. LEAP-2018 - Stress-strain response of Ottawa F65 sand in Cyclic Simple Shear. DesignSafe-CI, Dataset. https://doi.org/10.17603/DS2NM4W

El Ghoraiby, M. A., Park, H., and Manzari, M. T. 2017. *LEAP 2017: Soil characterization and element tests for Ottawa F65 sand*. The George Washington University, Washington, DC.

Finn, W. D. L. and Vaid, Y. P. 1977. Liquefaction potential from drained constant volume cyclic simple shear tests. In *Proceedings of the 6th World Conference on Earthquake Engineering, New Delhi, India*. pp. 2157–2162.

Humire, F., Lee, M., Ziotopoulou, K., Gomez, M. G., and DeJong, J. T. 2021. Development and evaluation of pre-conditioning protocols for sand specimens in constant-volume cyclic direct simple shear tests. *Geotechnical Testing Journal* (under review).

Humire, F., Ziotopoulou, K., Basson, M. S., and Martinez, A. 2019. Framework for tracking the accumulation of shear strains during cyclic mobility. In *Earthquake Geotechnical Engineering for Protection and Development of Environment and Constructions- Proceedings of the 7th International Conference on Earthquake Geotechnical Engineering, (ICEGE 2019), June 17-20, 2019, Rome, Italy*, edited by F. Silvestri and N.

Moraci. CRC Press, Taylor and Francis, London. pp. 906–2914. https://doi.org/10.1201/9780429031274

Idriss, I. M. and Boulanger, R. W. 2008. *Soil liquefaction during earthquakes*. Monograph MNO-12. Earthquake Engineering Research Institute, Oakland, CA.

Kammerer, A. M., Wu, J., Pestana, J. M., Riemer, M. F., and Seed, R. B. 2000. *Cyclic simple shear testing of Nevada sand for PEER center project 2051999*. Geotechnical Engineering Report No. UCB/GT/00-01. University of California, Berkeley, CA.

Khosravifar, A., Elgamal, A., Lu, J., and Li, J. 2018. A 3D model for earthquake-induced liquefaction triggering and post-liquefaction response. *Soil Dynamics and Earthquake Engineering* 110: 43–52. https://doi.org/10.1016/j.soildyn.2018.04.008

Kiyota, T., Sato, T., Koseki, J., and Abadimarand, M. 2008. Behavior of liquefied sands under extremely large strain levels in cyclic torsional shear tests. *Soils and Foundations* 48(5): 727–739. https://doi.org/10.3208/sandf.48.727

Kokusho, T., Hara, T., and Hiraoka, R. 2004. Undrained shear strength of granular soils with different particle gradations. *Journal of Geotechnical and Geoenvironmental Engineering* 130(6): 621–629. https://doi.org/10.1061/(asce)1090-0241(2004)130:6(621)

Konrad, J.-M. 1988. Interpretation of flat plate dilatometer tests in sands in terms of the state parameter. *Geotechnique* 38(2): 263–277. https://doi.org/10.1680/geot.1988.38.2.263

Kutter, B. L., Manzari, M. T., and Zeghal, M. 2020. *Model Tests and Numerical Simulations of Liquefaction and Lateral Spreading*. Cham, Switzerland: Springer. https://doi.org/https://doi.org/10.1007/978-3-030-22818-7

Lee, M., Gomez, M. G., El Kortbawi, M., and Ziotopoulou, K. 2022. Effect of light biocementation on the liquefaction triggering and post-triggering behavior of loose sands. *Journal of Geotechnical and Geoenvironmental Engineering* 148(1): 04021170. https://doi.org/10.1061/(ASCE)GT.1943-5606.0002707

Lunne, T., Knudsen, S., Blaker, Vestgården, T., Powell, J. J. M., Wallace, C. F., Krogh, L., Thomsen, N. V., Yetginer, G., and Ghanekar, R. K. 2019. Methods used to determine maximum and minimum dry unit weights of sand: Is there a need for a new standard? *Canadian Geotechnical Journal* 56(4): 536–553. https://doi.org/10.1139/cgj-2017-0738

Monkul, M. M., Gültekin, C., Gülver, M., Akin, Ö., and Eseller-Bayat, E. 2015. Estimation of liquefaction potential from dry and saturated sandy soils under drained constant volume cyclic simple shear loading. *Soil Dynamics and Earthquake Engineering* 75: 27–36. https://doi.org/10.1016/j.soildyn.2015.03.019

Morales, B., Humire, F., and Ziotopoulou, K. 2021. Direct Simple Shear Testing on Ottawa F50 and F65 Sand. DesignSafe-CI [publisher], Dataset. https://doi.org/10.17603/ds2-eahz-9466

National Academies of Sciences, Engineering, and Medicine. 2016. *State of the art and practice in the assessment of earthquake-induced soil liquefaction and its consequences*. The National Academies Press, Washington, DC. https://doi.org/10.17226/23474

Parra Bastidas, A. M. 2016. *Ottawa F-65 Sand Characterization*. PhD dissertation, University of California, Davis.

Seed, H. B. and Lee, K. L. 1966. Liquefaction of saturated sands during cyclic loading. *Journal of the Soil Mechanics and Foundations Division* 92(6): 105–134.

Seed, H. B., Lysmer, J., and Martin, P. P. 1976. Pore-water pressure changes during soil liquefaction. *Journal of the Geotechnical Engineering Division* 102(4): 323–346.

Shamoto, Y., Zhang, J.-M., and Goto, S. 1997. Mechanism of large post-liquefaction deformation in saturated sand. *Soils and Foundations* 37(2): 71–80. https://doi.org/10.3208/sandf.37.2_71

Sivathayalan, S. and Ha, D. 2011. Effect of static shear stress on the cyclic resistance of sands in simple shear loading. *Canadian Geotechnical Journal* 48(10): 1471–1484. https://doi.org/10.1139/t11-056

Sriskandakumar, S. 2004. *Cyclic loading response of Fraser River sand for validation of numerical models simulating centrifuge tests*. M.Sc. thesis, Department of Civil Engineering, University of British Columbia.

Sze, H. Y. and Yang, J. 2014. Failure modes of sand in undrained cyclic loading: Impact of sample preparation. *Journal of Geotechnical and Geoenvironmental Engineering* 140(1): 152–169. https://doi.org/10.1061/(asce)gt.1943-5606.0000971

Tasiopoulou, P., Ziotopoulou, K., Humire, F., Giannakou, A., Chacko, J., and Travasarou, T. 2020. Development and implementation of semiempirical framework for modeling postliquefaction shear deformation accumulation in sands. *Journal of Geotechnical and Geoenvironmental Engineering* 146(1): 4019120. https://doi.org/10.1061/(ASCE)GT.1943-5606.0002179

Ueda, K., Uemura, K., and Vargas, R. R. 2020. Data for: Dynamic torsional hollow-cylinder shear tests of Ottawa F-65 sand. Mendeley Data, V1. https://doi.org/doi: 10.17632/gv78bymth9.1

Vaid, J. P., Stedman, J. D., and Sivathayalan, S. 2001. Confining stress and static shear effects in cyclic liquefaction. *Canadian Geotechnical Journal* 38(3): 580–591. https://doi.org/10.1139/cgj-38-3-580

Vaid, Y. P. and Chern, J. C. 1985. Cyclic and monotonic undrained response of saturated sands. In *Advances in the Art of Testing Soils Under Cyclic Conditions*, edited by V. Khosla. ASCE, New York, NY. pp. 120–147.

Vaid, Y. P. and Sivathayalan, S. 2000. Fundamental factors affecting liquefaction susceptibility of sands. *Canadian Geotechnical Journal* 37(3): 592–606. https://doi.org/10.1139/t00-040

Vasko, A. 2015. *An Investigation into the Behavior of Ottawa Sand through Monotonic and Cyclic Shear Tests*. Master's thesis, George Washington University.

Wang, G. and Wei, J. 2016. Microstructure evolution of granular soils in cyclic mobility and post-liquefaction process. *Granular Matter* 18: 51. https://doi.org/10.1007/s10035-016-0621-5

Wang, R., Fu, P., Zhang, J. M., and Dafalias, Y. F. 2016. DEM study of fabric features governing undrained post-liquefaction shear deformation of sand. *Acta Geotechnica* 11(6): 1321–1337. https://doi.org/10.1007/s11440-016-0499-8

Wei, J., Huang, D., and Wang, G. 2018. Microscale descriptors for particle-void distribution and jamming transition in pre- and post-liquefaction of granular soils. *Journal of Engineering Mechanics* 144(8): 4018067. https://doi.org/10.1061/(ASCE)EM.1943-7889.0001482

Wichtmann, T. and Triantafyllidis, T. 2016. An experimental database for the development, calibration and verification of constitutive models for sand with focus to cyclic loading:

part I---tests with monotonic loading and stress cycles. *Acta Geotechnica* 11(4): 739–761. https://doi.org/10.1007/s11440-015-0402-z

Wijewickreme, D. and Soysa, A. 2016. Stress-strain pattern-based criterion to assess cyclic shear resistance of soil from laboratory element tests. *Canadian Geotechnical Journal* 53(9): 1460–1473. https://doi.org/10.1139/cgj-2015-0499

Yang, M., Taiebat, M., Mutabaruka, P., and Radjaï, F. 2021. Evolution of granular materials under isochoric cyclic simple shearing. *Physical Review E* 103(3): 032904. https://doi.org/10.1103/PhysRevE.103.032904

Zhang, J.-M., Shamoto, Y., and Tokimatsu, K. 1997. Moving critical and phase-transformation stress state lines of saturated sand during undrained cyclic shear. *Soils and Foundations* 37(2): 51–59. https://doi.org/10.3208/sandf.37.2_51

Zhang, J.-M. and Wang, G. 2012. Large post-liquefaction deformation of sand, part I: physical mechanism, constitutive description and numerical algorithm. *Acta Geotechnica* 7(2): 69–113. https://doi.org/10.1007/s11440-011-0150-7

Ziotopoulou, K. and Boulanger, R. W. 2016. Plasticity modeling of liquefaction effects under sloping ground and irregular cyclic loading conditions. *Soil Dynamics and Earthquake Engineering* 84: 269–283. https://doi.org/10.1016/J.SOILDYN.2016.02.013

4.6 Tables and figures

Table 4.1. Summary of constant-volume (equivalent undrained) cyclic DSS tests performed under uniform loading (UL) conditions.

Test ID	D_R (%)	σ'_{vo} (kPa)	τ_{cyc} (kPa)	Test ID	D_R (%)	σ'_{vo} (kPa)	τ_{cyc} (kPa)
UL-01	37.7	100	10	UL-17	50.6	50	7.5
UL-02	38.7	100	10	UL-18	56.0	50	10
UL-03	48.0	100	15	UL-19	60.1	50	10
UL-04	59.7	100	10	UL-20	63.4	50	7.5
UL-05	61.3	100	12	UL-21	66.3	50	7
UL-06	58.7	100	15	UL-22	69.6	50	8.5
UL-07	56.0	100	18	UL-23	79.6	50	10
UL-08	63.0	100	15	UL-24	42.3	400	60
UL-09	64.3	100	15	UL-25	52.4	400	40
UL-10	75.2	100	15	UL-26	55.4	400	40
UL-11	76.4	100	15	UL-27	60.4	400	60
UL-12	76.9	100	20	UL-28	64.9	400	34
UL-13	77.5	100	20	UL-29	66.2	400	60
UL-14	79.0	100	20	UL-30	70.4	400	60
UL-15	37.5	50	7.5	UL-31	78.5	400	80
UL-16	42.1	50	7.5				

Table 4.2. Summary of constant-volume (equivalent undrained) cyclic DSS tests performed under irregular loading (IL) conditions.

Test ID	D_R (%)	σ'_{vo} (kPa)	$\tau_{cyc,1}$ (kPa)	$\tau_{cyc,2}$ (kPa)	$\tau_{cyc,3}$ (kPa)
IL-01	61.5	100	15	7.5	3.75
IL-02	64.4	100	15	5	10
IL-03	66.6	100	12	6	12
IL-04	68.0	100	16	8	12

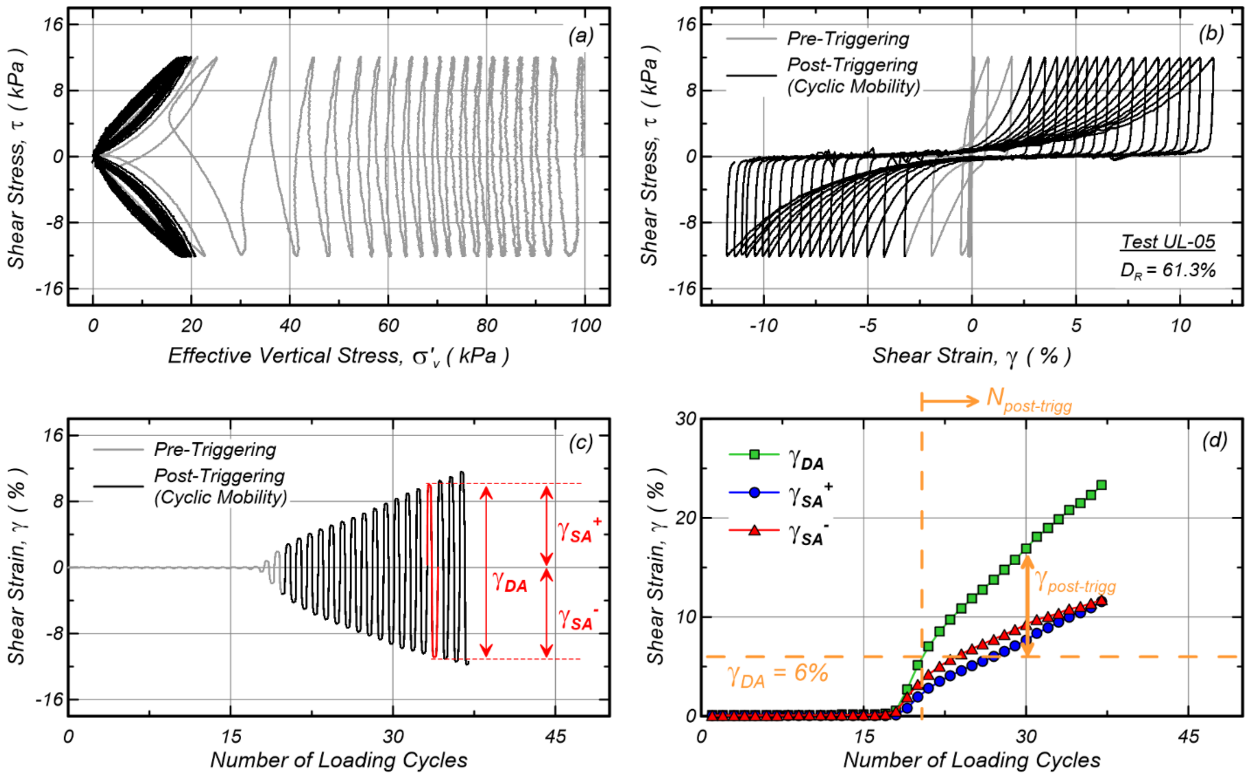

Figure 4.1. Results of a constant-volume (equivalent undrained) cyclic DSS test performed on a medium dense specimen of Ottawa F-65 sand: (a) effective stress path, (b) stress-strain response, (c) shear strain accumulation per loading cycle, and (d) evolution of single and double amplitude shear strains (γ_{SA} and γ_{DA}) per loading cycle, and definition of post-triggering shear strains ($\gamma_{post\text{-}trigg}$) and post-triggering cycles ($N_{post\text{-}trigg}$).

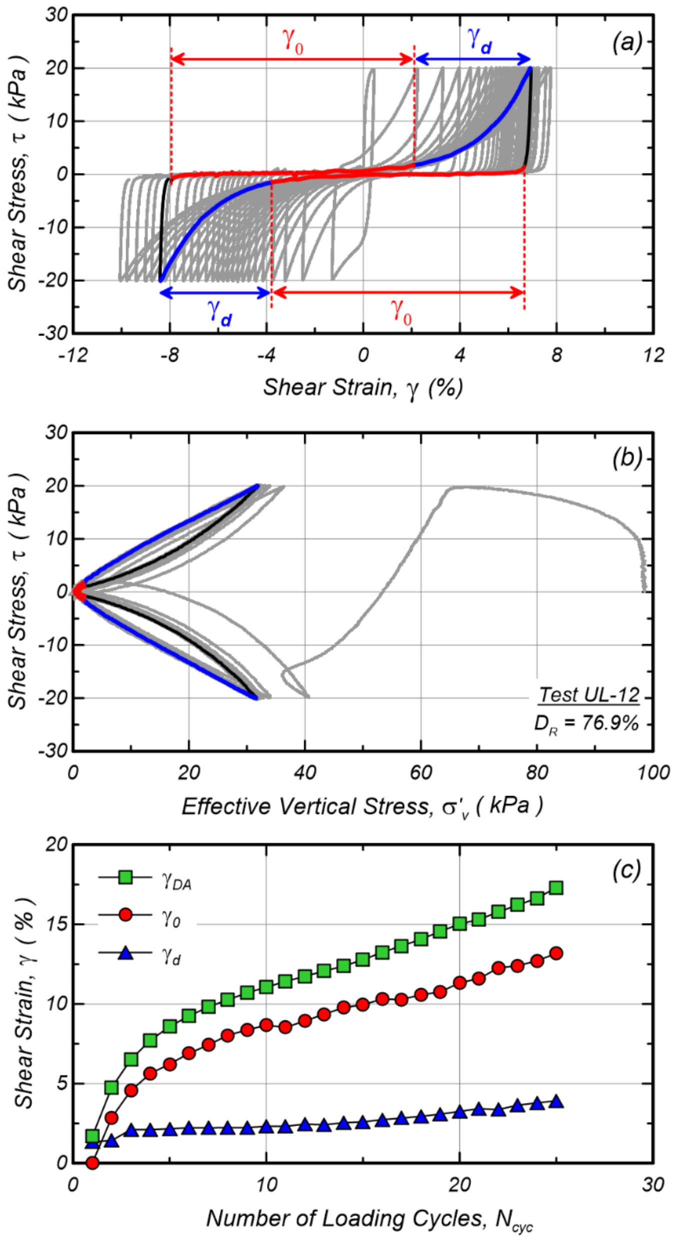

Figure 4.2. Near-zero effective stress shear strains (γ_0) and shear strains during dilation (γ_d) for a constant-volume cyclic DSS test on a dense specimen of Ottawa F-65 sand: (a) definition in stress-strain loop domain, (b) corresponding branches in stress path, and (c) evolution with number of loading cycles.

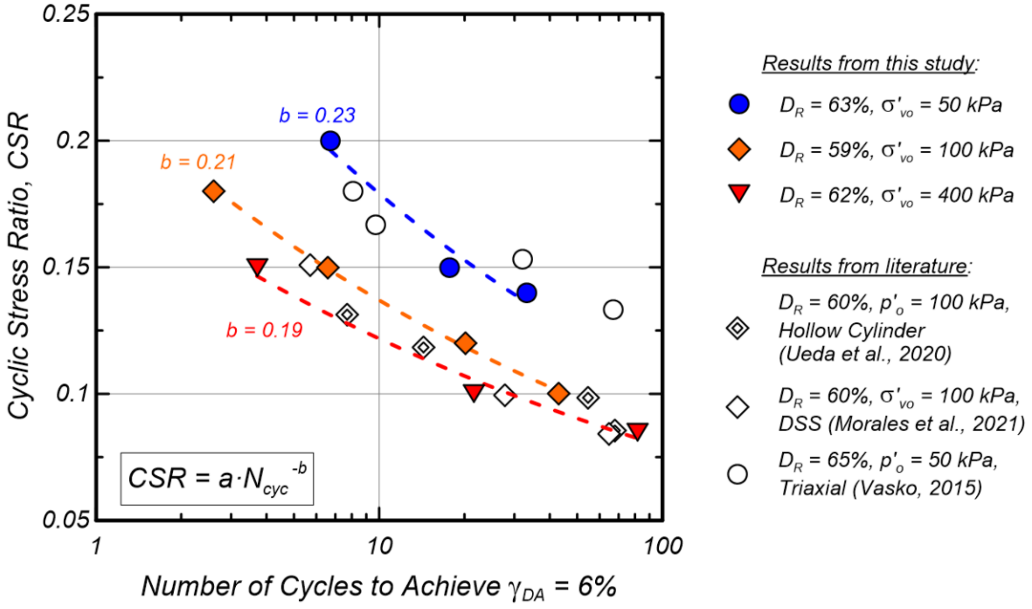

Figure 4.3. Liquefaction triggering curves for medium dense specimens of Ottawa F-65 sand, tested as part of this work, under varying effective overburden stresses σ'vo, and comparison with available results from literature.

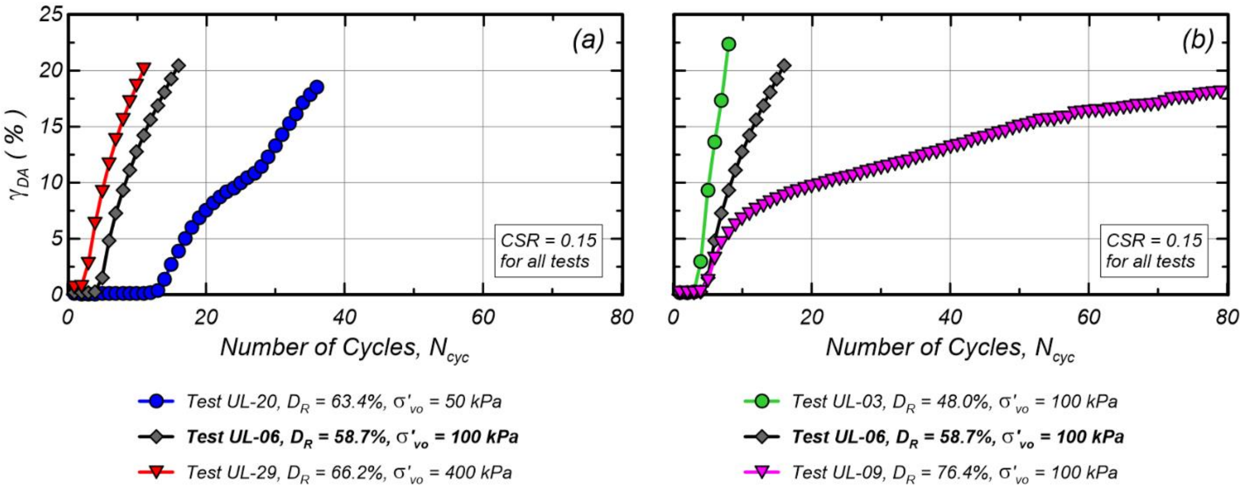

Figure 4.4. Shear strain accumulation per loading cycle in: (a) three DSS tests on medium dense specimens, under different σ'_{vo} values but same CSR (0.15) and similar D_R (59-66%) values, and (b) three DSS tests performed on specimens with different D_R values but same σ'_{vo} (100 kPa) and CSR (0.15).

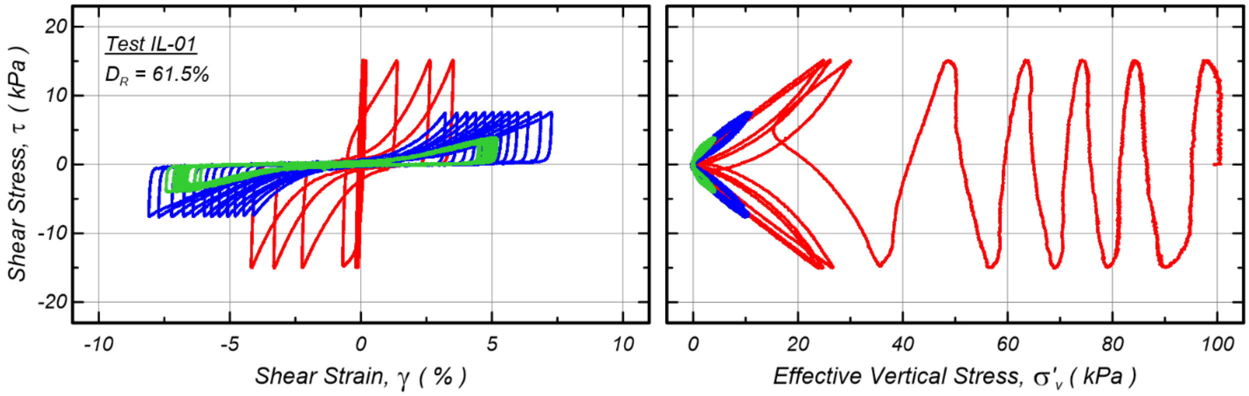

Figure 4.5. Example results of a constant-volume DSS test performed on a medium dense specimen of Ottawa F-65 sand under irregular cyclic loading conditions, wherein the amplitude of cyclic shearing is progressively reduced over three distinct stages.

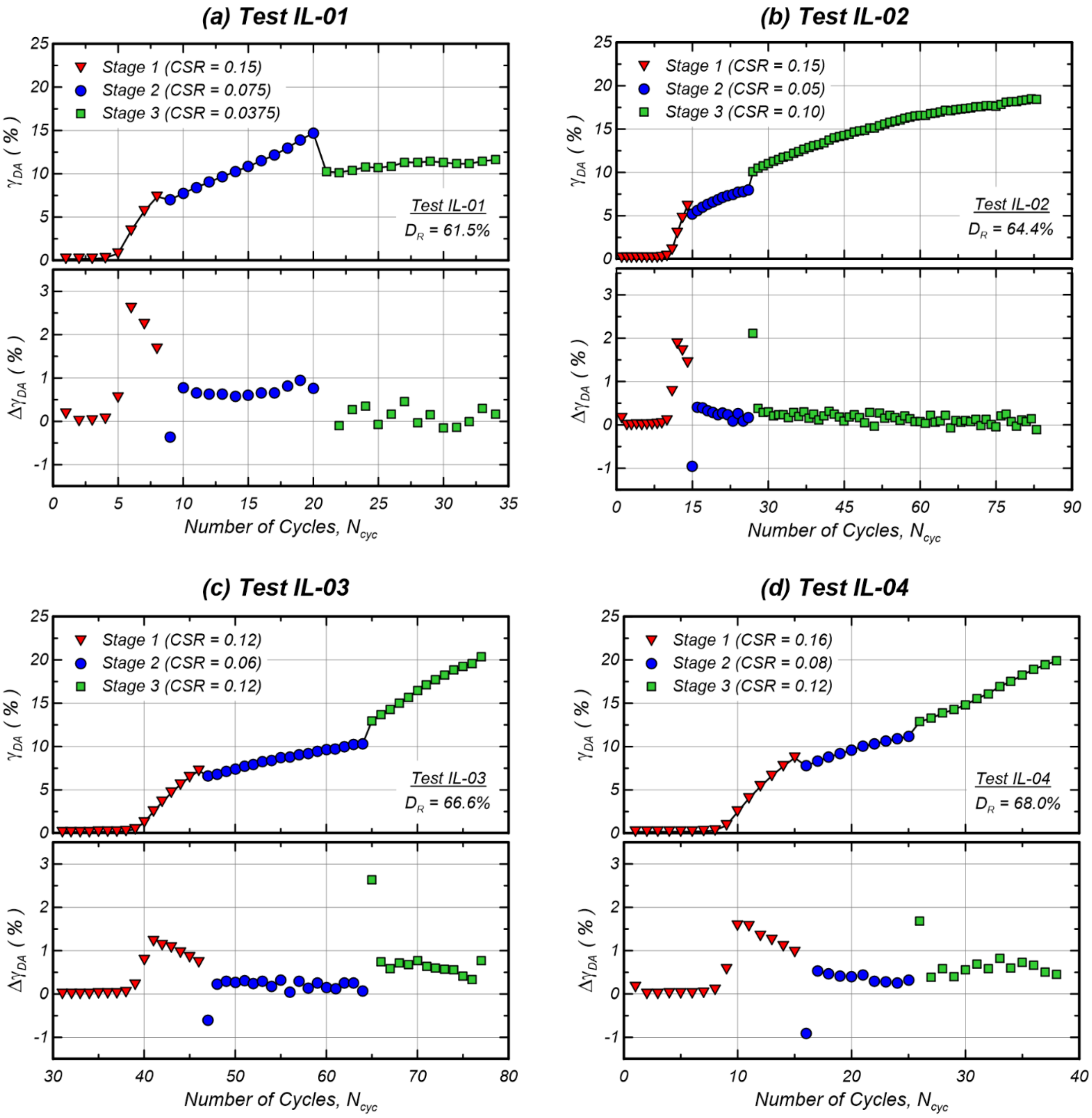

Figure 4.6. Results of four DSS tests performed under irregular loading conditions, with shear strain accumulation per loading cycle, and rate of shear strain accumulation ($\Delta\gamma_{DA}$) per loading cycle shown for each test: (a) test IL-01, (b) test IL-02, test IL-03, and (d) test IL-04.

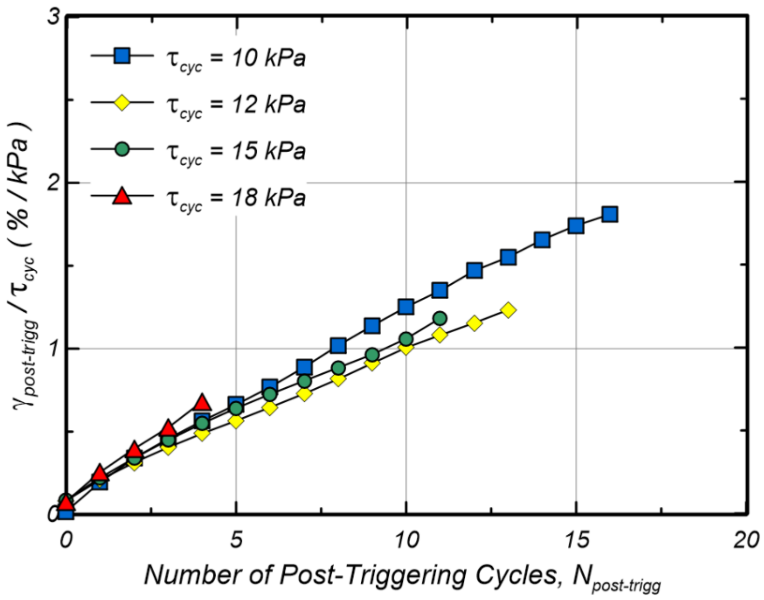

Figure 4.7. Evolution of $\gamma_{post-trigg}$ per post-triggering loading cycle normalized by the cyclic stress amplitude (τ_{cyc}) in tests UL-04 to UL-07.

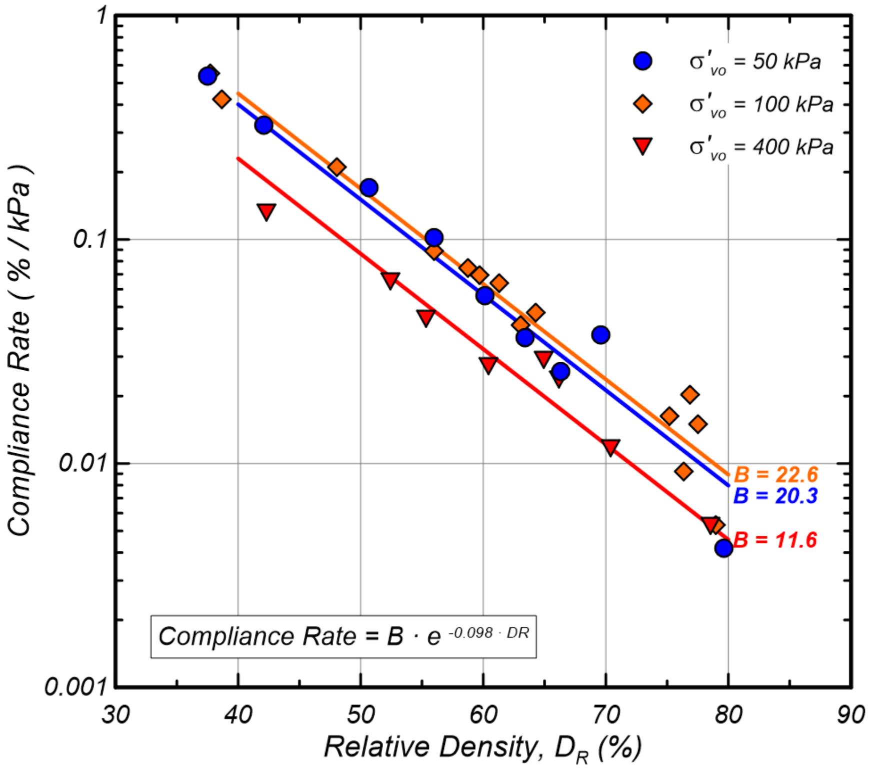

Figure 4.8. Compliance rates evaluated for all DSS tests performed within this work on specimens of Ottawa F-65 sand.

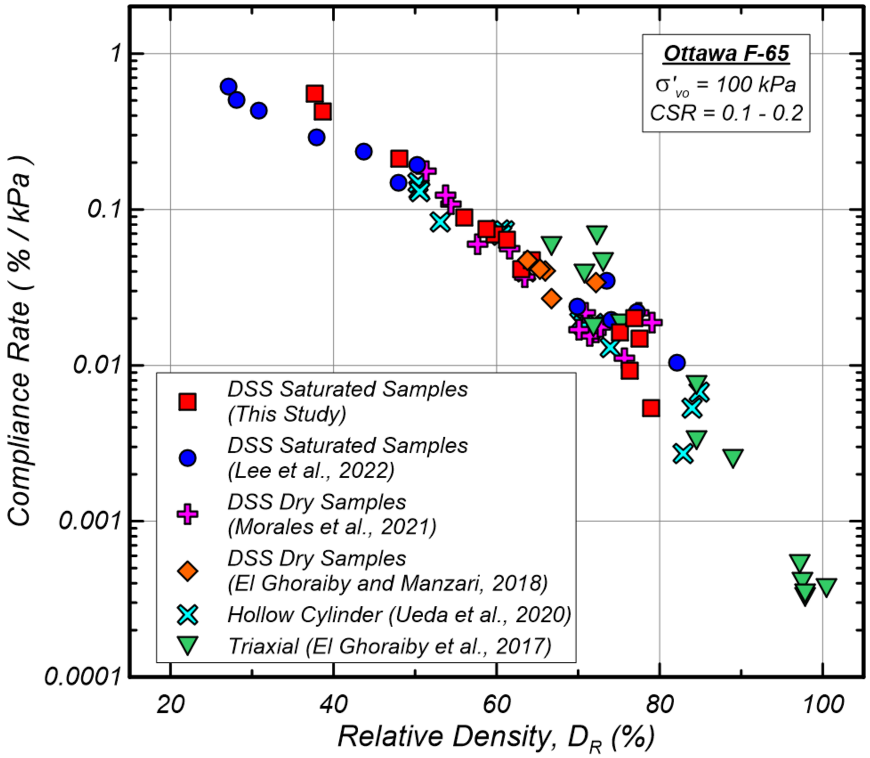

Figure 4.9. Comparison of compliance rates evaluated for different experimental databases on Ottawa F-65 sand under σ'vo = 100 kPa.

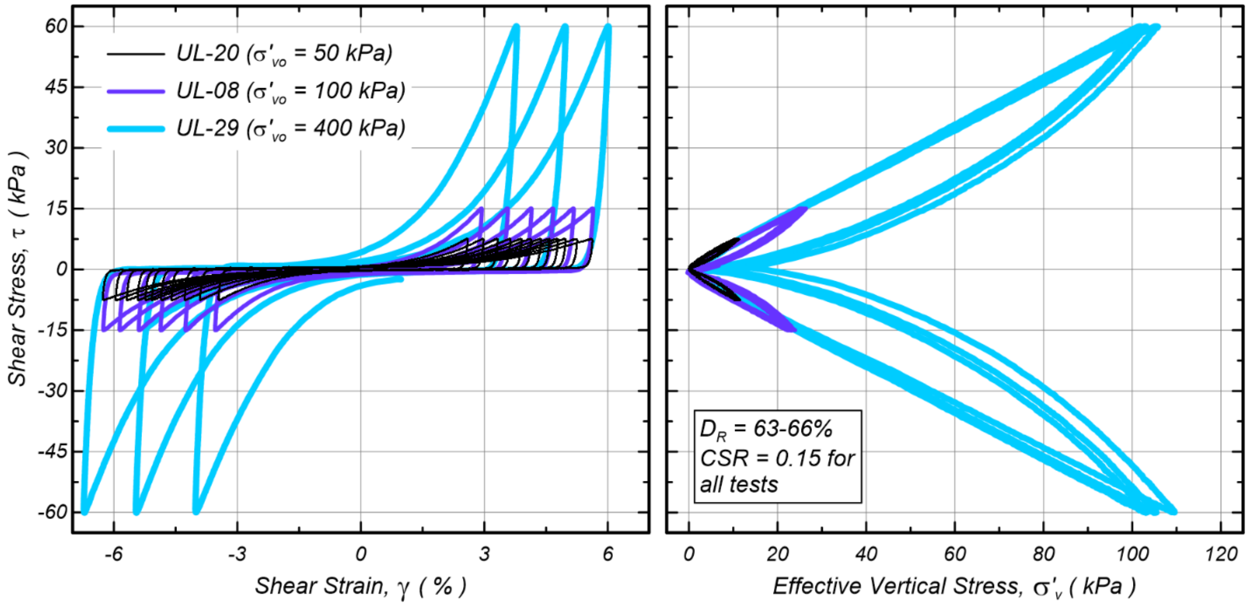

Figure 4.10. Comparison of (a) stress-strain and (b) stress path loops obtained and isolated between liquefaction triggering and until a γ_{DA} of 12% is achieved, for three DSS tests on medium dense sand specimens, similar CSRs, and under different effective overburden stresses (σ'vo of 50, 100 and 400 kPa).

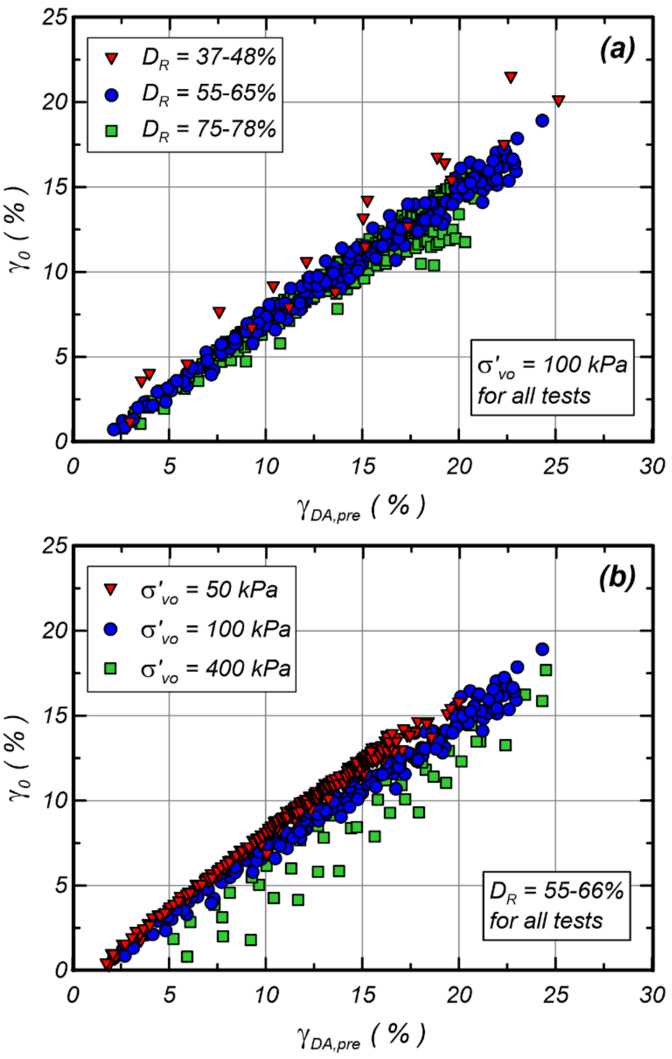

Figure 4.11. Dependency of γ_0 on the γ_{DA} achieved during the preceding loading cycle ($\gamma_{DA,pre}$) for the DSS tests performed under uniform loading conditions: (a) comparison for different densities under σ'$_{vo}$ = 100 kPa, and (b) comparison for different σ'$_{vo}$ with D_R = 55-66%.

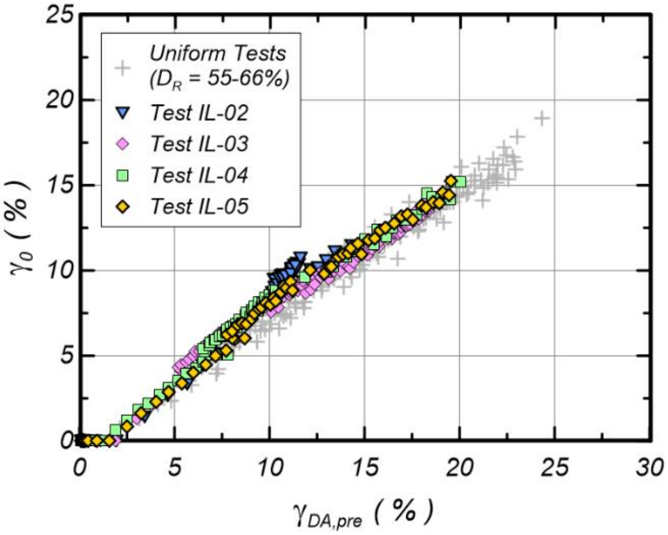

Figure 4.12. Dependency of γ_0 on the γ_{DA} achieved during the preceding loading cycle ($\gamma_{DA,pre}$) for the DSS tests performed under irregular loading conditions.

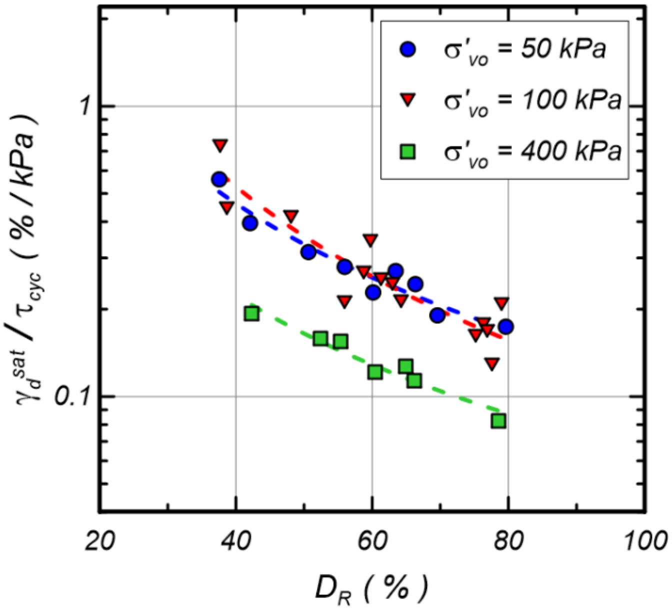

Figure 4.13. $\gamma_d^{sat}/\tau_{cyc}$ for all the experiments performed under uniform loading conditions evaluated as the average of γ_d/τ_{cyc} in the range of 6 to 10% double amplitude shear strain.

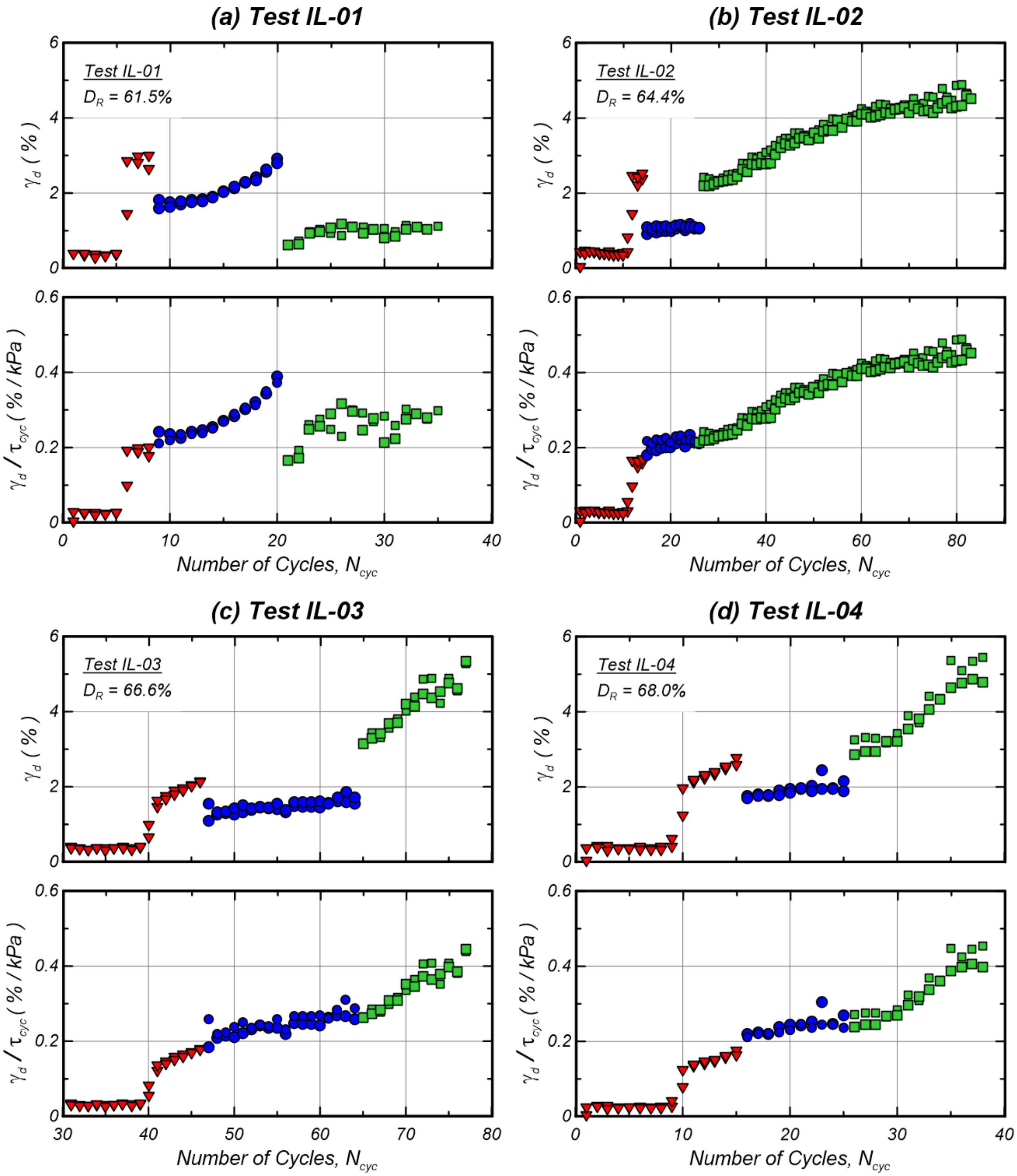

Figure 4.14. Evolution of γ_d and γ_d/τ_{cyc} per loading cycle for all the experiments under irregular loading conditions: (a) test IL-01, (b) test IL-02, test IL-03, and (d) test IL-04.

Chapter 5

Effect of gradation and grain size on the liquefaction and post-liquefaction behavior of coarse-grained soils

Author's note: This Chapter will be submitted as a journal paper for publication authored by Francisco Humire, Rachel A. Reardon, Katerina Ziotopoulou, and Jason T. DeJong. The paper is presented herein with some minor edits for consistency with the other chapters of this Dissertation.

Abstract

In order to investigate the role of gradation and grain size on the liquefaction and post-liquefaction behavior of coarse-grained soils, a series of cyclic constant-volume direct simple shear (CV-DSS) tests were performed using seven soil mixtures with different coefficients of uniformity (C_u) and median grain sizes (D_{50}). Empirical observations of liquefaction triggering, post-triggering shear strain accumulation, and post-liquefaction reconsolidation strains were synthesized to evaluate functional trends with C_u and D_{50}. Results showed that the effects of C_u and D_{50} on the liquefaction triggering resistance depend on the relative density (D_R) at which they are compared. For very loose specimens ($D_R \approx 25\%$), soils with different C_u and D_{50} values exhibited similar triggering resistances, while tests in medium dense specimens ($D_R \approx 65\%$) showed a decrease of the triggering resistance while increasing C_u and D_{50}. The triggering resistances exhibited by coarse-grained soils with higher C_u values were closer to those obtained when testing only their coarser

constituents at similar D_R's, which suggests that the cyclic behavior of well-graded soils may be primarily controlled by their coarser particles. Coarse-grained soils with broader gradations exhibited smaller rates of shear strain accumulation than poorly graded sands at similar D_R's, which was attributed to the smaller void ratios of soils with higher C_u values and, thus, the smaller room for particle rearrangement during shearing. The rate of shear strain accumulation also decreased while increasing D_{50}, which was attributed to enhanced dilation when testing coarser soils. Finally, results showed that an increase in C_u leads to smaller post-liquefaction reconsolidation volumetric strains, while changes in D_{50} had little effect on such strains.

5.1 Introduction

Well-graded coarse-grained soils encompass a broad range of soils often present in natural deposits near lakes and rivers and engineered fill materials used for the construction of geosystems (e.g., dams, levees). Despite the several liquefaction case histories on well-graded soils documented in the literature (e.g., Kokusho et al. 2004; Ghafghazi and DeJong 2016; Zalachoris et al. 2021), the evaluation of liquefaction effects on infrastructure founded upon or comprised by these soils remains a challenging task. This is partly due to the lack of understanding of the effects of gradation and grain size on the liquefaction and post-liquefaction behavior of coarse-grained soils. Given this knowledge gap, and particularly when site-specific experimental data are not available, the current engineering practice assumes that liquefaction effects can be assessed using: (1) empirical or semi-empirical correlations developed for clean uniform sands on the basis of laboratory testing, or (2) case history-based correlations that do not explicitly account for the effects of grain size and gradation. Recent centrifuge modeling investigations suggest that such correlations may misrepresent the actual response of well-graded soils leading to overestimations of the anticipated liquefaction-induced deformations in system level analyses (Sturm 2019; Carey et al. 2021).

Element level laboratory tests (e.g., direct simple shear, triaxial, torsional tests) have contributed to an improved understanding of the cyclic behavior of clean uniform sands, in terms of liquefaction triggering (e.g., Vaid and Sivathayalan 2000; Idriss and Boulanger 2008), post-triggering shear strain accumulation (e.g., Shamoto et al. 1997; Zhang and Wang 2012; Tasiopoulou et al. 2020), and post-liquefaction reconsolidation (e.g., Ishihara and Yoshimine 1992; Sento et al. 2004; Kim et al. 2016). However, contradictory and ambiguous findings regarding the effects of grain size and gradation on the liquefaction and post-liquefaction behavior of coarse-grained soils are reported in the literature, which can be attributed to: (1) differences and limitations of laboratory testing devices, and (2) the influence of other grain properties (e.g., grain shape) on the soil response. For example, results from cyclic undrained triaxial tests (Lee and Fitton 1969; Wong et al. 1975, Chang and Ko 1982; Yilmaz et al. 2008; Wichtmann et al. 2019) suggest the increase of liquefaction triggering resistance with increasing the median grain size (D_{50}) of clean uniform coarse-grained soils prepared to the same relative density. However, such increases could be attributed to membrane compliance effects that are more significant when increasing D_{50}, and that cause an artificial increase of the liquefaction triggering resistance as shown by Martin et al. (1978) and later corroborated by Evans et al. (1992). On the other hand, results from cyclic constant-volume direct simple shear (CV-DSS) tests suggest that increasing D_{50} has a negligible (Doygun et al. 2019) or detrimental effect (Chang et al. 2014; Hubler et al. 2017) on the liquefaction triggering resistance of clean uniform coarse-grained soils. Recent investigations with CV-DSS tests have also provided insights into the effects of grain size on the post-liquefaction behavior of coarse-grained soils. Post-cyclic monotonic CV-DSS tests by Hubler et al. (2017) performed on clean uniform gravels with similar grain shapes suggest a more dilative response following liquefaction triggering with increased D_{50}. In a later study, Hubler et al. (2018) showed that clean uniform gravels and sands with similar grain shapes can exhibit similar post-liquefaction volumetric reconsolidation strains.

The interpretation of the effects of soil gradation on the cyclic response of coarse-grained soils is more challenging because the results depend on the factors that are held constant in a testing program. For the same initial void ratio (e), it has been established that samples comprised of well-graded soils have a more contractive behavior and are more prone to liquefaction than uniform coarse-grained soils (Yang and Luo 2018; Kuei 2019). For the same relative density (D_R), however, other trends can be observed when evaluating the effects of gradation on the liquefaction behavior (Vaid et al. 1990; Kokusho et al. 2004; Doygun et al. 2019). For example, Vaid et al. (1990) performed a series of cyclic undrained triaxial tests on soils with identical D_{50} values and intrinsic grain properties but varying coefficients of uniformity (C_u). Those tests showed an increase in the liquefaction triggering resistance while increasing C_u for low D_R's, yet the opposite trend was observed when comparing the triggering resistance at high D_R's. Later, Kokusho et al. (2004) performed a similar testing plan involving soils with different C_u values but holding D_{10} as a constant instead of D_{50}. Results of those tests showed an almost negligible effect of gradation on the liquefaction triggering resistance; however, the application of post-cyclic undrained monotonic shearing showed a more dilative response after liquefaction triggering while increasing gradation. Other experimental investigations involving cyclic triaxial testing (Yilmaz et al. 2008; Wichtmann et al. 2019) also suggest that there is no clear correlation between C_u and the liquefaction triggering resistance for any combination of parameters held constant. In contrast, recent cyclic CV-DSS tests by Doygun et al. (2019) on uniform and well-graded coarse-grained soils with identical D_{90} values suggest a decrease of the liquefaction triggering resistance while increasing C_u.

Considering the importance of particle level mechanisms in the differences between the cyclic response of uniform and well-graded coarse-grained soils is key in the overall study of these effects. Particle level mechanisms such as the evolution of fabric (i.e., the spatial arrangement of solid particles, contacts, and pores in a soil matrix) have been shown to control the global-scale behavior of soils (e.g., Oda et al. 1985, O'Sullivan and Cui 2009). Discrete element model (DEM) simulations of laboratory tests have provided insights on the particle-level mechanisms controlling the liquefaction and post-liquefaction behavior of coarse-grained soils. From a particle-level perspective, the pre-liquefaction behavior can be characterized as a progressive reduction of the number of contacts per particle (i.e., coordination number C_N) and forces among particles, while the onset of liquefaction can be characterized as a sudden and drastic decrease of the coordination number below the minimum required to maintain a stable fabric (Wang and Wei 2016; Wang et al. 2016; Martin et al. 2020; Yang et al. 2021). Following liquefaction triggering, recent works have shown that the progressive development of shear deformations is accompanied by changes in the particle-void distribution within the grain assembly (Wang and Wei 2016; Wei et al. 2018) and distances between neighboring particles (Wang et al. 2016; Hu et al. 2020). However, none of those observations has been extended to understand the particle-level mechanisms controlling the cyclic response of well-graded materials, and DEM studies published so far have been limited to investigating the effect of C_u on the monotonic response (Wood and Maeda 2008; Liu et al. 2014; Li et al. 2015; Kuei 2019; He et al. 2021). Among those works, Kuei (2019) suggested two characteristic features of the particle-level response of well-graded soils: (1) smaller particles behave as "floaters" that do not contribute to the load-bearing stability of the grain assembly, and

(2) an enhanced dilation while increasing gradation as a result of the higher stability of the load-bearing network composed by the larger particles of the grain assembly.

As part of a broader effort to investigate the characterization and liquefaction response of well-graded coarse-grained soils in multiple scales, this paper presents findings from a laboratory testing program to systematically investigate the effect of gradation and grain size on the monotonic and cyclic behavior of coarse-grained soils. The testing program considered a series of constant-stress (CS) and constant-volume (CV) monotonic and cyclic direct simple shear (DSS) tests on seven coarse-grained soils with different coefficients of uniformity (C_u) and median grain sizes (D_{50}). Reardon et al. (2022) present the results and findings from the monotonic CS- and CV-DSS tests and some preliminary cyclic CV-DSS tests, while this paper presents a more comprehensive body of cyclic CV-DSS tests to address the cyclic component of the investigation. The specific objective of this paper is to investigate the effect of C_u and D_{50} on the liquefaction and post-liquefaction response of coarse-grained soils observed in cyclic CV-DSS tests for a broad range of relative densities (D_R). To this end, empirical observations of (i) liquefaction triggering resistance, (ii) post-triggering shear strain accumulation, and (iii) post-liquefaction reconsolidation strains are synthesized in order to identify and explain functional trends with C_u and D_{50}. Analyses and interpretations of results obtained for soils with different C_u values consider comparisons for both the same D_R and the same void ratio. Findings from this work form a physics-based basis to assess the appropriateness of current methods used in engineering practice to evaluate liquefaction effects in well-graded soils.

5.2 Experimental setup

5.2.1 Materials

Experiments were conducted on reconstituted specimens of sub-angular quarzitic coarse-grained soils with different grain size distributions (Figure 5.1), which were sourced from the Cape May Formation near Mauricetown, New Jersey (Sturm 2019). The sourced materials were isolated via sieving into four uniform coarse-grained soils with different D_{50} values: 100A, 100B, 100C, and 100D soils. These uniform soils were combined to form three soil mixtures with different gradations while holding an almost constant D_{10} value: 50AB (i.e., 50% 100A, 50% 100B by mass), 33ABC, and 25ABCD soils. Given their common geological origin, these soils are expected to isolate the effect of grain size and gradation on the cyclic response of coarse-grained soils from the effect of other grain properties (e.g., grain shape, mineralogy). Physical and index properties of these soils relevant to this work are summarized in Table 5.1, and more details regarding their index characterization are available in Sturm (2019).

The effect of C_u was investigated by comparing CV-DSS test results obtained for 100A, 50AB, 33ABC, and 25ABCD soils, which were selected to perform comparisons between soils with similar coefficients of permeability (Table 5.1). However, the maximum and minimum void ratios (e_{max} and e_{min}) of these soils tend to decrease while increasing C_u (Figure 5.2); thus, comparisons for the same D_R value may involve significant differences in the void ratio. On the other hand, the effect of D_{50} was investigated through comparisons of 100A, 100B, 100C, and 100D soils, which have similar e_{max} and e_{min} values (Figure 5.2) but are very different in terms of permeability (Table 5.1). Due to their high permeability, some soils in this group (e.g., 100C, 100D) may not even be susceptible to liquefaction in the field. However, the constant-volume conditions imposed in element-level laboratory tests force the occurrence of liquefaction without considering differences in soil permeability. For that reason, findings regarding the effect of D_{50} must be taken as results in an idealized situation in which permeability does not play a role in liquefaction triggering.

5.2.2 Testing equipment

The cyclic CV-DSS tests presented in this work were performed in an Electromechanical Dynamic Cyclic Simple Shear (EMDCSS) device manufactured by GDS Instruments. The active height control system implemented in this device allowed the performance of CV-DSS tests with vertical strains below the 0.025% threshold recommended by Zekkos et al. (2018) which automatically also satisfies the 0.05% threshold recommended by ASTM (2019).

Specimens were laterally enclosed by a stack of low-friction steel rings and a latex membrane of 0.35 mm (±0.05 mm) in thickness. Sintered steel porous discs with protruding ridges of 1 mm in height were mounted on the end caps to transmit shear forces to the samples. Most of the tests performed in this work were performed on cylindrical specimens of about 18 mm in height and 70 mm in diameter. In order to meet ASTM (2019) requirements regarding grain size and specimen height, tests on the 25ABCD and 100D soils were performed in large-size samples with a diameter of 150 mm and about 33 mm in height. A series of preliminary tests on soil 100A performed on both specimen sizes (70 and 150 mm in diameter) showed a slight increase of the liquefaction resistance measured with CV-DSS tests while increasing the size of specimens, which may be associated with differences in the vertical compliance for both specimen sizes and the smaller small-strain stiffness of shorter specimens (Reardon et al. 2022). In order to avoid the influence of specimen size on the trends regarding the effect of D_{50} and C_u on liquefaction triggering, all the comparisons of liquefaction triggering were made considering results obtained from specimens of the same size.

5.2.3 Sample preparation and testing procedures

Specimens with D_R's between 35 and 80% were prepared with the air pluviation method, which involved raining oven-dried sand from a fixed height into the soil container. The pluviator used in this investigation had a flow rate control system to target a specific D_R, and a mesh to evenly distribute the falling sand across the specimen area. Looser specimens (D_R = 25-35%) were prepared following a procedure similar to Method B of ASTM D4254 (2016) for performing minimum dry density tests. This procedure involved placing an acrylic cylinder with a diameter of about 70% of the specimen diameter above the bottom cap of the soil container, filling it with sand, and then quickly lifting the cylinder to fill the entire container. More details regarding the sample preparation equipment and procedures for this testing plan are available in Reardon (2021).

After applying a seating vertical stress of 25 kPa, a series of pre-conditioning strain-controlled drained cycles with an amplitude of 0.045% shear strain were applied to all specimens to ensure the engagement of the textured top platen with the sand specimens (Humire et al. 2021a). Based on a series of preliminary tests presented in Humire et al. (2021b), it was found that the application of 50 pre-conditioning drained cycles was appropriate for this testing plan to ensure a full engagement of the top platen while avoiding significant changes in the soil response. Following pre-conditioning, the samples were consolidated under a vertical stress of 100 kPa and then subjected to stress-controlled constant-volume cyclic shearing with a loading frequency of 0.05 Hz. For the tests that considered a post-cyclic monotonic shearing stage, the stress-controlled cyclic shearing stage was ended after achieving a shear strain of 3%. Then, the samples were subjected to constant-volume monotonic shearing with a shear strain rate of 50% per hour until a shear strain of 25% was achieved. For tests that considered a post-cyclic reconsolidation stage, the stress-controlled cyclic shearing was ended after achieving either a shear strain of 10-12% or more than 100 loading cycles in the post-triggering regime. Some of the tests on very loose to loose specimens (D_R = 25-45%) were subjected to an additional constant-volume strain-controlled cyclic shearing of 20-40 cycles with an amplitude of 12-14%, aimed to increase the shear strain accumulated during a test (γ_{acc}, Sento et al. 2004). This procedure allowed to explore higher values of post-liquefaction reconsolidation volumetric strains ($\varepsilon_{v,recons}$) for very loose to loose samples (D_R = 25-45%), which are associated with larger values of γ_{acc} that could not be explored without this additional strain-controlled cyclic shearing (Sento et al. 2004; Kim et al. 2016). Finally, specimens were re-centered to the position of zero shear strain and reconsolidated under a vertical stress of 100 kPa.

5.3 Test results and discussion

To illustrate the differences in the cyclic response of soils with different C_u and D_{50}, Figures 5.3 and 5.4 present the results of CV-DSS tests on 100A, 25ABCD, and 100D soils for loose (D_R = 41-48%) and medium dense (D_R = 57-61%) specimens, respectively. All tests show a progressive reduction of the effective vertical stresses (σ'_v); however, the number of loading cycles to trigger liquefaction in 100A (Figures 5.3a and 5.4a) is larger than those obtained for 25ABCD (Figures 5.3c and 5.4c) and 100D (Figures 5.3e and 5.4e), suggesting a decrease in the triggering resistance while increasing C_u and D_{50}. Following liquefaction triggering, the tests show shear strains increments per loading cycle ($\Delta\gamma$) much larger for 100A (Figure 5.3b and 5.4b) than those observed for 25ABCD (Figures 5.3d and 5.4d) and 100D (Figures 5.3f and 5.4f). Also, the test on 25ABCD with D_R = 57% (Figure 5.4d) exhibits a complete arrest on the shear strain accumulation after reaching a single-amplitude shear strain of 5%. These observations suggest that post-triggering shear deformations tend to decrease while increasing both C_u and D_{50}.

This section presents and discusses the results obtained in more than 100 cyclic CV-DSS tests performed in the seven soils shown in Figure 5.1 with D_R's between 25 and 80% and cyclic stress ratio (CSR) values ranging between 0.06 and 0.20. The analysis and interpretation of these tests aim to quantify and explain the effect of C_u and D_{50} on: (1) liquefaction triggering resistance, (2) shear strain accumulation, and (3) post liquefaction reconsolidation.

5.3.1 Liquefaction triggering resistance

The liquefaction triggering resistance was calculated with a 3% single amplitude shear strain criterion, and results were grouped to define triggering curves for the seven soil mixtures at different D_R values. Given the significant differences in e_{min} and e_{max} of soils with different gradations (Figure 5.2), the effect of C_u was investigated from comparisons with a constant D_R value, but also from comparisons with a constant void ratio. This subsection present analyses investigate the effect of C_u and D_{50} on the liquefaction triggering resistance, which include:

1) Comparing triggering curves of the seven soil mixtures for the same D_R value.
2) Comparing triggering curves of soils with different gradations (100A, 50AB, and 33ABC) for the same void ratio.
3) Assessing changes on triggering resistance with changes in D_R for the same CSR.

Figure 5.5 presents the triggering curves obtained from 70 mm CV-DSS tests on loose and medium dense specimens of soils with different C_u (100A, 50AB, and 33ABC) and D_{50} values (100A, 100B, and 100C). Results show a decrease of the liquefaction triggering resistance while increasing C_u, with a more substantial reduction for medium dense specimens (Figure 5.5b) than loose ones (Figure 5.5a). Results show similar decreasing trends of the triggering resistance while increasing D_{50} for loose (Figure 5.5c) and medium dense specimens (Figure 5.5d). These results suggest a decrease in liquefaction triggering resistance as C_u and D_{50} increase in CV-DSS testing conditions, which does not considered differences in permeability (Table 5.1).

Figure 5.6 compares the triggering curves obtained from 150 mm CV-DSS tests on loose and medium dense specimens of 100A, 100D, and 25ABCD soils. Results show 100D and 25ABCD soils to have similar triggering resistances, while the 100A sand exhibits a higher triggering resistance than 100D and 25ABCD for both D_R's. These results confirm observations from Figure 5.5 regarding the decreases in triggering resistance as C_u or D_{50} increases. The similarities between the triggering curves of 25ABCD and 100D suggest that the coarser constituents of these soils with broader gradations control their pre-triggering response and liquefaction triggering resistance. This observation is consistent with Kuei (2019), who, based on DEM analyses, suggested that the contacts among larger particles control the behavior of well-graded materials, while smaller particles can act as “floaters” within the soil matrix.

Figures 5.5 and 5.6 also include the values of the slopes (b) of the power functions fitted to the liquefaction triggering data. Most of the b values presented in Figure 5.5 are around 0.20 ± 0.03, except those obtained for medium dense specimens of 33ABC, 100B, and 100C (b = 0.25 to 0.27). On the other hand, the b values of 100A and 100D shown in Figure 5.6 are similar, but are smaller than those obtained for 25ABCD. Although the data is insufficient to establish functional dependencies for the b values, the results suggest that C_u and D_{50} have either a negligible or increasing effect on the slope of the triggering curve.

Given the differences in the e_{min} and e_{max} values of soils with different gradations (Figure 5.2), the effect of C_u on the liquefaction triggering resistance is also examined for the same void ratio (Figure 5.7). Comparisons for the same void ratio show a reduction in the liquefaction triggering resistance while increasing C_u, which is more significant than the observed one for comparisons with the same D_R value. This reduction in the triggering resistance is attributed to the presence of more particles that act as "floaters" within the soil matrix and do not contribute to their load-bearing stability (Kuei 2019). Although smaller particles may not contribute to the load-bearing stability that determines the triggering resistance, their presence decreases the void ratio that characterizes the granular assembly.

The degree to which D_R affects the triggering resistance varies depending on the D_{50} and C_u of the specimen. Comparisons between triggering curves for loose and medium dense states (Figures 5.5 and 5.6) show that the triggering resistance of 100A is more sensitive to changes in D_R than the other soils. This observation suggests that the sensitivity of the triggering resistance to changes in D_R also depends on C_u and D_{50}. To closely examine this sensitivity to changes in D_R, Figure 5.8 compares the triggering resistances obtained in tests performed on five different soils for a broader range of D_R's but subjected to the same CSR. Results show that (1) similar triggering resistances are obtained for the different soils when comparing results of very loose specimens ($D_R \approx 25\%$), and (2) differences in triggering resistances between 100A and the other soils become more significant while increasing D_R.

The similar triggering resistances obtained for very loose specimens could be explained by the smaller degree of strain softening experienced while increasing both C_u and D_{50} (Reardon 2021), and how that affects the number of cycles to trigger liquefaction. Very loose to loose specimens (D_R = 25 to 40%) of the seven soil mixtures presented in this work have strain softening tendencies (e.g., Figure 5.9), which are characterized by a transient peak shear stress (τ_{peak}) during contraction followed by a local minimum during phase transformation (τ_{pt}). As shown in Figure

5.10, this strain softening tendency also affects the cyclic stress-strain response, which causes a faster decay of σ'_v from 50 to 0 kPa in 100A compared to the one observed in 25ABCD and 100D soils. Therefore, reduced strain softening observed on very loose samples of 25ABCD and 100D compensates for the more rapid decrease in σ'_v observed at the beginning of shearing, and leads to a number of cycles to trigger liquefaction similar to 100A. As D_R increases, this effect becomes negligible, and the differences in triggering resistances become more significant.

5.3.2 Post-triggering shear strain accumulation

The cyclic CV-DSS tests were post-processed to examine and quantify the effect of C_u and D_{50} on the shear strain accumulation based on approaches presented in previous works (Shamoto et al. 1997, Humire et al. 2019, Tasiopoulou et al. 2020, Humire and Ziotopoulou, 2022). As illustrated in Figure 5.11, the post-processing of each test involved: (1) tracking the evolution of double amplitude and single amplitude maximum shear strains (γ_{DA} and γ_{SA}), and (2) decoupling shear strains developed at near-zero effective stress (γ_0) from those that developed during dilation (γ_d) according to the definitions of Shamoto et al. (1997). The implementation of the latter approach in cyclic undrained element tests in clean uniform sands showed that the evolution of γ_0 governs the development of large post-triggering shear deformations (Zhang and Wang 2012), and that their values are directly proportional to the maximum shear strain achieved in the preceding loading cycle (Shamoto et al. 1997, Humire and Ziotopoulou 2022). Considering the same materials presented in this work, Humire et al. (2021b) presented a discussion on the effects of C_u and D_{50} on the evolution of γ_{DA} for CV-DSS tests on medium dense specimens. This subsection builds upon the work of Humire et al. (2021b) to discuss the mechanisms driving the differences in shear strain accumulation for soils with varying gradations. For that purpose, this subsection presents:

1) Analyses of the differences in the evolution of γ_{DA} per post-triggering loading cycle for loose and medium dense specimens of soils with different values of C_u and D_{50}.
2) Interpretations of the mechanisms driving differences in shear strain accumulation for soils with different gradations based on observations of the evolution of γ_0. The implementation of this approach considered the procedure described in Humire et al. (2019) and the analyses followed those presented in Humire and Ziotopoulou (2022) for clean uniform sands.
3) Comparisons of the stress-strain responses observed in post-cyclic monotonic CV-DSS tests on soils with varying gradations to evaluate differences in dilative tendencies on the post-triggering regime.

Following the interpretations presented in Humire et al. (2021b), Figure 5.12 compares the evolution of γ_{DA} per post-triggering cycle obtained in CV-DSS tests on specimens of 100A sand for different D_R's and the evolutions of γ_{DA} obtained for the other soil mixtures. These results show that 50AB follows patterns of shear strain accumulation similar to those exhibited by 100A at similar D_R's (Figures 5.12a and 5.12b). On the other hand, soils with broader gradations (33ABC and 25ABCD) exhibit a progressive reduction of the rate of shear strain accumulation while increasing C_u for loose specimens ($D_R \approx 40\%$), and an arrest in the strain accumulation after exceeding a certain strain threshold on medium dense specimens ($D_R \approx 65\%$). As previously discussed in Humire et al. (2021b), these results suggest that well-graded soils can lead to smaller post-triggering shear deformations than poorly-graded sands given the arrest in the accumulation of shear strains. Regarding the effect of grain size, comparisons for similar D_R's show a reduction in the rate of shear strain accumulation per loading cycle with increasing D_{50} for both loose and medium dense specimens (Figures 5.12c and 5.12d).

Figures 5.13 and 5.14 present γ_0 as a function of the γ_{DA} achieved on the preceding loading cycle ($\gamma_{DA,pre}$) obtained in 70- and 150-mm CV-DSS tests with CSR's of 0.10. Comparisons of tests on samples with the same D_R show the development of smaller γ_0's for 33ABC compared to soils with smaller gradations (Figures 5.13a and 5.13b). On the other hand, comparisons between 100A, 100B, and 100C do not provide clear trends between γ_0 and D_{50} (Figure 5.13c and 5.13d). Similarly, 25ABCD soil exhibits smaller γ_0's than 100A and 100D for both loose and medium dense specimens (Figure 5.14). These results suggest a more significant effect of C_u on the evolution of γ_0 than D_{50}; therefore, the reduction on the shear strain accumulation with increasing gradation can be associated to a decrease in the shear strains developed at near-zero effective stress. It is hypothesized that soils with broader gradations are limited to smaller γ_0's than poorly-graded sands due to the smaller voids in the granular assembly, which reduce the room for particle rearrangement during shearing. The arrest of the strain accumulation for medium dense specimens of soils with broader gradations is likely to occur due to a stabilization of changes of the soil fabric in the post-triggering regime and, in particular, of changes in void-based fabric metrics as suggested by previous DEM research (Wang et al. 2016, Wei et al. 2018).

The decrease in the shear strain rate accumulation while increasing D_{50} is not explained by the trends of γ_0 presented in Figures 5.13 and 5.14. Instead, this decrease is attributed to enhanced dilation while increasing D_{50} that leads to steeper slopes of the stress-strain loops during dilation (Figures 5.3f and 5.4f). In order to confirm these differences in the post-triggering stress-strain response during dilation, Figure 5.15 presents post-cyclic monotonic CV-DSS tests performed on 100A, 100C, and 33ABC soils. Results show that the coarser soil (100C) exhibits a more dilative behavior, leading to smaller shear deformations compared to the other materials. These post-cyclic monotonic behaviors confirm the enhanced dilation in the post-triggering regime while increasing D_{50}, and are consistent with previous results by Hubler et al. (2017).

5.3.3 Post-liquefaction reconsolidation volumetric strains

Most of the 70mm CV-DSS tests presented in this paper included measurements of post-liquefaction reconsolidation volumetric strains ($\varepsilon_{v,recons}$). To explore functional dependencies with C_u and D_{50}, $\varepsilon_{v,recons}$ were analyzed with the frameworks proposed by Ishihara and Yoshimine (1992) and Sento et al. (2004). Both works proposed correlations between $\varepsilon_{v,recons}$ and metrics of the shear strain history during the preceding cyclic loading. Ishihara and Yoshimine (1992) proposed a correlation for $\varepsilon_{v,recons}$ with the maximum shear strain observed during cyclic loading (γ_{max}), which can be approximated with the following equation (Idriss and Boulanger, 2008):

$$\varepsilon_{v,recons} = 1.5 \cdot \exp(-2.5\, D_R) \cdot \min(8\%, \gamma_{max}) \tag{5.1}$$

On the other hand, Sento et al. (2004) observed a better correlation with the shear strain accumulated during the cyclic loading (γ_{acc}) as given by:

$$\varepsilon_{v,recons} = \rho \cdot \ln\left(\frac{1}{10^{-x}} + 1\right) \tag{5.2}$$

$$x = \frac{a \cdot \gamma_{acc}}{1 + \gamma_{acc}/b} \tag{5.3}$$

$$\gamma_{acc} = \int_0^t |\dot{\gamma}(t)| dt \tag{5.4}$$

where $\dot{\gamma}(t)$ is the shear strain rate at time t, b is a fitting parameter, and a and ρ are linear functions of the relative density (e.g., $a = c_1 + c_2 D_R$). The following paragraphs present a series of analyses to examine the effect of C_u and D_{50} on post-liquefaction volumetric deformations using the frameworks of Ishihara and Yoshimine (1992) and Sento et al. (2004) to: (1) compare their correlations to the empirical data presented in this work, and (2) identify functional trends for $\varepsilon_{v,recons}$ as function of the D_R and void ratio.

Figure 5.16 compares the correlations proposed by Ishihara and Yoshimine (1992) and Sento et al. (2004) with the $\varepsilon_{v,recons}$ measured in specimens of 100A sand. The $\varepsilon_{v,recons}$ in medium dense and dense specimens (D_R = 60-80%) of 100A sand agree with the correlations proposed by Ishihara and Yoshimine (1992), while the correlations for D_R = 40% overestimate the $\varepsilon_{v,recons}$ measured for loose samples of 100A that are much closer to the correlation for D_R = 60% (Figure 5.16a). On the other hand, the correlations of Sento et al. (2004) overestimate the $\varepsilon_{v,recons}$ for loose and medium dense specimens but provide good agreement for dense specimens (Figure 5.16b). However, the $\varepsilon_{v,recons}$ of 100A follow a clear increasing trend while increasing D_R within the framework of Sento et al. (2004), suggesting the need to modify the fitting parameters in Equations 5.2 and 5.3 to fit the 100A data. Figure 5.17 presents the correlations of Sento et al. (2004) modified to fit the empirical data of soils 100A, 100B, 100C, 50AB, and 33ABC, with fitting parameters of Equations 5.2 and 5.3 obtained with the linear least square method (Table 5.2). Results show that $\varepsilon_{v,recons}$ tend to decrease while increasing C_u for both loose and medium dense specimens (Figure 5.17a), while an increase in D_{50} also leads to smaller $\varepsilon_{v,recons}$ but with a smaller impact than C_u (Figure 5.17b).

The correlations of Ishihara and Yoshimine (1992) and Sento et al. (2004) also suggest that $\varepsilon_{v,recons}$ reach a threshold value after exceeding a γ_{max} of 8% or a γ_{acc} of 1000%. This observation is used to find functional dependencies between threshold values of $\varepsilon_{v,recons}$ and D_R. Figure 5.18 presents the $\varepsilon_{v,recons}$ obtained for specimens of 100A sand with D_R's ranging between 25 and 80%, but differentiating the data obtained with both γ_{max} > 8% and γ_{acc} > 1000%. Results show that $\varepsilon_{v,recons}$ with γ_{max} > 8% and γ_{acc} > 1000% are larger than the rest of the data and follow an almost linear trend with respect to D_R. Considering the same shear strain history criteria, Figure 5.19 compares the $\varepsilon_{v,recons}$ measured in soils 100A, 100B, 100C, 50AB, and 33ABC as functions of the relative density. Results show that, for the same relative density, an increase in C_u leads to a decrease of $\varepsilon_{v,recons}$, while changes in D_{50} had little effect on such strains.

The effect of C_u on reconsolidation deformations is also studied considering $\varepsilon_{v,recons}$ as a function of the void ratio. Figure 5.20 presents the $\varepsilon_{v,recons}$ for soils 100A, 50AB and 33ABC versus the void ratios of each test. The $\varepsilon_{v,recons}$ data for each soil are limited laterally by their extreme void ratios (e_{min} and e_{max}), and by an apparent linear bound that limits the maximum values of $\varepsilon_{v,recons}$ for all soils regardless of their C_u. As C_u increases, the $\varepsilon_{v,recons}$ data move towards the origin, thus leading to smaller reconsolidation strains. This decrease in $\varepsilon_{v,recons}$ can be associated with the decrease in void ratios (i.e., higher particle packing efficiencies) while increasing gradation, which hinders a more optimal particle rearrangement during reconsolidation.

5.4 Conclusions

A series of cyclic constant-volume direct simple shear (CV-DSS) tests were performed to systematically investigate the effect of gradation and grain size on the liquefaction behavior of coarse-grained soils. The testing plan considered four clean uniform coarse-grained soils with different median grain sizes (D_{50}) that were sourced from the same natural deposit, and were combined to form three soil mixtures with different coefficients of uniformities (C_u). Results of CV-DSS tests were synthesized to evaluate the effect of both D_{50} and C_u on the liquefaction triggering resistance, shear strain accumulation and post-liquefaction reconsolidation strains. The main findings from this testing plan were:

- The effects of C_u and D_{50} on the liquefaction triggering resistance were found to depend on the relative density at which they are compared. Results of loose ($D_R \approx 40\%$) and medium dense specimens ($D_R \approx 65\%$) showed a decrease on the triggering resistance while increasing both C_u and D_{50}, but such decreases were more significant at high relative densities. On the other hand, similar triggering resistances were obtained when comparing results of very loose specimens ($D_R \approx 25\%$) for soils with different C_u and D_{50} values. These differences were explained by the decrease on the degree of strain softening while increasing both C_u and D_{50}, which affects the number of cycles to trigger liquefaction on very loose specimens but has a negligible effect on denser samples.
- The triggering resistances of soils with broader gradations were found to be closer to those obtained when testing only their coarser constituents at similar relative densities, which indicates that the pre-triggering behavior of well-graded coarse-grained soils is mostly controlled by their coarser particles and the smaller particles may behave as "floaters" during shearing. The decrease of the liquefaction resistance while increasing C_u but maintaining the same void ratio is also explained by the presence of smaller particles that increase the packing efficiency, but do not contribute to the load-bearing stability of the grain assembly.
- Following liquefaction triggering, specimens of coarse-grained soils with broader gradations exhibited a reduction on the shear strains developed at near-zero effective stress, which led to a decrease of the rate of shear strain accumulation on loose specimens ($D_R \approx$ 40%), and an early arrest in the strain accumulation after exceeding a certain strain threshold on medium dense specimens ($D_R \approx 60\%$). Such effects on the shear strain accumulation can be explained by the smaller amount of voids in the granular assembly of

soils with broader gradations and, thus, the availability of less room for particle rearrangement during shearing.

- Additionally, an increase in D_{50} led to a reduction in the rate of shear strain accumulation per loading cycle for both loose and medium dense specimens. This reduction in the strain accumulation was attributed to an enhanced dilation in the post-triggering regime while increasing grain size, which was confirmed by post-cyclic monotonic CV-DSS tests performed within this work.
- An increase in C_u led to a decrease of post-liquefaction volumetric strains due to reconsolidation, while changes in D_{50} had little effect on such strains. The effect of C_u can be attributed to a higher particle packing efficiency while increasing gradation, which hinders the particle rearrangement during reconsolidation.

Although grain properties play a crucial role in soil behavior, most of the engineering correlations used in practice for assessing liquefaction effects do not consider their impact and, typically, consider only differences in relative density or the initial stress state. Results from this work indicate that correlations that do not explicitly consider the effect of varying C_u and D_{50} may not accurately predict the liquefaction triggering of well-graded coarse-grained soils. For instance, the results presented herein suggest that estimations of liquefaction triggering resistance from data of clean uniform sands may lead to overestimations of the triggering resistance of well-graded soils. Correction factors to adjust the liquefaction triggering resistance for the effects of soil gradation may help to resolve this issue, but additional work is needed (1) to establish the trends presented herein to an extent that correction factors can be formulated, and (2) to isolate the effect of other grain properties that were outside the scope of this paper (e.g., grain angularity, crushability). On the other hand, liquefaction-induced deformations of well-graded soils may be smaller than those exhibited by clean uniform sands, as suggested by the slower rate of shear strain accumulation and the smaller post-liquefaction volumetric strains observed on soils with higher C_u values. Therefore, correlations for the estimation of liquefaction-induced deformations that do not account for the effect of C_u and D_{50} may lead to overestimations of the anticipated damage in system level analyses, and thus to conservative, energy-costly and cost-inefficient engineering designs.

The findings presented in this study are based on experimental observations of seven soil mixtures, which were selected to isolate the effects of grain size and gradation on the liquefaction behavior of coarse-grained soils. These findings are constrained by the factors held constant in the testing program (e.g., constant D_{10} while increasing gradation, sub-angular grain shape) and the testing device used in this investigation but comprise a significant and extensive addition to the currently available body of experimental data and associated insights. Further studies are needed to: (1) assess the validity of these findings for soils with different intrinsic grain properties (e.g., grain angularity, crushability) and for other modes of shearing (e.g., torsional, triaxial), (2) extend the trends identified in this study for coarse-grained soils with higher C_u and D_{50} values, and (3) elucidate the combined effect of both C_u and D_{50} with other factors such as the fines content and sloping ground conditions.

5.5 References

ASTM International. 2016. *Standard Test Methods for Minimum Index Density and Unit Weight of Soils and Calculation of Relative Density*. ASTM D4254-16. West Conshohocken, PA: ASTM International, approved March 1, 2016. https://doi.org/10.1520/D4254-16

ASTM International. 2019. *Standard Test Method for Consolidated Undrained Cyclic Direct Simple Shear Test under Constant Volume with Load Control or Displacement Control*. ASTM D8296-19. West Conshohocken, PA: ASTM International, approved November 1, 2019. https://doi.org/10.1520/D8296-19

Carey, T. J., Chiaradonna, A., DeJong, J. T., and Ziotopoulou, K. 2021. The effects of gradation on the dynamic response of sloping ground. In *Proceedings of 20th International Conference on Soil Mechanics and Geotechnical Engineering (ICSMGE), Sydney, Australia*.

Chang, N. Y. and Ko, H. Y. 1982. Effects of grain size distribution on dynamic properties and liquefaction potential of granular soils. Research Report R82-103. Geotechnical Publication 111.

Chang, W. J., Chang, C. W., and Zeng, J. K. 2014. Liquefaction characteristics of gap-graded gravelly soils in K0 condition. *Soil Dynamics and Earthquake Engineering* 56: 74–85. https://doi.org/10.1016/j.soildyn.2013.10.005

Doygun, O., Brandes, H. G., and Roy, T. T. 2019. Effect of Gradation and Non-plastic Fines on Monotonic and Cyclic Simple Shear Strength of Silica Sand. *Geotechnical and Geological Engineering* 37(4): 3221–3240. https://doi.org/10.1007/s10706-019-00838-9

Evans, M. D., Seed, H. B., and Seed, R. B. 1992. Membrane compliance and liquefaction of sluiced gravel specimens. *Journal of Geotechnical Engineering* 118(6): 856–872. https://doi.org/10.1061/(ASCE)0733-9410(1992)118:6(856)

Ghafghazi, M. and DeJong, J. T. 2016. A review of liquefaction case histories in gravelly soils using SPT based triggering curves. In *69th Canadian Geotechnical Conference, Vancouver, BC, Canada.*

He, J., Liu, F., Deng, G., and Fu, P. 2021. Relationships between gradation and deformation behavior of dense granular materials: Role of high-order gradation characteristics. *International Journal for Numerical and Analytical Methods in Geomechanics* 45(12): 1791–1808. https://doi.org/10.1002/nag.3224

Hu, Q., Zhang, J. M., and Wang, R. 2020. Quantification of dilatancy during undrained cyclic loading and liquefaction. *Computers and Geotechnics* 128: 103853. https://doi.org/10.1016/j.compgeo.2020.103853

Hubler, J. F., Athanasopoulos-Zekkos, A. and Zekkos, D. 2017. Monotonic, cyclic, and postcyclic simple shear response of three uniform gravels in constant volume conditions. *Journal of Geotechnical and Geoenvironmental Engineering* 143(9): 04017043. https://doi.org/10.1061/(asce)gt.1943-5606.0001723

Hubler, J. F., Athanasopoulos-Zekkos, A. and Zekkos, D. 2018. Post-Liquefaction Volumetric Strain of Gravel-Sand Mixtures in Constant Volume Simple Shear. In *Geotechnical Earthquake Engineering and Soil Dynamics V,* edited by S. J. Brandenberg and M. T. Manzari. American Society of Civil Engineers. pp. 442–449. https://doi.org/doi:10.1061/9780784481455.042

Humire, F., Ziotopoulou, K., Basson, M. S., and Martinez, A. 2019. Framework for tracking the accumulation of shear strains during cyclic mobility. In *Earthquake Geotechnical Engineering for Protection and Development of Environment and Constructions-*

Proceedings of the 7th International Conference on Earthquake Geotechnical Engineering, (ICEGE 2019), June 17-20, 2019, Rome, Italy, edited by F. Silvestri and N. Moraci. CRC Press, Taylor and Francis, London. pp. 906–2914. https://doi.org/10.1201/9780429031274

Humire, F., Lee, M., Ziotopoulou, K., Gomez, M. G., and DeJong, J. T. 2021a. Development and evaluation of pre-conditioning protocols for sand specimens in constant-volume cyclic direct simple shear tests. *Geotechnical Testing Journal* (under review).

Humire, F., Ziotopoulou, K., and DeJong, J. T. 2021b. Evaluating shear strain accumulation of sands exhibiting cyclic mobility behavior. In *Proceedings of 20th International Conference on Soil Mechanics and Geotechnical Engineering (ICSMGE), Sydney, Australia*.

Humire, F. and Ziotopoulou, K. 2022. Mechanisms of shear strain accumulation in laboratory experiments on sands exhibiting cyclic mobility behavior. *Canadian Geotechnical Journal* (under review).

Idriss, I. M. and Boulanger, R. W. 2008. *Soil liquefaction during earthquakes*. Monograph MNO-12. Earthquake Engineering Research Institute, Oakland, CA.

Ishihara, K. and Yoshimine, M. 1992. Evaluation of settlements in sand deposits following liquefaction during earthquakes. *Soils and Foundations* 32(1): 173–188. https://doi.org/10.3208/sandf1972.32.173

Kim, J., Kawai, T., Kazama, M., and Mori, T. 2016. Density Index for Estimating the Postliquefaction Volumetric Strain of Silty Soils. *International Journal of Geomechanics* 16(5): 1–13. https://doi.org/10.1061/(asce)gm.1943-5622.0000574

Kokusho, T., Hara, T., and Hiraoka, R. 2004. Undrained Shear Strength of Granular Soils with Different Particle Gradations. *Journal of Geotechnical and Geoenvironmental Engineering* 130(6): 621–629. https://doi.org/10.1061/(asce)1090-0241(2004)130:6(621)

Kuei, K. 2019. *Pile Dynamics and Shearing Behavior of Granular Soils*. PhD dissertation, University of California, Davis.

Lee, K. L. and Fitton, J. A. 1969. Factors Affecting the Cyclic Loading Strength of Soil. In *Vibration Effects of Earthquakes on Soils and Foundations*, edited by E. T. Selig and D. Hampton. ASTM International. pp. 71–95. https://doi.org/10.1520/STP33637S

Li, G., Liu, Y.-J., Dano, C., and Hicher, P.-Y. 2015. Grading-Dependent Behavior of Granular Materials: From Discrete to Continuous Modeling. *Journal of Engineering Mechanics* 141(6): 04014172. https://doi.org/10.1061/(asce)em.1943-7889.0000866

Liu, Y. J., Li, G., Yin, Z. Y., Dano, C., Hicher, P. Y., Xia, X. H., and Wang, J. H. 2014. Influence of grading on the undrained behavior of granular materials. *Comptes Rendus - Mecanique* 342(2): 85–95. https://doi.org/10.1016/j.crme.2013.11.001

Martin, E. L., Thornton, C., and Utili, S. 2020. Micromechanical investigation of liquefaction of granular media by cyclic 3D DEM tests. *Geotechnique* 70(10): 906–915.

Martin, G. R., Finn, W. D. L., and Seed, H. B. 1978. Effects of system compliance on liquefaction tests. *Journal of the Geotechnical Engineering Division* 104(4): 463–479.

Oda, M., Nemat-Nasser, S., and Konishi, J. 1985. Stress-Induced Anisotropy in Granular Masses. *Soils and Foundations* 25(3): 85–97. https://doi.org/10.3208/sandf1972.25.3_85

O’Sullivan, C. and Cui, L. 2009. Micromechanics of granular material response during load reversals: Combined DEM and experimental study. *Powder Technology* 193(3): 289–302. https://doi.org/10.1016/j.powtec.2009.03.003

Reardon, R. A. 2021. *Monotonic and Cyclic Direct Simple Shear Testing of Coarse-Grained Soils*. Master’s thesis, University of California, Davis.

Reardon, R. A., Humire, F., Ziotopoulou, K., and DeJong, J. T. 2022. Monotonic and Cyclic Resistance of Coarse-Grained Soils with Varying Gradations. *Journal of Geotechnical and Geoenvironmental Engineering* (in preparation).

Sento, N., Kazama, M., and Uzuoka, R. 2004. Experiment and idealization of the volumetric compression characteristics of clean sand after undrained cyclic shear. *Journal of Japan Society of Civil Engineers* 2004(764): 307–317 (in Japanese). https://doi.org/10.2208/jscej.2004.764_307

Shamoto, Y., Zhang, J.-M., and Goto, S. 1997. Mechanism of large post-liquefaction deformation in saturated sand. *Soils and Foundations* 37(2): 71–80. https://doi.org/10.3208/sandf.37.2_71

Sturm, A. P. 2019. *On the Liquefaction Potential of Gravelly Soils: Characterization, Triggering and Performance*. PhD dissertation, University of California, Davis.

Tasiopoulou, P., Ziotopoulou, K., Humire, F., Giannakou, A., Chacko, J., and Travasarou, T. 2020. Development and implementation of semiempirical framework for modeling postliquefaction shear deformation accumulation in sands. *Journal of Geotechnical and Geoenvironmental Engineering* 146(1): 4019120. https://doi.org/10.1061/(ASCE)GT.1943-5606.0002179

Vaid, Y. P., Fisher, J. M., Kuerbis, R. H., and Negussey, D. 1990. Particle Gradation and Liquefaction. *Journal of Geotechnical Engineering* 116(4): 698–703. https://doi.org/10.1061/(ASCE)0733-9410(1990)116:4(698)

Vaid, Y. P. and Sivathayalan, S. 2000. Fundamental factors affecting liquefaction susceptibility of sands. *Canadian Geotechnical Journal* 37(3): 592–606. https://doi.org/10.1139/t00-040

Wang, G. and Wei, J. 2016. Microstructure evolution of granular soils in cyclic mobility and post-liquefaction process. *Granular Matter* 18: 51. https://doi.org/10.1007/s10035-016-0621-5

Wang, R., Fu, P., Zhang, J. M., and Dafalias, Y. F. 2016. DEM study of fabric features governing undrained post-liquefaction shear deformation of sand. *Acta Geotechnica* 11(6): 1321–1337. https://doi.org/10.1007/s11440-016-0499-8

Wei, J., Huang, D., and Wang, G. 2018. Microscale descriptors for particle-void distribution and jamming transition in pre- and post-liquefaction of granular soils. *Journal of Engineering Mechanics* 144(8): 4018067. https://doi.org/10.1061/(ASCE)EM.1943-7889.0001482

Wichtmann, T., Steller, K., Triantafyllidis, T., Back, M., and Dahmen, D. 2019. An experimental parametric study on the liquefaction resistance of sands in spreader dumps of lignite opencast mines. *Soil Dynamics and Earthquake Engineering* 122: 290–309. https://doi.org/10.1016/j.soildyn.2018.11.010

Wong, R. T., Seed, H. B., and Chan, C. K. 1975. Cyclic loading liquefaction of gravelly soils. *Journal of the Geotechnical Engineering Division* 101(6): 571–583.

Wood, D. M. and Maeda, K. 2008. Changing grading of soil: Effect on critical states. *Acta Geotechnica* 3(1): 3–14. https://doi.org/10.1007/s11440-007-0041-0

Yang, J. and Luo, X. D. 2018. The critical state friction angle of granular materials: does it depend on grading? *Acta Geotechnica* 13(3): 535–547. https://doi.org/10.1007/s11440-017-0581-x

Yang, M., Taiebat, M., Mutabaruka, P., and Radjaï, F. 2021. Evolution of granular materials under isochoric cyclic simple shearing. *Physical Review E* 103(3): 1–19. https://doi.org/10.1103/PhysRevE.103.032904

Yilmaz, Y., Mollamahmutoglu, M., Ozaydin, V. and Kayabali, K. 2008. Experimental investigation of the effect of grading characteristics on the liquefaction resistance of various graded sands. *Engineering Geology* 100(3–4): 91–100. https://doi.org/10.1016/j.enggeo.2007.12.002

Zalachoris, G., Zekkos, D., Athanasopoulos-Zekkos, A., and Gerolymos, N. 2021. The Role of Liquefaction on the Seismic Response of Quay Walls during the 2014 Cephalonia, Greece, Earthquakes. *Journal of Geotechnical and Geoenvironmental Engineering* 147(12): 04021137. https://doi.org/10.1061/(asce)gt.1943-5606.0002662

Zekkos, D., Athanasopoulos-Zekkos, A., Hubler, J., Fei, X., Zehtab, K. H., and Marr, W. A. 2018. Development of a large-size cyclic direct simple shear device for characterization of ground materials with oversized particles. *Geotechnical Testing Journal* 41(2): 263–279. https://doi.org/10.1520/GTJ20160271

Zhang, J.-M. and Wang, G. 2012. Large post-liquefaction deformation of sand, part I: physical mechanism, constitutive description and numerical algorithm. *Acta Geotechnica* 7(2): 69–113. https://doi.org/10.1007/s11440-011-0150-7

5.6 Tables and figures

Table 5.1. Properties of the soils used in this work (Sturm 2019): maximum and minimum void ratio (e_{max} and e_{min}), largest grain size in smallest 10% of grains by mass (D_{10}), median grain size (D_{50}), coefficient of uniformity (C_u), coefficient of curvature (C_c), and coefficient of permeability (k).

Soil Name	e_{max}	e_{min}	D_{10} (mm)	D_{50} (mm)	C_u	C_c	k (cm/s)
100A	0.881	0.579	0.12	0.18	1.68	1.02	0.017
100B	0.835	0.524	0.31	0.51	1.80	1.04	0.128
100C	0.839	0.557	0.91	1.31	1.54	1.04	1.028
100D	0.812	0.540	1.79	2.58	1.53	1.00	2.271
50AB	0.753	0.468	0.13	0.29	2.82	0.76	0.015
33ABC	0.622	0.397	0.15	0.51	4.41	0.68	0.022
25ABCD	0.544	0.303	0.16	0.80	7.44	0.67	0.021

Table 5.2. Fitting parameters used for the correlations of Sento et al. (2004) to fit the empirical data of 100A, 100B, 100C, 50AB, and 33ABC soils (Figure 5.17).

Soil	Fitting parameters for:					
	Loose Samples (D_R = 40-45%)			Medium Dense Samples (D_R = 59-66%)		
	a	b	ρ	a	b	ρ
Toyoura Sand (Sento et al. 2004)	23.0	0.5	0.00231	16.6	0.5	0.00211
100A	14.2	0.5	0.00228	11.1	0.5	0.00206
50AB	13.0	0.5	0.00230	10.3	0.5	0.00212
33ABC	8.3	0.5	0.00229	6.8	0.5	0.00210
100B	12.2	0.5	0.00227	10.2	0.5	0.00207
100C	11.6	0.5	0.00227	8.8	0.5	0.00205

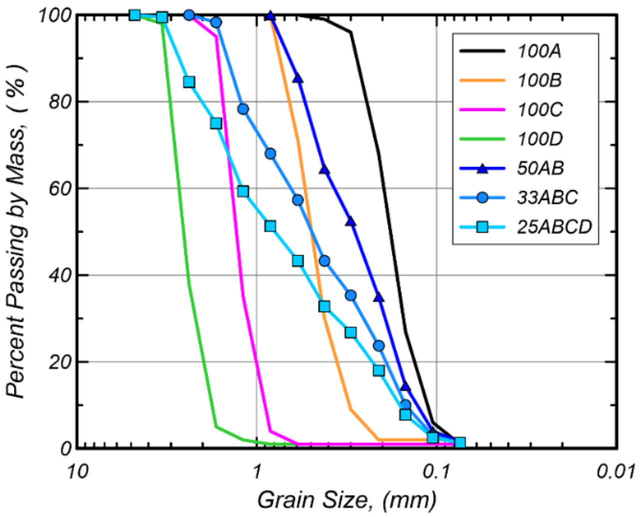

Figure 5.1. Grain size distributions of the soil mixtures presented in this work.

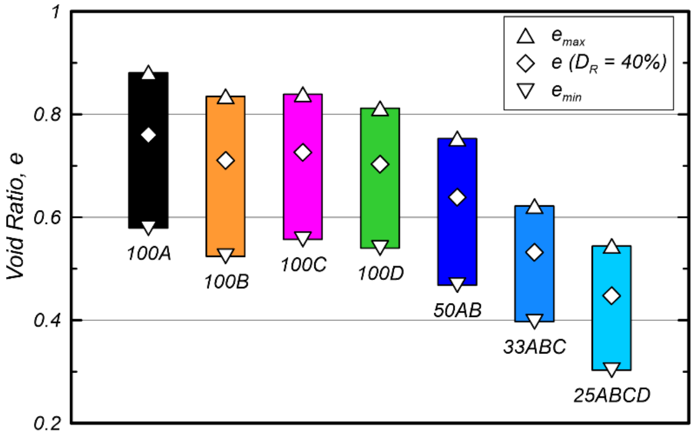

Figure 5.2. Comparison of the maximum and minimum void ratios (e_{max} and e_{min}) of the soil mixtures presented in this work (modified after Sturm 2019).

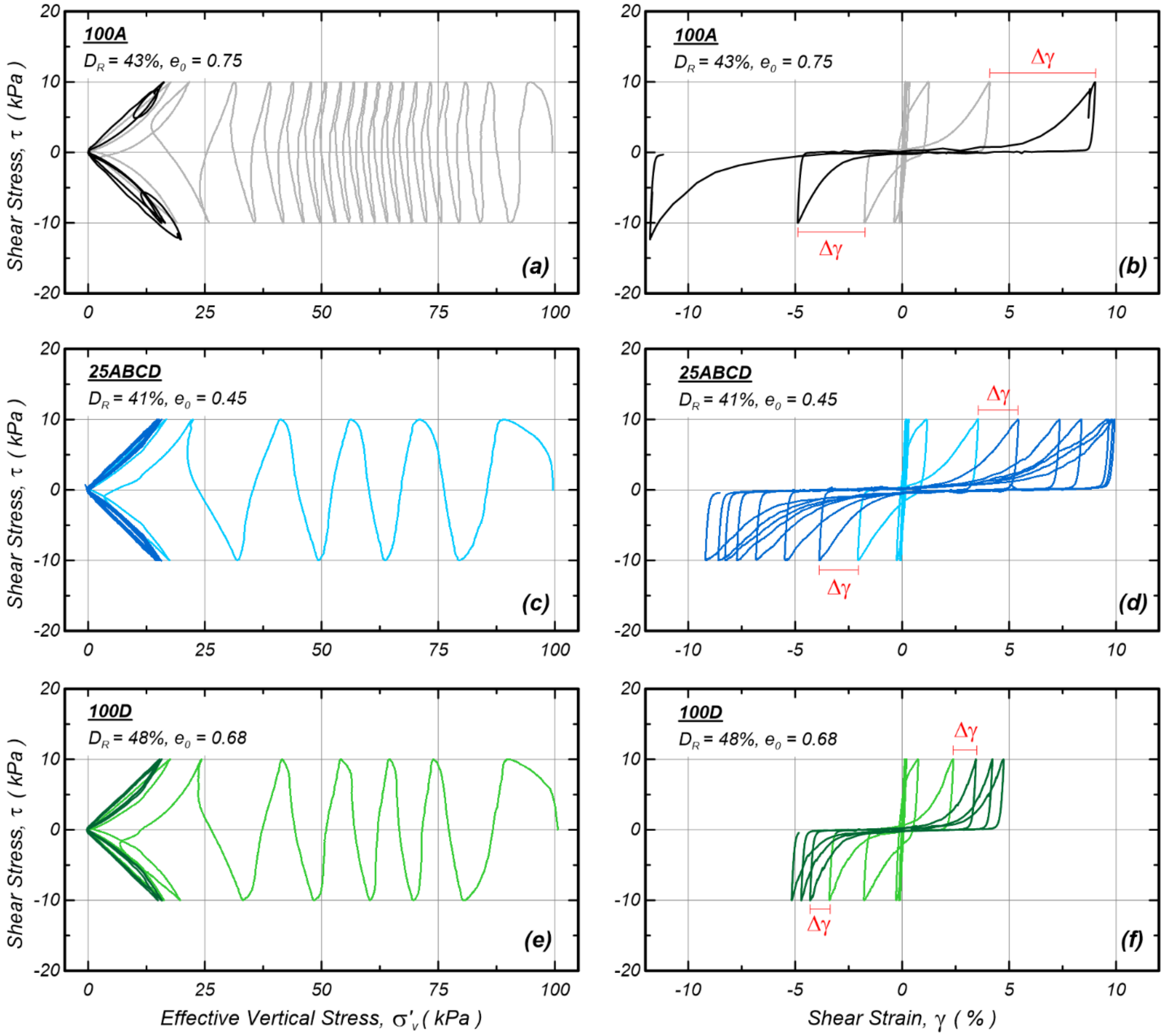

Figure 5.3. Comparison of the stress paths and stress-strain loops obtained for loose specimens ($D_R \approx$ 41-48%, but note different void ratios) of soil mixtures with different C_u and D_{50} values: (a), (b) 100A, (c), (d) 25ABCD, and (e), (f) 100D. Pre-triggering response is indicated with lighter colors and post-triggering response with darker colors. Shear strain increments (Δγ) in loading cycle after liquefaction are indicated in red.

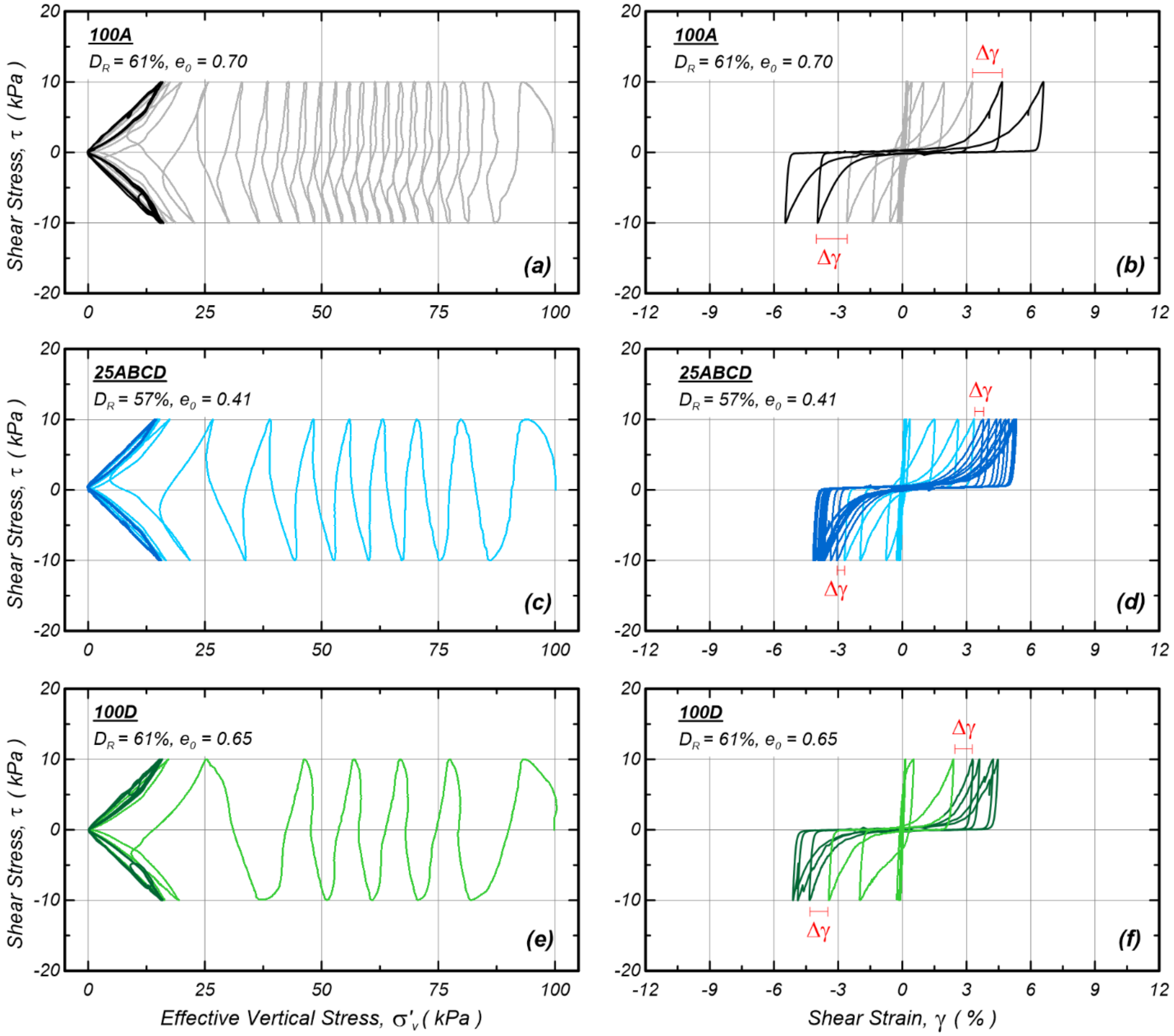

Figure 5.4. Comparison of the stress paths and stress-strain loops obtained for medium dense specimens ($D_R \approx$ 57-61%, but note different void ratios) of soil mixtures with different C_u and D_{50} values: (a), (b) 100A, (c), (d) 25ABCD, and (e), (f) 100D. Pre-triggering response is indicated with lighter colors and post-triggering response with darker colors. Shear strain increments (Δγ) in loading cycle after liquefaction are indicated in red.

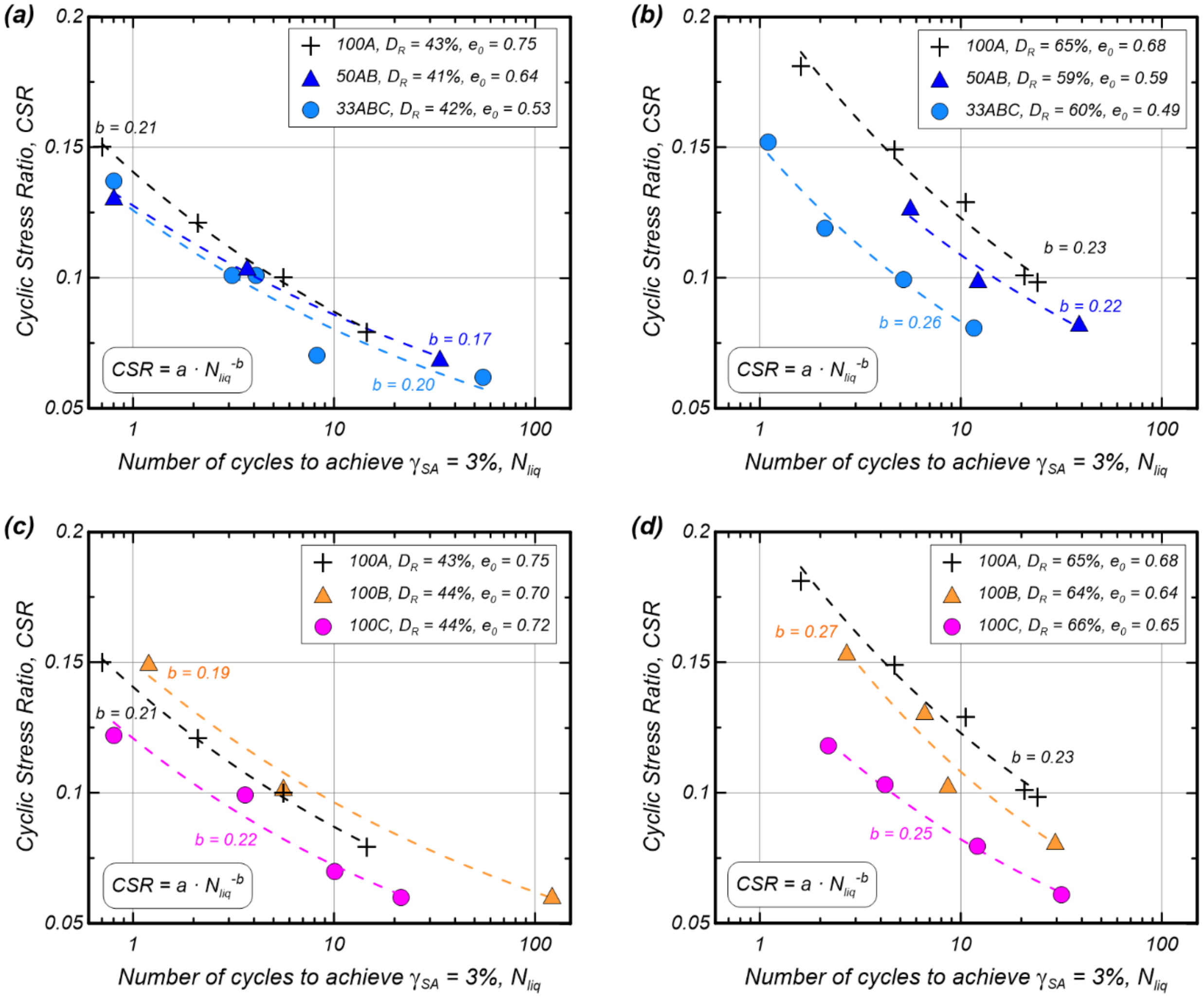

Figure 5.5. Liquefaction triggering curves obtained from CV-DSS tests on specimens of 70 mm in diameter: (a) effect of C_u on loose specimens, (b) effect of C_u on medium dense specimens, (c) effect of D_{50} on loose specimens, and (d) effect of D_{50} on medium dense specimens.

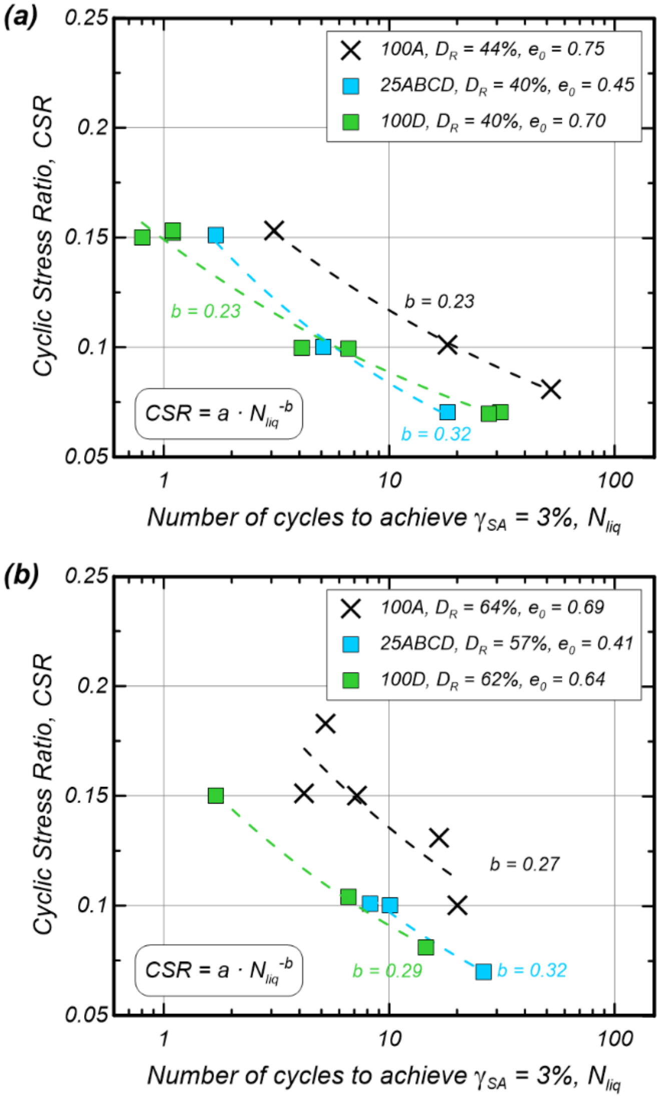

Figure 5.6. Liquefaction triggering curves obtained from CV-DSS tests on specimens of 150 mm in diameter: (a) loose specimens, and (b) medium dense specimens.

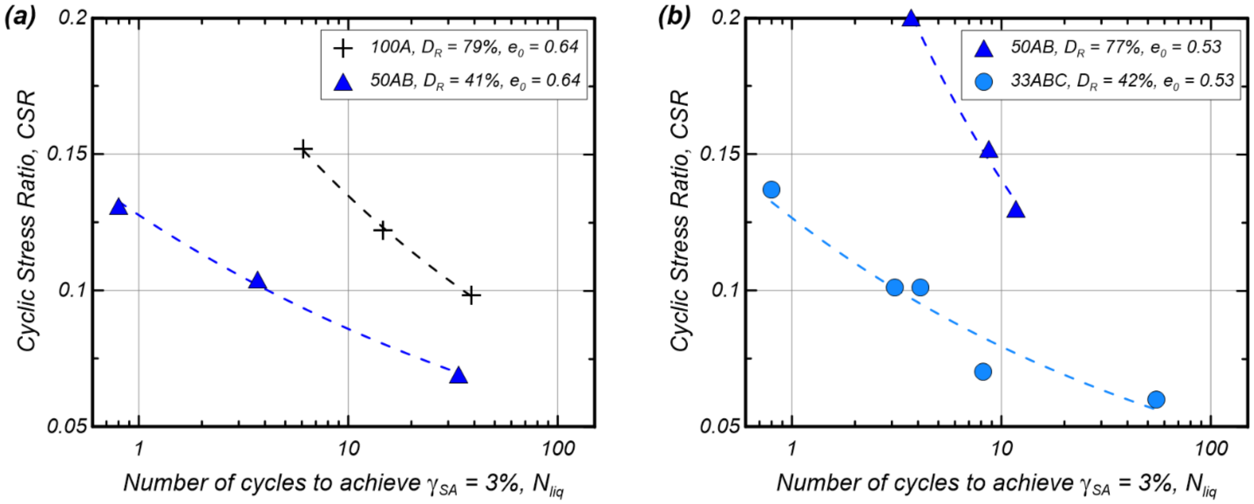

Figure 5.7. Comparison of liquefaction triggering curves for soils with different gradations but same void ratio: (a) 100A versus 50AB, and (b) 50AB versus 33ABC.

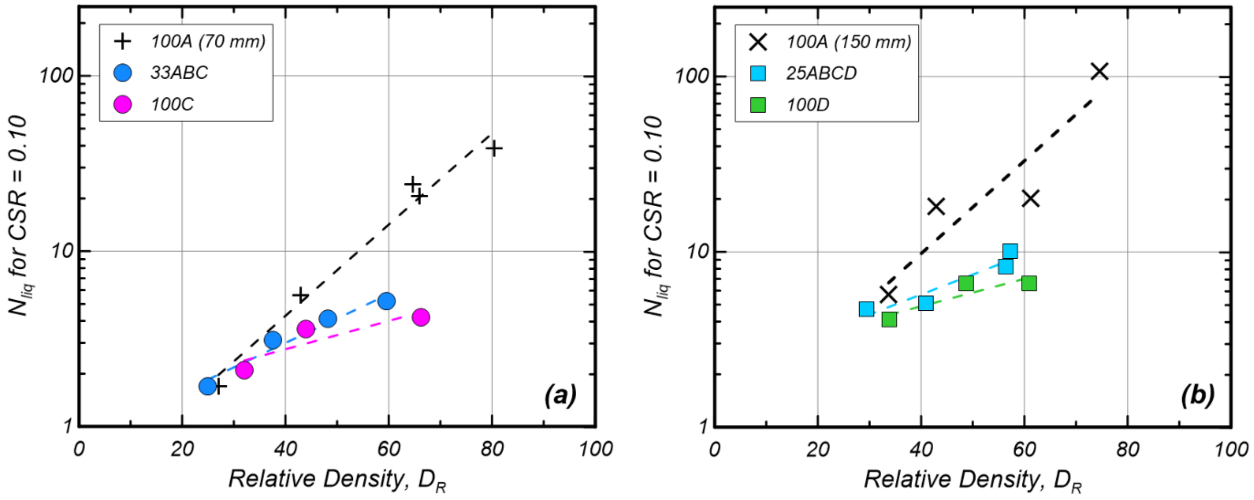

Figure 5.8. Number of cycles to trigger liquefaction (N_{liq}) for tests with CSR=0.10 versus relative density D_R: (a) comparison between 100A, 100C, and 33ABC (70 mm diameter specimens), and (b) comparison between 100A, 100D, and 25ABCD (150 mm diameter specimens).

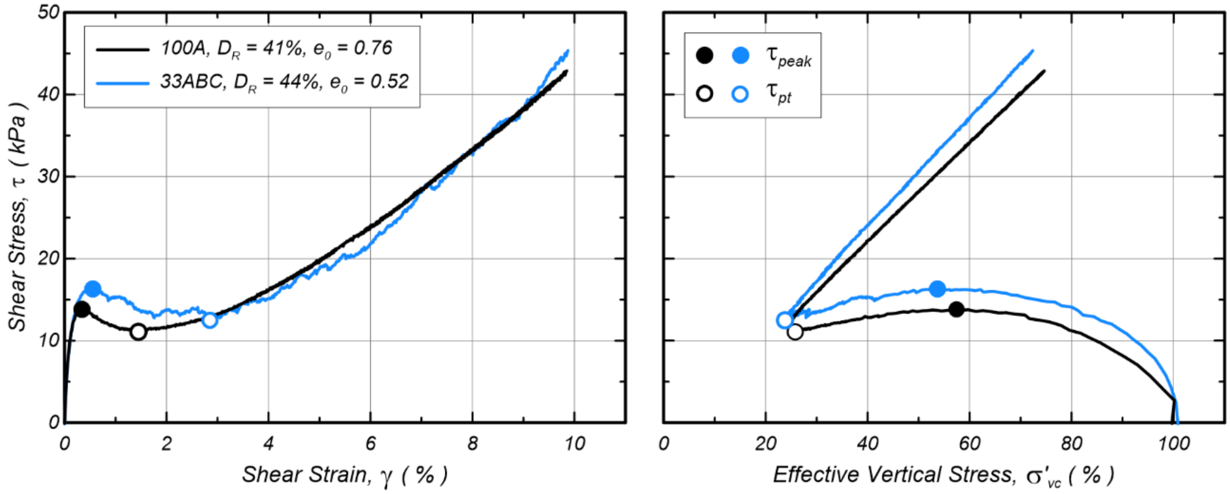

Figure 5.9. Results from monotonic CV-DSS tests on loose specimens of 100A and 33ABC soils, which illustrate the effect of gradation on the peak shear stress before strain softening (τ_{peak}) and the phase transformation shear stress (τ_{pt}).

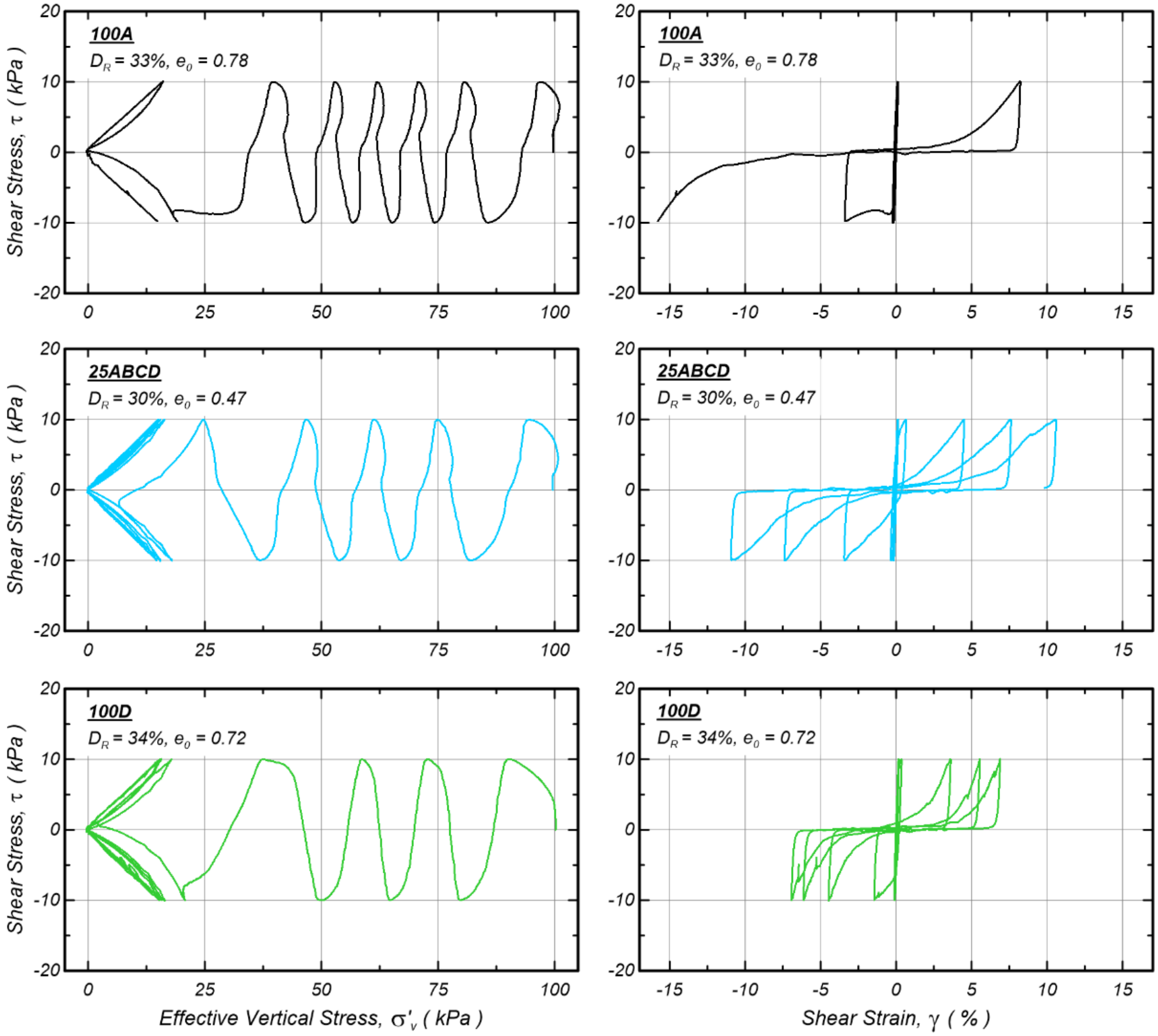

Figure 5.10. Comparison of stress paths (left column) and stress-strain loops (right column) obtained for very loose specimens of soil mixes with different C_u and D_{50} values (100A, 25ABCD and 100D).

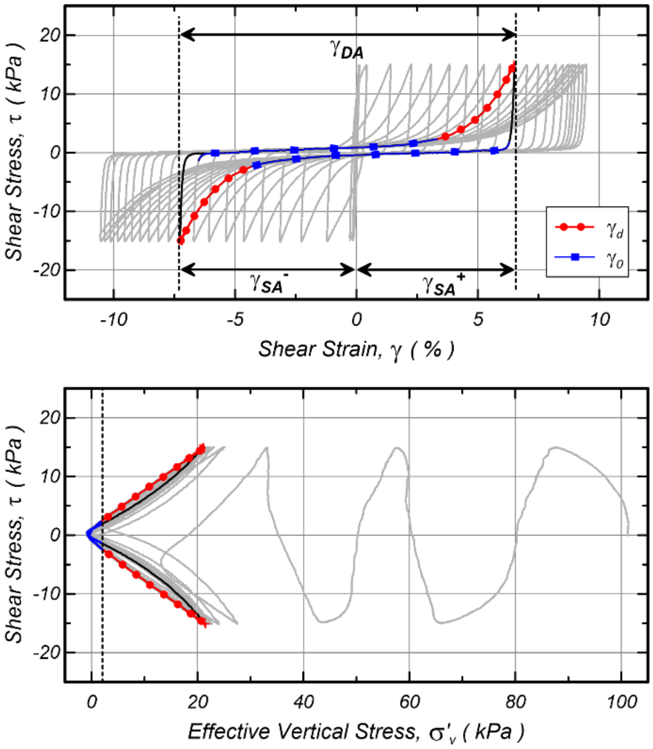

Figure 5.11. Results of a CV-DSS test performed on a specimen of 100A sand with D_R = 63%, including the definitions of double amplitude and single amplitude shear strains (γ_{DA} and γ_{SA}), and shear strain at near-zero effective stress (γ_0) and during dilation (γ_d).

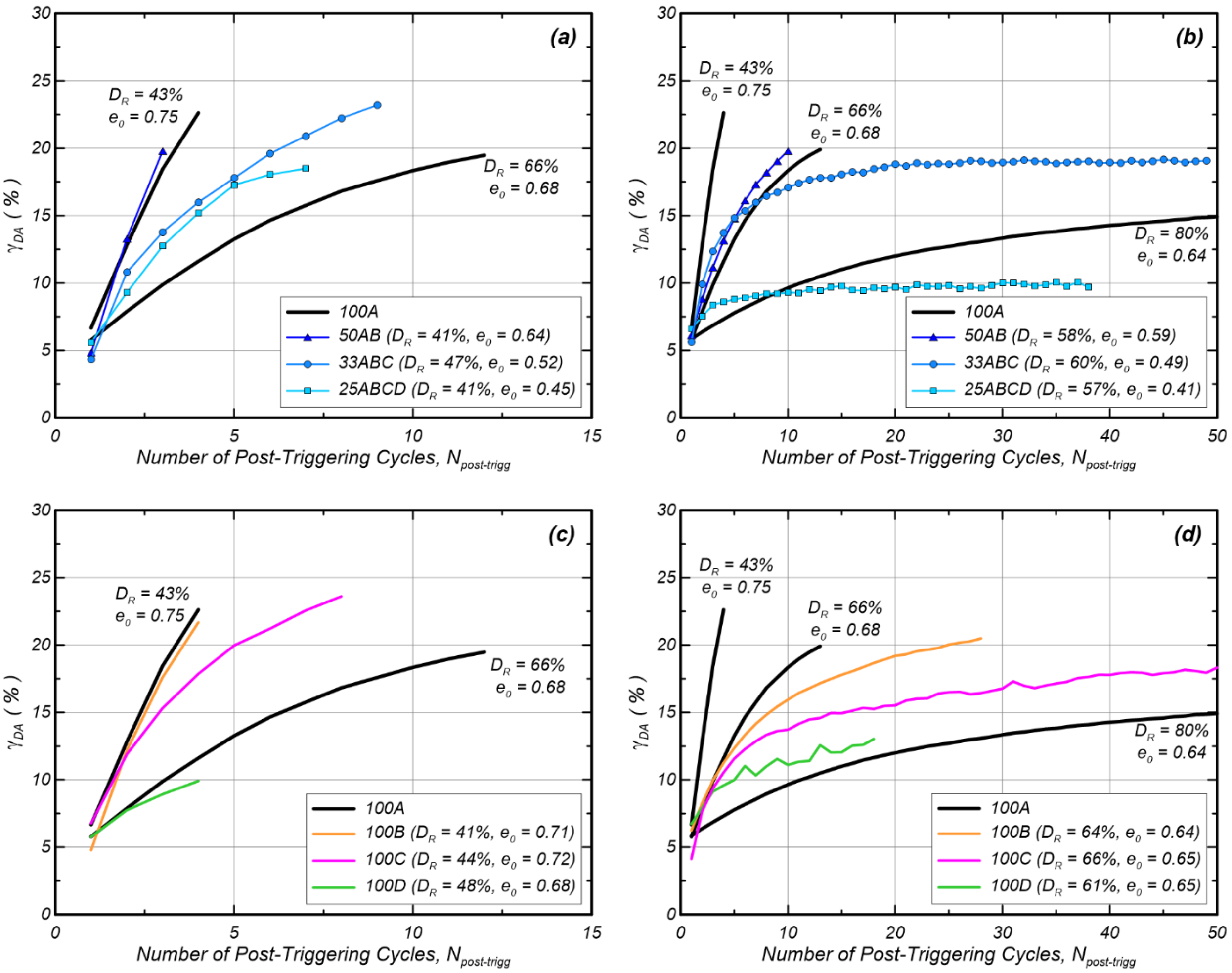

Figure 5.12. Comparison of the accumulation of γ_{DA} per loading cycle in the post-triggering regime observed in CV-DSS tests with CSR=0.10: (a) effect of C_u on loose specimens, (b) effect of C_u on medium dense specimens, (c) effect of D_{50} on loose specimens, and (d) effect of D_{50} on medium dense specimens.

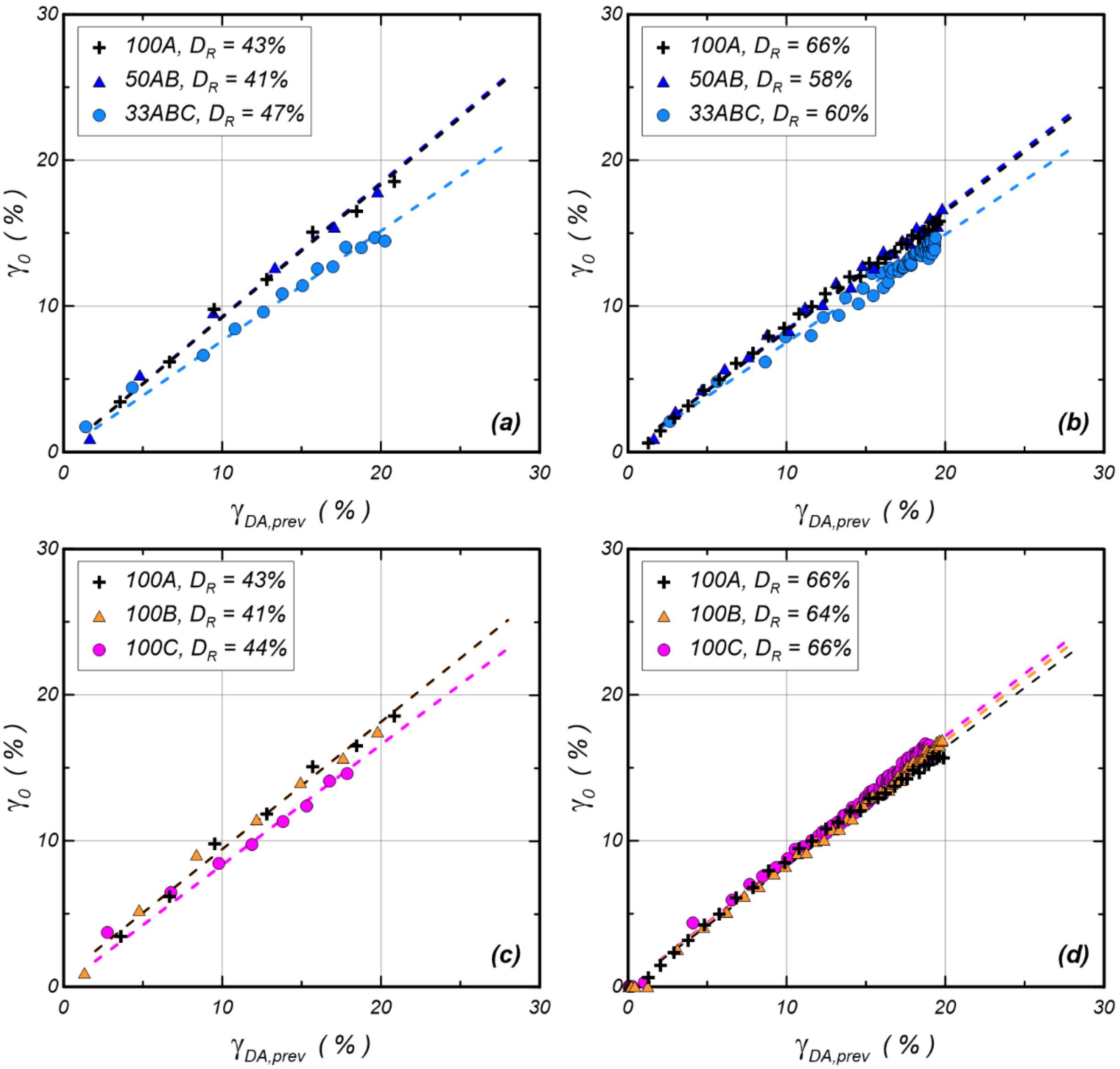

Figure 5.13. Dependency of γ_0 on the γ_{DA} achieved during the preceding loading cycle ($\gamma_{DA,pre}$) observed in CV-DSS tests on specimens of 70 mm in diameter with CSR=0.10: (a) effect of C_u on loose specimens, (b) effect of C_u on medium dense specimens, (c) effect of D_{50} on loose specimens, and (d) effect of D_{50} on medium dense specimens.

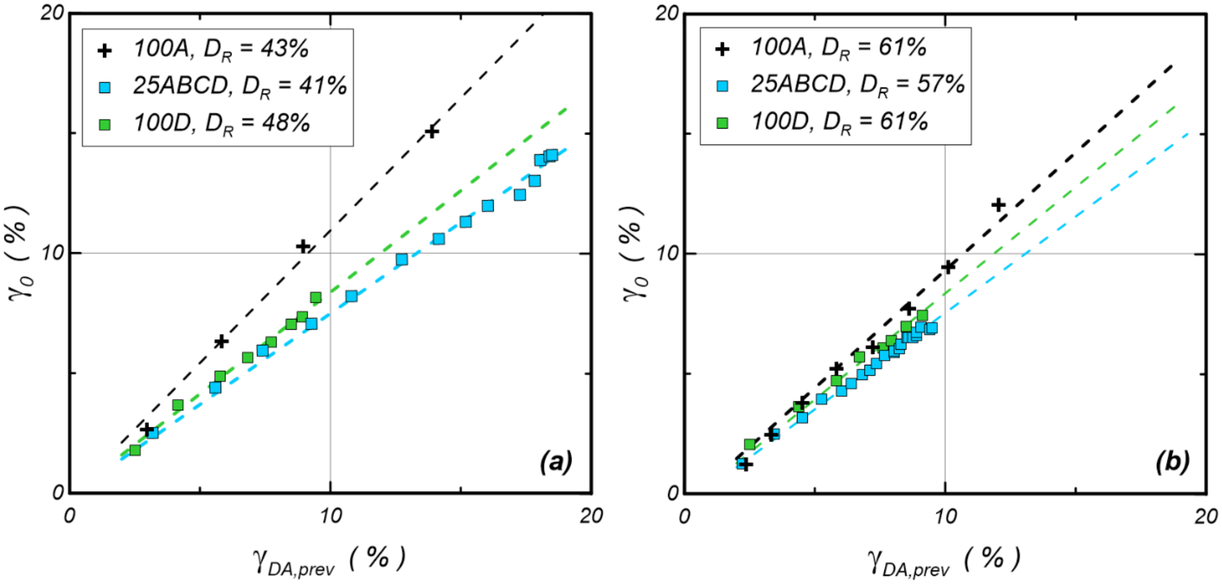

Figure 5.14. Dependency of γ_0 on the γ_{DA} achieved during the preceding loading cycle ($\gamma_{DA,pre}$) observed in CV-DSS tests on specimens of 150 mm in diameter with CSR=0.10: (a) loose specimens, and (b) medium dense specimens.

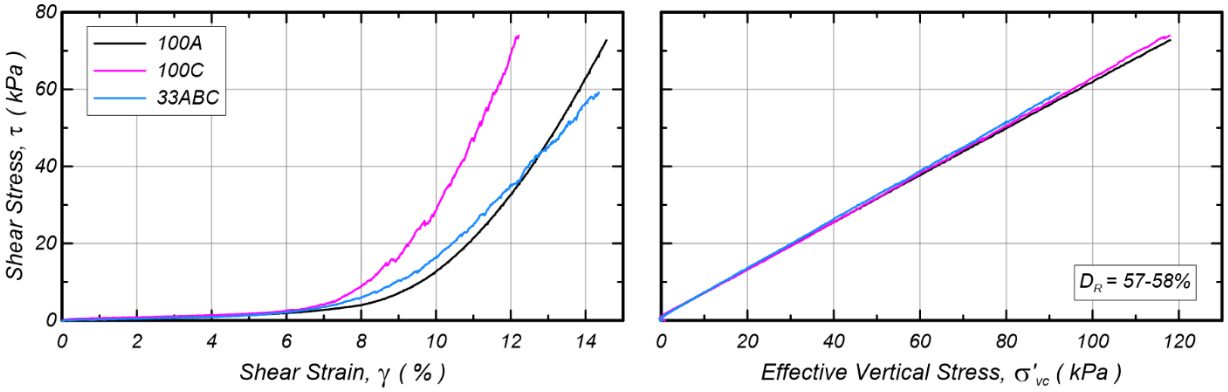

Figure 5.15. Results of post-cyclic monotonic CV-DSS tests performed on medium dense samples of 100A, 100C and 33ABC soils.

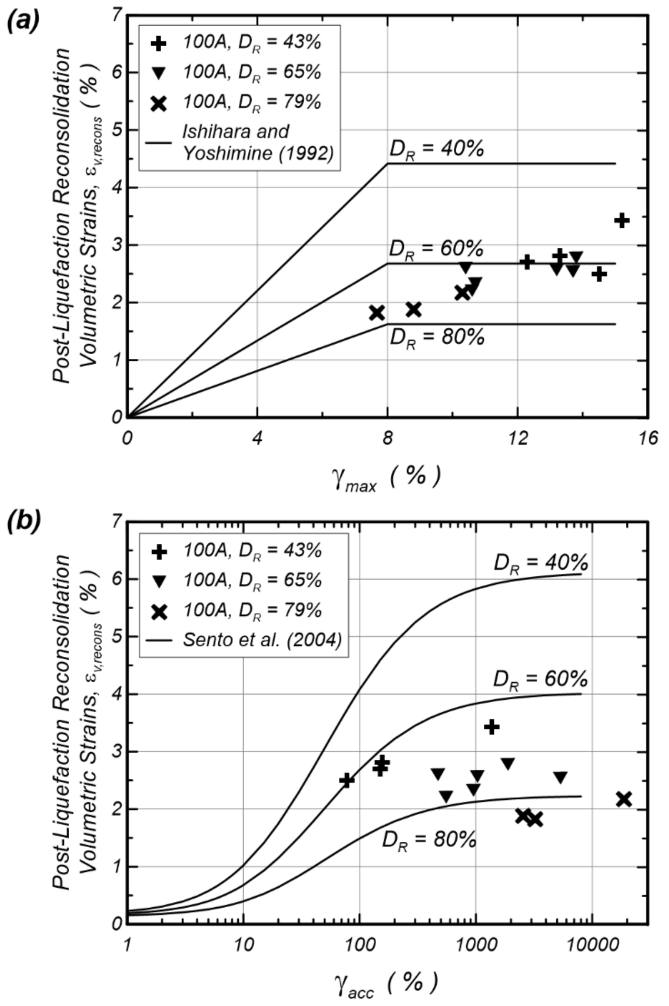

Figure 5.16. Post-liquefaction reconsolidation volumetric strains ($\varepsilon_{v,recons}$) on CV-DSS tests performed on specimens of 100A sand: (a) $\varepsilon_{v,recons}$ versus the maximum shear strains achieved during undrained cyclic loading (γ_{max}) with the correlations proposed by Ishihara and Yoshimine (1992), and (b) $\varepsilon_{v,recons}$ versus the cumulative shear strains during undrained cyclic loading (γ_{acc}) with the correlations proposed by Sento et al. (2004).

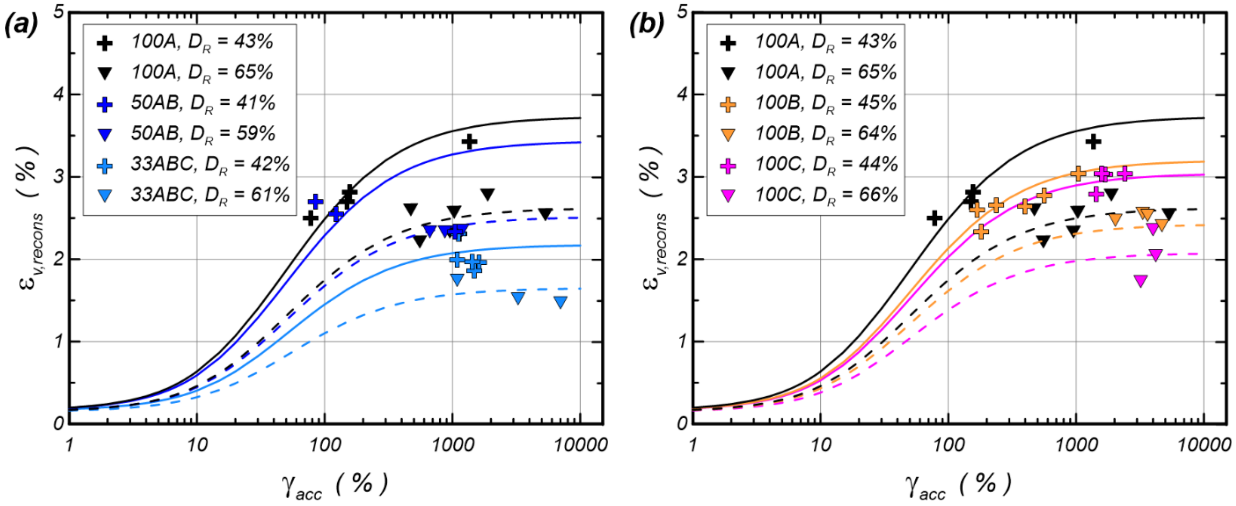

Figure 5.17. $\varepsilon_{v,recons}$ versus the cumulative shear strains during undrained cyclic loading (γ_{acc}), including the correlations of Sento et al. (2004) modified to fit the empirical data (continuous lines correspond to loose data, dashed lines correspond to medium dense data): (a) effect of C_u, and (b) effect of D_{50}.

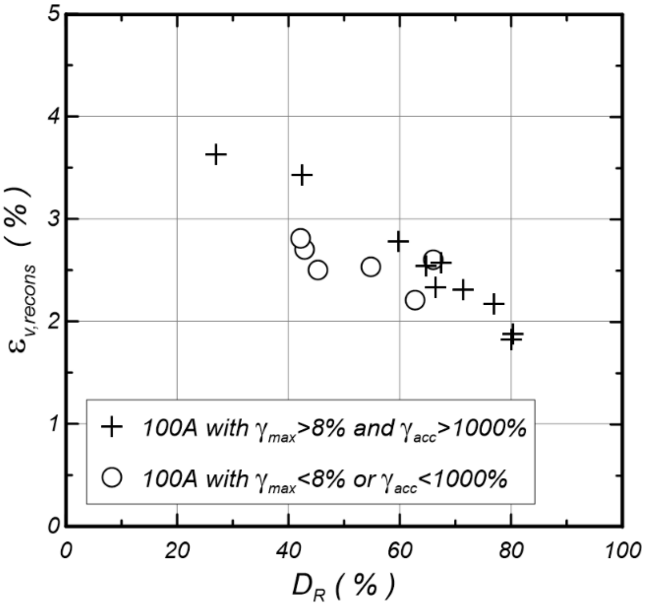

Figure 5.18. $\varepsilon_{v,recons}$ obtained for 100A sand as function of the relative density D_R.

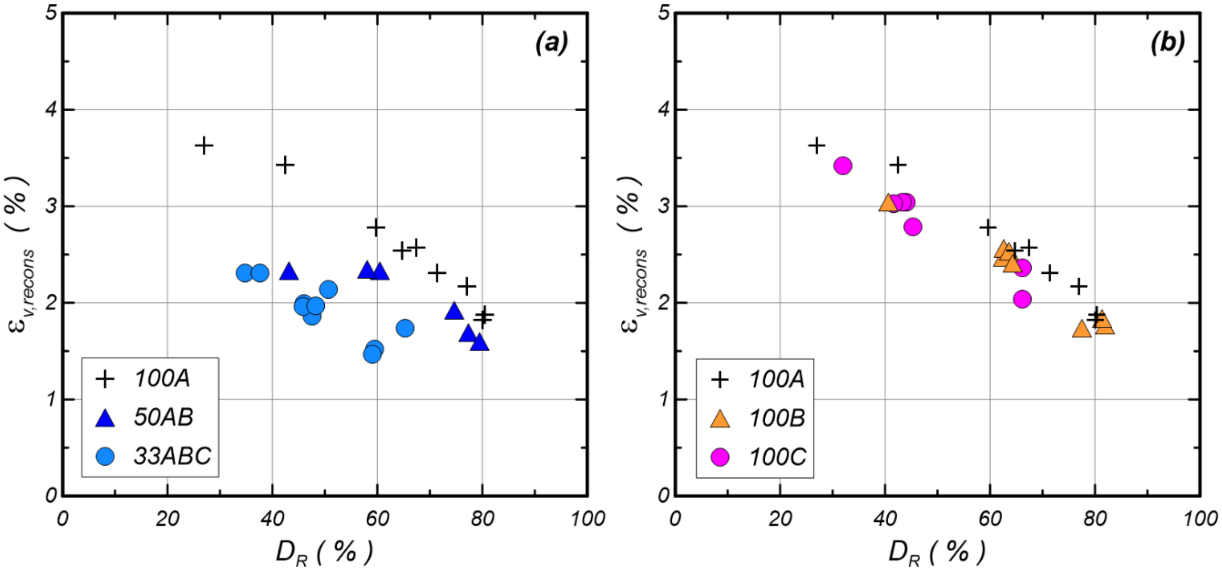

Figure 5.19. Comparison of the $\varepsilon_{v,recons}$ values (with $\gamma_{max} > 8\%$ and $\gamma_{acc} > 1000\%$) versus relative density D_R: (a) effect of D_{50}, and (b) effect of C_u.

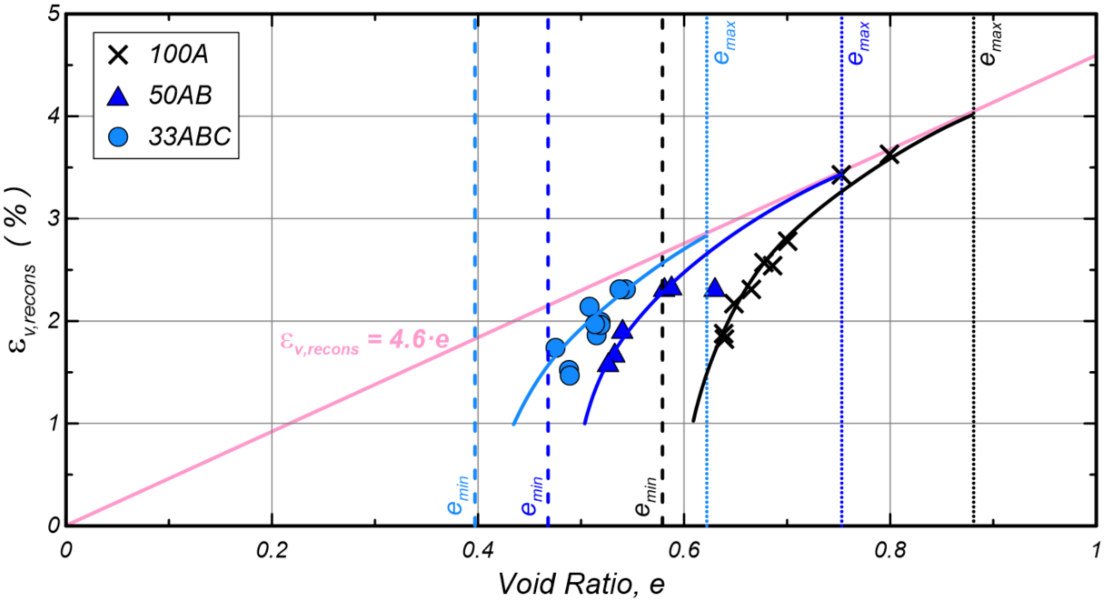

Figure 5.20. Comparison of the $\varepsilon_{v,recons}$ values (with $\gamma_{max} > 8\%$ and $\gamma_{acc} > 1000\%$) versus void ratio for soils with different C_u values.

Chapter 6

Undrained monotonic and cyclic response of loose sands with two different gradations under sloping ground conditions

Author's note: This Chapter will be submitted as a journal paper for publication authored by Francisco Humire, Katerina Ziotopoulou, and Jason T. DeJong. The paper is presented herein with some minor edits for consistency with the other chapters of this Dissertation.

Abstract

This paper presents a series of cyclic constant-volume direct simple shear (CV-DSS) tests aimed at investigating the effect of two different gradations on the monotonic and cyclic response of loose sands under sloping ground conditions. The testing plan considered a range of initial static shear stress ratios ($\alpha = 0$ to 0.5) and two sands with different coefficients of uniformities ($C_u = 1.68$ and 4.41). For monotonic tests, an increase in gradation resulted in a slight reduction of the degree of strain-softening, peak shear stress values, and strain-softening metrics. Results from cyclic tests depended on the degree of stress-reversal imposed, defined by the differences between the static and cyclic shear stresses (τ_{static} and τ_{cyclic}). For reversal and intermediate loading conditions ($\tau_{cyclic} > \tau_{static}$ and $\tau_{cyclic} = \tau_{static}$ respectively), the rate of shear strain accumulation per loading cycle decreased while increasing gradation, which was associated to the development of smaller shear strains at near-zero effective stress of the soil with higher C_u. On the other hand,

non-reversal ($\tau_{cyclic} < \tau_{static}$) loading conditions led to limited shear deformations, with no major differences between both soils studied in this work. An increase in α led to a decrease in the liquefaction triggering resistance for both soils; however, the decrease was more significant for the soil with the lower C_u value. Such differences were associated to the higher potential of strain-softening of that soil, which led to a larger reduction of effective vertical stresses in the cycle preceding liquefaction triggering. Finally, cyclic tests presented herein suggest an increase in the values of static shear stress correction factors (K_α) while increasing gradation.

6.1 Introduction

Sloping ground conditions are of particular importance in the seismic assessment and design of embankment dams and levees featuring liquefiable soils. Fundamental investigations of soil liquefaction have demonstrated that saturated sands under sloping ground conditions behave differently than sands under level ground (e.g., Lee and Seed 1967; Vaid and Chern 1983). An improved understanding of the effect of sloping ground conditions in soil liquefaction has been made possible predominantly through element level laboratory tests (e.g., direct simple shear, triaxial, torsional tests), which have led to correlations for incorporating sloping ground effects into assessments of liquefaction resistance (e.g., Seed 1981, Boulanger 2003). However, the current understanding of sloping ground effects is still mostly based on empirical data developed for clean uniform sands and, consequently, the derived correlations do not account for the effect of soil gradation. This knowledge gap extends to most of the available empirical and semi-empirical correlations for liquefaction assessments, including those to quantify the excess pore pressure generation during cyclic shearing (e.g., Ishihara and Nagase 1980; Boulanger et al. 1991) or the development of post-liquefaction shear deformations (e.g., Tasiopoulou et al. 2020). Recent centrifuge modeling efforts by Carey et al. (2021) have shown that well-graded coarse-grained soils lead to smaller liquefaction-induced slope deformations than clean uniform sands at the same relative density D_R, suggesting that disregarding the effect of gradation in liquefaction assessments may lead to overestimations of the earthquake-induced damage. Still, further research is needed to elucidate the effect of gradation in the liquefaction behavior of coarse-grained soils and to quantify the combined effect of gradation and sloping ground conditions.

As illustrated in Figure 6.1, soil elements within sloping grounds are subjected to a gravity-induced static and sustained shear stress (τ_{static}), also called static bias or static shear stress bias. During earthquakes, the shear stresses in those elements result from the superimposition of the pre-existing τ_{static} with the cyclic shear stress (τ_{cyclic}) caused by shear waves propagating through the soil deposit. Considering the definitions of Hyodo et al. (1991), stress-controlled element tests designed to replicate such conditions can be broadly subjected to three types of cyclic loadings patterns depending on the relative magnitude between τ_{static} and τ_{cyclic}: (a) reversal ($\tau_{cyclic} > \tau_{static}$), (b) intermediate ($\tau_{cyclic} = \tau_{static}$), and (c) non-reversal ($\tau_{cyclic} < \tau_{static}$) loadings. The undrained cyclic response of sands subjected to reversal and intermediate loadings is characterized by a decrease of effective stresses until reaching a zero effective stress state, followed by a progressive accumulation of shear strains in the direction of τ_{static} (Hyodo et al. 1991; Chiaro et al. 2012). On the other hand, non-reversal loadings lead to the development of residual shear deformations without reaching a zero effective stress state (Boulanger et al. 1991; Hyodo et al. 1991; Boulanger and Truman 1996). Based on elements tests performed under different degrees of stress reversal, Yang and Sze (2011a) defined three failure modes for sloping ground conditions: flow-type failures, cyclic mobility, and plastic strain accumulation. Among those, flow-type failures are the most critical mode as they involve a sharp decrease in effective stresses accompanied by an abrupt development of shear deformations (i.e., flow deformations), which can occur for any degree of stress reversal and can be initiated by slight dynamic disturbances (Chiaro et al. 2012).

Comparisons between monotonic and cyclic test results have provided baselines to better describe the failure modes that saturated loose sands may experience during undrained cyclic loading (Vaid and Chern 1983; Hyodo et al. 1994; Sivathayalan and Ha 2011; Chiaro et al. 2012; Yang and Pan 2017; Umar et al. 2021). For example, Vaid and Chern (1983) and Hyodo et al. (1994) showed that loose sands exhibiting strain-softening tendencies in undrained monotonic tests could exhibit flow deformations when subjected to undrained cyclic shearing. Later, Sivathayalan and Vaid (2002) showed that the degree of strain-softening, dictated by the magnitude of the stress decrease during monotonic shearing, can be a good indicator of the flow potential of saturated sands. Based on empirical observations of sands with different degrees of strain-softening, Sivathayalan and Ha (2011) and Chiaro et al. (2012) later showed that flow deformations would occur if the combination of τ_{cyclic} and τ_{static} exceeds the shear stress at which phase transformation (i.e., transition from contractive to dilative behavior) should occur according to the counterpart monotonic test results. Recently, Umar et al. (2021) extended the approach of Sivathayalan and Vaid (2002) and proposed a correlation between metrics of the degree of strain-softening, relative density D_R, and features of the failure mode during cyclic loading (e.g., occurrence of flow deformations or not). Collectively, these efforts suggest the importance of performing monotonic tests to investigate the occurrence of flow deformations during cyclic loading and the impact such deformations may have on the liquefaction triggering resistance. Despite significant progress, previous efforts to investigate the effect of sloping ground conditions in the cyclic response of sands have focused on the behavior of clean uniform sands and, thus, have not considered the role of gradation in their findings.

Sloping ground conditions are typically expressed in terms of the static shear stress ratio α, which is defined as the ratio between τ_{static} and the initial effective overburden stress σ'_{vo} ($\alpha = \tau_{static}/\sigma'_{vo}$). The effect of α in liquefaction triggering assessments is often accounted with the static shear stress correction factors (K_α) originally proposed by Seed (1981), which essentially are defined as the ratio of the cyclic resistance ratio (CRR) under a specific α value and under level ground conditions (α = 0) respectively:

$$K_\alpha = \frac{CRR_\alpha}{CRR_{\alpha=0}} \tag{6.1}$$

Previous works have demonstrated the dependency of K_α factors on the relative density D_R and σ'_{vo} (e.g., Vaid and Chern 1983; Vaid et al. 2001), or on their combined effect captured via the state or relative state parameter (e.g., Boulanger 2003; Yang and Sze 2011b). Other factors like the fines content (Wei ang Yang 2017), initial soil fabric as determined by the sample preparation method (Sze and Yang 2014), testing device (Sivathayalan and Ha 2011), liquefaction triggering criteria (Chiaro et al. 2012; Umar et al. 2021) or the strain-softening potential (Sivathayalan and Ha 2011; Yang and Pan 2017; Umar et al. 2021) have also been found to affect K_α relationships. This apparent dependency of K_α on multiple parameters may justify the large variability of the K_α relationships available in the literature, which is evident even when those relationships are obtained for similar testing conditions (e.g., Figure 6.2). For example, Sivathayalan and Ha (2011) observed opposite trends of K_α while increasing α for two clean uniform sands with different grain shape (sub-rounded Silica sand and sub-angular Fraser River sand in Figure 6.2) which were tested under the same conditions (e.g., sample preparation, D_R, and testing device), but exhibited different degrees of strain-softening during monotonic shearing. Recent results by Prasanna et al. (2020) suggest that the lack of coherence between K_α correlations may be associated with the effects of principal stress rotation during cyclic loading, which are not accounted by K_α factors. Still, the factors driving the large variability in K_α relationships remain not fully understood, thus adding uncertainty to liquefaction assessments in sloping grounds. More importantly, the lack of coherence amongst K_α correlations has led to recommendations about not implementing their use in routine engineering practice (Youd et al. 2001).

In addition to the large variability of K_α relationships, a second challenge in this investigation are the contradictory and ambiguous findings reported in the literature regarding the effect of gradation on monotonic and cyclic behaviors for level ground conditions alone (e.g., Vaid et al. 1990; Kokusho et al. 2004; Harehdasht et al. 2017; Kuei 2019). For example, Harehdasht et al. (2017) reported a negligible effect of gradation on different features of the drained monotonic response (e.g., peak strength, constant-volume friction angle, maximum dilation angle) of dense specimens under triaxial compression. On the other hand, simulations with the discrete element method (DEM) of drained triaxial experiments by Kuei (2019) showed that peak strengths tend to increase while increasing gradation for a broad range of relative densities. As discussed in Chapter 5, such contradictory findings can be explained by the influence of other factors that affect the soil response (e.g., D_R, testing device, median grain size D_{50}). For instance, Vaid et al. (1990) observed an increased triggering resistance while increasing gradation in a series of cyclic triaxial tests on loose soils with identical D_{50}; however, they observed the opposite trend in experiments on dense specimens of the same soils. All these uncertainties about the actual role of gradation in monotonic and cyclic responses suggest the need for further investigations with the ability to isolate the effect of gradation from other factors. This knowledge gap is accentuated for sloping ground conditions since no previous works have studied the effect of gradation under such boundary conditions.

As part of a broader research project to investigate the characterization and liquefaction response of well-graded coarse-grained soils, this paper presents an experimental investigation to examine the effect of two different gradations on the monotonic and cyclic response of loose specimens under sloping ground conditions. To this end, a series of monotonic and cyclic constant-volume direct simple shear (CV-DSS) tests were performed on two sands with different coefficients of uniformities (C_u = 1.68 and 4.41) for a broad range of static shear stress ratios (α = 0 – 0.5). Monotonic tests were analyzed to examine the effect of gradation on the stress-strain responses and the degree of strain-softening in loose sand specimens. Following the definitions of Hyodo et al. (1991), cyclic tests were performed with reversal, intermediate, and non-reversal loading patterns. Results from those tests were synthesized to systematically examine the effect of gradation on the patterns of pore pressure generation, liquefaction triggering resistance, and K_α correction factors. Additional cyclic tests under irregular loading conditions were performed to evaluate the role of gradation in the post-triggering shear strain accumulation. Findings from this work provide fundamental insights of the effects of gradation in the liquefaction response, and form a basis to reassess current methods used in engineering practice to evaluate liquefaction effects in well-graded soils subjected to sloping ground conditions.

6.2 Experimental setup

6.2.1 Tested sands

Experiments were conducted on reconstituted specimens of sub-angular quarzitic coarse-grained soils with two different grain size distributions (Figure 6.3). The tested sands were sourced from the Cape May Formation near Mauricetown, New Jersey (Sturm 2019), which were isolated via sieving into three uniform coarse-grained soils with different D_{50} values: 100A, 100B, and 100C soils (Table 6.1). These uniform soils were combined to form a soil mixture with a higher coefficient of uniformity (C_u) named 33ABC (i.e., 33.3% 100A, 33.3% 100B, 33.3% 100C by mass). Given their similar intrinsic grain properties (e.g., grain shape, mineralogy) and coefficients of permeability (Table 6.1), the effect of two different C_u values on soil liquefaction under sloping ground conditions was investigated by comparing CV-DSS test results obtained for 100A and 33ABC soils. Physical and index properties of these soils are summarized in Table 6.1, and more details regarding their index characterization are available in Sturm (2019).

6.2.2 Testing equipment and procedures

The cyclic CV-DSS tests presented in this work were performed in an Electromechanical Dynamic Cyclic Simple Shear (EMDCSS) device manufactured by GDS Instruments. The active height control system implemented in this device allowed the performance of CV-DSS tests with vertical strain oscillations of less than 0.01% in all tests, which met the 0.05% threshold recommended by ASTM (2019) and the 0.025% threshold recommended by Zekkos et al. (2018). Tests were performed on cylindrical specimens of about 18 mm in height and 70 mm in diameter, which were laterally enclosed by a stack of low-friction steel rings and a latex membrane of 0.35 mm (±0.05 mm) in thickness. Sintered steel porous discs with protruding ridges of 1 mm in height were mounted on the end caps to transmit shear forces to the samples. More details of the equipment and testing device used in this research are available in Reardon (2021) and Humire et al. (2022).

Specimens were prepared via air pluviation, which involved raining oven-dried sand from a fixed height into the soil container. The pluviator used in this investigation had a flow rate control system that allowed to target a specific D_R, and a mesh to redistribute the falling sand evenly across the specimen area. After applying a vertical stress of 25 kPa, specimens were subjected to a series of pre-conditioning strain-controlled drained cycles with an amplitude of 0.045% to improve the compliance between the textured top platen and sand specimens (Humire et al. 2022). Based on preliminary tests presented in Humire et al. (2021), it was found that the application of 50 pre-conditioning drained cycles was appropriate for this testing plan in order to ensure the engagement at the top platen-sand interface while avoiding significant changes in the subsequent soil response. Following pre-conditioning, all samples were consolidated under a vertical stress of 100 kPa. Then, the samples were subjected to constant-stress (drained) monotonic shearing with a shear strain rate of 50% per hour to apply the target τ_{static}. Finally, samples were subjected either to a constant-volume monotonic shearing with a shear strain rate of 50% per hour until 25% shear strain was achieved, or a constant-volume stress-controlled cyclic shearing with a loading frequency of 0.05 Hz.

6.2.3 Testing plan and loading conditions

The testing plan comprised of monotonic and cyclic CV-DSS tests performed on loose specimens ($D_R \approx 40\%$) of 100A and 33ABC soils subjected to a broad range of cyclic stress ratios (CSR) under different α values (Table 6.2). Following the definitions of Hyodo et al. (1991), cyclic CV-DSS tests were performed under three types of loading conditions: reversal ($\tau_{cyclic} > \tau_{static}$), intermediate ($\tau_{cyclic} = \tau_{static}$), and non-reversal ($\tau_{cyclic} < \tau_{static}$) loadings. The liquefaction triggering resistance for all the cyclic tests presented herein was calculated with a 3% single amplitude shear strain (γ_{SA}) criterion. The number of loading cycles to trigger liquefaction (N_{liq}) in each test are also indicated in Table 6.2.

An additional series of experiments were performed to evaluate the effect of gradation on the process of shear strain accumulation under irregular cyclic loading conditions. Similar to the tests presented by Ziotopoulou (2014), irregular loading tests involved varying the τ_{cyc} along the course of the post-triggering regime in three loading stages. In the first stage, specimens were subjected to reversal or intermediate loadings with uniform CSR until a 3% shear strain was exceeded. In the second stage, the CSR was reduced to half of the previous CSR to apply 20 loading cycles to specimens under non-reversal loading conditions. In the third and final stage, the CSR was increased to the value in the first stage and tests were ended after achieving 25-30% shear strain.

6.3 Undrained monotonic response

Figure 6.4 presents the stress-strain responses (τ vs. γ) and stress paths (τ vs. σ'_v) obtained in monotonic CV-DSS tests on loose samples of 100A and 33ABC soils for α values between 0 and 0.5. At the beginning of shearing, tests with α's of 0 and 0.1 applied to both soils exhibit contractive behaviors with marginal shear strain development (Figure 6.4a) and shear stresses increasing towards a local peak shear stress or τ_{peak} (Figure 6.4b). After reaching τ_{peak}, the tests exhibit strain-softening tendencies that lead to a decrease in shear stresses toward a local minimum value, defined herein as phase transformation shear stress, or τ_{pt}, accompanied by the development of limited flow deformations (2-3% shear strain). Upon further shearing, the tests exhibit dilative behavior, characterized by the development of large shear deformations (Figure 6.4a) and stress ratios (τ/σ'_v) converging towards the critical state lines (CSL) of each soil (Figure 6.4b). As further discussed by Reardon (2021), the higher stress ratios observed in the stress paths of 33ABC are associated with the CSL of this soil being slightly above the CSL of 100A.

For both soils, the results obtained for α's of 0.2 and 0.35 (Figures 6.4c and 6.4d) show more pronounced strain-softening than results obtained with lower α's. This increased strain-softening is reflected in: (1) decreases in τ occurring almost immediately after starting the tests, and (2) the phase transformation occurring at smaller shear stress levels than τ_{static}. The main difference between the responses of both soils is that 33ABC exhibits a more dilative behavior than 100A after reaching τ_{pt}, which results in smaller shear deformations than those obtained with 100A for the same shear stress levels (Figure 6.4c). On the other hand, tests with $\alpha = 0.5$ for both soils show dilative behavior almost immediately after the onset of shearing. In this case, 100A exhibits a more dilative behavior and smaller shear deformations for the same stress level relative to 33ABC (Figure 6.4c), which is attributed to the initial stress state of 100A being closer to the CSL (Figure 6.4d).

Figure 6.5 compares the values of τ_{peak} and τ_{pt} obtained for α values between 0 and 0.5 in both soils to examine the effects of α and gradation on the degree of strain-softening. Results show that both τ_{peak} and τ_{pt} increase while increasing α, consistent with the previous results of Sivathayalan and Ha (2011) and Umar et al. (2021). As α increases, τ_{peak} increases converging towards values similar to τ_{static} (Figure 6.5a), while τ_{pt} gradually increases for α's greater than 0.1 (Figure 6.5b). Regarding differences between soils, the τ_{peak}'s of 33ABC are larger than those of 100A for α = 0-0.1, but all tend to converge to τ_{static} at larger α values (Figure 6.5a). These results suggest that an increase in gradation may lead to larger τ_{peak} values, but such effects may become negligible at large α values. Conversely, the τ_{pt}'s of 33ABC are larger than those of 100A for α = 0-0.35, while the opposite trend is observed at $\alpha = 0.5$ (Figure 6.5b). These results suggest an increase in τ_{pt} as the gradation becomes broader for level- to moderately steep sloping-ground conditions (α = 0 to 0.35).

From a performance perspective, the stress decreases from τ_{peak} to τ_{pt} determine the degree of the strain-softening because larger stress decreases are associated with larger flow deformations, as shown by laboratory tests on specimens with strain-softening tendencies (e.g., Vaid and Chern 1983; Verdugo and Ishihara 1996). Figure 6.6a compares the ratio between τ_{pt} and τ_{peak} obtained for both soils to quantify the magnitude of the shear stress decreases during strain-softening. In both soils, τ_{pt}/τ_{peak} tends to decrease while increasing α until reaching a value of α = 0.2, after which τ_{pt}/τ_{peak} tends to increase. There are no significant differences between the τ_{pt}/τ_{peak} ratios of the two soils, except for tests under an α of 0.2 that demonstrate larger stress decreases from τ_{peak} to τ_{pt} for 100A. Alternatively, Sivathayalan and Vaid (2002) proposed to quantify the degree of strain-softening with the modified brittleness index (I'_b), which quantifies the difference between peak values (τ_{peak} and τ_{pt}) with respect to the initial static shear bias and is calculated as:

$$I'_B = \frac{\tau_{peak} - \tau_{pt}}{\tau_{peak} - \tau_{static}} \qquad (6.2)$$

Following the interpretation of Sivathayalan and Vaid (2002), the degree of strain-softening increases while increasing I'_b, with values greater than 1 corresponding to phase transformation occurring at shear stresses below τ_{static} and, thus, implying a greater potential for the development of flow deformations if τ_{peak} is exceeded. Figure 6.6b shows that I'_b increases while increasing the static shear bias for both soils for α values between 0 and 0.35, and then its value decreases significantly for steeper conditions (α = 0.5) at which strain-softening does not occur. The results shown in Figure 6.6b suggest that the degree of strain-softening of 100A is more severe than 33ABC for α values of 0.2 and 0.35, but there are no significant differences between the two soils for other α values. The results for both soils also suggest the existence of: (i) a domain of intermediate α values in which there is a large degree of strain softening, and (ii) a threshold α value after which the behavior becomes purely dilative.

Collectively, the comparisons between responses, shear stress peak values, and strain-softening metrics (Figures 6.4**,** 6.5, and 6.6) suggest that an increase in gradation, while holding the same D_R and α values, leads to a slight reduction of the degree of strain-softening for level- to moderately steep sloping-ground conditions ($\alpha = 0$ to 0.35). While the differences between 100A and 33ABC are seemingly small compared to the effect of α, such differences are relevant for analyzing and explaining the effect of gradation on the cyclic response of coarse-grained soils (Section 6.4).

6.4 Undrained cyclic response

6.4.1 Comparisons for different degrees of stress reversal

Figures 6.7, 6.8, and 6.9 present illustrative responses obtained for loose specimens of 100A and 33ABC soils subjected to reversal, intermediate, and non-reversal loading conditions, respectively. Each figure presents tests on 100A and 33ABC soils with similar D_R's under the same α value and subjected to similar CSRs, in order to examine the effect of gradation on cyclic responses. In addition, the same number of post-triggering loading cycles are plotted for both soils in each figure to illustrate differences in the shear strain accumulation and to examine the effect of soil gradation on it.

Tests under reversal loading conditions (Figure 6.7) exhibit a gradual decrease in effective vertical stresses (σ'_v) towards zero, followed by a progressive accumulation of limited shear strains in each loading cycle towards the positive direction. Tests under intermediate loading conditions (Figure 6.8) also exhibit a progressive decrease of σ'_v towards zero, but the shear strain increments per loading cycle in the post-triggering regime are smaller than those observed for reversal loading conditions. Both tests presented in Figure 6.7 exhibit the same number of loading cycles to reach $\gamma_{SA} = 3\%$ (N_{liq}), while the examples presented in Figure 6.8 exhibit a larger N_{liq} for the test in 100A. The main difference between the responses of both soils under these types of loading is the development of smaller shear strain increments per loading cycle for 33ABC compared to those observed for 100A. For example, the test on 100A presented in Figure 6.7 accumulates more than 25% shear strain after the application of 4 post-triggering loading cycles, while the test on 33ABC for similar loading conditions develops around 16% shear strain in the same number of cycles. Similar differences in the shear strain accumulation of 100A and 33ABC are observed for the tests under intermediate loading conditions presented in Figure 6.8.

For non-reversal loading conditions (Figure 6.9), σ'_v also progressively decreases in both soils but arrests above zero (e.g., about 10 kPa in the examples presented in Figure 6.9). Also, most of the tests with non-reversal loadings exhibit strain-softening tendencies that lead to the development of shear strains of about 2-3% in the loading cycle preceding liquefaction triggering or in which liquefaction is triggered. As discussed earlier in Section 6.3, 100A exhibits a greater degree of strain-softening than 33ABC, which in cyclic tests is reflected in the greater decreases of σ'_v in the cycle in which strain-softening occurs. For example, the test on 100A presented in Figure 6.9 exhibits a decrease of σ'_v from 50 to 20 kPa in the loading cycle preceding liquefaction triggering, while the test on 33ABC for a similar D_R and loading conditions only exhibits a decrease from 30 to 20 kPa. For the examples presented in Figure 6.9, the smaller decrease in σ'_v observed for 33ABC in the cycle preceding liquefaction triggering compensates for the faster decrease in σ'_v observed at the beginning of shearing, leading to a number of loading cycles to develop flow deformations similar to that obtained for 100A. In terms of shear strain accumulation, tests under non-reversal conditions exhibit very small shear strain increments per loading cycle in the post-triggering regime compared to those observed for intermediate and reversal loading conditions. Figures 6.10 compares the single amplitude shear strains (γ_{SA}) achieved in each post-triggering loading cycle of tests presented in Figures 6.7 to 6.9. Results illustrate the higher rate of shear strain accumulation per cycle obtained for tests under reversal and intermediate loading conditions in comparison to those obtained with non-reversal loadings. These observations are compatible with past findings by Ziotopoulou and Boulanger (2016), who observed strong dilative tendencies with very small shear strain increments in similar non-reversal loading regimes.

6.4.2 Strain accumulation under irregular loading

Figure 6.11 presents the stress-strain responses obtained in CV-DSS tests under irregular cyclic loadings obtained with the loading sequences explained in Section 6.2.3. Since the shear stresses in the first loading stage exceed τ_{pt}, the four tests exhibit a strain-softening behavior in the cycle in which liquefaction is triggered. As cycling continues after the CSR is reduced, the tests exhibit smaller shear strain increments in each loading cycle that lead to an additional 5% shear strain for tests 13 and 35 (Figures 6.11a and 6.11b), and less than 2% shear strain for tests 17 and 39 (Figures 6.11c and 6.11d) after 20 loading cycles. The increase in CSR in the third loading stage leads to larger shear strain increments per loading cycle, with greater increments observed for reversal (Figures 6.11a and 6.11b) than for intermediate loading conditions (Figures 6.11c and 6.11d).

To assess differences in shear strain accumulation for both soils, Figure 6.12 presents the γ_{SA} achieved in each loading cycle of irregular loading tests. In the four irregular loading tests, post-triggering shear deformations are mostly controlled by the shear strain increments developed under reversal and intermediate loadings. 100A exhibits shear strain increments per loading cycle larger than those exhibited by 33ABC, as evident by the evolution of γ_{SA} in the third stage of irregular loading tests (Figure 6.12). These differences between 100A and 33ABC confirm previous observations in Section 6.4.1 where smaller shear deformations under reversal and intermediate loadings occur as the gradation is increased. As discussed in Chapter 5, an increase in gradation leads to a reduction of shear strains developed at near-zero effective stress due to the smaller void ratios of well-graded soils and, thus, the smaller room for particle rearrangement during shearing. This effect explains the reduction in the strain accumulation observed for tests under reversal and intermediate loadings, in which a minimum σ'_v of zero is achieved in each post-triggering loading cycle. On the other hand, shear strain increments developed during non-reversal stages are very similar for both soils, suggesting that gradation does not affect the shear strain accumulation under this type of loading. Consistent with the interpretation of Ziotopoulou and Boulanger (2016) of similar irregular loading tests, the results present herein suggest that under non-reversal loading conditions the soil matrix remains largely stable while accumulating minor strains in the direction of the static shear stress bias due to incremental particle rearrangement.

6.4.3 Effect of gradation on liquefaction triggering

Figure 6.13 presents the liquefaction triggering curves determined for loose specimens of 100A and 33ABC with α's between 0 and 0.2 obtained from the cyclic CV-DSS tests listed in Table 6.2. Both soils exhibit a progressive decrease in the triggering resistance while increasing α, consistent with previous experimental work on loose soils with strain-softening tendencies (e.g., Sivathayalan and Ha 2011; Umar et al. 2021). Also, triggering curves for α's of 0.1 and 0.2 are flatter than the curves obtained for level ground conditions, as reflected by their b values (i.e., slopes of the power fits) indicated in Figure 6.13. These b values are relevant for the development of magnitude scale factors (MSF) to adjust cyclic resistances to a common earthquake magnitude (M), with smaller b values leading to flatter relationships between MSF and M (Idriss and Boulanger 2008). The significant differences between b values for different α's suggest the need for future work to revisit MSF relationships for soils exhibiting strain-softening tendencies under sloping ground conditions.

To examine the effect of gradation on the triggering resistance under sloping ground conditions, Figure 6.14 presents the cyclic resistance ratio or CRR (i.e., CSR to trigger liquefaction in 10 loading cycles) obtained for each triggering curve of 100A and 33ABC soils (Figure 6.13) versus their corresponding α value. Although both soils exhibit a decrease in CRR while increasing α, such a decrease is more significant for 100A than 33ABC. The differences between soils suggest that the effect of gradation on the triggering resistance depends on the static shear bias at which such effects are assessed. For example, the results in Figure 6.14 suggest that the triggering resistance may decrease with increasing gradation for level ground conditions; however, the opposite trend is observed for α values between 0.1 and 0.2. Such deviating trends are attributed to the greater relevance that strain-softening tendencies acquire in the pre-triggering behavior while increasing α, and the higher strain-softening potential of 100A that leads to a larger reduction of σ'_v in the cycle preceding liquefaction triggering.

Figure 6.15 presents the static shear stress correction factors (K_α) calculated for 100A and 33ABC soils with Equation 6.1. The K_α factors of 100A are closer to the lower limit of the data obtained from the literature (Figure 6.2), consistent with the K_α curves obtained for clean uniform sands with strain-softening tendencies (e.g., Silica sand in Sivathayalan and Ha 2011). The K_α factors of 33ABC are above those calculated for 100A, which is attributed to the differences in the degree of strain-softening of both soils. These results suggest that an increase in gradation for the same D_R leads to an increase in K_α factors, confirming that K_α factors do not depend only on the D_R and overburden stress. Still, differences in gradation alone do not explain the large variability in K_α factors in the literature (e.g., Figure 6.2); therefore, it is necessary to use the approaches and frameworks of this Chapter to extend the investigation of changes in K_α factors to wider gradations as well as other factors that may be contributing to this variability (e.g., fines content, sample preparation).

Strain-softening tendencies not only affect the number of loading cycles to trigger liquefaction, but also the evolution of excess pore pressure ratio (r_u) leading up to liquefaction. Following the analyses presented by Idriss and Boulanger (2008), Figure 6.16 presents pore pressure generation plots obtained from CV-DSS tests in 100A and 33ABC soils with different α values, which illustrate the ratio between r_u and the limiting value of r_u in each test or $r_{u,lim}$ (Ishihara and Nagase 1980; Boulanger et al. 1991) as a function of the cycle ratio (i.e., number of loading cycles normalized by the number of cycles to trigger liquefaction or N/N_{liq}). The pore pressure generation patterns of 100A and 33ABC obtained for level ground conditions (Figure 6.16a) reasonably agree with the curve presented in Idriss and Boulanger (2008). On the other hand, greater differences are observed between the curves for tests presented in this work with the curves of Idriss and Boulanger (2008) while increasing α (Figure 6.16b to 6.16d). These differences are attributed to the greater degree of strain-softening exhibited by the tests in 100A and 33ABC with increasing α, which causes a large decrease of σ'_v in the cycle preceding liquefaction triggering. The greater degree of strain-softening is seen in the plots of Figure 6.16 as a sudden increase in $r_u/r_{u,lim}$ when approaching $N/N_{liq} = 1$. These results also show that there no significant differences between the pore pressure generation patterns of 100A and 33ABC, suggesting that the difference in gradation between these two soils had little effect on these relationships compared to other factors (e.g., α, degree of strain-softening).

6.5 Conclusions

A series of cyclic constant-volume direct simple shear (CV-DSS) tests were performed to investigate the effect of two different gradations on the monotonic and cyclic response of loose sands under sloping ground conditions. The testing plan considered different initial static shear stress ratios ($\alpha = 0$ to 0.5), and two sands with different coefficients of uniformity ($C_u = 1.68$ and 4.41) that were composed of soils sourced from the same natural deposit. The main findings from this testing plan were:

- The undrained monotonic response on the majority of the CV-DSS tests presented herein was characterized by a limited strain-softening at the beginning of shearing ($\gamma < 2$-3%). The degree of strain-softening was found to be more dramatic for the CV-DSS tests with α values between 0.2 and 0.35 as those tests yield to shear stresses below the static shear stress. An increase in gradation resulted in a slight reduction of the degree of strain-softening, which was delineated from comparisons between stress-strain responses, peak values, and strain-softening metrics. After transitioning from contractive to dilative behavior, an increase in gradation led to more dilative response for α values between 0.2 and 0.35. For steeper slope conditions, clean uniform sands may exhibit a more dilative response than well-graded sands as their initial stress conditions may be closer to the critical state line.
- The cyclic response under reversal ($CSR > \alpha$) and intermediate ($CSR = \alpha$) loading conditions was characterized by a progressive accumulation of shear strains in each loading cycle. The shear strain increments in each loading cycle decrease with increasing gradation for both loading conditions. This decrease was attributed to the development of smaller shear strains at near-zero effective stress of the soil with the higher C_u. On the other hand, the response under non-reversal ($CSR < \alpha$) loading conditions was characterized by a limited development of shear strains, with no major differences between both soils. It was interpreted that under non-reversal loading conditions, the soil matrix remains largely stable while accumulating minor strains in the direction of the static shear stress bias due

to incremental particle rearrangement. These observations were confirmed by CV-DSS tests performed under cyclic irregular loading conditions.

- An increase in the α values led to a decrease in the liquefaction triggering resistance (defined as γ_{SA}=3%) for both soils; however, the decrease was more significant for the soil with the lower C_u value. These differences were attributed to the higher potential of strain-softening of that soil, which in turn led to a larger reduction of effective vertical stresses in the cycle preceding liquefaction triggering. The strain-softening tendencies of both soils also affected the patterns of pore pressure generation per loading cycle; however, a correlation between these patterns and soil gradation was not found.

The large variability of K_α curves available in the literature presents a challenge for liquefaction assessments under sloping ground conditions which are very frequently encountered in the practice of embankment dams, levees etc. Populating these datasets is crucial for the cost-effective design and mitigation for liquefaction effects on critical infrastructure featuring slopes. Results from this work showed that the selection of K_α curves for design purposes should not be based only on the relative density and the overburden stress, but should also consider factors like the soil gradation or the potential of strain-softening. The results presented herein systematically show that an increase in gradation leads to a slight increase in K_α factors. It is hypothesized that this increase may be more significant for sands with wider gradations as they are expected to have a smaller degree of strain-softening. In that sense, further work is required to evaluate K_α factors for wider gradations, and to study the effect of other factors such as the fine content, sample preparation or the testing device (e.g., triaxial, torsional shear).

6.6 References

ASTM International. 2019. *Standard Test Method for Consolidated Undrained Cyclic Direct Simple Shear Test under Constant Volume with Load Control or Displacement Control*. ASTM D8296-19. West Conshohocken, PA: ASTM International, approved November 1, 2019. https://doi.org/10.1520/D8296-19

Boulanger, R. W. 2003. Relating Kα to Relative State Parameter Index. *Journal of Geotechnical and Geoenvironmental Engineering* 129(8): 770–773.

Boulanger, R. W., Seed, R. B., Chan, C. K., Seed, H. B., and Sousa, J. B. 1991. *Liquefaction Behavior of Saturated Sands under Uni-Directional and Bi-Directional Monotonic and Cyclic Simple Shear Loading*. Geotechnical Engineering Report No. UCB/GT/91-08, University of California, Berkeley.

Boulanger, R. W. and Truman, S. P. 1996. Void redistribution in sand under post-earthquake loading. *Canadian Geotechnical Journal* 33: 829–34.

Carey, T. J., Chiaradonna, A., DeJong, J. T., and Ziotopoulou, K. 2021. The effects of gradation on the dynamic response of sloping ground. In *Proceedings of 20th International Conference on Soil Mechanics and Geotechnical Engineering (ICSMGE), Sydney, Australia*.

Chiaro, G., Koseki, J., and Sato, T. 2012. Effects of initial static shear on liquefaction and large deformation properties of loose saturated Toyoura sand in undrained cyclic torsional shear tests. *Soils and Foundations* 52(3): 498–510. https://doi.org/10.1016/j.sandf.2012.05.008

Harehdasht, S. A., Karray, M., Hussien, M. N., and Chekired, M. 2017. Influence of particle size and gradation on the stress-dilatancy behavior of granular materials during drained triaxial compression. *International Journal of Geomechanics* 17(9): 1–20. https://doi.org/10.1061/(ASCE)GM.1943-5622.0000951

Humire, F., Lee, M., Ziotopoulou, K., Gomez, M. G., and DeJong, J. T. 2022. Development and evaluation of pre-conditioning protocols for sand specimens in constant-volume cyclic direct simple shear tests. *Geotechnical Testing Journal* (under review).

Humire, F., Ziotopoulou, K., and DeJong, J. T. 2021. Evaluating shear strain accumulation of sands exhibiting cyclic mobility behavior. In *Proceedings of 20th International Conference on Soil Mechanics and Geotechnical Engineering (ICSMGE), Sydney, Australia*.

Hyodo, M., Murata, H., Yasufuku, N., and Fujii, T. 1991. Undrained cyclic shear strength and residual shear strain of saturated sand by cyclic triaxial tests. *Soils and Foundations* 31(3): 60–76. https://doi.org/doi.org/10.3208/sandf1972.31.3_60

Hyodo, M., Tanimizu, H., Yasufuku, N., and Murata, H. 1994. Undrained cyclic and monotonic triaxial behavior of saturated loose sand. *Soils and Foundations* 17(11): 1460–1462.

Idriss, I. M. and Boulanger, R. W. 2008. *Soil liquefaction during earthquakes*. Monograph MNO-12. Earthquake Engineering Research Institute, Oakland, CA.

Ishihara, K. and Nagase, H. 1980. Cyclic simple shear tests on saturated sand in multi-directional loading. *Soils and Foundations* 20(1), March, closure to discussion.

Kokusho, T., Hara, T., and Hiraoka, R. 2004. Undrained Shear Strength of Granular Soils with Different Particle Gradations. *Journal of Geotechnical and Geoenvironmental Engineering* 130(6): 621–629. https://doi.org/10.1061/(asce)1090-0241(2004)130:6(621)

Kuei, K. 2019. *Pile Dynamics and Shearing Behavior of Granular Soils*. PhD dissertation, University of California, Davis.

Lee, K. L. and Seed, H. B. 1967. Dynamic strength of anisotropically consolidated sand. *Journal of the Soil Mechanics and Foundations Division* 93(5): 169–190. https://doi.org/10.1061/jsfeaq.0001019

Prasanna, R., Sinthujan, N., and Sivathayalan, S. 2020. Effects of initial direction and subsequent rotation of principal stresses on liquefaction potential of loose sand. *Journal of Geotechnical and Geoenvironmental Engineering* 146(3): 04019130. https://doi.org/10.1061/(asce)gt.1943-5606.0002182

Reardon, R. A. 2021. *Monotonic and Cyclic Direct Simple Shear Testing of Coarse-Grained Soils*. Master’s thesis, University of California, Davis.

Seed, H. B. 1981. Earthquake-Resistant Design of Earth Dams. In *Proceedings: First International Conference on Recent Advances in Geotechnical Earthquake Engineering and Soil Dynamics*, 1157–1173. Rolla, MO: University of Missouri-Rolla.

Sivathayalan, S. and Ha, D. 2011. Effect of static shear stress on the cyclic resistance of sands in simple shear loading. *Canadian Geotechnical Journal* 48(10): 1471–1484. https://doi.org/10.1139/t11-056

Sivathayalan, S. and Vaid, Y. P. 2002. Influence of generalized initial state and principal stress rotation on the undrained response of sands. *Canadian Geotechnical Journal* 39(1): 63–76. https://doi.org/10.1139/t01-078

Sturm, A. P. 2019. *On the Liquefaction Potential of Gravelly Soils: Characterization, Triggering and Performance*. PhD dissertation, University of California, Davis.

Sze, H. Y. and Yang, J. 2014. Failure modes of sand in undrained cyclic loading: Impact of sample preparation. *Journal of Geotechnical and Geoenvironmental Engineering* 140(1): 152–169. https://doi.org/10.1061/(asce)gt.1943-5606.0000971

Tasiopoulou, P., Ziotopoulou, K., Humire, F., Giannakou, A., Chacko, J., and Travasarou, T. 2020. Development and implementation of semiempirical framework for modeling postliquefaction shear deformation accumulation in sands. *Journal of Geotechnical and Geoenvironmental Engineering* 146(1): 4019120. https://doi.org/10.1061/(ASCE)GT.1943-5606.0002179

Umar, M., Chiaro, G., Kiyota, T., and Ullah, N. 2021. Deformation and cyclic resistance of sand in large-strain undrained torsional shear tests with initial static shear stress. *Soils and Foundations* 61(3): 765–781. https://doi.org/10.1016/j.sandf.2021.02.008

Vaid, J. P., Stedman, J. D., and Sivathayalan, S. 2001. Confining stress and static shear effects in cyclic liquefaction. *Canadian Geotechnical Journal* 38(3): 580–591. https://doi.org/10.1139/cgj-38-3-580

Vaid, Y. P. and Chern, J. C. 1983. Effect of static shear on resistance to liquefaction. *Soils and Foundations* 23(1): 47–60.

Vaid, Y. P., Fisher, J. M., Kuerbis, R. H., and Negussey, D. 1990. Particle gradation and liquefaction. *Journal of Geotechnical Engineering* 116(4): 698–703. https://doi.org/10.1061/(ASCE)0733-9410(1990)116:4(698)

Verdugo, R. and Ishihara, K. 1996. The steady state of sandy soils. *Soils and Foundations* 36(2): 81–91. https://doi.org/10.3208/sandf.36.2_81

Wei, X. and Yang, J. 2019. Cyclic behavior and liquefaction resistance of silty sands with presence of initial static shear stress. *Soil Dynamics and Earthquake Engineering* 122: 274–289. https://doi.org/10.1016/j.soildyn.2018.11.029

Yang, J. and Sze, H. Y. 2011a. Cyclic behaviour and resistance of saturated sand under non-symmetrical loading conditions. *Geotechnique* 61(1): 59–73. https://doi.org/10.1680/geot.9.P.019

Yang, J. and Sze, H. Y. 2011b. Cyclic strength of sand under sustained shear stress. *Journal of Geotechnical and Geoenvironmental Engineering* 137(12): 1275–1285. https://doi.org/10.1061/(ASCE)GT.1943-5606.0000541

Yang, Z. X. and Pan, K. 2017. Flow deformation and cyclic resistance of saturated loose sand considering initial static shear effect. *Soil Dynamics and Earthquake Engineering* 92: 68–78. https://doi.org/10.1016/j.soildyn.2016.09.002

Youd, T. L. et al. 2001. Liquefaction Resistance of Soils: Summary Report from the 1996 NCEER and 1998 NCEER/NSF Workshops on Evaluation of Liquefaction Resistance of Soils. *Journal of Geotechnical and Geoenvironmental Engineering* 127(10): 817–833.

Zekkos, D., Athanasopoulos-Zekkos, A., Hubler, J., Fei, X., Zehtab, K. H., and Marr, W. A. 2018. Development of a Large-Size Cyclic Direct Simple Shear Device for Characterization of Ground Materials with Oversized Particles. *Geotechnical Testing Journal* 41(2): 263–279. https://doi.org/10.1520/GTJ20160271

Ziotopoulou, K. 2014. *A Sand Plasticity Model for Earthquake Engineering Applications*. PhD dissertation, University of California, Davis.

Ziotopoulou, K. and Boulanger, R. W. 2016. Plasticity modeling of liquefaction effects under sloping ground and irregular cyclic loading conditions. *Soil Dynamics and Earthquake Engineering* 84: 269–283. https://doi.org/10.1016/J.SOILDYN.2016.02.013

6.7 Tables and figures

Table 6.1. Properties of the soils used in this work (Sturm 2019): maximum and minimum void ratio (e_{max} and e_{min}), largest grain size in smallest 10% of grains by mass (D_{10}), median grain size (D_{50}), coefficient of uniformity (C_u), and coefficient of permeability (k).

Soil Name	**e_{max}**	**e_{min}**	**D_{10} (mm)**	**D_{50} (mm)**	**C_u**	**k (cm/s)**
100A	0.881	0.579	0.12	0.18	1.68	0.017
100B	0.835	0.524	0.31	0.51	1.80	0.128
100C	0.839	0.557	0.91	1.31	1.54	1.028
33ABC	0.622	0.397	0.15	0.51	4.41	0.022

Table 6.2. Summary of the constant-volume direct simple shear (CV-DSS) tests performed in this work.

ID	Soil	Type of Test	$\alpha = \tau_{static}/\sigma'_{vc}$	D_R (%)	CSR = $\tau_{cyclic}/\sigma'_{vc}$	Type of Loading	Number of Cycles to $\gamma_{SA} = 3\%$
1	100A	Monotonic	0	40.5	-	-	-
2			0.1	44.1	-	-	-
3			0.2	42.7	-	-	-
4			0.35	43.9	-	-	-
5			0.5	46.4	-	-	-
6	100A	Cyclic	0	42.2	0.08	Reversal	14.6
7				42.9	0.10	Reversal	5.6
8				42.5	0.12	Reversal	2.1
9				45.3	0.15	Reversal	0.7
10	100A	Cyclic	0.05	41.6	0.05	Intermediate	55.2
11				42.6	0.08	Reversal	8.2
12				41.7	0.10	Reversal	1.3
13				44.1	0.08 - 0.04 - 0.08	Irregular	7.9
14	100A	Cyclic	0.1	44.0	0.04	Non-reversal	498.2
15				35.5	0.05	Non-reversal	8.3
16				44.6	0.055	Non-reversal	6.1
17				42.8	0.10 - 0.05 - 0.10	Irregular	0.2
18	100A	Cyclic	0.2	39.8	0.015	Non-reversal	57.3
19				44.3	0.02	Non-reversal	9.1
20				39.8	0.024	Non-reversal	1.3
21				42.0	0.05	Non-reversal	0.2
22	33ABC	Monotonic	0	44.2	-	-	-
23			0.1	40.9	-	-	-
24			0.2	44.6	-	-	-
25			0.35	43.1	-	-	-
26			0.5	45.8	-	-	-
27	33ABC	Cyclic	0	45.8	0.06	Reversal	55.1
28				34.8	0.07	Reversal	8.2
29				37.6	0.10	Reversal	3.1
30				48.2	0.10	Reversal	4.1
31				46	0.14	Reversal	0.8
32	33ABC	Cyclic	0.05	39.2	0.05	Intermediate	40.2
33				37.0	0.06	Reversal	18
34				41.4	0.075	Reversal	8.2
35				48.3	0.08 - 0.04 - 0.08	Irregular	7.4
36	33ABC	Cyclic	0.1	42.4	0.05	Non-reversal	51.2
37				40.0	0.06	Non-reversal	4.2
38				46.5	0.065	Non-reversal	1.3
39				42.8	0.10 - 0.05 - 0.10	Irregular	0.2
40	33ABC	Cyclic	0.2	42.7	0.02	Non-reversal	175.2
41				40.0	0.025	Non-reversal	5.3
42				42.0	0.03	Non-reversal	6.3
43				41.2	0.035	Non-reversal	0.4
44				44.3	0.05	Non-reversal	0.2

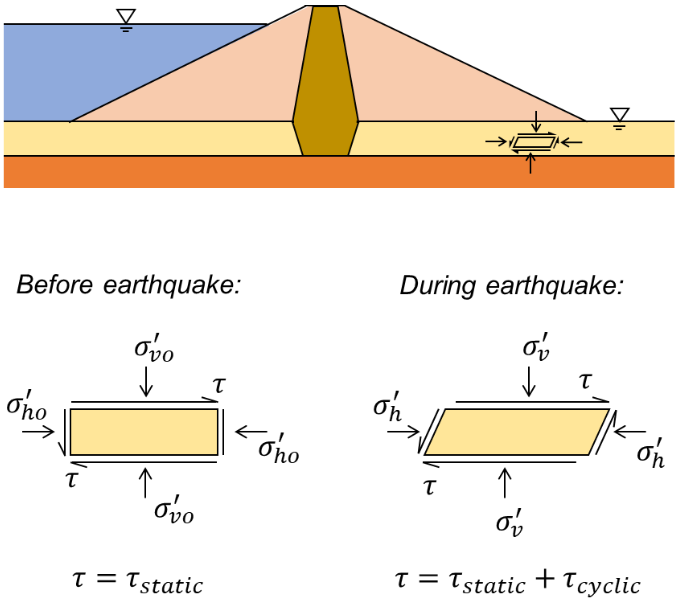

Figure 6.1. Scheme of the stress conditions in a soil element beneath an embankment due to sloping ground conditions.

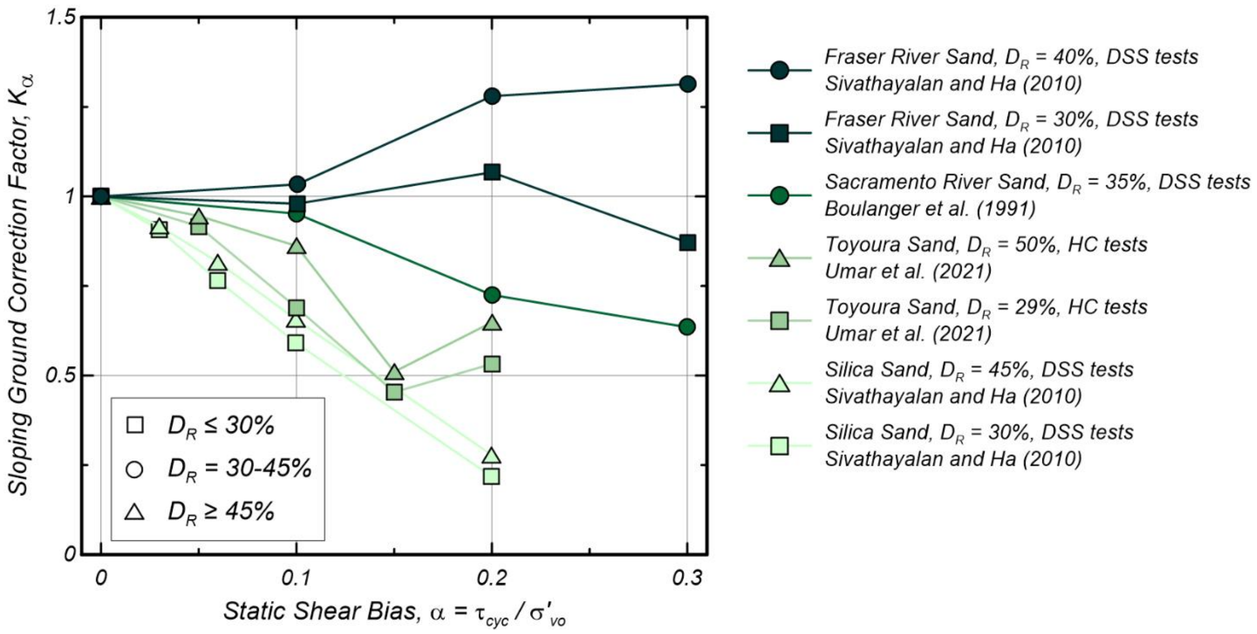

Figure 6.2. Sloping ground conditions correction factors ($K_\alpha = CRR_\alpha / CRR_{\alpha=0}$) available in the literature for loose specimens of clean uniform sands under a range of initial static shear stress ratios ($\alpha = \tau_{cyc} / \sigma'_{vo}$) obtained with direct simple shear (DSS) or hollow cylinder (HC) torsional shear tests, with relative densities (D_R) ranging between 29 and 50% and overburden stresses (σ'_{vo}) of 100 kPa. Light green colors assigned to curves affected by strain-softening tendencies, while darker tones correspond to curves not affected by strain-softening.

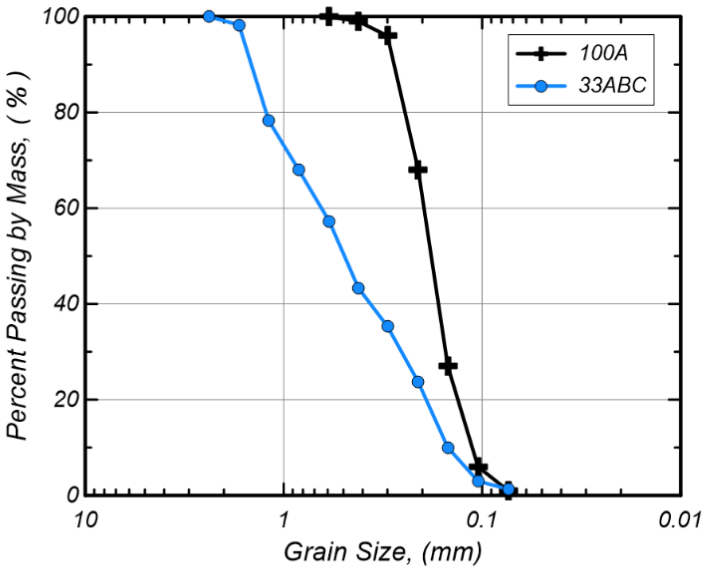

Figure 6.3. Grain size distribution of the soil mixtures presented in this work.

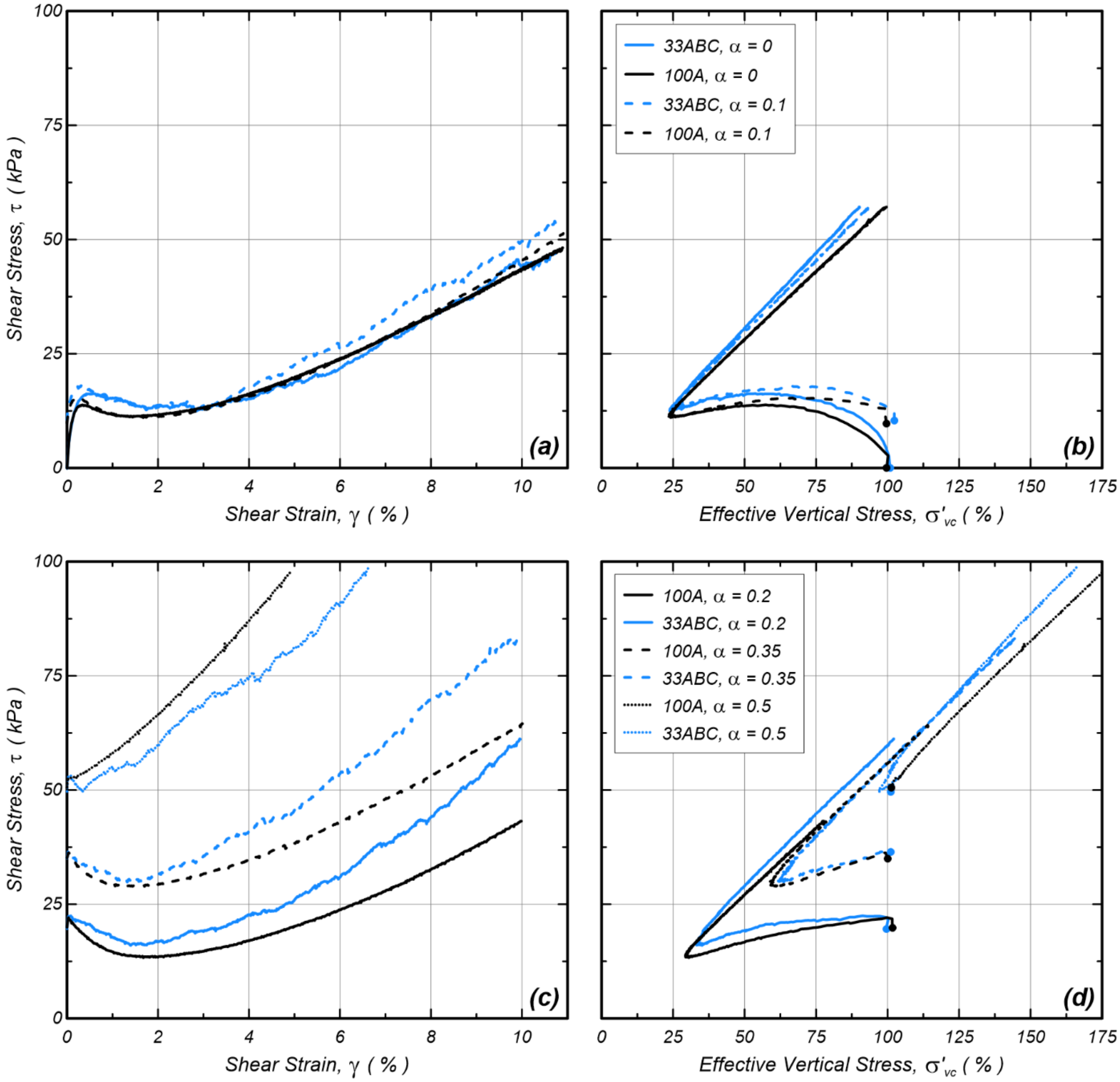

Figure 6.4. Comparison of the monotonic CV-DSS tests results obtained on loose specimens (D_R = 40 - 44%) of 100A and 33ABC sands with different initial static shear stress ratios (α): (a) stress-strain responses and (b) stress paths for tests with $\alpha = 0$ and 0.1; and (c) stress-strain responses and (d) stress paths for tests with $\alpha = 0.2$ to 0.5.

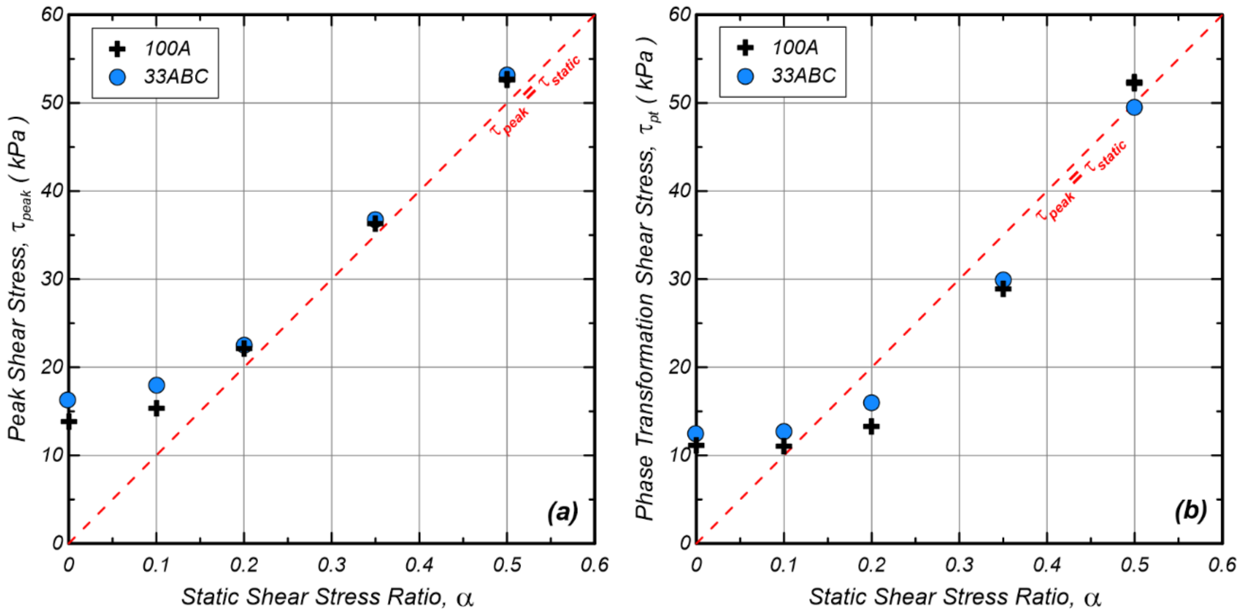

Figure 6.5. Effect of gradation on the (a) peak shear stress (τ_{peak}) and (b) phase transformation shear stress (τ_{pt}) obtained for different initial static shear stress ratios (α).

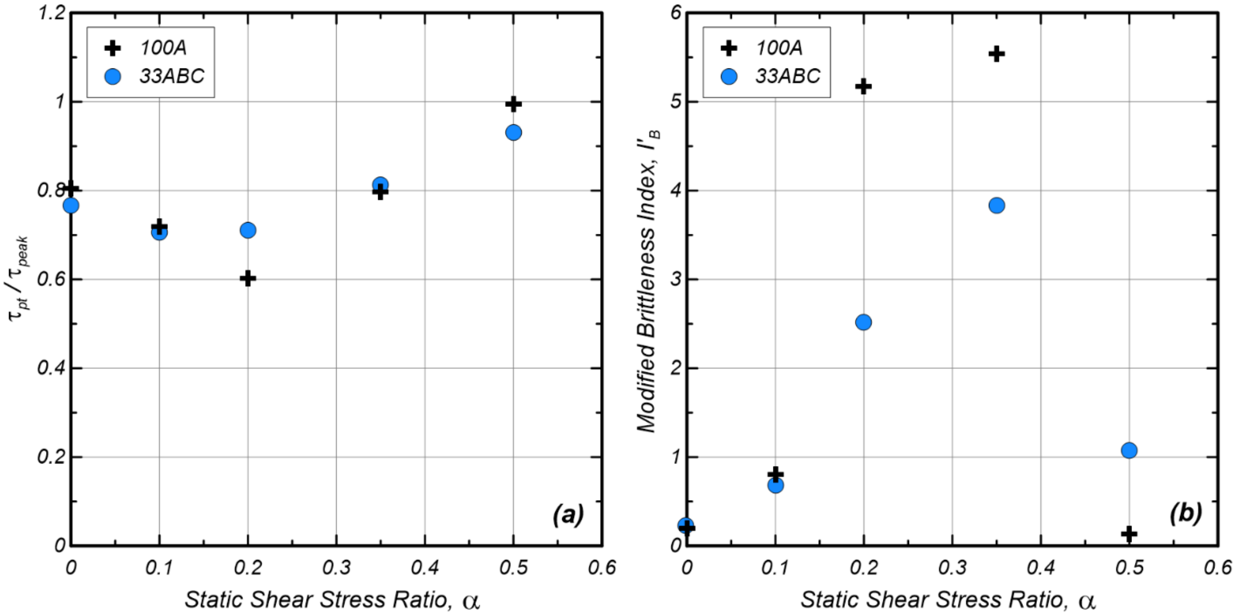

Figure 6.6. Comparison of (a) τ_{pt}/τ_{peak} ratio, and (b) the modified brittleness index (I'_B) defined by Sivathayalan and Ha (2010) for 100A and 33ABC soils under different initial static shear stress ratios (α).

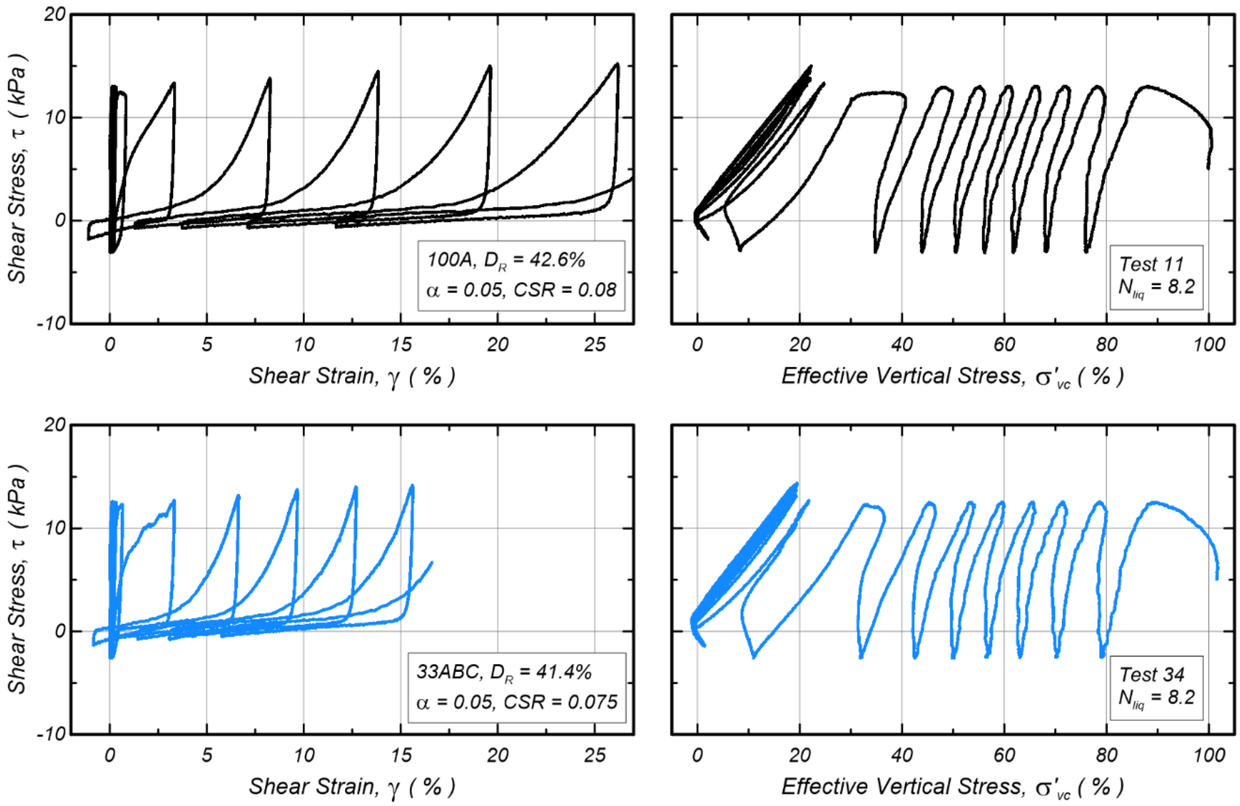

Figure 6.7. Results of cyclic CV-DSS tests performed on loose specimens (D_R = 41-43%) of 100A and 33ABC soils subjected to reversal stress loading conditions ($\tau_{cyclic} > \tau_{static}$).

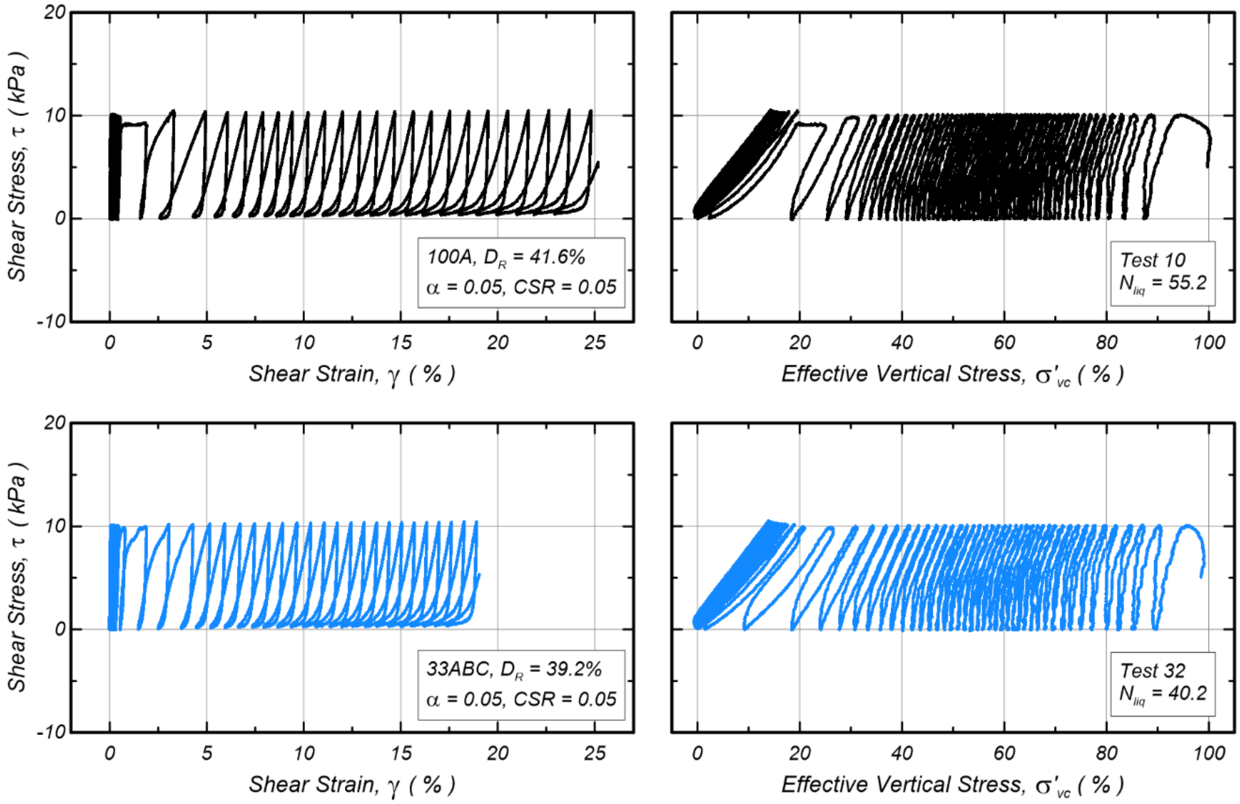

Figure 6.8. Results of cyclic CV-DSS tests performed on loose specimens (D_R = 39-42%) of 100A and 33ABC soils subjected to intermediate stress loading conditions ($\tau_{cyclic} = \tau_{static}$).

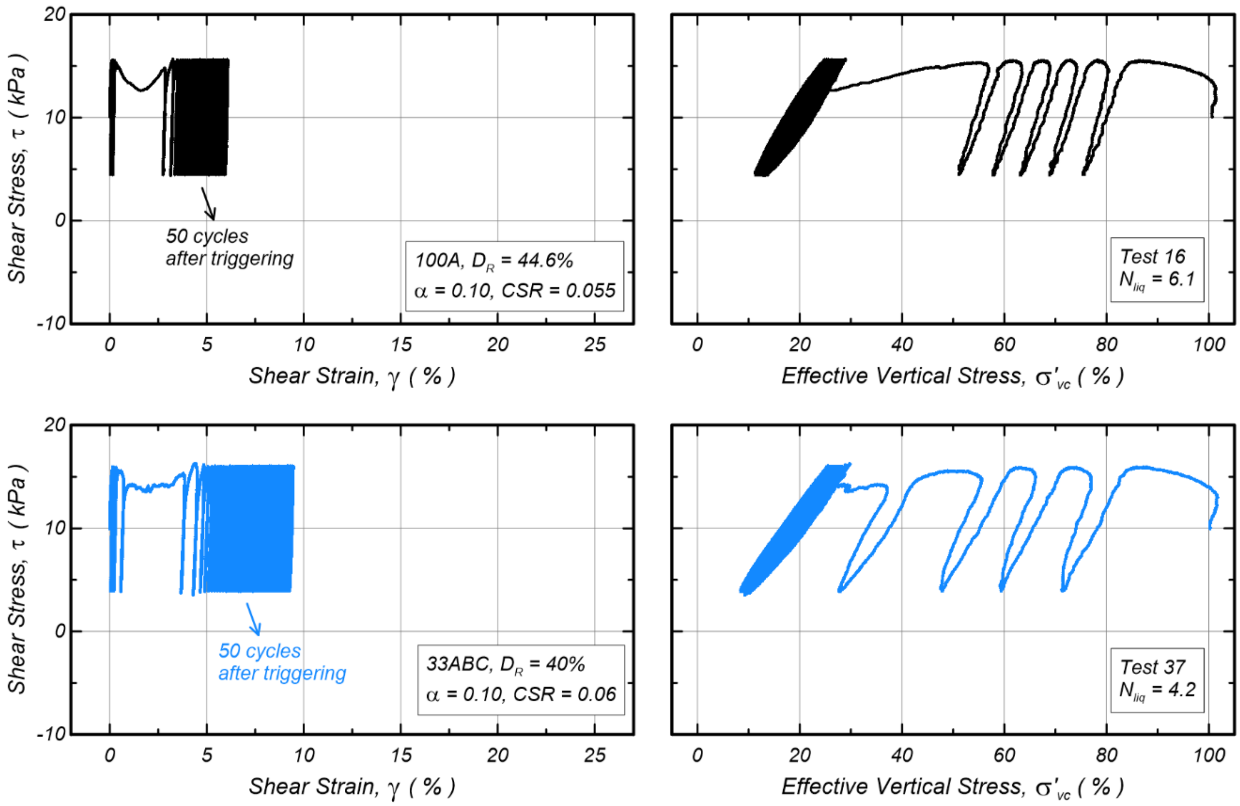

Figure 6.9. Results of cyclic CV-DSS tests performed on loose specimens (D_R = 42-44%) of 100A and 33ABC soils subjected to non-reversal stress loading conditions ($\tau_{cyclic} < \tau_{static}$).

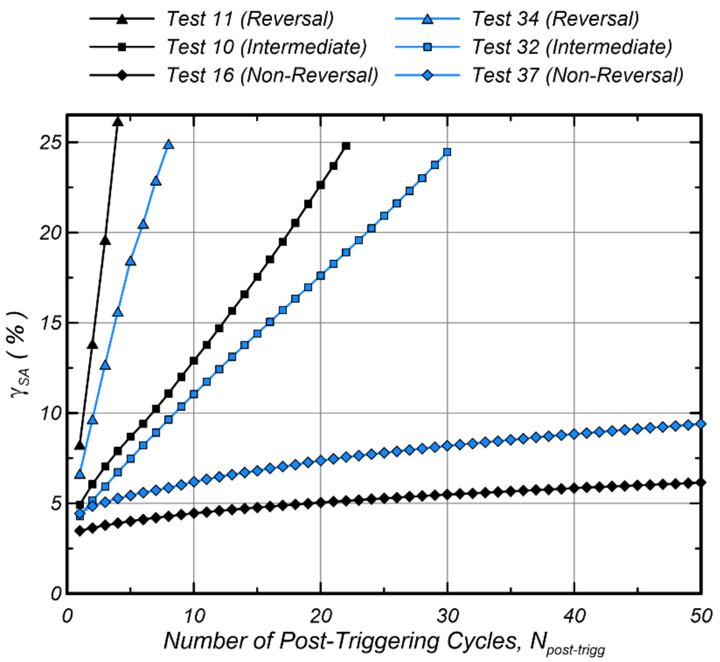

Figure 6.10. Accumulation of single amplitude shear strains (γ_{SA}) in the CV-DSS tests presented in Figures 6.7 to 6.9 per post-triggering loading cycle (i.e., cycles with γ_{SA} > 3%).

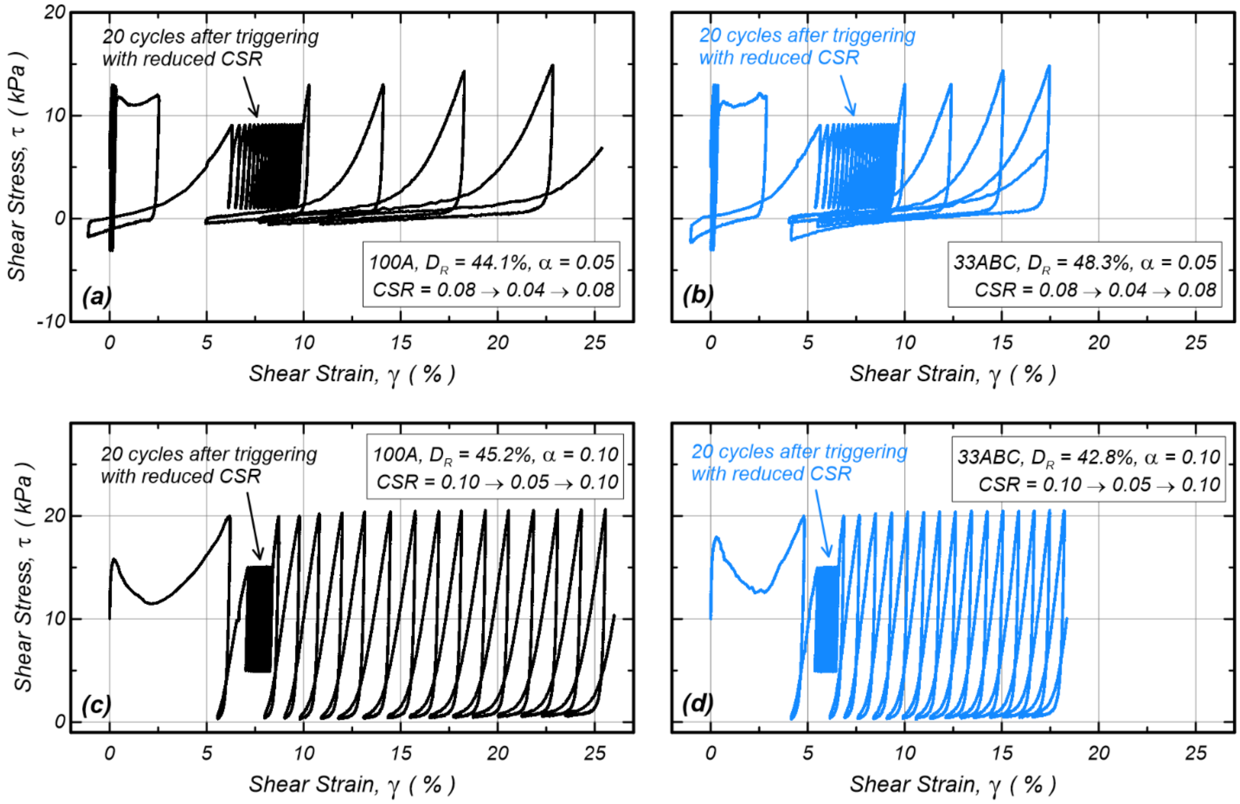

Figure 6.11. Stress-strain responses obtained in irregular cyclic CV-DSS tests performed on loose specimens (D_R = 43-48%) of 100A and 33ABC soils subjected to three distinct stages of cyclic loading, wherein the second stage is a non-reversal type of loading: (a) Test 13, (b) Test 35, (c) Test 17, and (d) Test 39 with reference to Table 6.2.

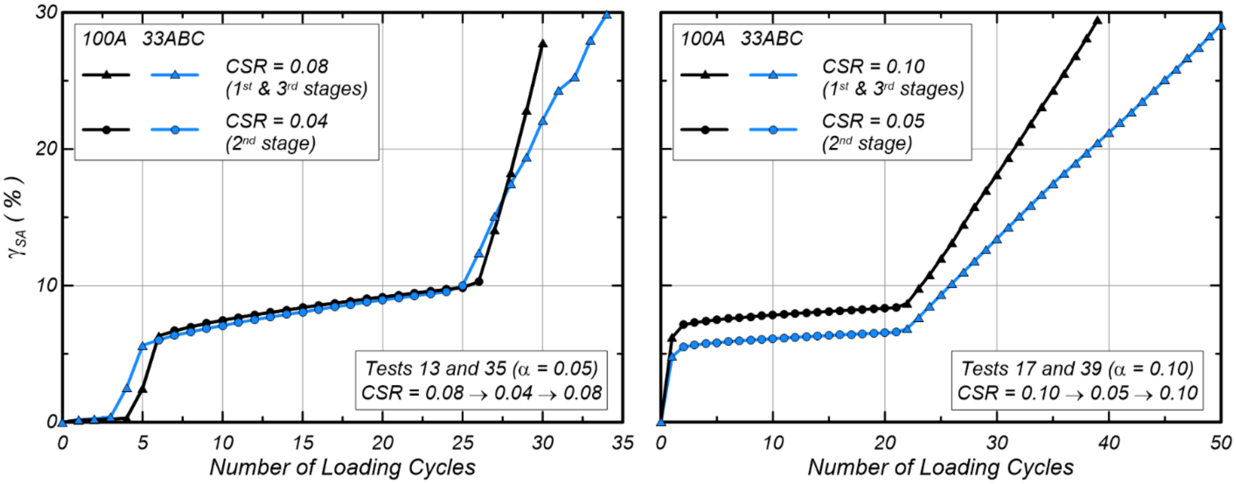

Figure 6.12. Accumulation of single amplitude shear strains (γ_{SA}) per loading cycle in the irregular cyclic CV-DSS tests presented in Figure 6.10.

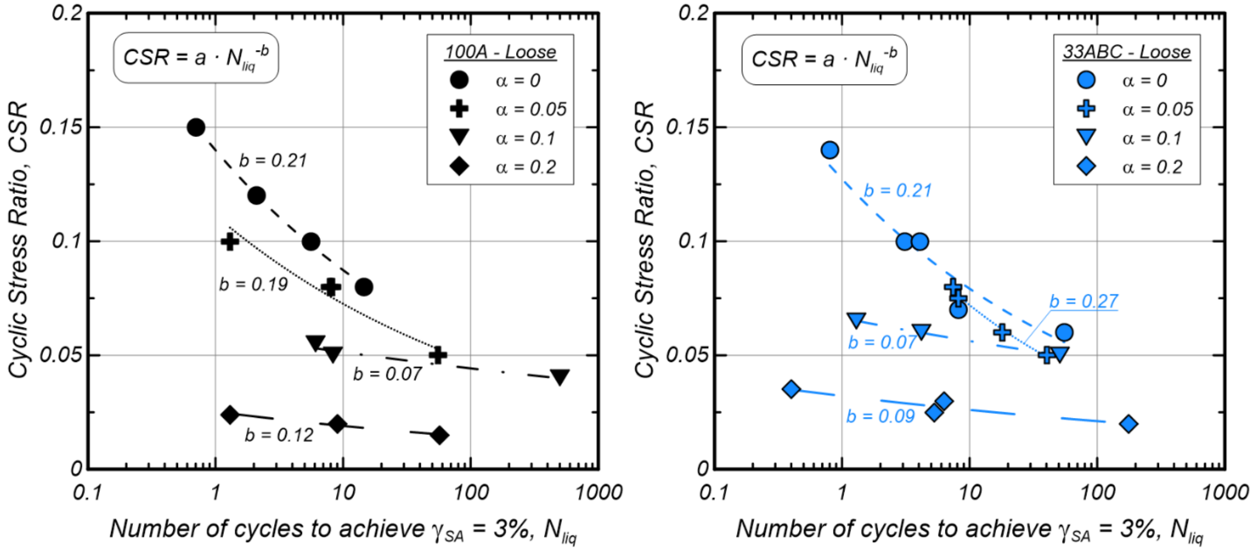

Figure 6.13. Liquefaction triggering curves obtained from cyclic CV-DSS tests on loose specimens of 100A and 33ABC soils under different initial static shear stress ratios (α).

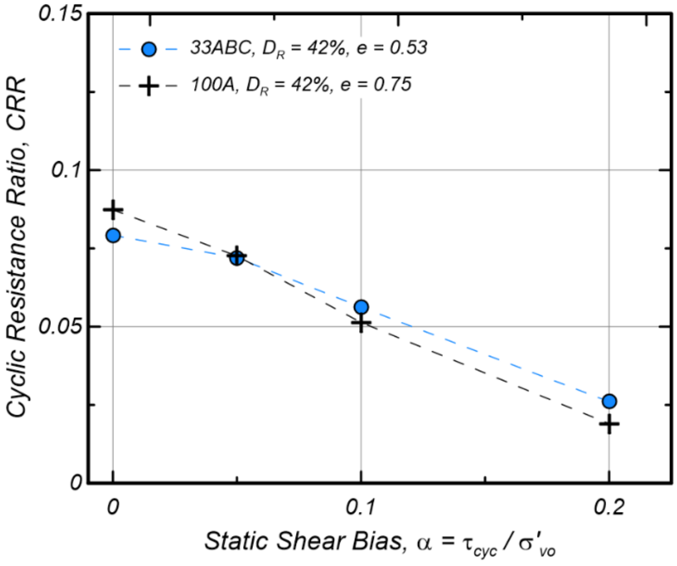

Figure 6.14. Cyclic resistance ratio (CRR, defined as the CSR to reach γ_{SA} =3% in 10 cycles) obtained for loose specimens of 100A and 33ABC soils under different initial static shear stress ratios (α).

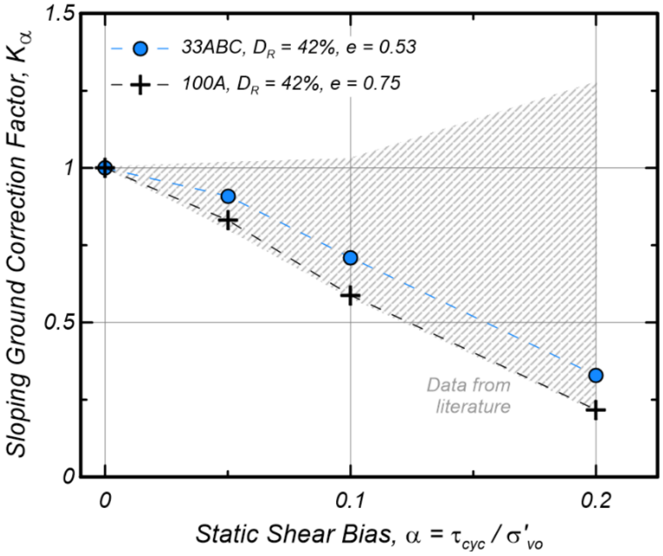

Figure 6.15. Sloping ground conditions correction factors ($K_\alpha = CRR_\alpha / CRR_{\alpha=0}$) for loose specimens of 100A and 33ABC soils under different initial static shear stress ratios (α), and comparison with curves from the literature in Figure 6.2.

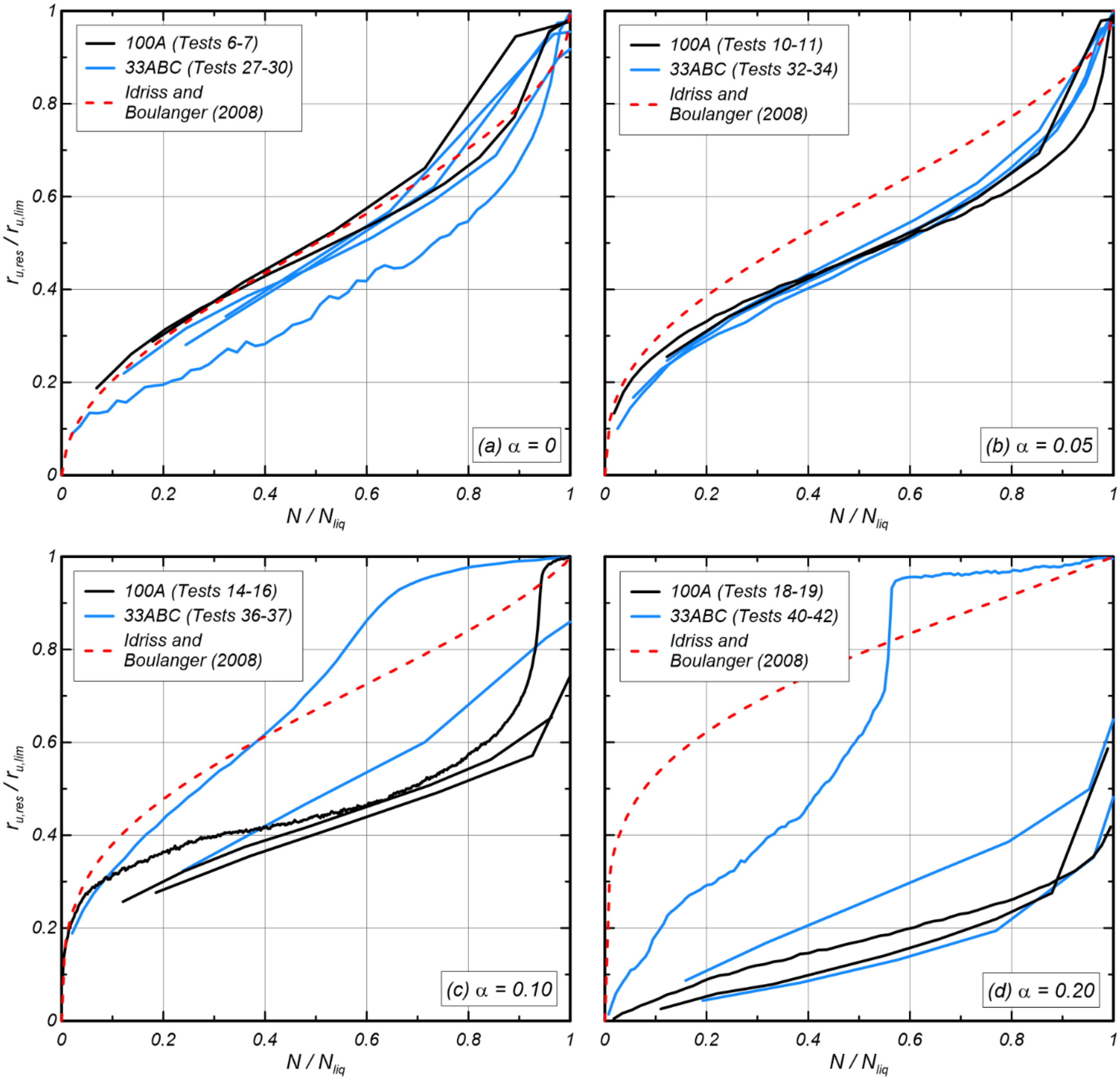

Figure 6.16. Ratio between the residual pore pressure ratio and the limit residual pore pressure ratio at liquefaction ($r_u/r_{u,lim}$) versus the number of loading cycles normalized by the number of cycles to trigger liquefaction (N/N_{liq}). Data correspond to cyclic CV-DSS tests listed in Table 6.2 performed on loose specimens of 100A and 33ABC soils with different initial static shear stress ratios: (a) α = 0, (b) α = 0.05, (c) α = 0.1, and (d) α = 0.2, which are compared with the empirical curves by Idriss and Boulanger (2008) for the same α values.

Chapter 7

Modeling the element response of two sands with different gradations under level and sloping ground loading conditions with PM4Sand

Author's note: This Chapter will be submitted as a journal paper for publication authored by Francisco Humire and Katerina Ziotopoulou. The paper is presented herein with some minor edits for consistency with the other chapters of this Dissertation.

Abstract

This paper examines the capabilities and limitations of the PM4Sand constitutive model in capturing key features of the liquefaction behavior of two sands with different gradations under sloping ground conditions. Experimental data used for the calibration process consisted of a series of monotonic and cyclic constant-volume direct simple shear (CV-DSS) tests performed on two sands with different coefficients of uniformity (C_u = 1.68 – 4.41), considering a broad range of static shear stress ratios (α = 0 – 0.5) and cyclic stress ratios (CSR). Simulations with PM4sand successfully captured the monotonic response and liquefaction triggering resistance for both soils presented in this paper. Still, the calibration process required: (1) activating some of the secondary parameters of the model, and (2) using alternative parameter sets depending on the target responses

prioritized during calibration. The simulation of large post-liquefaction shear deformations required adjusting two secondary parameters implemented in the model (C_ε and n^b). However, the model could not capture the gradual arrest on the accumulation of shear strains observed under non-reversal loading conditions ($CSR < \alpha$) for both soils, and on medium dense specimens of the soil with higher C_u.

7.1 Introduction

Advanced constitutive models capable of capturing the element response of liquefiable sands (e.g., Beaty and Byrne 2011; Tasiopoulou and Gerolymos 2016; Boulanger and Ziotopoulou 2017; Khosravifar et al. 2018) have contributed to improved estimations of liquefaction effects at the system level. The development of such models has been guided by theoretical frameworks, empirical observations of the monotonic and cyclic response of sands at the element level, and the extensive body of laboratory- and case history-based correlations used for liquefaction assessments in engineering practice. However, the current understanding of the liquefaction phenomenon is predominantly based on fundamental research conducted on clean uniform sands and, consequently, available correlations do not explicitly consider, for example, the effect of soil gradation. Although the predictive capabilities of constitutive models may be limited by these knowledge gaps, such limitations are not prohibitive for engineering practice and constitutive models are widely used without considering differences in gradation. However, and as one example, recent centrifuge modeling research by Sturm (2019) and Carey et al. (2021) has shown that well-graded coarse-grained soils generally undergo smaller liquefaction-induced deformations than clean uniform sands at the same relative density, suggesting that disregarding the effect of soil gradation in liquefaction assessments may lead to overestimations of earthquake-induced damages. As such, and to reduce uncertainties of liquefaction assessments in engineering practice, further research is needed to improve current constitutive modeling capabilities to capture the behavior of well-graded coarse-grained soils.

PM4Sand is a plane strain constitutive model developed for sands in geotechnical earthquake engineering applications, with the goal of capturing the stress-strain behavior of sands for a wide range of seismic hazard levels and in-situ stress conditions, while being able to be calibrated with a reasonable amount of engineering effort as well as with the information most commonly available in engineering projects (Boulanger and Ziotopoulou 2017). The model features three primary input parameters that need to be set by the user as well as 21 secondary parameters with values set by the developers as part of the generalized calibration of the model. In the lack of site-specific or lab information, the generalized calibration of the model ensures that it can at least reasonably capture the range of behaviors demonstrated by the literature and its established correlations. However, if more data are available, it is advised that the users (i) evaluate how the model behaves against them and if deemed necessary calibrate secondary parameters accordingly, as well as (ii) confirm that the model still behaves reasonably across the broader body of important behaviors. Previous numerical efforts (e.g., Ziotopoulou and Boulanger 2016; Tasiopoulou et al. 2020) have demonstrated the ability of PM4Sand to capture the liquefaction response of clean uniform sands at the element and system levels. Given the availability of the experimental data presented in Chapters 5 and 6, this Chapter aims to evaluate the performance of PM4Sand in capturing the liquefaction behavior of two sands with different gradations under sloping ground conditions. Section 2 of this Chapter briefly introduces the PM4Sand model, emphasizing the relevance of calibrating its parameters against available laboratory element testing data. Section 3 presents the experimental data used for the calibration process, consisting of monotonic and cyclic constant-volume direct simple shear (CV-DSS) tests performed on two sands with different gradations under level and sloping ground loading conditions. Section 4 presents in detail the calibration process to capture the response of both sands, and presents three alternative parameter sets for each sand calibrated to capture the response of loose specimens under i) monotonic loading under sloping ground conditions, ii) cyclic loading under level ground conditions, and iii) cyclic loading under sloping ground conditions. A fourth parameter set captures the response of medium dense specimens subjected to cyclic loading under level ground conditions. Section 5 discusses the ability of the current constitutive formulation and generalized calibration, which essentially sets the default values of secondary parameters, to capture the liquefaction triggering resistance and post-triggering shear deformations under sloping ground loading conditions for a range of gradations.

7.2 Background on PM4Sand and its generalized calibration

PM4Sand is a critical state compatible, stress ratio-controlled, bounding surface plasticity model, based on the framework presented by Dafalias and Manzari (2004), with modifications to capture stress-strain responses and engineering correlations relevant for earthquake engineering applications (Ziotopoulou and Boulanger 2016; Boulanger and Ziotopoulou 2017). The model has three primary input parameters that must be assigned prior its use: the apparent relative density (D_R), the shear modulus coefficient (G_o) that controls the small-strain shear modulus, and the contraction rate parameter (h_{po}) that can be adjusted to obtain a target cyclic strength. The model also has 21 secondary parameters with default values or functions previously calibrated by Boulanger and Ziotopoulou (2017) to capture the broader established body of behaviors of sands. However, secondary parameters also can be modified by the user when advanced laboratory testing data is available. The secondary parameters of relevance to this paper are: Q and R that control the position of the critical state line according to Bolton's relationship (1986); constant volume friction angle (ϕ'_{cv}); minimum and maximum void ratios (e_{min} and e_{max}); h_o that controls the ratio of plastic modulus to elastic modulus and can be used to adjust the small-strain stiffness and secant shear modulus reduction, n^d that controls the location of dilatancy surface and can be used to adjust the stress ratio at which phase transformation (i.e., transition from contractive to dilative behavior, or vice versa) occurs; n^b that controls the bounding surface and can be used to adjust the dilatancy and peak friction angle; and C_ε that controls the rate of shear strain accumulation in undrained cyclic loading.

The systematic validation and calibration of constitutive models against empirical data (e.g., laboratory testing data, engineering correlations) provides the opportunity to examine the performance of constitutive models in single element simulation studies (e.g., Ziotopoulou et al. 2014; Wichtmann et al. 2019; Pretell et al. 2020), which can in turn lead to improvements of constitutive formulations and modeling procedures (Boulanger and Ziotopoulou 2018). For example, Ziotopoulou et al. (2014) evaluated the performance of four constitutive models (Yang et al. 2003; Dafalias and Manzari 2004; Beaty and Byrne 2011; Boulanger and Ziotopoulou 2013) in capturing the liquefaction behavior under sloping ground conditions on the basis of results of cyclic CV-DSS tests on Nevada sand and sloping ground correction factors (K_α) available in the literature (Harder and Boulanger 1997; Boulanger 2003). They identified that version 2 of PM4Sand (Boulanger and Ziotopoulou 2012) provided reasonable stress paths compared to CV-DSS testing data; however, the simulated K_α curves deviated significantly from experimental trends as the model was unable to reproduce neither a decrease of cyclic strength while increasing the static shear stress bias α (= τ_{static} / σ'_{vo}) for loose sands, nor the opposite trend for dense sands.

This examination, combined with system level observations from numerical simulation comparisons to centrifuge model tests (Kamai 2011), led to modifications in the PM4Sand model to overcome such limitations (Ziotopoulou and Boulanger 2016), which also considered the performance of additional CV-DSS tests under sloping ground conditions subjected to irregular cyclic loadings to guide such changes. These modifications in PM4Sand's formulation included changes in the dependencies of the dilatancy line and plastic modulus on the loading history and fabric damage (Ziotopoulou and Boulanger 2016), which are now part of the current version 3.1 of PM4Sand (Boulanger and Ziotopoulou 2017).

In practice, constitutive models should be calibrated to approximate properties and behaviors (e.g., small-strain stiffness, cyclic resistance, shear strain accumulation) that are relevant for the system at hand (Boulanger and Ziotopoulou 2018), while considering overburden stresses and initial static shear ratios within the ranges of interest (Boulanger and Beaty 2016). The calibration process of constitutive models for sands is often based on engineering correlations to field testing data (Boulanger and Ziotopoulou 2018); however, representative laboratory testing data can help capture aspects of the soil response such as the accumulation of post-triggering shear strains of soils exhibiting cyclic mobility behavior (Tasiopoulou et al. 2020). To facilitate the calibration process, previous works have outlined procedures to calibrate PM4Sand or similar advanced models (Anthi and Gerolymos 2019; Boulanger and Wijewickreme 2019; Pretell et al. 2020) or proposed frameworks to guide the calibrations (Giannakou et al. 2011; Tasiopoulou et al. 2020). The broad range and uniqueness in the combination of seismic hazard levels and boundary value problems that employ such advanced constitutive models, make the development of a unique approach to their calibration challenging if not impossible. As such, their use in practice should consider a thorough assessment of their limitations and strengths, and comparisons with laboratory testing results or published relationships (Boulanger and Beaty 2016, Duque et al. 2021).

7.3 Experimental data

Experimental data presented herein were obtained from an extensive laboratory testing program aimed to investigate the characterization and liquefaction response of well-graded coarse-grained soils (e.g., Sturm 2019; Humire et al. 2021; Ahmed 2021). The experiments selected for this paper were performed on two sub-angular quarzitic coarse-grained soils with different grain size distributions (Figure 7.1). Soil 100A is a clean uniform sand, which was combined with other two sands with higher median grain sizes (D_{50}) to for a soil mixture (33ABC) with a higher coefficient of uniformity (C_u). Given the common geological origin of these soils (Sturm 2019) and their similar intrinsic grain properties (Table 7.1), these soils are expected to isolate the effect of gradation on the monotonic and cyclic response of coarse-grained soils. Physical and index properties of both soils are summarized in Table 7.1, and more details regarding their index characterization are available in Sturm (2019).

The ability of PM4Sand to capture key features of the liquefaction behavior of sands with two different gradations, as well as under variable sloping ground boundary conditions, was examined using the results from monotonic and cyclic CV-DSS performed on loose (D_R = 40%) and medium dense (D_R = 60–65%) specimens of 100A and 33ABC soils, which were previously presented in Sections 5 and 6 of this Dissertation. The availability of these datasets presents an opportunity to (i) evaluate the performance of the model across variable conditions, (ii) explore options for calibration protocols that achieve a good match, and (iii) draw conclusions regarding the need for a reformulation subject to the availability of more data.

Tests were performed on air-pluviated specimens with an effective overburden stress (σ'_{vo}) of 100 kPa, considering a broad range of static shear stress ratios ($\alpha = 0 – 0.5$) and cyclic stress ratios (CSR). According to the definitions of Hyodo et al. (1991), tests were performed under reversal (CSR > α), intermediate (CSR = α), and non-reversal (CSR < α) loading conditions. Also, the dataset presented herein included two experiments under irregular cyclic loading conditions for each soil, which involved varying the CSR along the course of the post-triggering regime across three loading stages. All tests were conducted in compliance with ASTM (2019) specifications, with vertical strain oscillations of less than 0.01%. Also, isotropically-consolidated monotonic drained and undrained triaxial compression (TXC) tests performed by Ahmed (2021) were used to determine the parameters associated to the critical state line (CSL). The TXC tests were also performed on air-pluviated specimens with D_R's ranging between 20 and 70% and initial confining pressures between 100 and 400 kPa. Details of the testing procedures and the equipment used for those tests are available in Reardon (2021) and Ahmed (2021) respectively.

7.4 Calibration of PM4Sand

This section describes the calibration process of the PM4Sand model to capture key features of the monotonic and cyclic behavior of 100A and 33ABC soils observed in CV-DSS tests with different D_R and α values. Calibrations were conducted using single-element simulations with the finite difference software FLAC (Itasca 2020), in which PM4Sand is implemented as a user-defined dynamic link library (Ziotopoulou and Boulanger 2013; Boulanger and Ziotopoulou 2017).

First, a base set of parameters was developed for each soil, which considered two primary parameters of the model (D_R and G_o) and other five secondary parameters (Q, R, ϕ'_{cv}, e_{min}, e_{max}).

The assigned D_R value corresponded to the average D_R measured at the beginning of shearing in the CV-DSS tests. The G_o parameter was calculated using the following equation:

$$G_o = \frac{G_{max}}{p_A} \left(\frac{p_A}{p'}\right)^{1/2} \tag{7.1}$$

where p_A is the atmospheric pressure, p' is the mean effective stress, and G_{max} is the elastic shear modulus that can be estimated from shear wave velocity (V_s) measurements. In this case, G_{max} was estimated with the following equation:

$$G_{max} = \rho \cdot (V_s)^2 \tag{7.2}$$

where ρ corresponds to the bulk density of specimens. Based on the empirical correlations of Andrus and Stokoe (2000), a V_s = 160 m/s was used for loose specimens, and a V_s = 180 m/s was used for medium dense specimens of both soils. As shown in Figure 7.2, the secondary parameters Q and R were adjusted to fit the empirical CSL defined by monotonic drained and undrained TXC tests (Ahmed 2021). These parameters were modified from their default values given the availability of TXC data. However, for a problem featuring a dense-of-critical sand undergoing cyclic mobility, the location of the CSL will not affect the response and only will change the initial value of the relative state parameter. This is in turn will be reflected by the calibration of the contraction rate parameter and the cyclic strength but in terms of response, the system will behave the same. This was also shown by the calibration efforts of Chiaradonna et al. (2022) who presented two comparative calibrations, one incorporating TXC data and modified Q and R values, and one that did not, both however targeting at the same cyclic strength. Their results in terms of both element level DSS and system level centrifuge model simulations demonstrated that the responses were identical. The values of ϕ'_{cv} used in the simulations were also informed by the TXC data. Finally, the available values of e_{min} and e_{max} in Table 7.1 were used for the calibrations.

The calibration process was aimed to capture the monotonic and cyclic response of 100A and 33ABC soils, as intended for system-level assessments of flow liquefaction or cyclic mobility-induced deformations. For that purpose, four calibrations were conducted for each soil as summarized in Table 7.2, each of them focused on capturing different target responses. Three of those calibrations focused on the response of loose specimens subjected to i) monotonic loading under sloping ground conditions (Calibration 1), ii) cyclic loading under level ground conditions (Calibration 2), and iii) cyclic loading under mildly sloping ground conditions (Calibration 3). On the other hand, Calibration 4 aimed to capture the cyclic response of medium dense specimens under level ground conditions. The calibration process presented herein can be summarized in three main steps:

(1) Assign values of D_R, G_o, Q, R, ϕ'_{cv}, e_{min} and e_{max}, and assign a trial value of h_{po}.

(2) Simulate strain-controlled cyclic drained DSS tests to adjust the secondary parameter h_o according to empirical curves proposed by EPRI (1993). The calibrations presented herein provide a reasonable agreement between G/G_{max} and damping ratio curves from simulations and those recommended by EPRI (1993) for depths representative of the σ'_{vo} of the tests. Figure 7.3 illustrates these results in terms of G/G_{max} and damping curves, as well as the reference EPRI (1993) curves and the predictions with the default calibration of h_o.

(3) Simulating undrained monotonic and cyclic CV-DSS tests considering the data and target responses indicated in Table 7.2. This step involved iterating the value of h_{po} to capture the cyclic strength, and activating three secondary parameters (n^d, n^b, C_ε) to capture details of the responses. This step also involved verifying that the value of h_o was adequate to fit the small-strain stiffness exhibited by monotonic tests.

The four calibrations led to eight parameter sets (four for each soil) as summarized in Table 7.3, which were named after the modeled soil followed by the calibration number (e.g., 100A_01).

7.4.1 Calibration 01: Loose tests – Monotonic response

Figures 7.4 and 7.5 compare the responses obtained from single-element simulations with PM4Sand, with those measured in monotonic CV-DSS tests with α values between 0 and 0.5 on loose samples of 100A and 33ABC, respectively. As discussed in Section 6.3, monotonic tests with $\alpha = 0 – 0.35$ exhibited strain-softening tendencies at the beginning of shearing, characterized by a transient peak shear stress with limited shear strain development, followed by a decrease in shear stresses towards a transient minimum value at which phase transformation occurred (i.e., transition from contractive to dilative behavior). Upon further shearing, those tests exhibited dilative behaviors, characterized by the development of large shear deformations and stress ratios (τ/σ'_v) converging towards the CSL. On the other hand, tests with $\alpha = 0.5$ exhibited dilative behaviors almost immediately at the beginning of shearing as their initial stress states were closer to the CSL.

The monotonic DSS data can inform the calibration of parameters that control the peak strength, phase transformation, and post-peak dilatancy. Thus, in order to capture the monotonic responses, one primary parameter (h_{po}) and two secondary parameters (n^d, n^b) were iterated until a reasonable agreement was observed between laboratory data and simulations (Figures 7.4 and 7.5). First, the parameter h_{po} was iterated to capture the transient peak shear stress observed during contraction. Then, the parameter n^d was increased from its default value of 0.10 to capture the stress ratios (τ/σ'_v) at which phase transformation occurs, while the parameter n^b was modified to capture the stress-strain response during dilation. As can be seen in Figures 7.4 and 7.5 and Table 7.3, and further elaborated in the Conclusions section, one set of calibration parameters for both soils was able to capture the experimentally recorded responses across all different static shear bias values. Additionally, the parameter C_ε, although listed under the set of parameters of Calibration 1, does not affect the monotonic response and is listed there informed from cyclic data calibrations.

7.4.2 Calibration 02: Loose tests – Cyclic response for level ground conditions

Figure 7.6 compares the liquefaction triggering curves for loose specimens of 100A and 33ABC obtained from simulations with PM4Sand, with those recorded in cyclic CV-DSS tests under level ground and uniform stress-controlled loading conditions. In this case, the parameter h_{po} was adjusted to capture the liquefaction triggering resistance exhibited by both soils. A reasonable agreement was obtained between experimental and simulated triggering curves of both soils for a range of 4 to 10 loading cycles (Figure 7.6). During the calibration process, it was noticed that the parameter n^d could be increased to capture better the slopes of the triggering curves (b-values in Figure 7.6). However, it was decided not to adjust this parameter from the one defined in Calibration 01 to honor the stress ratio at which phase transformation occurred for both soils.

Figures 7.7 and 7.8 compare the stress-strain responses and stress paths obtained from simulations with PM4Sand to those recorded in CV-DSS tests for loose specimens of 100A and 33ABC soils. The post-triggering response of cyclic CV-DSS tests in loose samples of 100A and 33ABC (Figures 7.7a and 7.8a) was characterized by the progressive accumulation of limited shear strains in each loading cycle (cyclic mobility). As previously discussed in Chapters 2 and 4, most of the post-triggering shear strains occur at near-zero effective stress, while a smaller portion of those strains occur while the soil dilates. In this case, the post-triggering shear strain accumulation was captured by adjusting two secondary parameters (n^b and C_ε), which were adjusted to obtain a reasonable agreement between experimental (Figures 7.7a and 7.8a) and simulated stress-strain responses (Figures 7.7b and 7.8b). More specifically, the parameter C_ε was modified from its default value to capture the development of shear strains at near-zero effective stress, while the parameter n^b was adjusted to capture the stress-strain response during dilation. As illustrated in Figures 7.7c and 7.8c, the default values of C_ε lead to smaller rates of shear strain accumulation than those observed in the laboratory data. Also, the use of the n^b values informed by the monotonic tests ($n^b = 0.14$) resulted in larger shear deformations during dilation (Figures 7.7d and 7.8d). For that reason, it was needed to increase the value of the n^b parameter to 0.4 (Figures 7.7b and 7.8b). As shown by parameters sets 100A-02 and 33ABC-02 in Table 7.3, differences in shear strain accumulation between both soils were reasonably captured by assigning different values to the parameter C_ε.

7.4.3 Calibration 03: Loose tests – Cyclic response for sloping ground conditions

As discussed in Chapter 6, the liquefaction triggering resistance for varying α's can be synthesized with plots of the cyclic resistance ratio or CRR (i.e., CSR to trigger liquefaction in 10 loading cycles) and static shear stress correction factors (K_α) as a function of α. Figure 7.9 presents CRR and K_α curves obtained from cyclic CV-DSS tests with $\alpha = 0 - 0.2$, and those obtained from simulations with PM4Sand. As shown in Figures 7.9a and 7.9b, simulations with parameters sets 100A-02 and 33ABC-02 tend to overestimate the triggering resistance for large α values. For Calibration 03, the values of n^b and h_{po} were adjusted from those used in Calibration 02 to capture better the CRR values under sloping ground conditions. Following this, a reasonable agreement was observed between simulated CRR curves (100A-03 and 33ABC-03 in Figure 7.9a and 7.9b) and those obtained with CV-DSS tests for α's between 0.05 and 0.20. On the other hand, the simulated K_α curves (Figure 7.9c and 7.9d) fell within the range of K_α curves typically found in the literature for loose sands (e.g., Figure 6.2 in Chapter 6), but they were above those obtained with CV-DSS tests on 100A and 33ABC soils**.**

Figures 7.10 and 7.11 compare the stress path and stress-strain responses measured in cyclic CV-DSS tests on 100A and 33ABC subjected to non-reversal loading conditions (CSR < α) with those simulated with parameter sets 100A-03 and 33ABC-03. In most cases, the stress paths were reasonably captured by PM4Sand, including the strain-softening tendencies that lead to sudden drops of σ'_V in the cycle preceding liquefaction triggering (e.g., from 50 to 20 kPa in Figure 7.10). However, simulations tended to underestimate the triggering resistances of experiments exhibiting a large number of cycles for the onset of liquefaction (e.g., larger than 40 as in the case presented in Figure 7.11). On the other hand, the accumulation of shear strains per loading cycle following triggering (i.e., $\gamma > 3\%$) exhibited by CV-DSS tests under non-reversal loading was largely overestimated by all the simulations. As discussed in Chapter 6, the accumulation of shear strains under non-reversal loadings is given by strains that develop only while the soil dilates. The parameter n^b can be used to capture the shear strains developed during dilation. However, it was found that increasing n^b to improve the capture of those strains led to overestimations of the liquefaction triggering resistance for α values between 0.1 and 0.2. Alternatively, the secondary parameter C_{kaf} can be increased from its default value to reduce the rate of shear strain accumulation observed under non-reversal loading conditions (Ziotopoulou and Boulanger 2016). However, adjusting C_{kaf} was not considered in this work, because modifying this parameter affects a broader range of behaviors for both non-reversal and reversal loading conditions.

Calibrations 03 were also evaluated in their ability to capture the accumulation of shear strain under irregular cyclic patterns. Figures 7.12 and 7.13 compare the experimentally recorded and simulated responses under two irregular cyclic loading patterns for the 100A and 33ABC soils.

Tested specimens and simulated single-elements were subjected to reversal or intermediate loading conditions (CSR ≥ α) with uniform CSR until a 3% shear strain was exceeded, after which the CSR was reduced to half of the previous CSR to apply 20 loading cycles under non-reversal loading conditions (CSR < α). After completing those 20 cycles, the CSR was increased to the value in the first stage to end the cyclic shearing with 5 loading cycles under reversal or intermediate loading conditions (CSR ≥ α). Simulations for 100A reached shear strains of about 4-5 times those observed in CV-DSS tests, while simulations for 33ABC reached strains 5-7 times those observed in CV-DSS tests. For both soils, the discrepancies are greater in the second stage, in which experiments exhibited shear strains increments of 0.1-0.25% per loading cycle, while simulations exhibited shear strain increments of about 1-3% per cycle. These results illustrate how parameter sets well-calibrated to capture the triggering resistance may lead to a significant overestimation of post-liquefaction shear deformations. For the irregular loadings presented herein, such overestimations were larger for the stage with non-reversal loading conditions. Depending on the importance of this behavior for system level simulations, further calibrations can help refine this response. Ziotopoulou and Boulanger (2016) for example presented calibrations for irregular cyclic loading that activated two secondary parameters in order to capture the non-reversal loading phase. Those were z_{max} and C_{kaf} which control the maximum value that the fabric tensor can achieve and the effect that sustained static shear stresses have on plastic modulus, respectively. This approach was outside of the scope of this paper.

7.4.4 Calibration 04: Medium dense tests – Cyclic response for level ground conditions

This calibration aimed to capture the liquefaction triggering and shear strain accumulation observed on CV-DSS tests on medium dense specimens of 100A and 33ABC soils for level-ground conditions. Similar to Calibration 02, the liquefaction triggering resistance was captured by iterating the h_{po} parameter, while the shear strain accumulation was captured by modifying the secondary parameters C_ε and n^b. The parameter h_{po} was adjusted for the simulated triggering curves to reasonably agree with experimental data (Figure 7.14), with an emphasis in the CSR required to trigger liquefaction in 10 loading cycles. The parameter C_ε was reduced from the one used in Calibrations 01-03 to capture the smaller shear strains at near-zero effective stress observed in medium dense specimens. Also, the parameter n^b was assigned to its default value to capture the stress-strain response during dilation. Comparisons between single-element simulations from Calibration 04 and experimental responses are presented in Figures 7.15 and 7.16.

Following the approach presented in Humire et al. (2021), Figure 7.17 compares the accumulation of double amplitude shear strains (γ_{DA}) in each post-triggering loading cycle obtained in simulations with PM4Sand and those measured with CV-DSS tests. As discussed in Section 7.4.2, the accumulation of shear strains for loose specimens under level ground conditions was reasonably captured with parameters sets 100A-02 and 33ABC-02. On the other hand, only the strain accumulation of 100A was reasonably captured for the simulations of medium dense tests at level ground conditions (100A-04 in Figure 7.17), as the model was unable to capture the gradual arrest in the rate of strain accumulation of medium dense samples of 33ABC (33ABC-04 in Figure 7.17). Given this limitation, the parameters C_ε and n^b of parameter set 33ABC-04 were calibrated to capture the shear strains accumulated after the application of 10 to 12 post-triggering loading cycles.

7.5 Discussion on the performance of PM4Sand

PM4Sand successfully captured the monotonic behavior and liquefaction triggering of 100A and 33ABC soils for different values of α; however, the calibration process required activating some of the secondary parameters implemented in the model. It was not possible to develop a unique set of parameters for the three calibrations targeting the behavior of loose sands, and the adjustment of two parameters (h_{po} and n^b) was necessary (Table 7.3). A good agreement for all the monotonic CV-DSS tests performed with different values of α was obtained with a single set of parameters for each soil; however, two additional calibrations were needed to capture the cyclic behavior under level- and sloping-ground conditions. The need for specific calibrations for each condition is attributed to the strain-softening tendencies exhibited by both soils. As discussed in Chapter 6, this strain-softening behavior leads to a significant decrease in the triggering resistance and, as consequence, to K_α relationships that are different to those used for the generalized calibrations of the current version of PM4Sand (Ziotopoulou and Boulanger 2016). In practical applications and depending on the availability of data, the analyst can prioritize the applicable behaviors of importance and choose which ones to emphasize during the calibration. Datasets like the ones available in this paper serve the goal of exploring the capabilities of the PM4Sand model and demonstrating avenues for constraining various secondary parameters.

The model also captured differences in the post-triggering shear strain accumulation of loose specimens of 100A and 33ABC soils for level ground conditions. This agreement was possible by adjusting the secondary parameter C_ε, which mostly controls the shear strains developed at near-zero effective stress and thus only affects the shear strain accumulation under reversal or intermediate loading conditions ($CSR \geq \alpha$). During calibrations, it was necessary to use a smaller C_ε for 33ABC than the one used for 100A to capture the differences in shear strain accumulation for both soils under such loading conditions. These results suggest that C_ε may need a new generalized calibration as a function of C_u to capture the effect of gradation on the shear strain accumulation. Conversely, the model was limited in capturing the gradual arrest of the accumulation of shear strains that is observed (1) under non-reversal loading conditions (CSR < α) for both soils, and (2) for medium dense specimens of the sand with the higher C_u. For non-reversal loadings, the shear strain accumulation can be controlled with the parameter n^b, which affects the shear strains developed during dilation. However, this value also affects liquefaction triggering resistance under sloping ground conditions, and increasing its value to capture the shear strain accumulation may lead to overestimations of the triggering resistance for cases with $\alpha > 0$. Past calibrations have demonstrated other options for controlling this behavior (Ziotopoulou and Boulanger 2016). Regardless of the approach, it is generally suggested that in the cases where secondary parameters are activated, all relevant behaviors are examined and replicated such that the analyst can make sure that all look reasonable. Discrepancies in the strain accumulation of simulated and measured data potentially suggest the need for revisiting aspects of the formulation of PM4Sand associated with the development of plastic strains during dilation. Still, this is (1) subject to the availability of further experimental data to confirm the gradual arrest on the shear strain accumulation for a broader spectrum of D_R's, loading conditions, and gradations, and (2) dependent on the importance of this behavior in the design or assessment of a geosystem (e.g., performance-based assessment for a system that undergoes deformations past the liquefaction triggering point).

7.6 Conclusions

Simulations with PM4sand successfully captured the monotonic response of loose samples under level and sloping ground conditions for both soils presented in this paper. Simulations also captured the liquefaction triggering resistance exhibited by cyclic CV-DSS tests on both soils for different α values; however, it was not possible to obtain a unique set of parameters across level and sloping ground conditions. The simulation of large post-liquefaction shear deformations required adjusting two secondary parameters implemented in the model (C_ε and n^b). However, the model could not capture the gradual arrest on the accumulation of shear strains observed under non-reversal loading conditions ($CSR< \alpha$) in both soils, and on medium dense specimens of the sand with the higher C_u. Differences in the simulated responses for each parameter set emphasize that the calibration process requires a close examination of: (1) the soil behavior under representative loading conditions at the field (e.g., static shear bias), and (2) the failure mechanisms expected at the system level to define and prioritize behaviors of interest.

The present study showed that the current formulation of PM4Sand can capture the monotonic behavior and liquefaction resistance of well-graded soils under different levels of static shear bias. One set of calibration parameters was able to capture the monotonic responses across all static shear stress bias conditions as well as across the two different gradations (calibrations 100A-01 and 33ABC-01). However, more than one set of parameters was required to capture both level and sloping ground conditions for the datasets considered herein. In addition, the calibration had to be slightly adjusted to capture the cyclic response of both gradations. While the investigation of the impacts of sloping ground conditions and gradation on the cyclic strength and post-triggering response of sands is an open research front, there are some indications that can guide the calibration and validation of constitutive models to capture these effects. Based on the results shown in this paper and in order to improve the estimation of post-liquefaction shear deformations, the PM4Sand model might benefit from: (1) a new generalized calibration for the C_ε parameter as a function of the soil gradation, and (2) a slight reformulation on the development of plastic strains during dilation to capture the gradual arrest on the accumulation of shear strains. This is assuming that site- and soil-specific lab experiments are not available for all projects so the inherent ability of a model to capture shear strain accumulations can be important. On the other hand, the establishment of robust K_a relationships as already presented in Chapter 6 will guide the selection and calibration of cyclic strengths appropriate for the boundary conditions at hand. Following that, the ability of a model like PM4Sand to reasonably replicate the dependency of cyclic strengths on static shear stress bias will determine the ability of the model to perform well in system-level simulations all while having a reasonable calibration effort. Last but not least, additional experimental data for other gradations, relative densities, and initial loading conditions are required to confirm these recommendations as well as form a validation basis for further developments.

7.7 References

Ahmed, S. S. 2021. *Study on Particle Shape, Size and Gradation Effects on the Mechanical Behavior of Coarse-Grained Soils*. PhD dissertation, University of California, Davis.

Andrus, R. D. and Stokoe II, K. H. 2000. Liquefaction Resistance of Soils from Shear-Wave Velocity. *Journal of Geotechnical and Geoenvironmental Engineering* 126(11): 1015–1025. https://doi.org/10.1061/(ASCE)1090-0241(2000)126:11(1015)

Anthi, M. and Gerolymos, N. 2019. A calibration procedure for sand plasticity modeling in earthquake engineering: Application to Ta-Ger, UBCSAND and PM4Sand. In *Earthquake Geotechnical Engineering for Protection and Development of Environment and Constructions- Proceedings of the 7th International Conference on Earthquake Geotechnical Engineering, (ICEGE 2019), June 17-20, 2019, Rome, Italy,* edited by F. Silvestri and N. Moraci. CRC Press, Taylor and Francis, London. pp. 1138–1145. https://doi.org/10.1201/9780429031274

ASTM International. 2019. *Standard Test Method for Consolidated Undrained Cyclic Direct Simple Shear Test under Constant Volume with Load Control or Displacement Control*. ASTM D8296-19. West Conshohocken, PA: ASTM International, approved November 1, 2019. https://doi.org/10.1520/D8296-19

Beaty, M. H. and Byrne, P. M. 2011. *UBCSAND constitutive model: Version 904aR. Documentation Report: UBCSAND Constitutive Model on Itasca UDM Web Site, February 2011*.

Bolton, M. D. 1986. The strength and dilatancy of sands. *Geotechnique* 36(1): 65–78. https://doi.org/10.1680/geot.1986.36.1.65

Boulanger, R. W. and Wijewickreme, D. 2019. Calibration of a constitutive model for the cyclic loading responses of Fraser River Delta silt. In *Earthquake Geotechnical Engineering for Protection and Development of Environment and Constructions- Proceedings of the 7th International Conference on Earthquake Geotechnical Engineering, (ICEGE 2019), June 17-20, 2019, Rome, Italy*, edited by F. Silvestri and N. Moraci. CRC Press, Taylor and Francis, London. pp. 121–137. https://doi.org/10.1201/9780429031274

Boulanger, R. W. and Ziotopoulou, K. 2013. Formulation of a sand plasticity plane-strain model for earthquake engineering applications. *Soil Dynamics and Earthquake Engineering* 53: 254–267. https://doi.org/https://doi.org/10.1016/j.soildyn.2013.07.006

Boulanger, R. W. and Ziotopoulou, K. 2012. *PM4Sand (version 2): A sand plasticity model for earthquake engineering applications*. Report No. UCD/CGM-12/01. Center for Geotechnical Modeling, Department of Civil and Environmental Engineering, University of California, Davis, CA.

Boulanger, R. W. and Ziotopoulou, K. 2017. *PM4Sand (version 3.1): A sand plasticity model for earthquake engineering applications*. Report No. UCD/CGM-17/01. Center for Geotechnical Modeling, Department of Civil and Environmental Engineering, University of California, Davis, CA.

Boulanger, R. W. 2003. Relating Kα to Relative State Parameter Index. *Journal of Geotechnical and Geoenvironmental Engineering* 129(8): 770–773.

Boulanger, R. W. and Ziotopoulou, K. 2018. On NDA Practices for Evaluating Liquefaction Effects. In *Geotechnical Earthquake Engineering and Soil Dynamics V: Liquefaction Triggering, Consequences, and Mitigation*, edited by S. J. Brandenberg and M. T. Manzari. Austin, TX. pp. 1–20. https://doi.org/doi:10.1061/9780784481455.001

Boulanger, R. W. and Beaty, M. H. 2016. Seismic Deformation Analyses of Embankment Dams: A Reviewer’s Checklist. In *Proceedings of 36th USSD Annual Meeting and Conference*. pp. 535–546.

Carey, T. J., DeJong, J. T., Ziotopoulou, K., Martinez, A., and Chiaradonna, A. 2021. The effects of gradation on the dynamic response of sloping ground. In *Proceedings of 20th International Conference on Soil Mechanics and Geotechnical Engineering (ICSMGE), Sydney, Australia*.

Chiaradonna, A., Ziotopoulou, K., Carey, T. J., DeJong, J. T., and Boulanger, R. W. 2021. Dynamic Behavior of Uniform Clean Sands: Evaluation of Predictive Capabilities in the Element- and the System-Level. In *Proceedings of Geo-Congress 2022, Charlotte, NC.*

Dafalias, Y. F. and Manzari, M. T. 2004. Simple Plasticity Sand Model Accounting for Fabric Change Effects. *Journal of Engineering Mechanics* 130(6): 622–634. https://doi.org/10.1061/(ASCE)0733-9399(2004)130:6(622)

Duque, J., Yang, M., Fuentes, W., Mašín, D., and Taiebat, M. 2021. Characteristic limitations of advanced plasticity and hypoplasticity models for cyclic loading of sands. *Acta Geotechnica*. https://doi.org/10.1007/s11440-021-01418-z

Electric Power Research Institute. 1993. *Guidelines for site specific ground motions, Rept. TR-102293*. Palo Alto, CA.

Giannakou, A., Travasarou, T., Ugalde, J., Chacko, J., and Byrne, M. 2011. Calibration Methodology for Liquefaction Problems Considering Level and Sloping Ground Conditions. In *Proceedings of the 5th International Conference on Earthquake Geotechnical Engineering, Santiago, Chile*.

Harder Jr., L. F. and Boulanger, R. W. 1997. Application of Kσ and Kα correction factors. In *Proceedings of the NCEER Workshop on Evaluation of Liquefaction Resistance of Soils*, edited by T. L. Youd and I. M. Idriss. National Center for Earthquake Engineering Research, SUNY, Buffalo, NY. pp. 167–190.

Humire, F., Ziotopoulou, K., and DeJong, J. T. 2021. Evaluating shear strain accumulation of sands exhibiting cyclic mobility behavior. In *Proceedings of 20th International Conference on Soil Mechanics and Geotechnical Engineering (ICSMGE), Sydney, Australia*.

Hyodo, M., Murata, H., Yasufuku, N., and Fujii, T. 1991. Undrained cyclic shear strength and residual shear strain of saturated sand by cyclic triaxial tests. *Soils and Foundations* 31(3): 60–76. https://doi.org/doi.org/10.3208/sandf1972.31.3_60

Itasca. 2020. *Fast Lagrangian Analysis of Continua, User's Guide, Version 8.1*. Itasca Consulting Group, Inc., Minneapolis, MN.

Kamai, R. 2011. *Liquefaction-Induced Shear Strain Localization Processes in Layered Soil Profiles*. PhD dissertation, University of California, Davis.

Khosravifar, A., Elgamal, A., Lu, J., and Li, J. 2018. A 3D model for earthquake-induced liquefaction triggering and post-liquefaction response. *Soil Dynamics and Earthquake Engineering* 110: 43–52. https://doi.org/10.1016/j.soildyn.2018.04.008

Pretell, R., Humire, F., and Ziotopoulou, K. 2020. On the performance of two advanced constitutive models in capturing the element response of tailings. In *Proceedings of Tailings and Mine Waste 2020*. pp. 381–392.

Reardon, R. A. 2021. *Monotonic and Cyclic Direct Simple Shear Testing of Coarse-Grained Soils*. Master's thesis, University of California, Davis.

Sturm, A. P. 2019. *On the Liquefaction Potential of Gravelly Soils: Characterization, Triggering and Performance*. PhD dissertation, University of California, Davis.

Tasiopoulou, P. and Gerolymos, N. 2016. Constitutive modeling of sand: Formulation of a new plasticity approach. *Soil Dynamics and Earthquake Engineering* 82: 205–221. https://doi.org/10.1016/j.soildyn.2015.12.014

Tasiopoulou, P., Ziotopoulou, K., Humire, F., Giannakou, A., Chacko, J., and Travasarou, T. 2020. Development and implementation of semiempirical framework for modeling postliquefaction shear deformation accumulation in sands. *Journal of Geotechnical and*

Geoenvironmental Engineering 146(1): 4019120. https://doi.org/10.1061/(ASCE)GT.1943-5606.0002179

Wichtmann, T., Fuentes, W., and Triantafyllidis, T. 2019. Inspection of three sophisticated constitutive models based on monotonic and cyclic tests on fine sand: Hypoplasticity vs. Sanisand vs. ISA. *Soil Dynamics and Earthquake Engineering* 124: 172–183. https://doi.org/10.1016/j.soildyn.2019.05.001

Yang, Z., Elgamal, A., and Parra, E. 2003. Computational Model for Cyclic Mobility and Associated Shear Deformation. *Journal of Geotechnical and Geoenvironmental Engineering* 129(12): 1119–1127. https://doi.org/10.1061/(ASCE)1090-0241(2003)129:12(1119)

Ziotopoulou, K., Maharjan, M., Boulanger, R. W., Beaty, M. H., Armstrong, R. J., and Takahashi, A. 2014. Constitutive modeling of liquefaction effects in sloping ground. In *Proceedings of the 10th U.S. National Conference on Earthquake Engineering, Anchorage, AK.*

Ziotopoulou, K. and Boulanger, R. W. 2013. Calibration and implementation of a sand plasticity plane-strain model for earthquake engineering applications. *Soil Dynamics and Earthquake Engineering* 53: 268-280, 10.1016/j.soildyn.2013.07.009

Ziotopoulou, K. and Boulanger, R. W. 2016. Plasticity modeling of liquefaction effects under sloping ground and irregular cyclic loading conditions. *Soil Dynamics and Earthquake Engineering* 84: 269–283. https://doi.org/10.1016/J.SOILDYN.2016.02.013

7.8 Tables and figures

Table 7.1. Properties of the soils used in this work (Sturm 2019): maximum and minimum void ratio (e_{max} and e_{min}), mean grain size (D_{50}), coefficient of uniformity (C_u), and coefficient of permeability (k).

Soil Name	e_{max}	e_{min}	D_{50} (mm)	C_u	k (cm/s)
100A	0.881	0.579	0.18	1.68	0.017
33ABC	0.622	0.397	0.51	4.41	0.022

Table 7.2. Summary of the calibrations conducted for each soil.

Calibration	**D_R**	**α**	**Target Response**	**Related System-Level Phenomenon**
01	40%	0.2-0.5	Monotonic response	Flow liquefaction for moderate to steep slopes
02		0	Cyclic strength and post-triggering shear strain accumulation	Cyclic mobility-induced deformations under level-ground conditions
03		0-0.2		Cyclic mobility-induced deformations under mildly sloping ground conditions
04	60-65%	0		Cyclic mobility-induced deformations under level-ground conditions

Table 7.3. Model parameters for the element level simulations of soils 100A and 33ABC with PM4Sand.

Parameter [a]	Target Behavior	Default Value	**Calibrations for 100A**				**Calibrations for 33ABC**			
			100A-01 Monotonic D_R = 40% α = 0 - 0.5	100A-02 Cyclic D_R = 40% α = 0	100A-03 Cyclic D_R = 40% α = 0 - 0.2	100A-03 Cyclic D_R = 65% α = 0	33ABC-01 Monotonic D_R = 40% α = 0 - 0.5	33ABC-02 Cyclic D_R = 40% α = 0	33ABC-03 Cyclic D_R = 40% α = 0 - 0.2	33ABC-04 Cyclic D_R = 60% α = 0
D_R	Measurement at beginning of DSS test	[b]	0.40	0.40	0.40	0.65	0.40	0.40	0.40	0.60
e_{min} e_{max}	Constrain relative state parameter	0.5 0.8	0.579 0.881				0.397 0.622			
Q R ϕ'_{cv}	Critical state line measured from TXC and DSS tests	10 1.5 33	10 1 32.5				9 0.65 34			
G_o	Shear modulus reduction and V_s correlations from literature	[b]	436	436	436	576	499	499	499	650
h_o		[c]	0.2				0.2			
h_{po}	**Liquefaction triggering and peak shear strength**	**[b]**	**0.005**	**0.05**	**0.02**	**0.015**	**0.005**	**0.018**	**0.012**	**0.002**
n^d	Phase transformation angle informed by DSS tests	0.1	0.24				0.24			
n^b	**Stress-strain behavior during dilation**	**0.5**	**0.14**	**0.4**	**0.14**	**0.5**	**0.14**	**0.4**	**0.14**	**0.5**
C_ε	Shear strain accumulation under reversal loading conditions (CSR > α)	[d]	20	20	20	0.9	1.2	1.2	1.2	0.5

[a] Other parameters were left with their preset default value.

[b] Primary input parameter without a preset default value.

[c] $h_o = (0.25+D_R)/2$

[d] $C_\varepsilon = 0.5$ if $D_R \leq 0.55$; $C_\varepsilon = 0.2$ if $D_R \geq 0.75$; $C_\varepsilon = 0.5–0.3(D_R–0.55)/0.2$ if other D_R

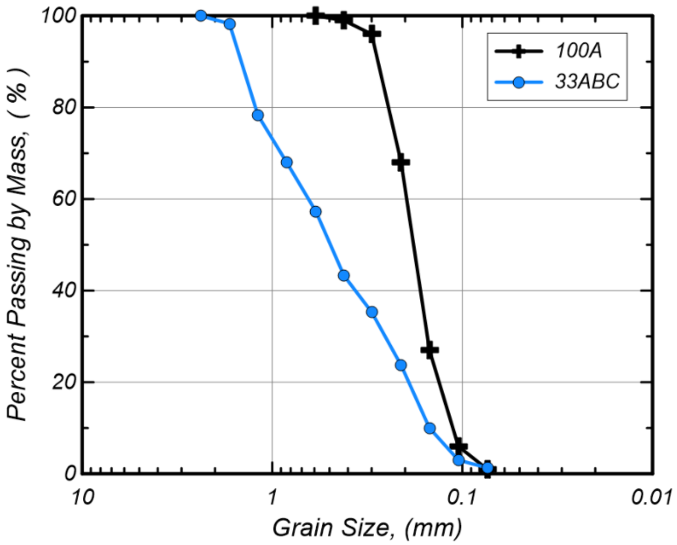

Figure 7.1. Grain size distribution of the soil mixtures presented in this work.

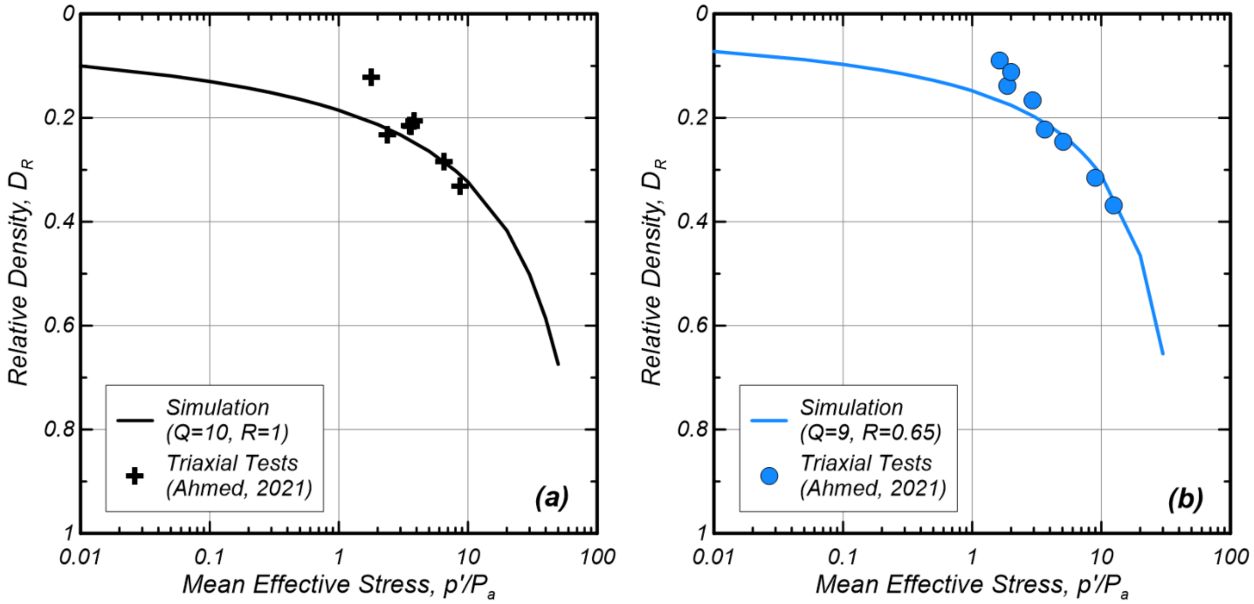

Figure 7.2. Critical state lines used for the simulations with PM4Sand, fitted to results of drained and undrained monotonic triaxial compression tests on: (a) 100A and (b) 33ABC soils.

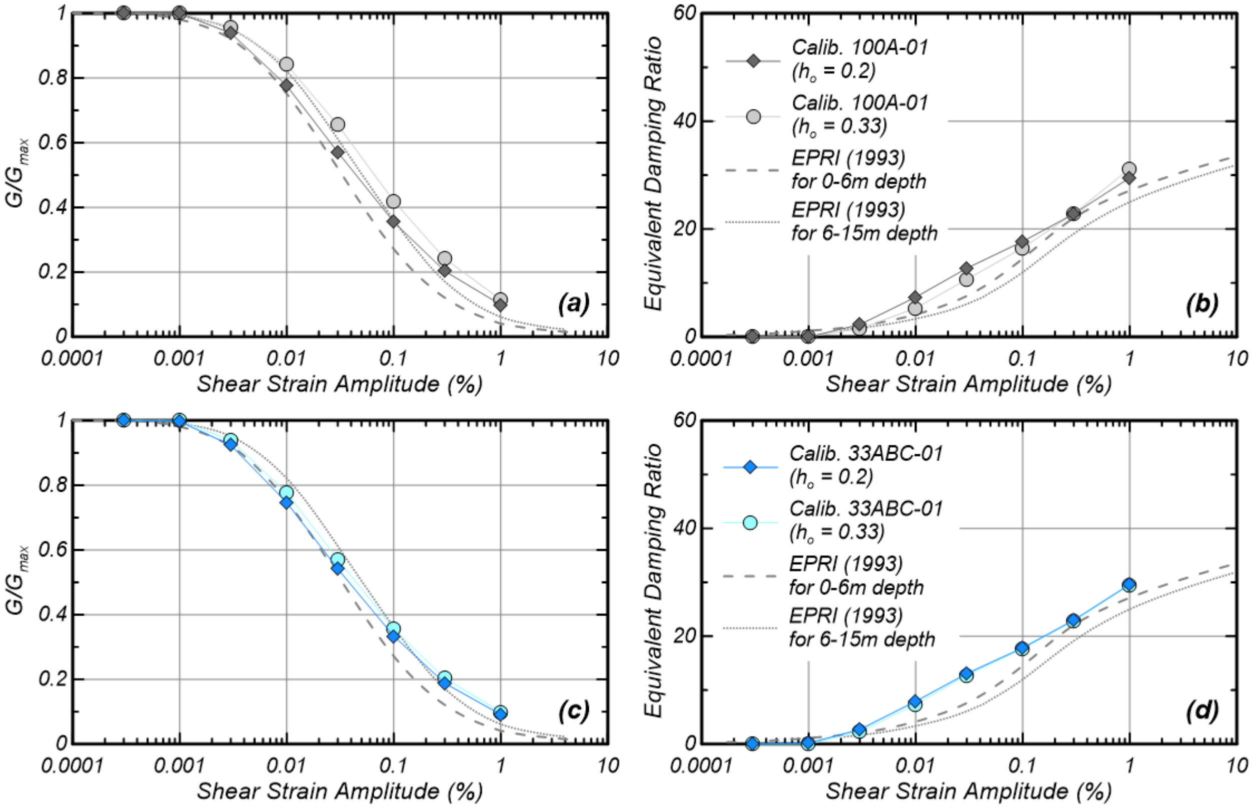

Figure 7.3. Shear modulus reduction (G/G_{max}) and equivalent damping ratio curves obtained from simulations with PM4Sand and comparison with curves recommended by EPRI (1993): (a)-(b) 100A, and (c)-(d) 33ABC. For reference, all figures include the curves for the default value of h_o as well.

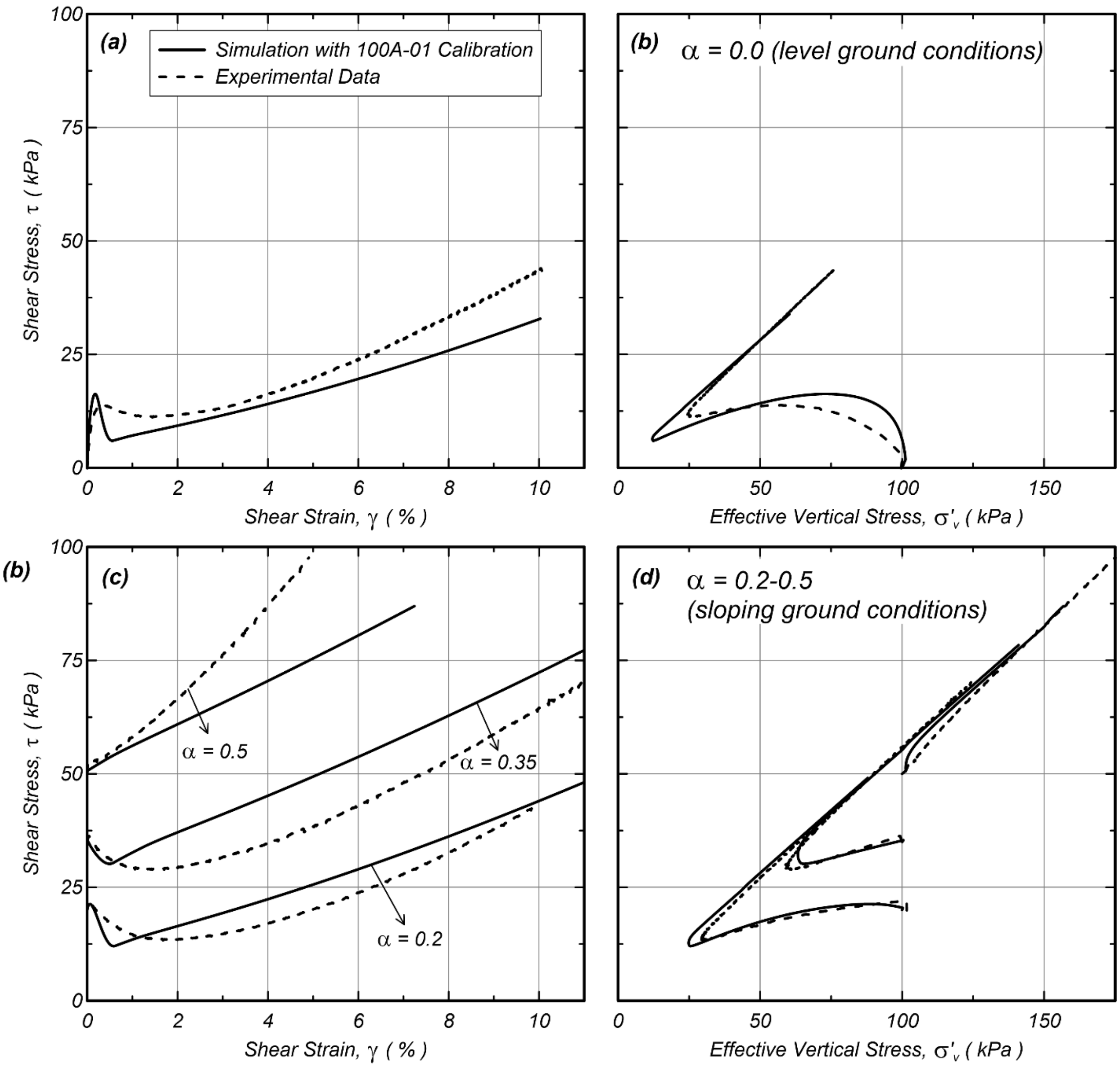

Figure 7.4. Simulations of undrained monotonic DSS tests (Calibration 100A-01) aimed to capture the response of loose specimens (D_R = 40%) of 100A soils under: (a)-(b) level ground conditions, and (c)-(d) sloping ground conditions with α = 0.2-0.5.

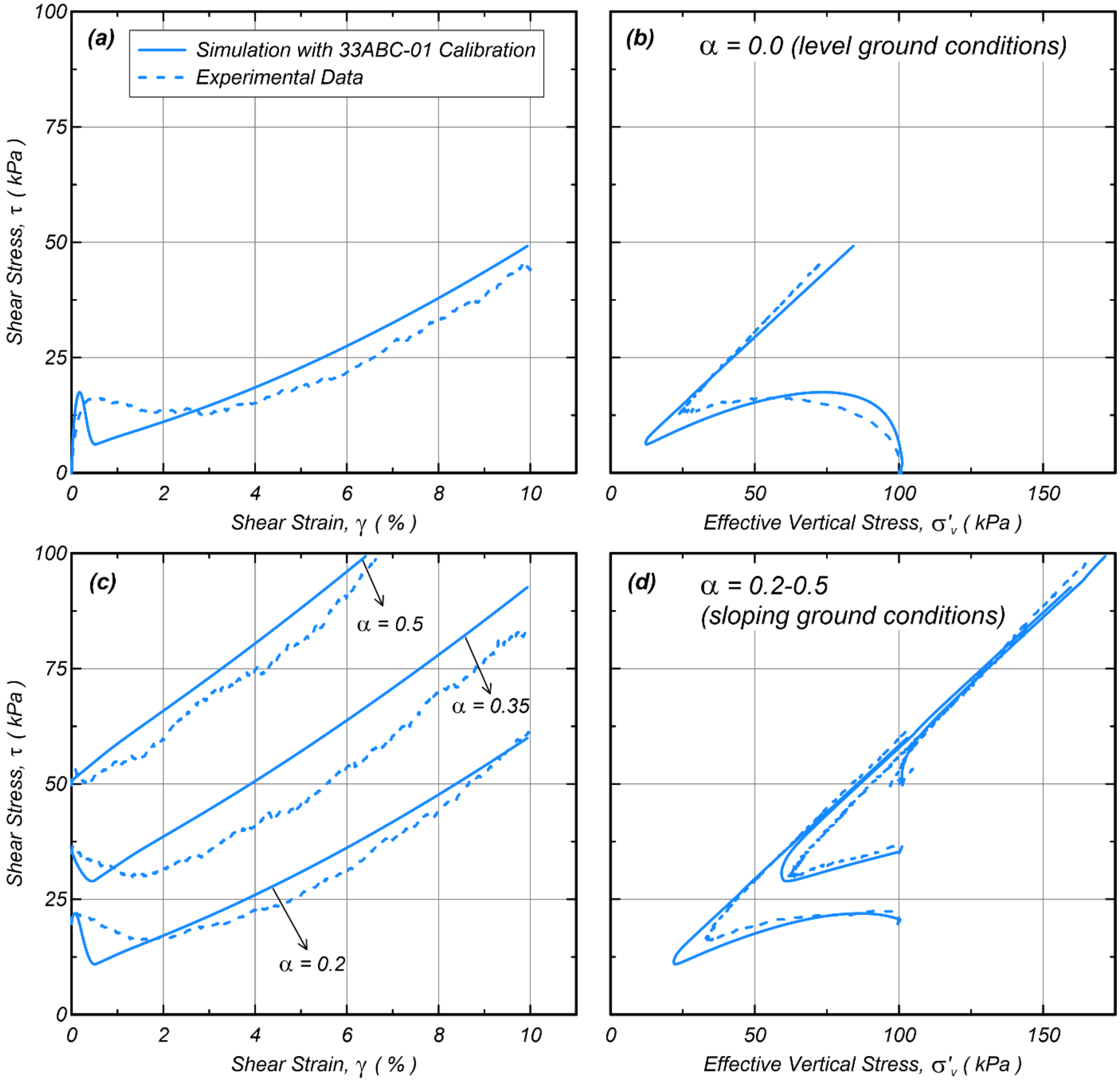

Figure 7.5. Simulations of undrained monotonic DSS tests (Calibration 33ABC-01) aimed to capture the response of loose specimens (D_R = 40%) of 33ABC soils under: (a)-(b) level ground conditions, and (c)-(d) sloping ground conditions with α = 0.2-0.5.

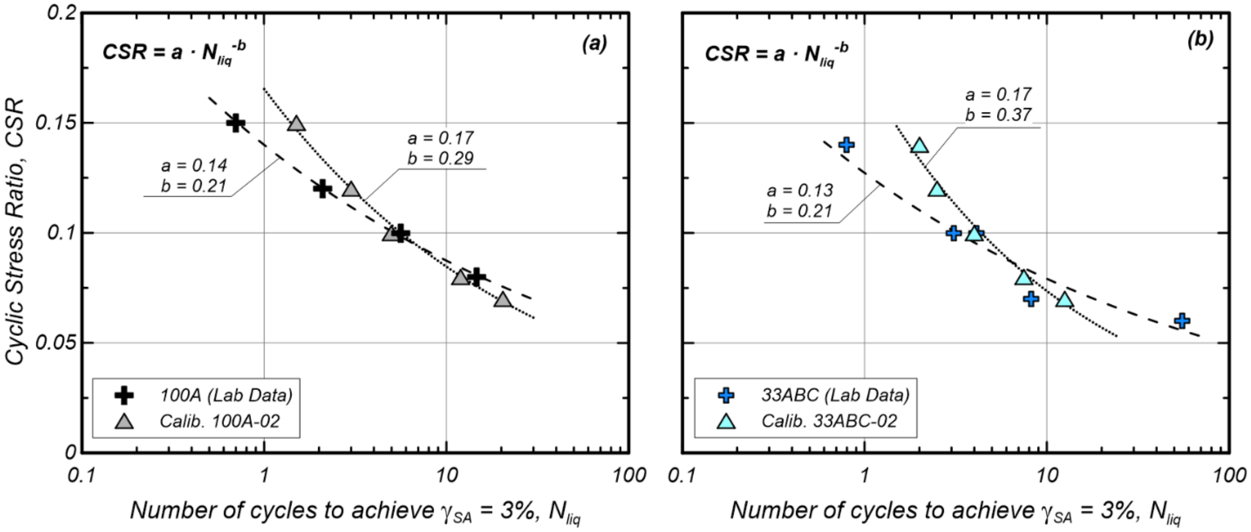

Figure 7.6. Liquefaction triggering curves obtained from DSS tests on loose specimens compared to those obtained from simulations with PM4Sand: (a) 100A and (b) 33ABC.

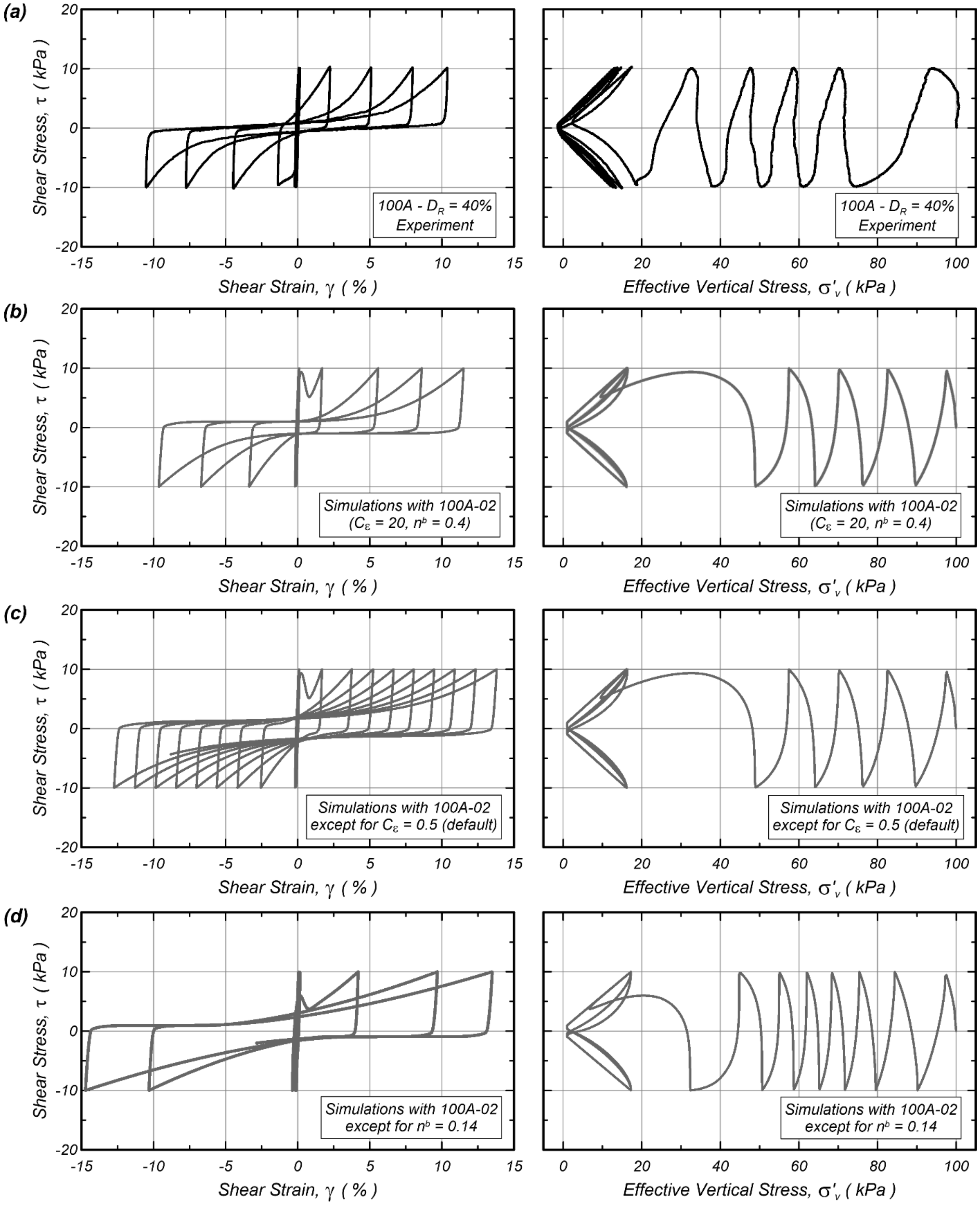

Figure 7.7. Comparison of experimental data and simulations of undrained cyclic DSS tests (Calibration 100A-02) aimed to capture the cyclic response of loose specimens (D_R = 40%) of 100A soil under level ground conditions: (a) laboratory data, (b) simulations with 100A-02, (c) simulations with 100A-02 except for C_ε = 0.5 (default value), and (d) simulations with 100A-02 except for n^b = 0.14 (same than used for Calibration 01).

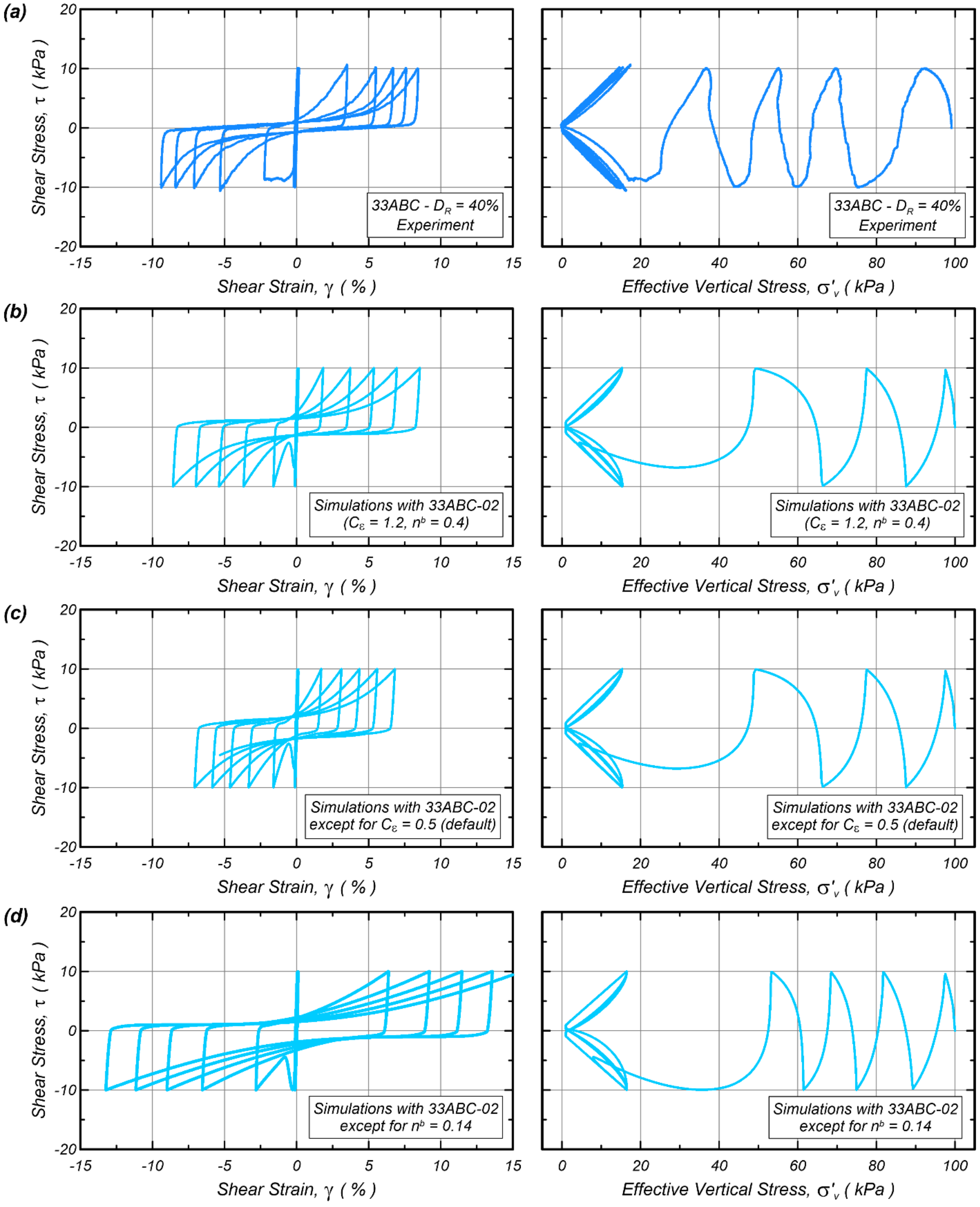

Figure 7.8. Comparison of experimental data and simulations of undrained cyclic DSS tests (Calibration 33ABC-02) aimed to capture the cyclic response of loose specimens (D_R = 40%) of 33ABC soil under level ground conditions: (a) laboratory data, (b) simulations with 33ABC-02, (c) simulations with 33ABC-02 except for C_ε = 0.5 (default value), and (d) simulations with 33ABC-02 except for n^b = 0.14 (same than used for Calibration 01).

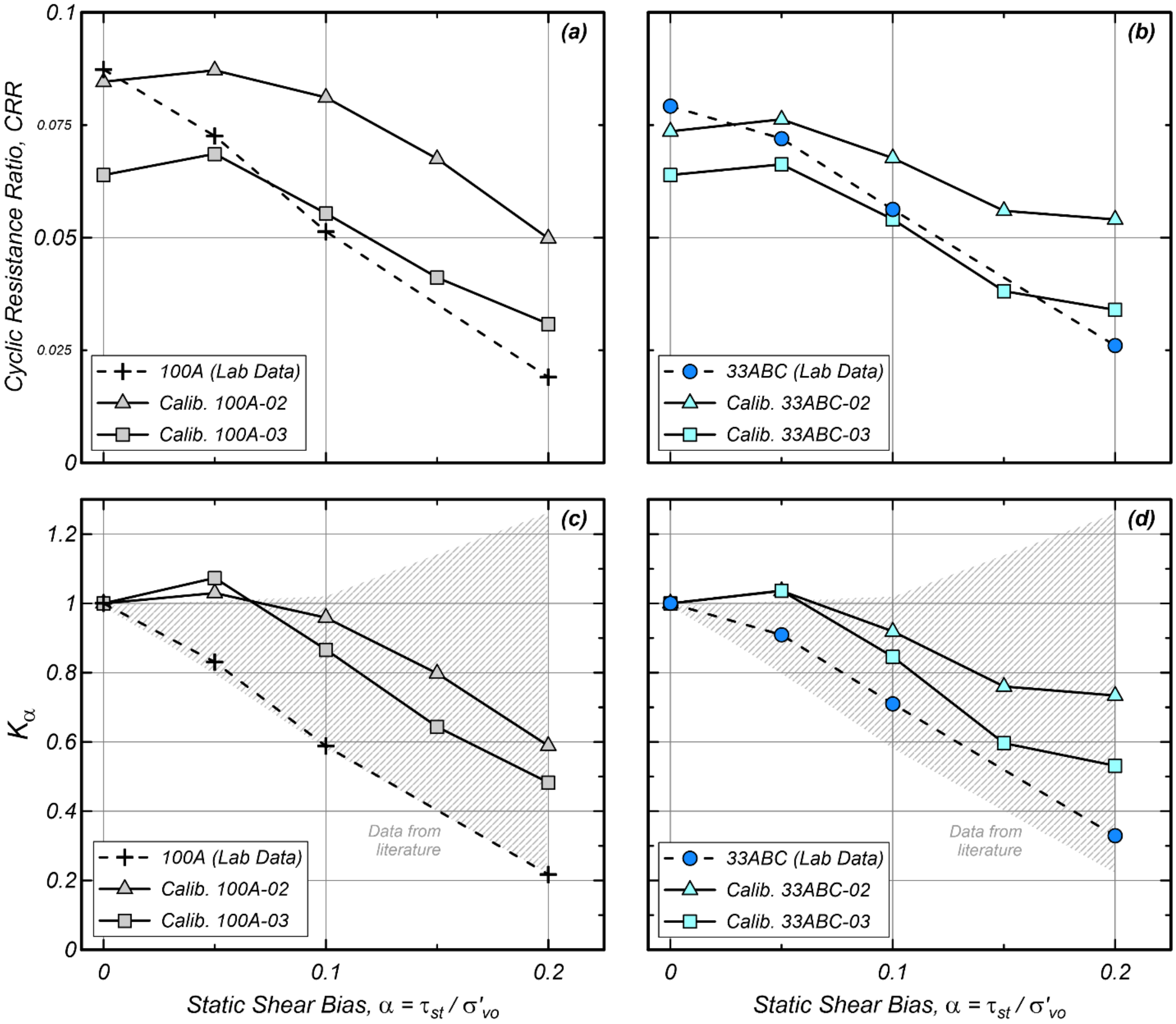

Figure 7.9. Cyclic resistance ratio (CRR, defined as the CSR to reach γ_{SA} =3% in 10 cycles) **and static shear stress correction factors (K_α)** for α values between 0 and 0.2 obtained with CV-DSS tests and simulated with PM4Sand: (a), (c) 100A and (b), (d) 33ABC.

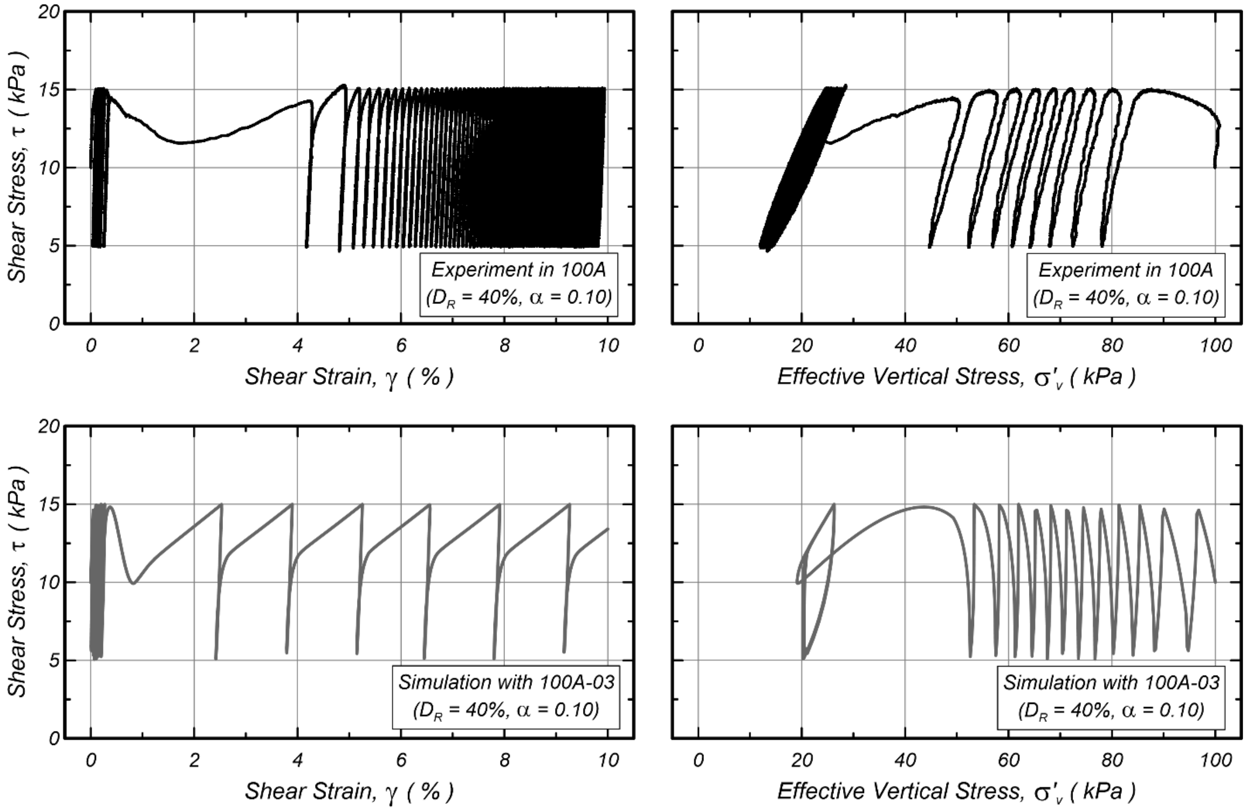

Figure 7.10. Comparison of experimental data and simulations of undrained cyclic DSS tests (Calibration 100A-03) aimed to capture the triggering response of loose specimens (D_R = 40%) of 100A soil under sloping-ground conditions (α = 0.1).

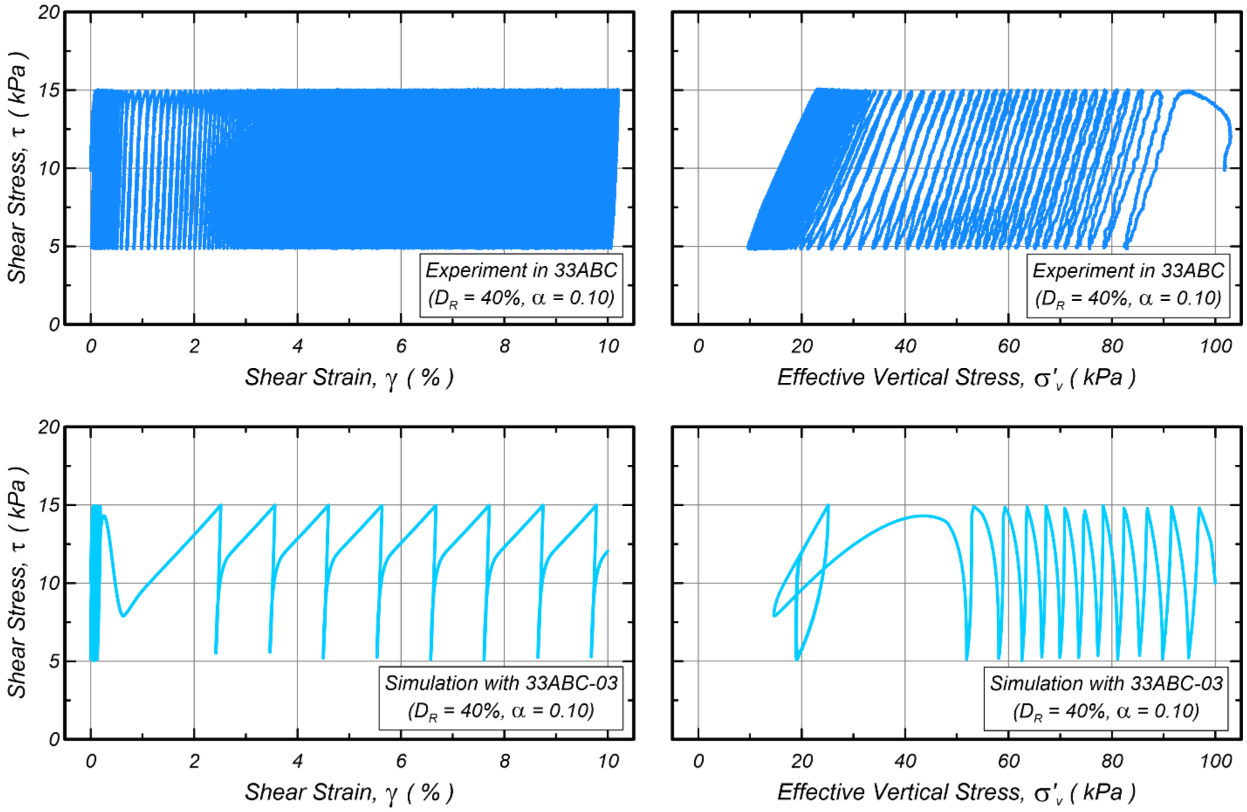

Figure 7.11. Comparison of experimental data and simulations of undrained cyclic DSS tests (Calibration 33ABC-03) aimed to capture the triggering response of loose specimens (D_R = 40%) of 100A soil under sloping-ground conditions (α = 0.1).

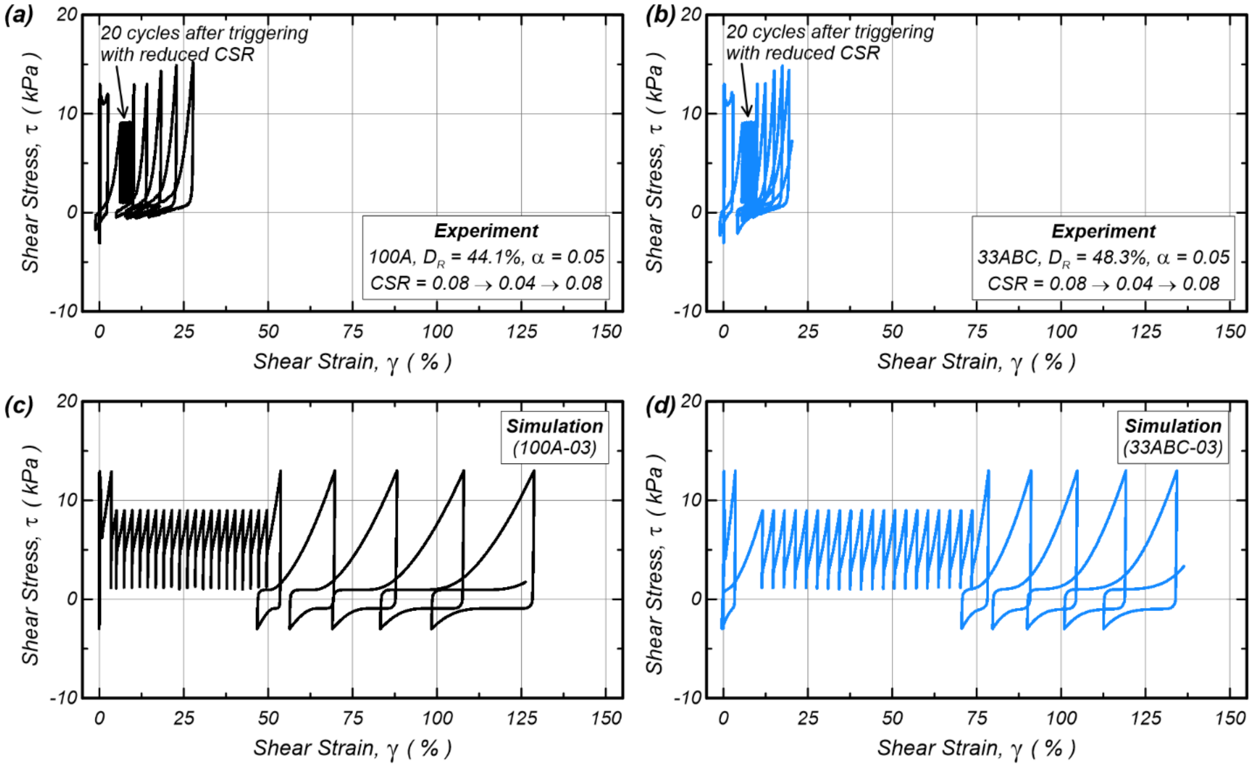

Figure 7.12. Comparison of the stress-strain responses obtained with experiments and simulations of DSS tests with α = 0.05 subjected to an irregular loading sequence (reversal → non-reversal → reversal): (a), (b) laboratory results for 100A and 33ABC, and (c), (d) simulations with parameter sets 100A-03 and 33ABC-03.

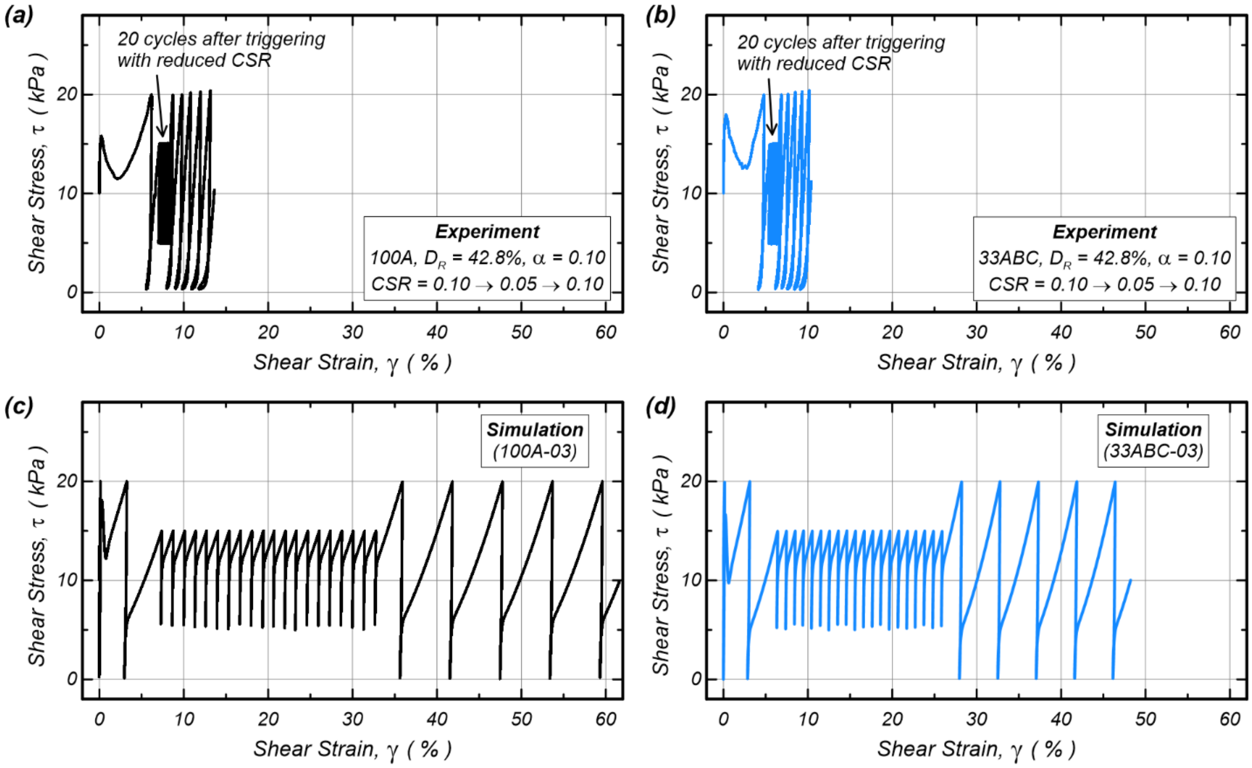

Figure 7.13. Comparison of the stress-strain responses obtained with experiments and simulations of DSS tests with α = 0.10 subjected to an irregular loading sequence (intermediate → non-reversal → intermediate): (a), (b) laboratory results for 100A and 33ABC, and (c), (d) simulations with parameter sets 100A-03 and 33ABC-03.

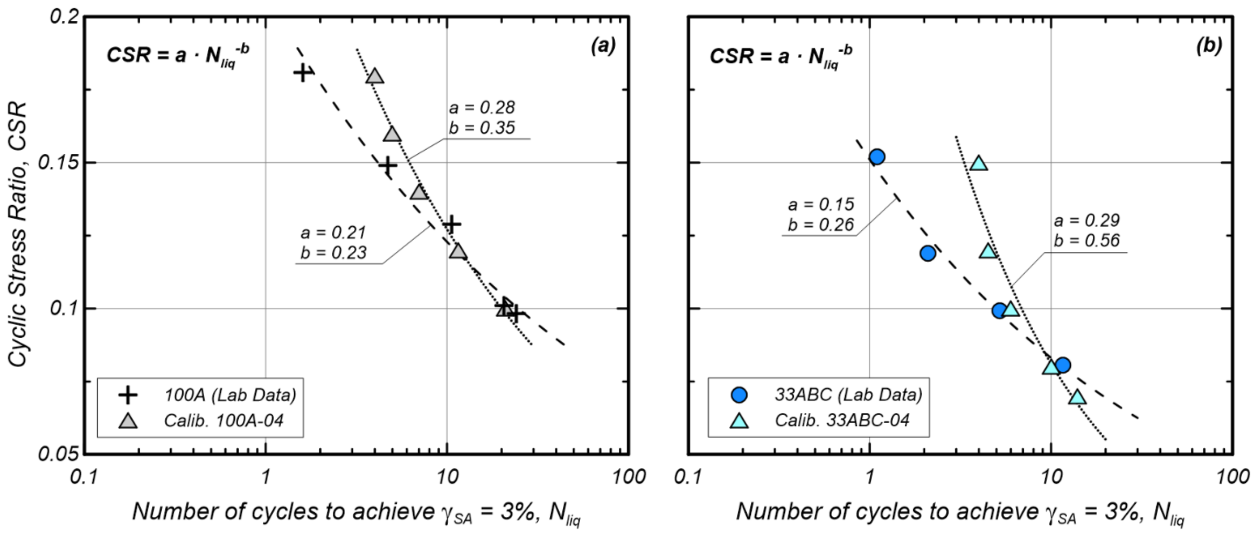

Figure 7.14. Liquefaction triggering curves obtained from DSS tests on medium dense specimens compared with those obtained from simulations with PM4Sand: (a) 100A and (b) 33ABC.

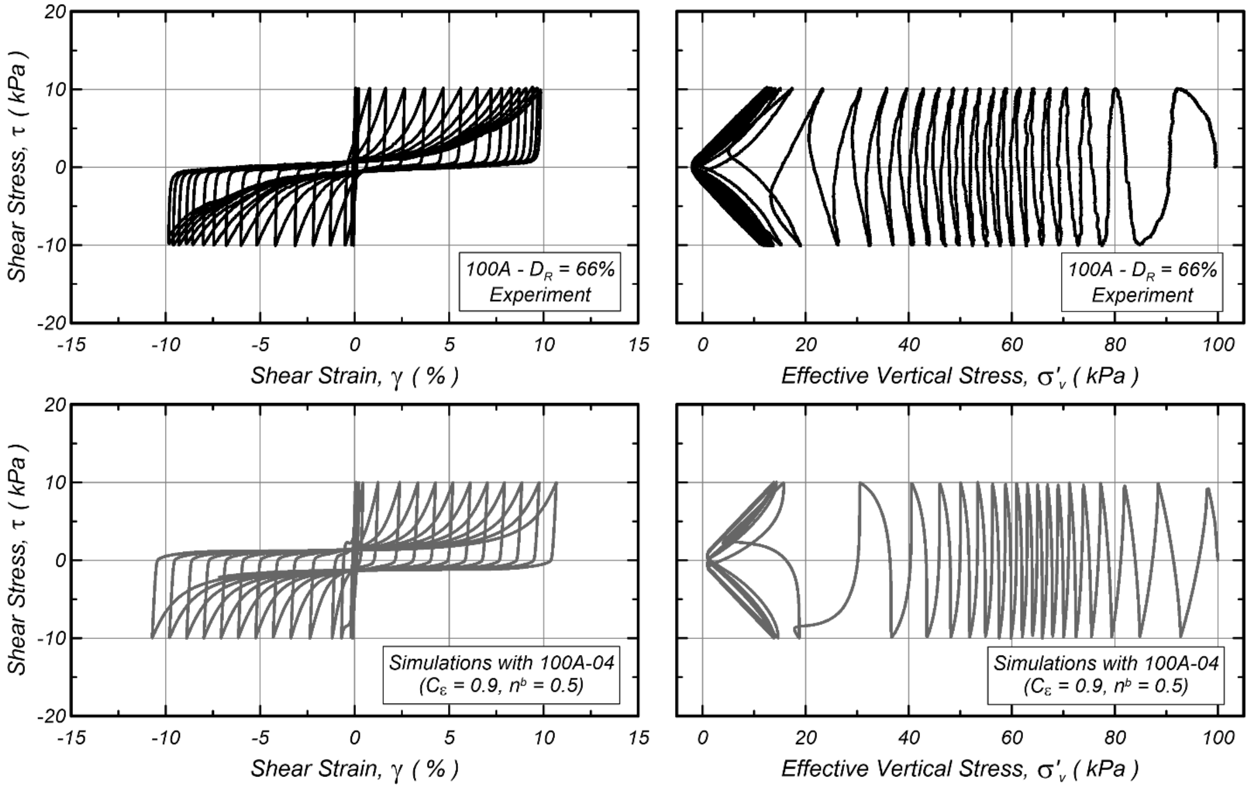

Figure 7.15. Comparison of experimental data and simulations of undrained cyclic DSS tests (Calibration 100A-04) aimed to capture the triggering response of medium dense specimens (D_R = 65%) of 100A soil under level ground conditions.

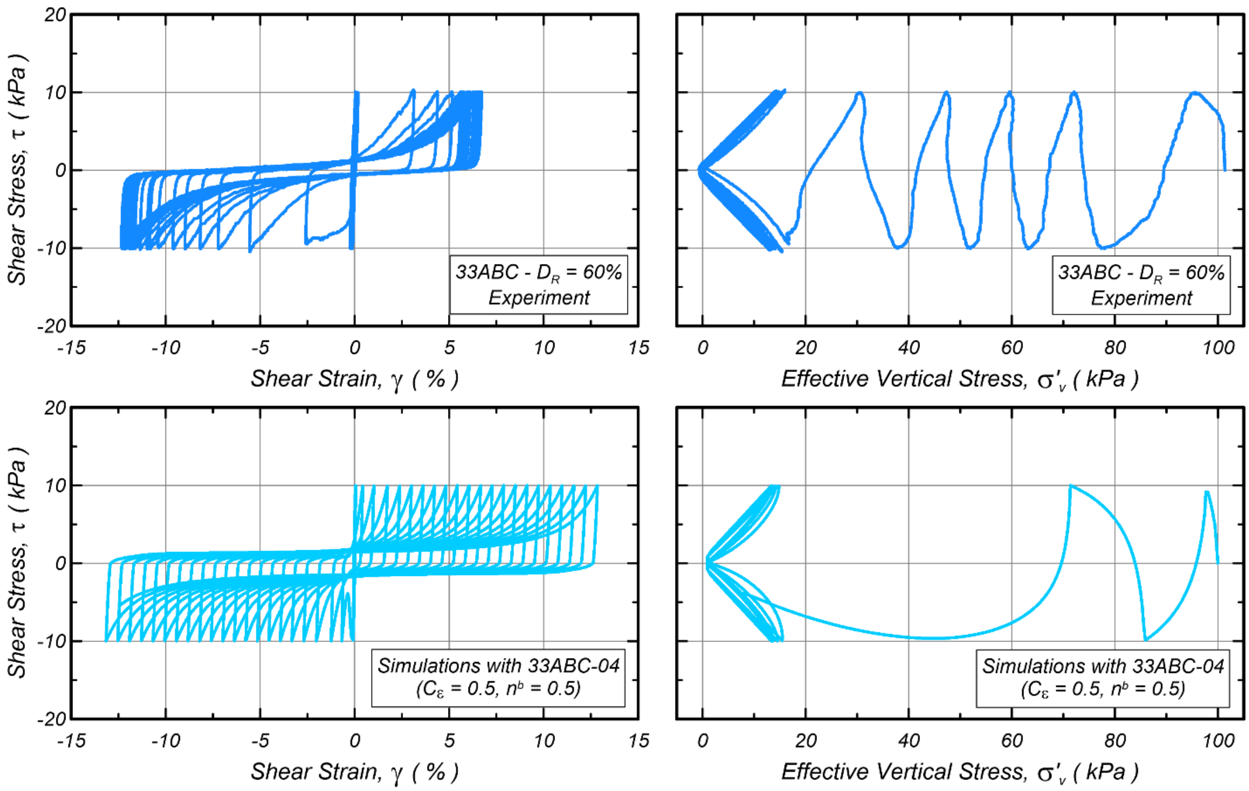

Figure 7.16. Comparison of experimental data and simulations of undrained cyclic DSS tests (Calibration 33ABC-04) aimed to capture the triggering response of medium dense specimens (D_R = 65%) of 100A soil under level ground conditions.

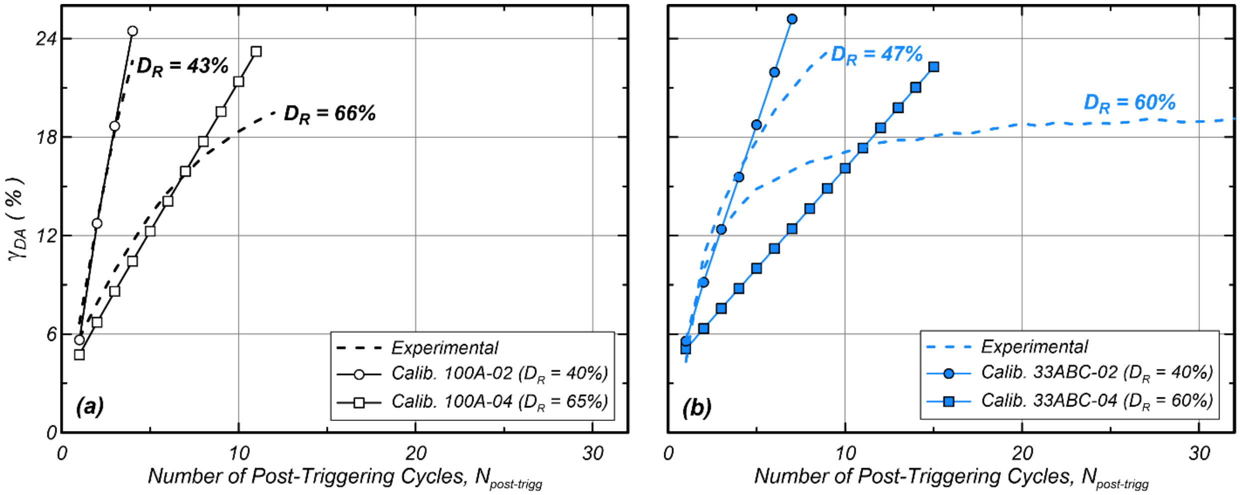

Figure. 7.17. Comparison of the accumulation of double amplitude shear strains (γ_{DA}) per loading cycle in the post-triggering regime observed on CV-DSS tests with CSR=0.10 and simulations with PM4Sand: (a) 100A and (b) 33ABC.

Chapter 8

Conclusions and future directions

This Dissertation presented an investigation on the element level response of coarse-grained soils prior and after liquefaction triggering. The first part of this Dissertation (Chapters 2-4) provided a basis for the interpretation and performance of cyclic constant-volume direct simple shear (CV-DSS) tests on coarse-grained soils, with emphasis on the process of shear strain accumulation after liquefaction is triggered. The second part (Chapters 5-7) presented a systematic investigation of the combined effects of relative density (D_R), soil gradation, and sloping ground conditions on the liquefaction triggering resistance and post-triggering shear strain accumulation. This part also included an examination of: (1) engineering correlations typically used in practice for liquefaction assessments, and (2) the capabilities of the PM4Sand constitutive model (Boulanger and Ziotopoulou, 2017) to capture key features of the cyclic response of well-graded coarse-grained soils. This section summarizes the main findings of this work and recommendations for further research.

8.1 Summary and conclusions

8.1.1 Framework for tracking the accumulation of shear strains during cyclic mobility (Chapter 2)

Based on the approach of Shamoto et al. (1997), a framework for tracking the accumulation of post-liquefaction shear strains in element laboratory tests was presented. The shear strain generated within each post-triggering loading cycle was decoupled in two components: the shear strain at near-zero effective stress, denoted by γ_0, and the shear strain that occurs during dilation, denoted by γ_d. A critical effective vertical stress $\sigma'_{v,crit}$ is considered as the limit between γ_0 and γ_d. The framework was successfully applied in two undrained cyclic experiments (direct simple shear and triaxial tests). According to the analysis results, γ_d is triggered when the specimen starts exhibiting dilative behavior, and monotonically increases until it reaches a saturation value (γ_d^{sat}) at liquefaction triggering or few cycles after that. On the other hand, γ_0 initiates at liquefaction triggering and its evolution per loading cycle follows an almost linear trend in the first few cycles following liquefaction triggering.

The evolution of different fabric descriptors in previous Discrete Element Modeling (DEM) works (Wang and Wei 2016; Wang et al. 2016; Wei et al. 2018) was compared to the evolution of γ_0 and γ_d observed in the experimental data. Despite contact-based descriptors being the most straightforward to work with, they provide limited information during the post-liquefaction stage. For example, the coordination number shows no correlation with the accumulation of γ_0 during cyclic mobility. Conversely, void-based and distance-based fabric descriptors seem to have better relationship with the development of post-liquefaction shear strains.

8.1.2 Development and evaluation of pre-conditioning protocols for sand specimens in constant-volume cyclic direct simple shear tests (Chapter 3)

A pre-conditioning protocol to effectively transfer shear stresses to sand specimens with textured end platens was required for the CV-DSS tests presented in this Dissertation. This protocol involved the application of strain-controlled drained cycles prior to consolidation to the target overburden stress. The number of pre-conditioning drained cycles ($N_{pre\text{-}cond}$) required to ensure specimen engagement was determined by: (1) analyzing changes in D_R resulting from the application of drained cycles, and (2) comparing the number of loading cycles required to trigger liquefaction (N_{liq}) to past experimental data available for the same tested material. A pre-conditioning phase consisting of the application of 115 strain-controlled drained cycles (0.045% shear strain amplitude) under a vertical effective stress of 25 kPa was found to effectively engage sand specimens at the top platen-sand interface, without significantly affecting the stress-strain response of reconstituted Ottawa F-65 sand specimens as suggested by the consistency between the achieved data and the results of similar past studies. Although the identified pre-conditioning protocol is specific to the materials, equipment, and procedures used in this study, recommendations are provided which can be used to develop similar procedures for tests involving other conditions including textured platens with varying geometries, other equipment and preparation procedures, and different sandy soil types.

While pre-conditioning sequences can improve specimen engagement at platen-sand interfaces, pre-conditioning can also result in significant changes in subsequent soil responses. These effects can include changes in specimen volumetric tendencies during the onset of undrained cyclic loading, such as the case when pre-conditioning is applied at a vertical stress similar to the target consolidation stress, as well as dramatic increases in triggering resistances, such as the case when an excessive number of pre-conditioning drained cycles is applied. The selection of pre-conditioning procedures should always be evaluated with reference to a testing plan's primary objectives and scope in order to ensure that its effects on the soil behaviors of interest (e.g., liquefaction resistance) are more fully understood.

8.1.3 Mechanisms of shear strain accumulation in laboratory experiments on sands exhibiting cyclic mobility behavior (Chapter 4)

A series of CV-DSS tests were performed to investigate the accumulation of shear strains in clean uniform sands undergoing cyclic mobility for a broad range of D_R's and loading conditions. In the majority of the experiments under uniform loading, the accumulation of shear strains per loading cycle was characterized by a monotonically increasing trend following initial liquefaction with an almost constant rate of shear strain accumulation in the post-triggering regime (γ_{DA}>6%). In experiments performed on denser specimens (D_R = 65-80%), the rate of shear strain accumulation per loading cycle was found to be gradually decreasing. Experiments under irregular loading comprised of uniform loading stages of a varying amplitude each, showed that shear strains developed in each loading stage depend on: (1) the cyclic stress amplitude (τ_{cyc}) of the current stage, and (2) the shear strains developed in previous loading stages.

The framework proposed by Tasiopoulou et al. (2020) was implemented to investigate the effect of different factors on the shear strain accumulation for tests conducted under uniform loading conditions. The results confirmed the observations of Tasiopoulou et al. (2020) regarding the dependency of the rate of post-triggering shear strain accumulation on the D_R of the specimen and τ_{cyc}. Compliance rates (i.e., rate of shear strain accumulation normalized by τ_{cyc}) evaluated in this work exhibited trends similar to those obtained from other experimental databases available in the literature for the same tested material but with other testing devices. Testing results also showed that increasing the effective overburden stress (σ'_{vo}) can affect the rate of shear strain accumulation, as shown by the series of tests performed under 400 kPa, which resulted in smaller compliance rates compared to those obtained under lower σ'_{vo} values (50 and 100 kPa). The decrease in compliance rate observed for tests at 400 kPa was explained by the shear strains in those tests being controlled by strains developed when the soil is dilating (i.e., regaining stiffness).

The framework presented in Chapter 2 was implemented to examine the evolution of γ_d and γ_0 in the post-triggering regime. Results confirmed previous empirical observations about: (1) the evolution of γ_d tending to stabilize after liquefaction triggering, and (2) the monotonically increasing trend of γ_0 after triggering. Similar to the experimental results presented in Shamoto et al. (1997), the tests performed in this work showed that the process of shear strain accumulation is governed by the development of γ_0, whose magnitude depends on the maximum shear strain developed in the previous half loading cycle ($\gamma_{DA,prev}$). The results also showed that γ_d depends on τ_{cyc} and the relative density of the specimen with similar functional dependencies to those obtained for the compliance rate. Combined, the quasi-stabilization of γ_d and the dependency of γ_0 on $\gamma_{DA,prev}$ explain the gradual decrease and eventual saturation of the rate of shear strain accumulation per loading cycle observed on dense specimens.

8.1.4 Effect of gradation and grain size on the liquefaction and post-liquefaction behavior of coarse-grained soils (Chapter 5)

A series of CV-DSS tests were performed to systematically investigate the effect of gradation and grain size on the liquefaction behavior of coarse-grained soils. The testing plan considered four clean uniform coarse-grained soils with different median grain sizes (D_{50}) that were sourced from the same natural deposit, and were combined to form three soil mixtures with different coefficients of uniformities (C_u). Results of CV-DSS tests were synthesized to evaluate the effect of both D_{50} and C_u on the liquefaction triggering resistance, shear strain accumulation and post-liquefaction reconsolidation strains. The main findings from this testing plan were:

- The effects of C_u and D_{50} on the liquefaction triggering resistance were found to depend on the relative density at which they are compared. Results of loose ($D_R \approx 40\%$) and medium dense specimens ($D_R \approx 65\%$) showed a decrease on the triggering resistance while increasing both C_u and D_{50}, but such decreases were more significant at high relative densities. On the other hand, similar triggering resistances were obtained when comparing results of very loose specimens ($D_R \approx 25\%$) for soils with different C_u and D_{50} values.

These differences were explained by the decrease on the degree of strain softening while increasing both C_u and D_{50}, which affects the number of cycles to trigger liquefaction on very loose specimens but has a negligible effect on denser samples.

- The triggering resistances of well-graded mixes were found to be closer to those obtained when testing only their coarser constituents at similar relative densities, which confirms that the pre-triggering behavior of well-graded coarse-grained soils is mostly controlled by their coarser particles and the smaller particles behave as “floaters” during shearing. The decrease of the liquefaction resistance while increasing C_u but maintaining the same void ratio is also explained by the presence of smaller particles that increase the packing efficiency, but do not contribute to the load-bearing stability of the grain assembly.
- Following liquefaction triggering, specimens of well-graded coarse-grained soils exhibited a reduction on the shear strains developed at near-zero effective stress, which led to a decrease of the rate of shear strain accumulation on loose specimens ($D_R \approx 40\%$), and an early arrest in the strain accumulation after exceeding a certain strain threshold on medium dense specimens ($D_R \approx 60\%$). Such effects on the shear strain accumulation can be explained by the smaller amount of voids in the granular assembly of well-graded soils and, thus, the availability of less room for particle rearrangement during shearing.
- Additionally, an increase in D_{50} led to a reduction in the rate of shear strain accumulation per loading cycle for both loose and medium dense specimens. This reduction in the strain accumulation was attributed to an enhanced dilation in the post-triggering regime while increasing grain size, which was confirmed by post-cyclic monotonic CV-DSS tests performed within this work.

- An increase in C_u led to a decrease of post-liquefaction volumetric strains due to reconsolidation, while changes in D_{50} had little effect on such strains. The effect of C_u can be attributed to a higher particle packing efficiency while increasing gradation, which hinders the particle rearrangement during reconsolidation.

8.1.5 Undrained monotonic and cyclic response of loose sands with two different gradations under sloping ground conditions (Chapter 6)

A series of CV-DSS tests were performed to investigate the effect of two different gradations on the monotonic and cyclic response of loose sands under sloping ground conditions. The testing plan considered different initial static shear stress ratios ($\alpha = 0$ to 0.5), and two sands with different coefficients of uniformity ($C_u = 1.68$ and 4.41) that were composed of soils sourced from the same natural deposit. The main findings from this testing plan were:

- The undrained monotonic response on the majority of the CV-DSS tests presented herein was characterized by a limited strain-softening at the beginning of shearing ($\gamma < 2$-3%). The degree of strain-softening was found to be more dramatic for the CV-DSS tests with α values between 0.2 and 0.35 as those tests yield to shear stresses below the static shear stress. An increase in gradation resulted in a slight reduction of the degree of strain-softening, which was delineated from comparisons between stress-strain responses, peak values, and strain-softening metrics. After transitioning from contractive to dilative behavior, an increase in gradation led to more dilative response for α values between 0.2 and 0.35. For steeper slope conditions, clean uniform sands may exhibit a more dilative response than well-graded sands as their initial stress conditions may be closer to the critical state line.

- The cyclic response under reversal (CSR > α) and intermediate (CSR = α) loading conditions was characterized by a progressive accumulation of shear strains in each loading cycle. The shear strain increments in each loading cycle decrease with increasing gradation for both loading conditions. This decrease was attributed to the development of smaller shear strains at near-zero effective stress of the soil with the higher C_u. On the other hand, the response under non-reversal (CSR < α) loading conditions was characterized by a limited development of shear strains, with no major differences between both soils. It was interpreted that under non-reversal loading conditions, the soil matrix remains largely stable while accumulating minor strains in the direction of the static shear stress bias due to incremental particle rearrangement. These observations were confirmed by CV-DSS tests performed under cyclic irregular loading conditions.
- An increase in the α values led to a decrease in the liquefaction triggering resistance (defined as γ_{SA}=3%) for both soils; however, the decrease was more significant for the soil with the lower C_u value. These differences were attributed to the higher potential of strain-softening of that soil, which in turn led to a larger reduction of effective vertical stresses in the cycle preceding liquefaction triggering. The strain-softening tendencies of both soils also affected the patterns of pore pressure generation per loading cycle; however, a correlation between these patterns and soil gradation was not found.

8.1.6 Modeling the element response of two sands with different gradations under level and sloping ground loading conditions with PM4Sand (Chapter 7)

Simulations with PM4sand successfully captured the monotonic response of loose samples under level and sloping ground conditions for both soils presented in this Chapter. Simulations also captured the liquefaction triggering resistance exhibited by cyclic CV-DSS tests on both soils for different α values; however, it was not possible to obtain a unique set of parameters across level and sloping ground conditions. The simulation of large post-liquefaction shear deformations required adjusting two secondary parameters implemented in the model (C_ε and n^b). However, the model could not capture the gradual arrest on the accumulation of shear strains observed under non-reversal loading conditions (CSR< α) in both soils, and on medium dense specimens of the sand with the higher C_u. Differences in the simulated responses for each parameter set emphasize that the calibration process requires a close examination of: (1) the soil behavior under representative loading conditions at the field (e.g., static shear bias), and (2) the failure mechanisms expected at the system level to define and prioritize behaviors of interest.

8.2 Future directions

This section recommends future research directions that may resolve some of the limitations and knowledge gaps identified in this Dissertation, but also may contribute towards further developments and improvements in: (i) laboratory testing equipment, (ii) the understanding of the fundamental mechanisms and factors controlling liquefaction-related behaviors, and (iii) correlations and tools for liquefaction assessments in engineering practice. The recommended future directions include the following:

1) As discussed along this Dissertation, responses measured with CV-DSS tests may be affected by: (1) slippages at the top platen and sand specimen interface (Chapter 3), and (2) boundary effects (e.g., rotation of specimen, arching in specimen corners) accentuated at high shear strain levels (Chapter 4). Further work is required to define the extent to which such limitations affect the responses measured in CV-DSS tests, and to improve DSS testing equipment to mitigate these issues. Investigations on the compatibility between sand grain sizes and different platens

geometries (e.g., pinned, ridged, grooved) and/or surface roughness may contribute to improve current testing capabilities, and may lead to definitions of optimal geometries and/or roughness that can be specified in DSS testing standards (e.g., ASTM 2019). Other aspects that need attention in future investigations are the effects of specimen size, lateral confinement systems (e.g., stacked rings, reinforced membranes, or combinations of these two), and vertical compliance on the response measured by monotonic and cyclic DSS tests on sand specimens with different gradations.

2) The development of large post-liquefaction shear deformations can be further investigated with torsional shear tests on hollow cylindrical specimens, which have been used in previous works to investigate the behavior of clean uniform sands to shear strains of 50% and even higher (e.g., Kiyota et al. 2008; Chiaro et al. 2013). In that sense, hollow cylinder torsional tests could be used to experimentally capture the cyclic mobility behavior at large strain levels across the broader spectrum of relative densities, loading conditions, and grain properties. However, future investigations must consider that the measured responses at large strain levels with this type of testing can be affected by the development of strain localizations, changes in the specimen’s cross-sectional area during shearing, and local drainage through membrane wrinkles (Chiaro et al. 2013; Koseki 2021). A newer testing device named stacked-ring torsional shear apparatus (Wahyudi et al. 2016) has been proposed to overcome those limitations, but further work is required to reduce the large amount of friction generated within this device for its use at large shear strain levels.
3) Findings from previous works with DEM (e.g., Wang et al. 2016; Kuei 2019) were used to explain the particle-level mechanisms associated to the development of large post-liquefaction shear deformations (Chapters 2 and 4), and the effect of gradation on the cyclic response of

coarse-grained soils (Chapter 5). Still, further fundamental investigations are needed to fully elucidate the particle-level behavior (i.e., fabric evolution) prior and after liquefaction triggering, and its interdependency with the element-level response. Also, further simulations of undrained cyclic element tests with DEM under a broad range of gradations and loading conditions may resolve the inconsistencies in the literature described in Chapter 5 regarding the effect of gradation on the liquefaction behavior. Observations of the particle-level behavior from DEM simulations can be experimentally validated with laboratory element testing devices implemented with X-Ray computed tomography, which have been recently used to measure the fabric evolution of sand specimens during shearing (e.g., Wiebicke et al. 2020).

4) Findings about the effect of C_u and D_{50} on the liquefaction behavior (Chapters 5 and 6) are constrained by the factors held constant in the testing plan (e.g., effective overburden stress, sub-angular grain shape) and the testing device used in this investigation. Further cyclic laboratory tests are needed to: (1) assess the validity of these findings for soils with different intrinsic grain properties (e.g., grain angularity, crushability), other modes of shearing (e.g., torsional, triaxial), and other sample preparation methods (e.g., moist tamping), (2) extend the trends identified in this study for coarse-grained soils with higher C_u and D_{50} values, and (3) elucidate the combined effect of both C_u and D_{50} with other factors such as the fines content and initial stress state. Further experimental work is also required to identify the factors contributing to the strain-softening tendencies described in Chapter 6, which were found to largely affect the liquefaction behavior under sloping ground conditions. Additional monotonic CV-DSS and undrained triaxial tests on coarse-grained soils with varying intrinsic grain properties and gradations may provide insights of the factors controlling strain-softening tendencies.

5) Results from this work show that correlations that do not explicitly consider the effect of varying C_u and D_{50} may not be appropriate for the assessment of liquefaction effects on well-graded coarse-grained soils. Correction factors to adjust the liquefaction triggering resistance to a reference clean uniform sand may help to account for the effects of soil gradation. Examples of envisioned correction factors for varying C_u and D_{50} values are provided in Figure 8.1, which were developed based on the experimental data presented in Chapter 5 and previous efforts in the literature (Lee and Fitton 1969; Vaid et al. 1990; Kokusho et al. 2004; Doygun et al. 2019). Still, additional experimental work is needed (1) to establish the trends presented in Chapter 5 to an extent that correction factors for varying C_u and D_{50} can be formulated, and (2) to isolate the effect of other grain properties that were outside the scope of this Dissertation (e.g., grain angularity, crushability). Also, it is recommended to evaluate these correction factors as functions of other metrics, such as the void ratio, that could be more appropriate to incorporate the effects of varying gradation (Figure 8.2).

6) Results presented in Chapter 6 showed a slight increase in sloping ground correction factors (K_α) while increasing C_u. It is hypothesized that this increase may be more significant for sands with wider gradations as they are expected to have a smaller degree of strain-softening. In that sense, further experimental work is required to evaluate K_α factors for wider gradations, and to study the effect of other factors such as the fine content, sample preparation or testing device (e.g., triaxial, torsional shear) on K_α relationships. Also, additional laboratory test results for a broader range of overburden stress levels are recommended to: (1) evaluate the effect of gradation on overburden stress correction factors (K_σ), and (2) mapping the combined effects of gradation and sloping ground conditions within a critical state framework.

7) Newer findings on the effects of gradation on the liquefaction and post-liquefaction behaviors of coarse-grained soils should be used towards the improvement of current constitutive modeling capabilities. The systematic calibration and validation of constitutive models such as PM4Sand (Boulanger and Ziotopoulou 2017) or PDMY03 (Khosravifar et al. 2018) against new experimental data and correlations may lead to: (1) refinements of their formulations, (2) updated generalized calibrations, and (3) calibration protocols for their use in engineering practice. For example, the calibrations presented in Chapter 7 suggested that PM4Sand model might benefit from: (i) a new generalized calibration of the C_ε parameter as a function of the soil gradation, and (ii) a slight reformulation on the development of plastic strains during dilation to capture the gradual arrest on the accumulation of shear strains. However, those recommendations must be confirmed with additional experimental data for other gradations, relative densities, and initial loading conditions.

8.3 References

ASTM International. 2019. *Standard Test Method for Consolidated Undrained Cyclic Direct Simple Shear Test under Constant Volume with Load Control or Displacement Control*. ASTM D8296-19. West Conshohocken, PA: ASTM International, approved November 1, 2019. https://doi.org/10.1520/D8296-19

Boulanger, R. W. and Ziotopoulou, K. 2017. *PM4Sand (version 3.1): A sand plasticity model for earthquake engineering applications*. Report No. UCD/CGM-17/01. Center for Geotechnical Modeling, Department of Civil and Environmental Engineering, University of California, Davis, CA.

Chiaro, G., Kiyota, T., and Koseki, J. 2013. Strain localization characteristics of loose saturated Toyoura sand in undrained cyclic torsional shear tests with initial static shear. *Soils and Foundations* 53(1): 23–34. https://doi.org/10.1016/j.sandf.2012.07.016

Doygun, O., Brandes, H. G., and Roy, T. T. 2019. Effect of Gradation and Non-plastic Fines on Monotonic and Cyclic Simple Shear Strength of Silica Sand. *Geotechnical and Geological Engineering* 37(4): 3221–3240. https://doi.org/10.1007/s10706-019-00838-9

Khosravifar, A., Elgamal, A., Lu, J., and Li, J. 2018. A 3D model for earthquake-induced liquefaction triggering and post-liquefaction response. *Soil Dynamics and Earthquake Engineering* 110: 43–52. https://doi.org/10.1016/j.soildyn.2018.04.008

Kiyota, T., Sato, T., Koseki, J., and Abadimarand, M. 2008. Behavior of liquefied sands under extremely large strain levels in cyclic torsional shear tests. *Soils and Foundations* 48(5): 727–739. https://doi.org/10.3208/sandf.48.727

Kokusho, T., Hara, T., and Hiraoka, R. 2004. Undrained Shear Strength of Granular Soils with Different Particle Gradations. *Journal of Geotechnical and Geoenvironmental Engineering* 130(6): 621–629. https://doi.org/10.1061/(asce)1090-0241(2004)130:6(621)

Koseki, J. 2021. Several challenges in advanced laboratory testing of geomaterials with emphasis on unconventional types of liquefaction tests. *Geomechanics for Energy and the Environment* 27: 100157. https://doi.org/10.1016/j.gete.2019.100157

Kuei, K. 2019. *Pile Dynamics and Shearing Behavior of Granular Soils*. PhD Dissertation, University of California, Davis.

Lee, K. L. and Fitton, J. A. 1969. Factors Affecting the Cyclic Loading Strength of Soil. In *Vibration Effects of Earthquakes on Soils and Foundations*, edited by E. T. Selig and D. Hampton. ASTM International. pp. 71–95. https://doi.org/10.1520/STP33637S

Shamoto, Y., Zhang, J.-M., and Goto, S. 1997. Mechanism of large post-liquefaction deformation in saturated sand. *Soils and Foundations* 37(2): 71-80.

Tasiopoulou, P., Ziotopoulou, K., Humire, F., Giannakou, A., Chacko, J., and Travasarou, T. 2020. Development and implementation of semiempirical framework for modeling postliquefaction shear deformation accumulation in sands. *Journal of Geotechnical and Geoenvironmental Engineering* 146(1): 4019120. https://doi.org/10.1061/(ASCE)GT.1943-5606.0002179

Vaid, Y. P., Fisher, J. M., Kuerbis, R. H., and Negussey, D. 1990. Particle Gradation and Liquefaction. *Journal of Geotechnical Engineering* 116(4): 698–703. https://doi.org/10.1061/(ASCE)0733-9410(1990)116:4(698)

Wang, G. and Wei, J. 2016. Microstructure evolution of granular soils in cyclic mobility and post-liquefaction process. *Granular Matter* 18: 51. https://doi.org/10.1007/s10035-016-0621-5

Wang, R., Fu, P., Zhang, J. M., and Dafalias, Y. F. 2016. DEM study of fabric features governing undrained post-liquefaction shear deformation of sand. *Acta Geotechnica* 11(6): 1321–1337. https://doi.org/10.1007/s11440-016-0499-8

Wahyudi, S., Koseki, J., Sato, T. and Chiaro, G. 2016. Multiple-Liquefaction Behavior of Sand in Cyclic Simple Stacked-Ring Shear Tests. *International Journal of Geomechanics* 16(5): C4015001. https://doi.org/10.1061/(asce)gm.1943-5622.0000596

Wei, J., Huang, D., and Wang, G. 2018. Microscale descriptors for particle-void distribution and jamming transition in pre- and post-liquefaction of granular soils. *Journal of Engineering Mechanics* 144(8): 4018067. https://doi.org/10.1061/(ASCE)EM.1943-7889.0001482

Wiebicke, M., Andò, E., Viggiani, G., and Herle, I. 2020. Measuring the evolution of contact fabric in shear bands with X-ray tomography. *Acta Geotechnica* 15(1): 79–93. https://doi.org/10.1007/s11440-019-00869-9

8.4 Tables and figures

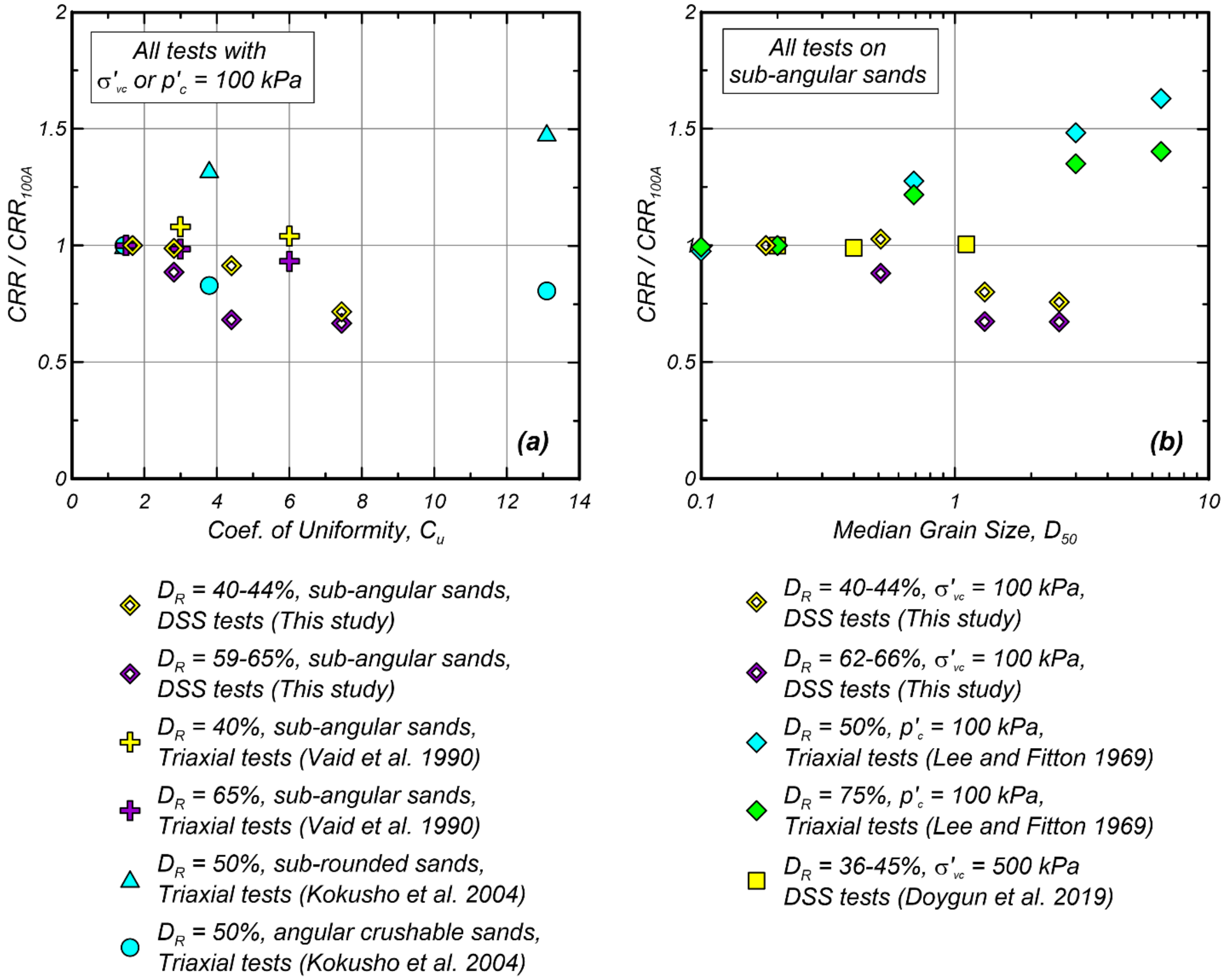

Figure 8.1. Cyclic resistance ratio (CRR, defined as the CSR to reach γ_{SA} = 3% in 10 cycles) normalized by the CRR obtained for 100A or other sands with similar gradations (CRR_{100A}): (a) results for soil mixes with different C_u values, and (b) results for soil mixes with different D_{50} values.

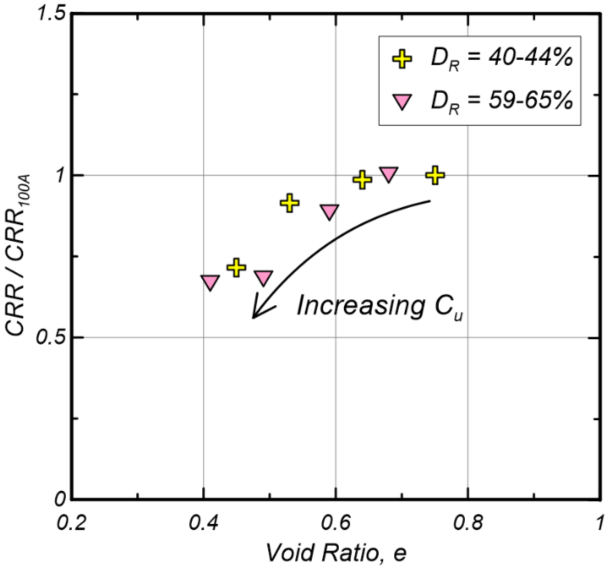

Figure 8.2. CRR obtained in this study for soils with different gradations (100A, 50AB, 33ABC, and 25ABCD) normalized by CRR_{100A} versus their corresponding void ratios.

Appendix A

Procedures and specifications for Direct Simple Shear (DSS) testing of sands with the EMDCSS GDS device

Author's note: Appendix A presents the procedures followed to perform the CV-DSS tests presented in this Dissertation, which will be publicly shared as a report authored by Francisco Humire, Rachel A. Reardon, Khoa Tran, Katerina Ziotopoulou, and Jason T. DeJong. The procedures presented herein correspond to the latest draft of that report available by December 2021. The draft report presented in this Appendix is subject to changes before its publication.

A.1 Equipment and materials

- DSS hardware:
    - Base pedestal and top caps mounted with porous discs (Figure A.1).
    - Stack of 21-26 teflon-coated confining rings with a black mark in the inner side of the third ring from the top, and the upper surface of all rings marked with a black dot (Figure A.2).
    - 4 O-rings: 2 for top cap and 2 for bottom cap.
    - Vacuum kit for sample preparation: vacuum former, 3 extension bars, and 1 red sealing O-ring (Figure A.3).
    - Set of brackets to restrict tilting: two lateral brackets and one top collar that is placed above rings.
- Sample:

    - Oven-dried and grounded soil.
    - 1 membrane (bottom half of triaxial size membranes).
    - DI water (optional for saturation of specimen).
- Measuring devices:
    - Caliper.
    - Scales.
    - Spirit level.
- Assistant devices and equipment:
    - Hex key Allen wrenches. Sizes: 2mm, 2.4mm, 3mm, 5mm, 6mm, 8mm
    - Expander cylinder (former Shelby tube).
    - Nonabrasive delicate task wipes.
    - Silicone oil (pure silicone fluid 5cSt at 25^{o}C/77 ^{o}F).
    - Air pluviation setup: granite surface plate, support stand, and clamp.
    - Pluviator assembly with desired mesh installed.
    - Vacuum pump, pressure regulator system, and connection tubing to the vacuum former inlet.
    - Set for vacuuming excess of soil: vacuum cleaner, 500mL Erlenmeyer flask and tubing (Figure A.4).
    - Set for vacuuming guidance: frame and aluminum bar support (Figure A.5).
    - Desiccator (optional for tests on dry specimens).
    - Burette and tubing for saturation (optional for saturation of specimen).

A.2 Procedure

A.2.1 Device and equipment preparation

1) Take your specimen out of the oven and leave to cool at room temperature. The use of a vacuum sealed desiccator is recommended when performing tests on dry specimens.
2) Make sure you have everything that you will need and that your equipment and workspace are clean; especially the confining rings and vacuum former. Always use nonabrasive delicate wipes and the air compressor to remove any sand particles from the confining rings.
3) Select a set of pedestal and top cap, confining rings and porous discs, and make sure you use consistent sets throughout your testing plan.
4) Select a membrane and record its thickness (average of three measurements).
5) Make sure that: (1) porous discs are dry and clean, and (2) voids in the bolt heads of both porous discs are filled with gypsum (Figure A.1).
6) Stretch and slide two O-rings around the top cap. If saturating, connect the exit saturation tube into the top cap outlet
7) Attach the top cap to the device using a 6mm wrench. Place the top cap in such a way that the flat surface around the top cap is pointing towards the front of the device (Figure A.6).
8) The axial displacement (long range) LVDT of the device must be calibrated in such a way that its zero value corresponds to a vertical distance of 30 mm between the ridges of both porous discs. This sensor is used to compute the height of the sample and should be re-calibrated, at least, every 10 tests. Proceed to Section A.3.1 if is necessary to re-calibrate that sensor.

9) Check that the length of the vacuum hose is long enough to transfer the sample from the pluviation station to the DSS device.

A.2.2 Specimen mold setup

10) Stretch the membrane over the bottom specimen cap and make sure that it is level on all sides.
11) Take one by one two O-Rings and stretch them over the expander (Figure A.7).
12) Lower the expander over the membrane and gently slide the first O-ring off the expander until it snaps around the base pedestal and membrane (Figure A8). The O-ring should be very close to the bottom edge of the membrane.
13) Attach the first collar (dark grey color) to the base pedestal. The three bolts can be attached to any of the six holes in the base pedestal with a 2.4mm wrench.
14) Again, lower the expander over the membrane and slide the second O-ring around the membrane (Figure A.9), and attach the second collar (light gray collar) with a 2mm wrench.
15) Lubricate one by one the confining rings with silicone oil. Before lubricating, make sure that confining rings are clean from the silicone oil of the previous test. The recommended sequence for lubrication is: (1) put the confining rings on a paper towel next to the silicon oil container, (2) dip each ring eight times into the silicon oil container and spread the oil around the ring, and (3) continue this process for each ring and place them back in the exact order as previously stacked.
16) Place the stack of confining rings on the base pedestal above the light gray collar (Figure A.10). Check that the rings are aligned and leveled.
17) Assemble the vacuum former using a 3mm wrench to attach the two lateral bolts. Leave a small gap (~1 mm) between both halves of the vacuum former to have room to slide it

around the stack of confining rings. Put the red sealing O-ring in the bottom of the vacuum former (Figure A.11).

18) Lower the vacuum former over the stack of confining rings until it reaches the top of the light gray collar. The vacuum outlet should be pointing in the opposite direction than the water inlet of the base pedestal (Figure A.12). Tight the two lateral bolts of the vacuum former and check that the red ring is not visible from the bottom openings of the vacuum former to see if the sealing O-ring has slipped (Figure A.13). If the red ring is visible, the vacuum former must be removed, and this step must be repeated.

19) Place the three extension bars of the vacuum former until the top of the bars cover the entire height of the stack of confining rings (Figure A.14). The height of the extension bars can be adjusted with the lateral clamps around the vacuum former. Check that the top 3 confining rings are tight and aligned with the rest of confining rings and that the confining rings are leveled. This may take some time because the extension bars tend to tilt when the lateral clamps are tightened.

20) Connect the vacuum hose to the vacuum pump. Turn the vacuum pump on.

21) Stretch the membrane and fold back around the vacuum former (Figure A.15). If everything works well, there should not be air pockets between membrane and confining rings and the 3nd black-marked ring should be visible (reference mark for the top surface of the pluviated specimen). If vacuum is not working well, check that:

    a. Lateral bolts around the vacuum collar are tightened.
    b. The extension bars are not above the height of the rings stack.
    c. The membrane does not have any hole.
    d. Bottom red ring is not visible.

22) **Measure the inner diameter of the assembly (measure three times and take an average).**

A.2.3 Pluviation

23) Adjust the opening of the pluviator to the target relative density[1]. Install the pluviator and protect the outside of the ring stack from excess soil when pluviating by placing the expander cylinder on top of the ring stack. Use a level to check tilting of the pluviation system. Check to make sure the pluviator opening is set to closed and plug the pluviator into a socket to ground it electrically during pluviation (Figure A.16).

24) Fill the pluviator up with soil and with the help of a funnel to ensure the height of the soil inside the cylinder is uniform (Figure A.17). Pluviate the soil into the membrane by keeping the height of the pluviator constant. Stop pluviating when the upper confining ring is covered completely.

    ***** From this point and on be really careful with any moves on the specimen and around your working station to avoid any disturbance *****

25) After pluviating, slowly remove the pluviation cylinders from above the sample, leaving the expander cylinder in place.

26) Assemble the shop vacuum, hose, and glass flask with a quarter of its volume filled with sand.

27) Gently remove most of the excess of soil above the stack of rings by vacuuming the top surface with the vacuum cleaner (Figure A.18). Do not remove sand inside the confining rings.

---

[1] *Based on the pluviation curve that you have calibrated – see Section A.3.2.*

28) Remove the expander cylinder (Figure A.19) and vacuum any soil on the rim of the vacuum former and on the base pedestal.

29) Remove the excess soil inside the rings by vacuuming the top surface using the vacuum cleaner and the guiding frame. Continue vacuuming by sliding the metal guide back and forth in slow linear motions until the black marking on the 3rd confining ring at the top can be seen (Figure A.20). Adjust the vacuum tube within the guide bar as needed, lowering in 0.5 to 1 mm increments until target height is achieved. **Make sure of vacuuming most of the grains of sand trapped in the inner side of the confining rings since they may create a bridge between confining rings and top cap during docking.**

30) Vacuum up any extra soil that is stuck on the vacuum former or bottom pedestal. View the top of specimen from all angles to ensure a flat, even and level surface is obtained.

A.2.4 Transportation

31) Carefully transfer and mount the assembled specimen on the device. Extend the vacuum hose as much as possible before transfer the sample. Insert the sample from the right side of the machine with the vacuum outlet pointing to the right (Figure A.21).

32) Attach the four bolts of the base pedestal to the travelling plate.

33) Connect the saturation tubing inlet to the base pedestal and tight it with a wrench.

A.2.5 Seating

34) Open the GDSLab Software. In the upper left-hand corner, you should observe an icon called “Station 1” with a simple shear symbol. Otherwise, if you see a blank paper icon above “Station 1”, click on that icon to create a station, and select the option “EMDCSS_AdvDCS_ini”.

35) Click on the “Management” tab on the lower right-hand side of the screen, and select the option “Object Display”. A new window will pop up where live sensor readings will be displayed throughout the test. Click “Read” and make sure that all the sensors are displaying numbers in blue. If any number is in red, click “Read” twice to refresh the sensors.

36) Click “CP” and click once on “CP Horizontal Displacement LVDT”. Set the horizontal displacement for a “Target” of 0 mm, and click “Hold” after some seconds. Close the small window and click “Read” to check that the “Horizontal Displacement LVDT” displays 0 ± 0.0005 mm.

37) Click the Control Box image located in the upper middle of the window to open the “ADVDCS v2 Device Overview” control center. Select the “Docking” tab, and make sure the Axis is set to “0-Vertical Axis”. In bold, the window will read “Docking using secondary channel.” If the status is “Docked”, click the “Set Undocked” button to change it to “Undocked”.

38) Extend vertical actuator / piston with a velocity of 0.5 mm/sec and maximum load of 0.040 kN (Figure 22). Stop once the top cap is close to the specimen (Figure A.23) and **zero (“Apply Offset”) the following transducers: (1) Axial Load, (2) Horizontal Load, and (3) Horizontal Load 2.**

39) Extend vertical actuator / piston but now with a velocity of 0.1 mm/sec. At this step, it is very important to monitor simultaneously the top cap and the computer, and **make sure that the top cap is aligned with the sample**. The status will change to “Docked” once it perceives the top cap is in contact with the soil sample, and the system will stop automatically once the maximum load of 0.040 kN is achieved. It is also important to check

that the top cap is in contact with the sample (Figure A.24). If it is not in contact (e.g. ridges of the porous discs can still be noticed), manually change the status to “Undocked” and try to slightly push the confining rings with your fingers if they are touching the sides of the top cap (you can release one or more extension bars to facilitate this process).

40) After the vertical displacement stabilizes, pull the membrane on the top cap and place the two top O-rings (Figure A.25). Then, disconnect the vacuum source from the sample. Turn off the vacuum pump only after disconnecting the vacuum tube from the sample, and place the top collar using a 3mm wrench (Figure A.26).

41) Remove the vacuum former from the sample.

42) Record height and loads at end of seating.

A.2.6 Axial LVDT setup

43) Install lateral brackets to avoid tilting of the specimen using the 6mm wrench (Figure A.27).

44) Install the short range axial LVDT: First, go to the controller of axial displacement readings and remove the offset. After that, lower the axial LVDT and insert it into the bottom hole. Finally, move the LVDT vertically until the reading in the axial LVDT indicates -2.00mm (∓0.1 mm) and tight the bolt using a 2mm wrench (Figure A.27). Try to move upwards the LVDT to check that the it is tight enough.

45) Lower the acrylic cover (it must remain closed during the entire test).

46) Apply offset to zero the following transducers: “Axial Displacement LVDT”, and “Axial Displacement Encoder”. **IMPORTANT: DO NOT CHANGE THE HORIZONTAL LVDT.**

47) Record height and loads at end of this stage.

A.2.7 Running the test

48) Click on “Data Save” and then click on “Choose Data File”. Select the option “Single Directory” and click “next”. Then, select the Standard GDSLAB format (.gds), choose a linear data saving type with 2 msec of saving interval, and make sure the option “Save calculated data?” is checked. After clicking “next”, assign a filename indicating day, time, and test identifier.
49) Click on “Sample” and then click on “Setup Sample Details”. If following this procedure, the sample should be docked at this point, and it should be the first time testing the sample. So, answer the questions “Is this the first test on a new specimen?” and “Is the specimen docked?” by clicking “Yes”.
50) Select “Cylindrical” specimen and setup the dimensions (diameter and height) of the sample. The diameter was measured in step 22 and the height should be the same than the recorded in step 47 (check that the secondary axial LVDT has not changed from that step).
51) Create (or load) the testing loading sequence by clicking on “Add Test”. If a loading sequence has been previously saved, just click “Load List From File”. The sequence will depend on the type of experiment to be performed. Click “Test List” to see the order of the loading sequence and explore the features of each stage by double clicking in the white rows of each test. Test stages can be created by clicking on “Create New Test Stage”. The created stage will be always the last stage from the existing list. Two options can be chosen when adding a loading stage: “GDS_ssAdvanced_Shear” or “GDS_ssDynamic_Shear”.
    a. If “GDS_ssAdvanced_Shear” is chose, a window with three steps will open: (1) selection of the loading/deformation applied in the vertical and horizontal

directions, (2) pore pressure measurements, and (3) termination of the stage. Only the first and the last are needed (second step can be skipped).

  b. If “GDS_ssDynamic_Shear” is chose, a window with two steps will open: (1) selection of the loading/deformation applied in the vertical and horizontal directions, and (2) termination of the stage.

For details of each option/parameter of these modules, please read Chapters 6n and 6o of the GDSLab Handbook. **Important: Always finish with a stress-controlled stage.**

Saturation of the specimen should be performed after pre-conditioning the sample with a series of drained strain-controlled cycles that improve the engagement between the ridged porous discs and specimen. If saturating the specimen, proceed with steps 52 to 56 after completing the pre-conditioning loading stage and before proceeding with the rest of loading stages. If not saturating the specimen, proceed with the following loading stages until the end of the test and skip steps 52 to 56.

A.2.8 Saturation

52) Close the burette and fill it up with deionized water. Make sure that there no bubbles in the water inside the burette.
53) Place the exit saturation tubing into a breaker with water.
54) Open the burette valve and the clamp of the exit saturation tubing and watch out for bubbles coming out the tube into the beaker (1 drop per second is a good rate). Check for water leakages that may occur in the tubing connections or in the specimen, specially, if bubbles are not coming out into the breaker. Leaking in the inlet and outlet tubing connections can be solved with sealing tape.

55) Saturate until no air bubbles can be seen in the outgoing water. Typically, 1.5 to 2 hours are required for the full saturation of the specimen. It is recommended to gradually increase the head difference until no bubbles can be seen in the receiving breaker.
56) At the end, leave the burette valve and the clamp of the "outgoing" tube open; the burette water should be at the about same "level" as the water "outgoing" tube so that there is no difference in head during the test.

A.2.9 Disassembly

57) After all the stages has been completed, move the horizontal LVDT to a target of 0 mm using the "CP Horizontal Displacement LVDT" (same than step 36).
58) Remove axial LVDT. **Important: Only if the last stage is a stress-controlled stage.**
59) Remove lateral brackets, top collar, and bolts of top cap and base pedestal.
60) Retract using "Docking" window with a speed of 0.5 mm/sec.
61) Remove the full sample from the device (Figure A.28).
62) Disconnect the saturation tubes from top cap and base pedestal.
63) Transfer the sample to the specimen preparation station to measure the relative density.
64) Move all the sand from the DSS container to a bowl, weight it, and calculate the relative density of the sample. If specimen was saturated, let it dry for 24 hours in the oven. Consider the weight of all the sand that may get stuck in the membrane or porous discs.
65) Clean all the confining rings using nonabrasive wipes to remove all the residual silicone oil and re-mark the black dots. Clean all the other DSS hardware and tools with compressed air and paper towels.

A.2.10 Next Test Preparation

66) Make sure that top cap and base pedestal will be dry for the following test. For that purpose, it is recommended to remove most of the water with compressed air and let them dry in the oven.
67) Leave sand in the oven for the following test. The buckets where the material is stored must be grounded before that.
68) Clean the pluviator and leave it grounding before the following test.
69) Check that the voids in the bolt heads of both porous discs are still filled with gypsum. If necessary, gypsum will need to be reapplied in the bolts following the instructions in Section A.3.3. Also, the porous discs should be removed and cleaned, at least, every 10 tests according to the instructions in Section A.3.3.

A.3 Other procedures

A.3.1 Recalibration of long-range axial LVDT

- Remove one of the angle brackets that hold is used to hold any of the lateral brackets. Check with a caliper the height of the bracket (that should be 30.00 mm).
- Install the top cap and base pedestal in the device (Figure A.29).
- Extend the vertical actuator using the “Docking” window, and press “Hold” when the Long-Range Axial LVDT is around -0.1 mm. That should give enough clearance to place the bracket in the middle between top cap and base pedestal (Figure A.30).
- Modify the speed of the vertical actuator to 0.001 mm/sec (minimum speed) and the load after docking to 0.012 kN as indicated in Figure A.31.

- Click on “Extend”, and monitor the evolution of the axial load in the computer. Once the top cap is in contact with the angle bracket, the status will change to “Docked” and the machine will automatically stop.
- In the sensor windows, zero (“Apply Offset”) the long-range axial LVDT.
- Retract the vertical actuator and remove the angle bracket.

A.3.2 Pluviation curves

- Before the initiation of the testing plan, a pluviation calibration curve should be obtained. This shall facilitate the decision on the opening of the pluviator so as to obtain a specific target relative density D_R.
- Use a standard mold. Measure its diameter and height and calculate its volume. Weigh it and get its initial mass.
- Pluviate your soil into the mold selecting different openings (degrees) of the pluviator every time. It is advised that you maintain a constant height of pluviation and that you perform the pluviation at each opening 3 times.
- Eventually you will obtain a plot of D_R versus degrees of opening.
- The pluviation of the actual specimen into the stack of confining rings should follow then the same specifications and be performed under the same conditions as the calibration of the pluviation:
- Since the calibration of the pluviation took place for a dry mold, porous stones should not be saturated when used. Especially, if the bottom one is saturated then the soil might absorb water during pluviation.
- For the same reason as above the material should be over-dried.
- The pluviation height should be the same.

A.3.3 Cleaning porous discs

- Gently remove the gypsum from the voids of all the bolt heads connecting the porous discs with the caps.
- Detach the porous discs using a 3mm wrench.
- Fill the sonic bath with deionized water and clean the discs for 30 minutes.
- Remove most of the water in the discs with compressed air and paper towels. Let the discs drying at room temperature for 1 hour over paper towels.
- After the discs are dried, attach them to the base pedestal and top cap using a 3mm wrench. **Important: Make sure that the discs are aligned with the caps.**
- Mix a teaspoon of gypsum with water in a small container. Add water slowly until obtain a thick mix.
- Use an eyedropper to place the gypsum mix in the voids of the bolt heads. Fill from bottom to top with the outlet of the eyedropper placed on the bottom ends of the voids. Make sure that there are no air bubbles in the gypsum inserted in the voids, and that the voids are completely filled with the mix.
- Let the gypsum drying for 1 hour.
- Carefully scratch the excess of gypsum to make it flush with the bolt heads. Make sure the top surface of the gypsum is flush and does not have any hole.

A.4 Figures

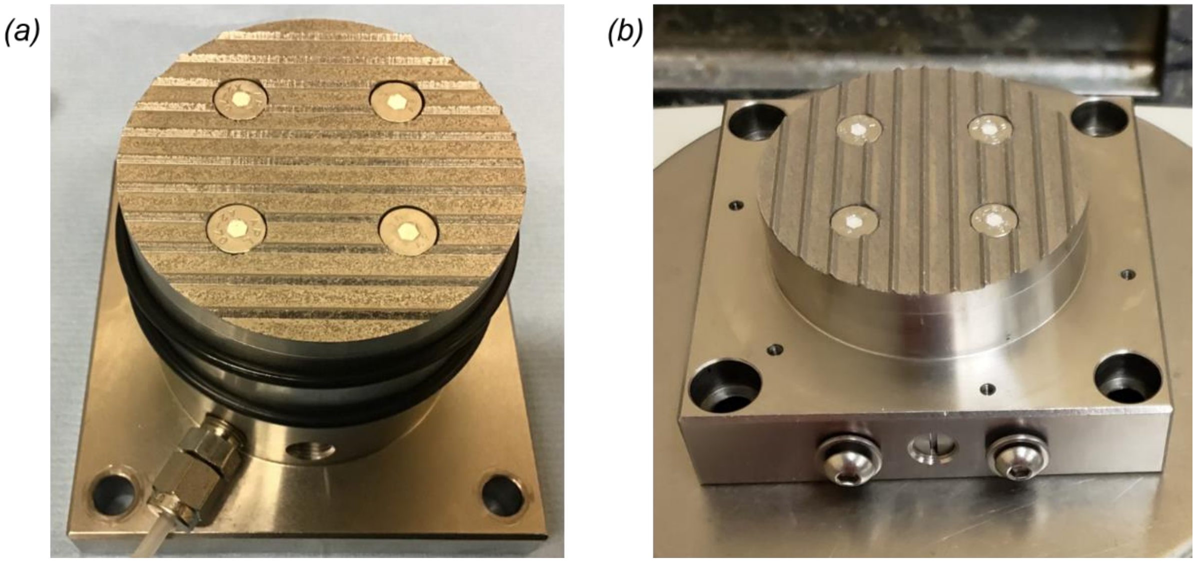

Figure A.1. (a) Top cap and (b) base pedestal mounted with ridged porous discs. Voids in the bolt heads are filled with gypsum.

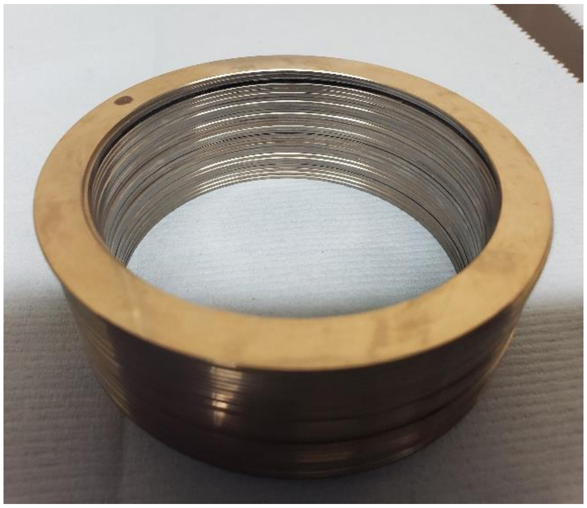

Figure A.2. Stacks of confining rings. The upper surface of each ring is marked with a black dot.

Figure A.3. Vacuum former with 3 extension bars and 1 red sealing O-ring.

Figure A.4. Flask and tubing for vacuuming excess of soil after pluviation.

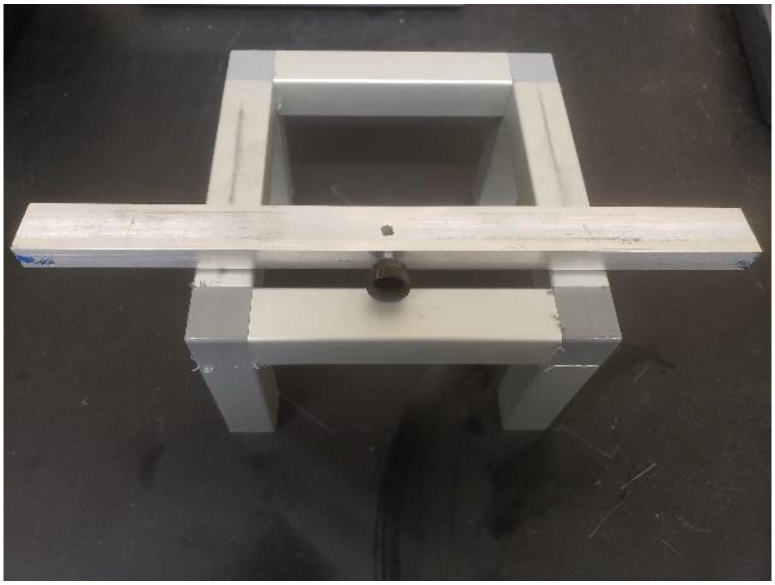

Figure A.5. Frame and help-bar for vacuuming excess of soil after pluviation.

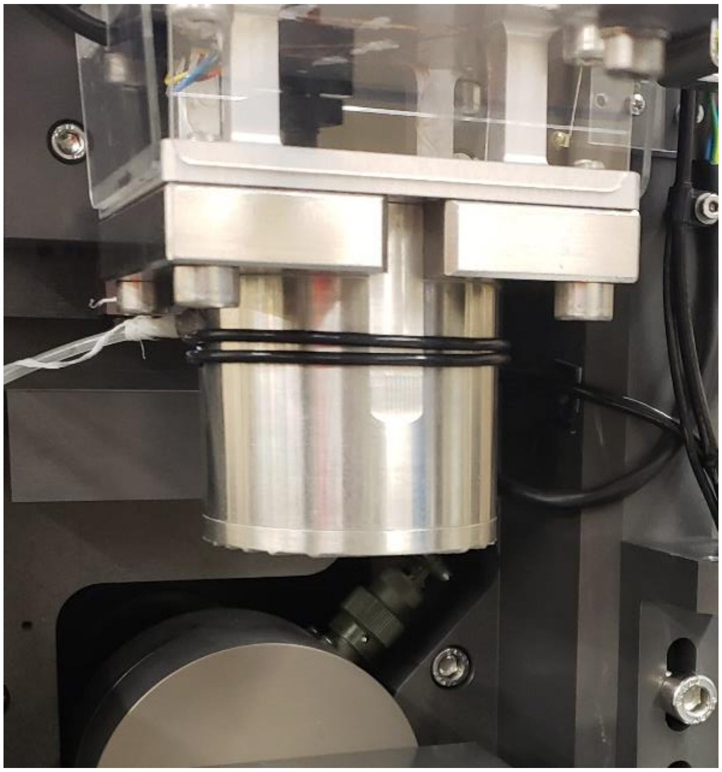

Figure A.6. Top cap mounted into the DSS device with O-rings stretched around it.

Figure A.7. O-Rings after being stretched over the expander.

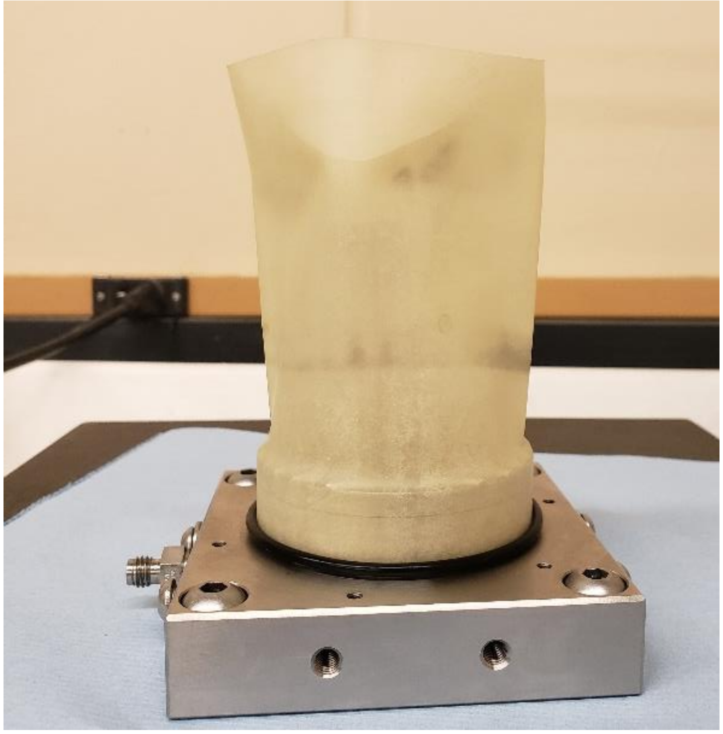

Figure A.8. First O-ring after being snapped around the membrane and base pedestal.

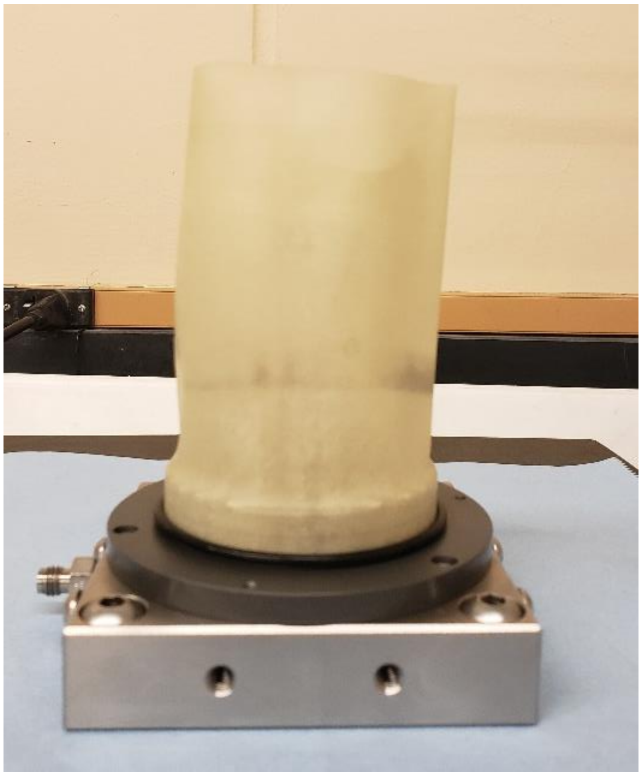

Figure A.9. Second O-ring after being snapped around the membrane and base pedestal.

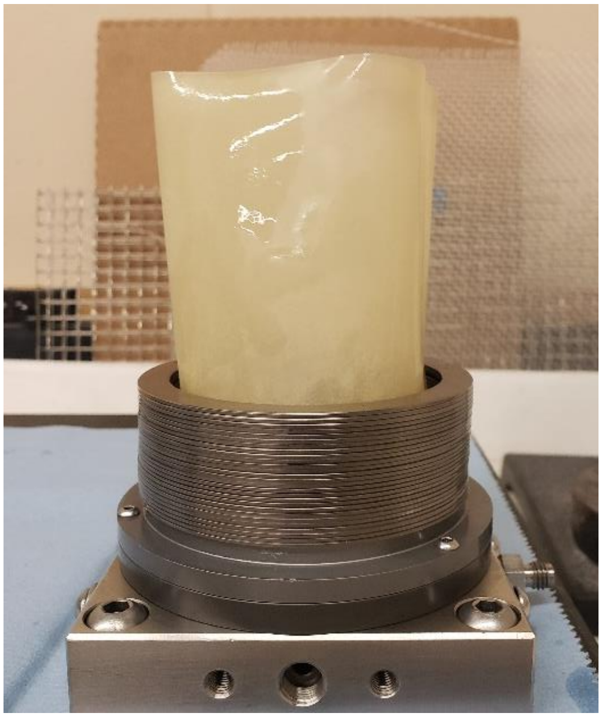

Figure A.10. Stack of lubricated confining rings placed above the base pedestal.

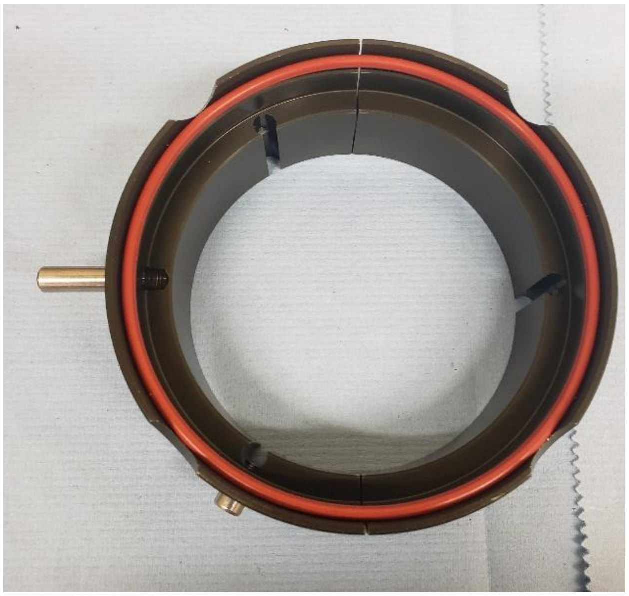

Figure A.11. Assembled vacuum former with a small gap between both halves.

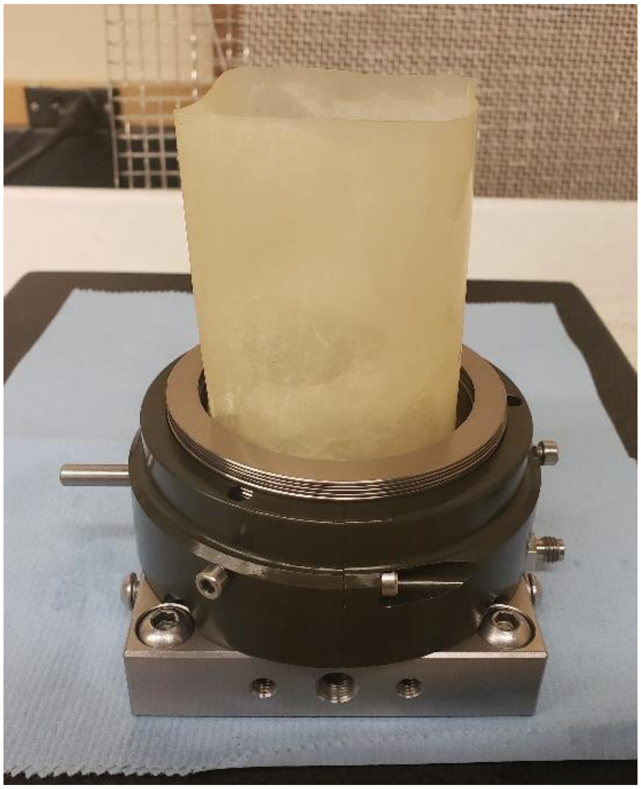

Figure A.12. Vacuum former installed around the confining rings.

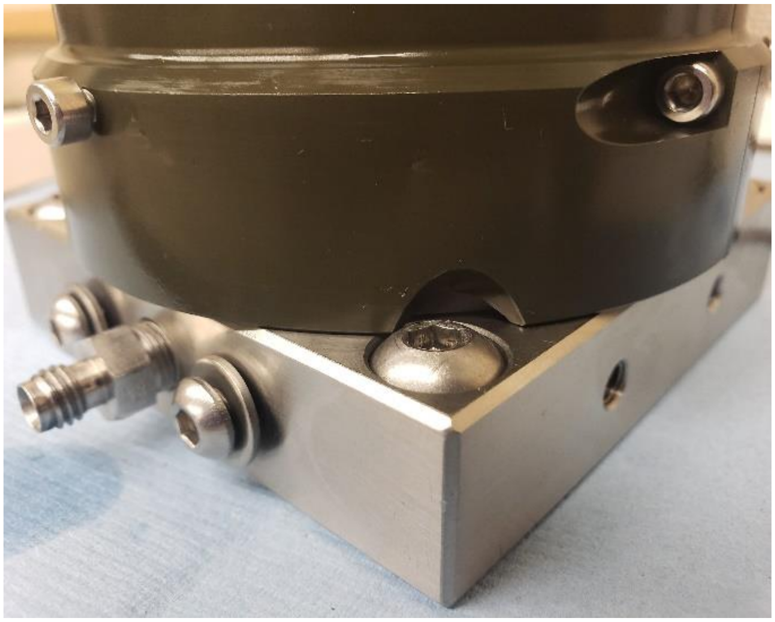

Figure A.13. View of the opening at the corners of the base pedestal. Red O-ring should not be visible from this angle.

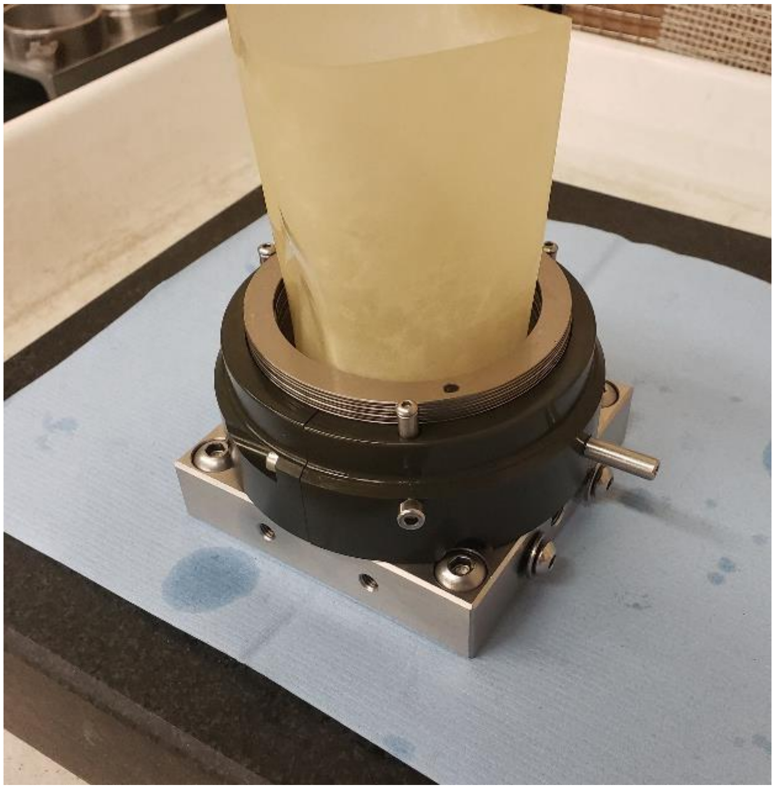

Figure A.14. Vacuum former with extension bars raised to cover all the rings.

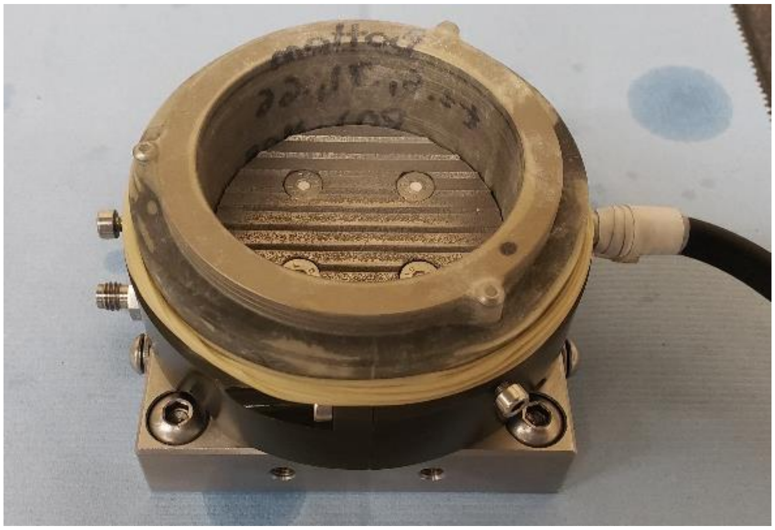

Figure A.15. Membrane after being stretched and folded back around the vacuum former.

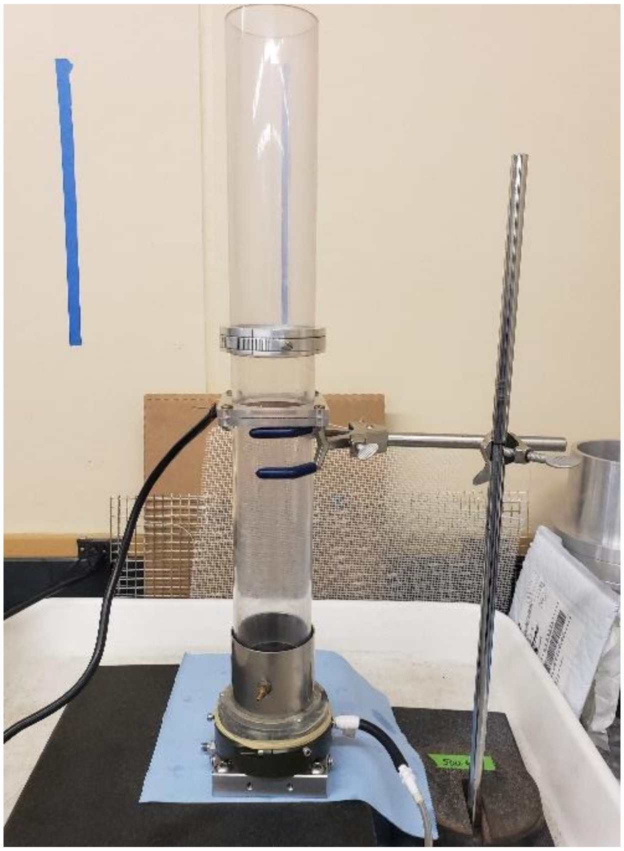

Figure A.16. Setup for sand pluviation.

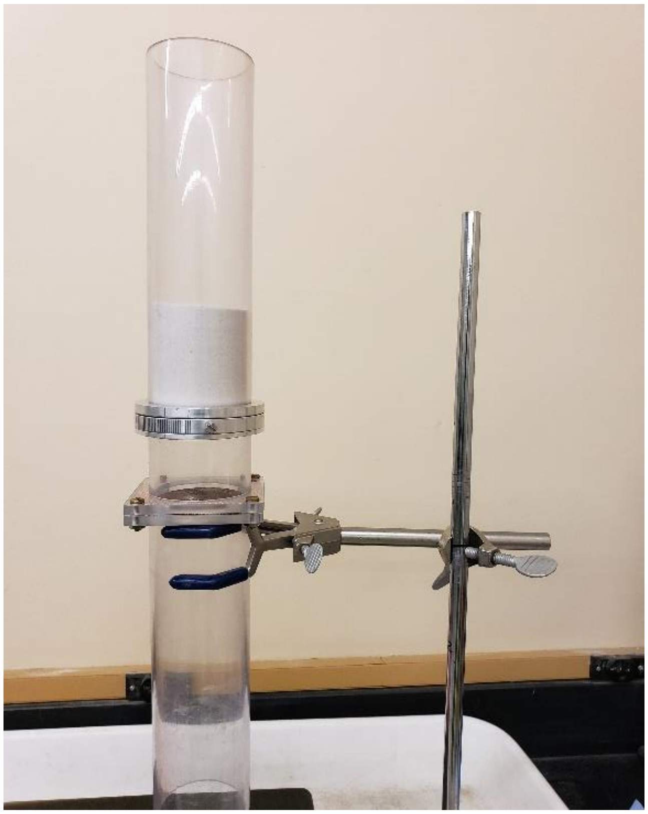

Figure A.17. Pluviator filled with sand.

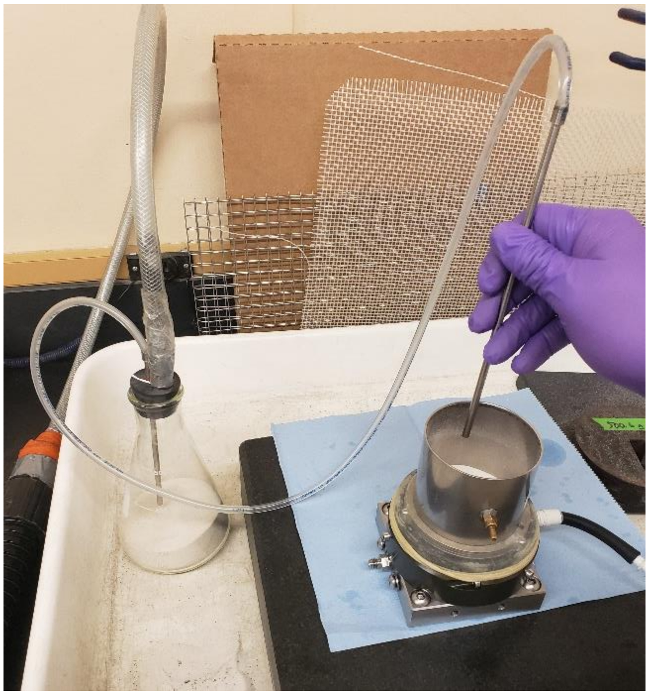

Figure A.18. Setup for vacuuming the excess of sand on the top of the specimen.

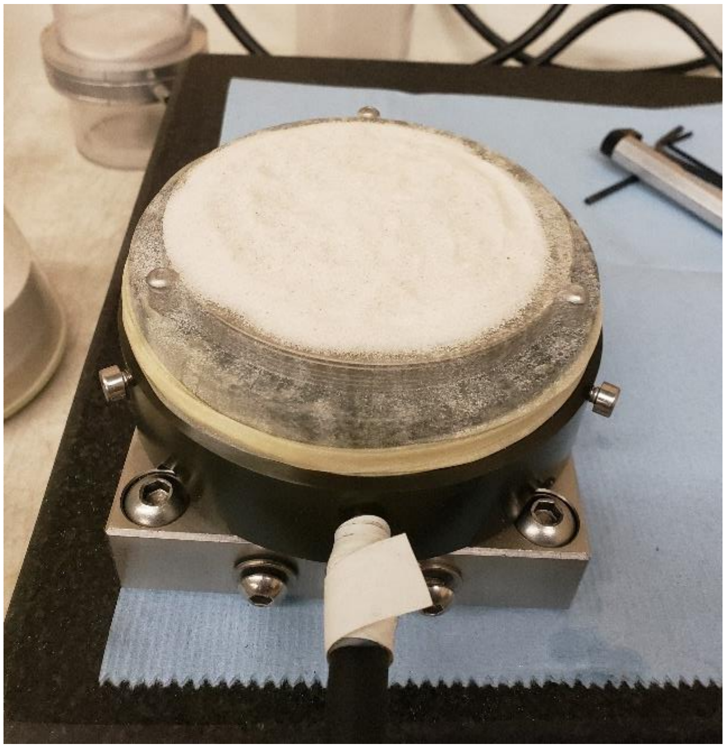

Figure A.19. Specimen after removing the expander cylinder on the top.

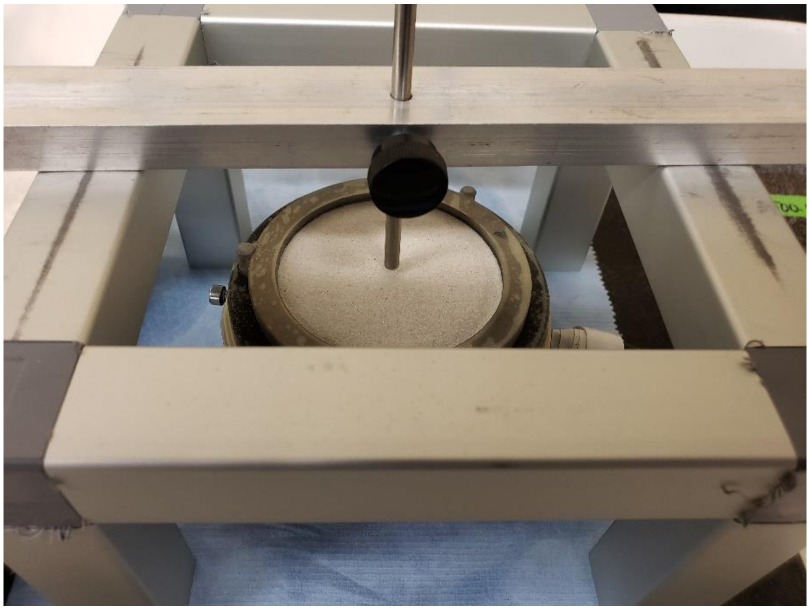

Figure A.20. Vacuuming the top surface of the sample using the guiding frame and help-bar.

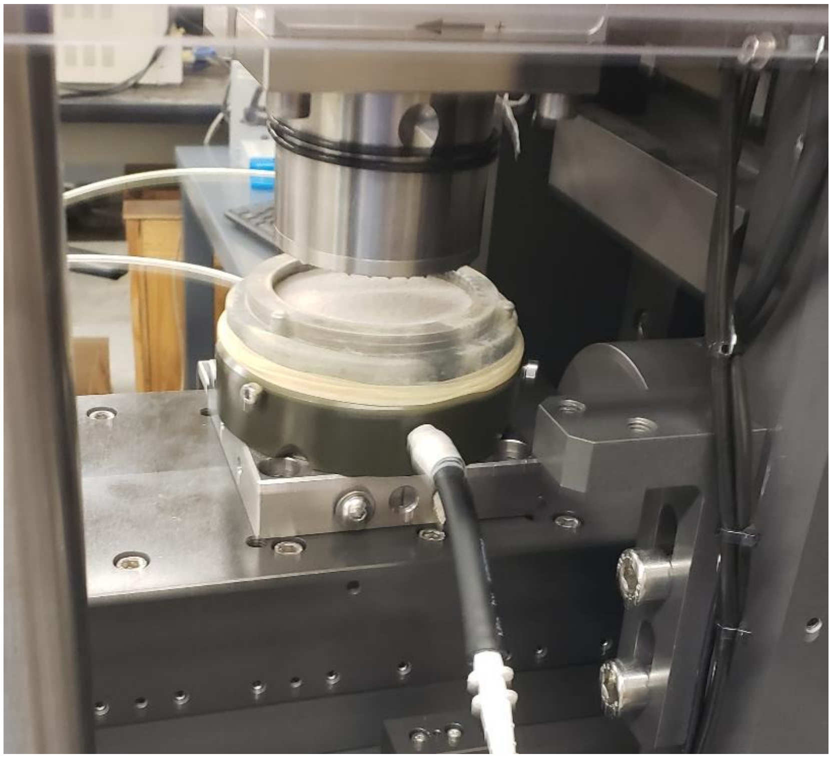

Figure A.21. Sample mounted on the device.

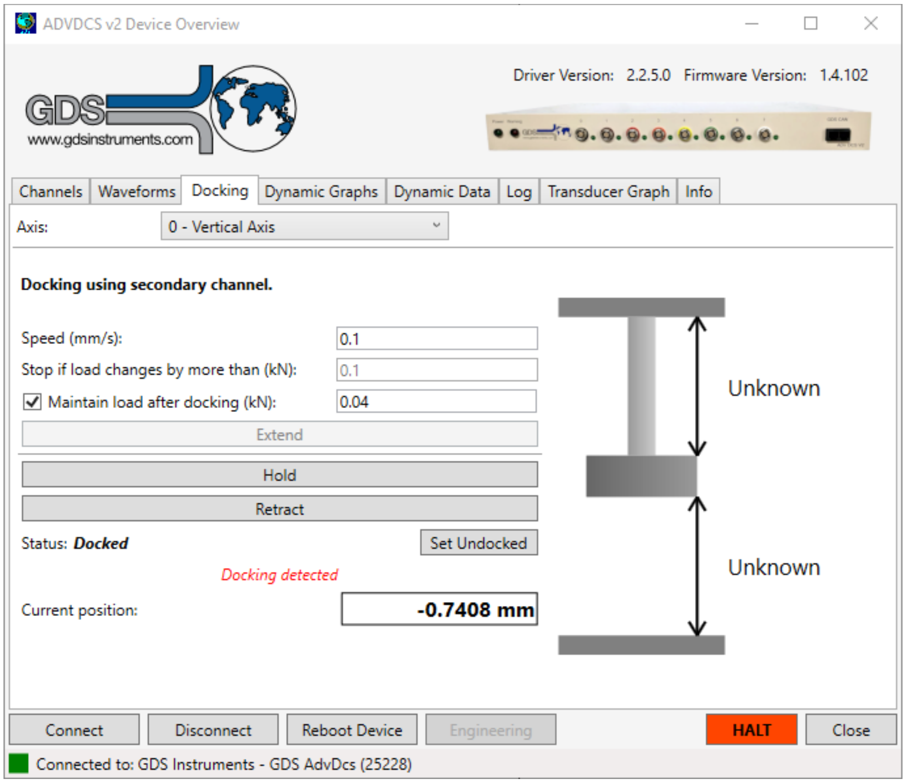

ADVDCS v2 Device Overview

Driver Version: 2.2.5.0 Firmware Version: 1.4.102

Axis: 0 - Vertical Axis

Docking using secondary channel.

Speed (mm/s): 0.1

Stop if load changes by more than (kN): 0.1

☑ Maintain load after docking (kN): 0.04

Status: ***Docked***

Docking detected

Current position: **-0.7408 mm**

Connected to: GDS Instruments - GDS AdvDcs (25228)

Figure A.22. Docking windows set up to 0.1 mm/sec and to stop at 0.040 kN.

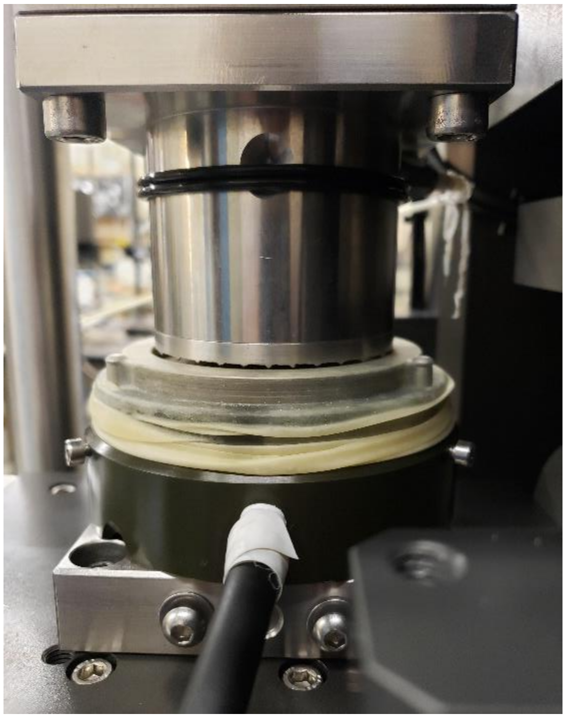

Figure A.23. Top cap before slightly above the stack of confining rings. Load transducers are zeroed at this step.

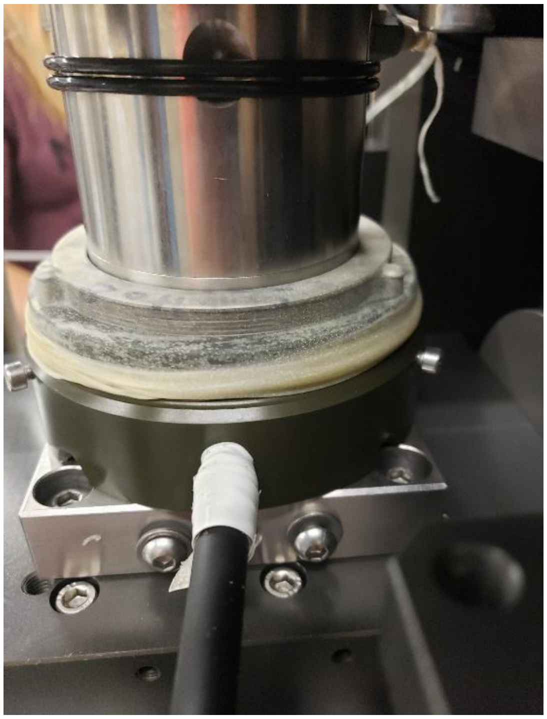

Figure A.24. Top cap in contact with the specimen at the end of docking.

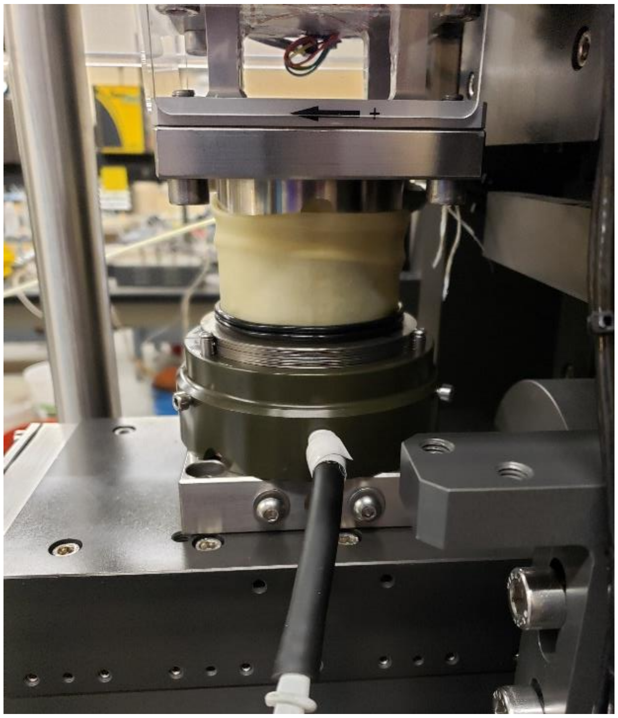

Figure A.25. Membrane pulled around the membrane and secured with two O-rings.

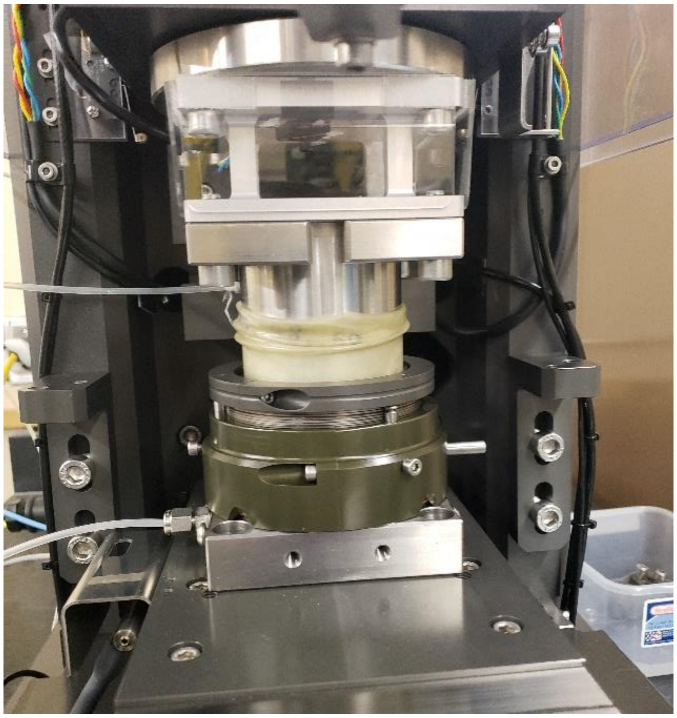

Figure A.26. Top collar of the lateral bracket system placed above confining rings.

Figure A.27. Short-range axial LVDT installed in the device.

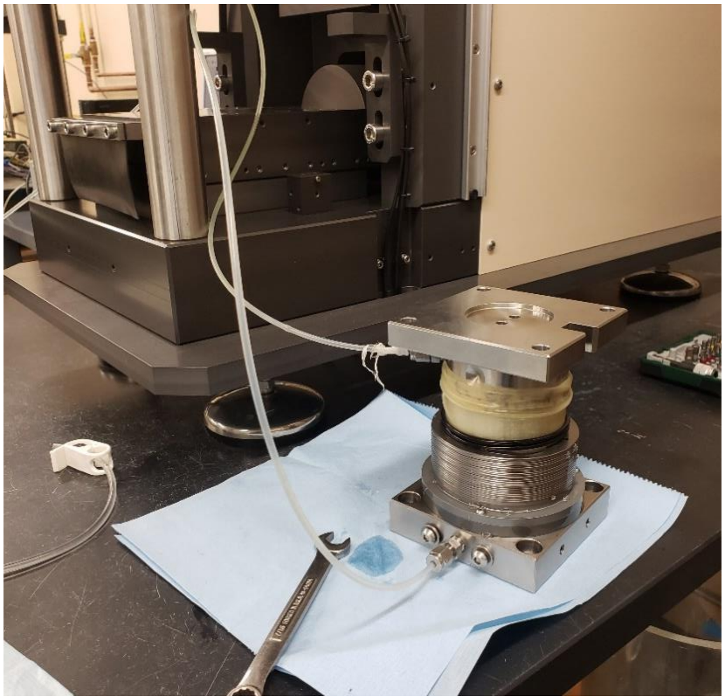

Figure A.28. Sample removed from the device.

Figure A.29. Top cap and base pedestal mounted in the device.

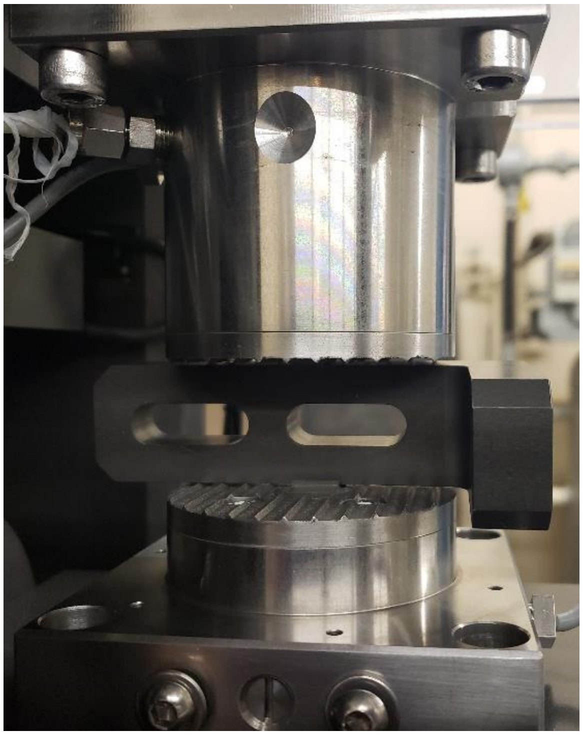

Figure A.30. Angle bracket placed between top cap and base pedestal to setup height reference.

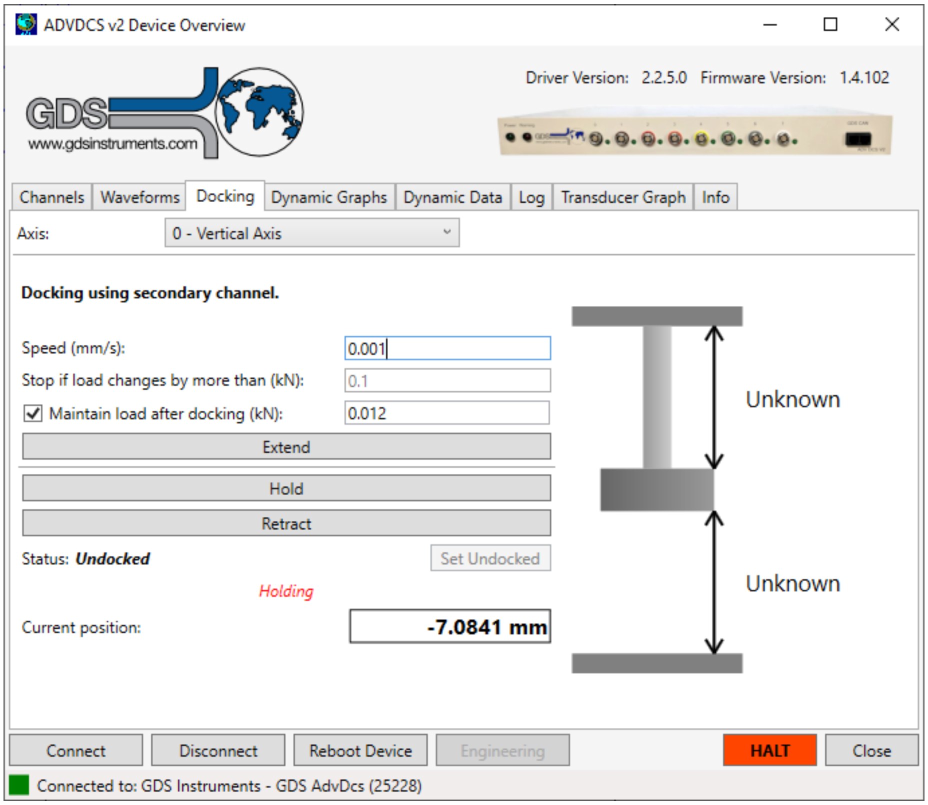

Driver Version: 2.2.5.0 Firmware Version: 1.4.102

Axis: 0 - Vertical Axis

Docking using secondary channel.

Speed (mm/s): 0.001

Stop if load changes by more than (kN): 0.1

☑ Maintain load after docking (kN): 0.012

Status: ***Undocked***

Holding

Current position: **-7.0841 mm**

🟩 Connected to: GDS Instruments - GDS AdvDcs (25228)

Figure A.31. Configuration for docking stage.

Appendix B

Summary of DSS testing program

Author's note: Appendix B summarizes the direct simple shear (DSS) tests presented in Chapters 4 to 6 of this Dissertation. Those tests will be publicly shared in DesignSafe-CI as experimental datasets with the following citations:

- *Humire, F. and Ziotopoulou, K. 2022. Direct simple shear testing on Ottawa F-65 sand under uniform and irregular cyclic loading. DesignSafe-CI [PRJ-3363].*
- *Humire, F., Reardon, R. A., Ziotopoulou, K., and DeJong J. T. 2022. Direct simple shear testing program on coarse-grained soils with varying gradations under monotonic and cyclic loading. DesignSafe-CI [PRJ-3364].*

This Appendix presents the memos attached to those databases with some minor edits for consistency with the rest of the Dissertation.

B.1 Direct simple shear testing on Ottawa F-65 sand under uniform and irregular cyclic loading (Chapter 4)

This memo summarizes the cyclic constant-volume direct simple shear (CV-DSS) tests performed on specimens of Ottawa F-65 sand as presented in Chapter 4. Experiments were conducted using the Electromechanical Dynamic Cyclic Simple Shear (EMDCSS) device manufactured by GDS Instruments available at UC Davis. The data available in the data depot of DesignSafe is the raw data (without any post-processing or filtering) for all the experiments presented in Chapter 4.

B.1.1 Tested sand

Ottawa F-65 is a standardized sand commercialized by US Silica and produced at their plant in Ottawa, IL. The grain size distribution of the batch utilized within this testing plan is shown in Figure B.1, which is consistent with those reported in the product data sheets of US Silica (2016) and Parra Bastidas (2016) that are also shown for comparison. Other properties available from Carey et al. (2020) for this sand are summarized in Table B.1.

B.1.2 Testing procedure

Specimens were prepared with the air pluviation method, which involved raining oven-dried sand from a constant height into the soil container. Following saturation with deionized water, all samples were subjected to a series of pre-conditioning strain-controlled drained cycles with an amplitude of 0.01 mm (about 0.045% shear strain) to ensure the engagement of the textured top platen with the specimen (Humire et al., 2022). This pre-conditioning stage consisted of 50 drained cycles applied under a vertical stress of 100 kPa for tests with an effective overburden stress (σ'_{vo}) of 100 or 400 kPa, and 115 drained cycles at a vertical stress of 25 kPa for tests with a σ'_{vo} of 50 kPa. Both pre-conditioning sequences were found to lead to similar results in terms of stress-strain response and liquefaction resistance (Humire et al., 2022). Following pre-conditioning, the vertical stress was raised to the target σ'_{vo} if the target value was larger than the vertical stress during pre-conditioning. Finally, specimens were subjected to a stress-controlled constant-volume cyclic shearing with a loading frequency of 0.05 Hz.

B.1.3 Summary of tests

The testing program comprised of 31 cyclic CV-DSS tests subjected to uniform cyclic loading conditions under level ground conditions. The relative density (D_R) after consolidation, effective overburden stress (σ'_{vo}), and the cyclic shear stress amplitude (τ_{cyc}) of those tests are summarized in Table B.2. Additionally, the testing program considered four CV-DSS tests under irregular cyclic loading conditions, which involved varying τ_{cyc} along the course of the post-triggering regime in three loading stages (Table B.3). The first loading stage of irregular tests ended after exceeding a shear strain of 4%, while the second stage ended after achieving a shear strain of 5-7%. All tests in Tables B.2 and B.3 are available in DesignSafe as *.txt files with the following columns: (1) shear strain in %, (2) shear stress in kPa, (3) effective overburden stress in kPa, and (4) vertical strain in %.

B.2 Direct simple shear testing program on coarse-grained soils with varying gradations under monotonic and cyclic loading (Chapters 5 and 6)

This memo summarizes the monotonic and cyclic constant-volume direct simple shear (CV-DSS) tests performed on specimens of coarse-grained soils with varying gradations presented in Chapters 5 and 6. Experiments were conducted using the Electromechanical Dynamic Cyclic Simple Shear (EMDCSS) device manufactured by GDS Instruments available at UC Davis. Most of the tests were performed on cylindrical specimens of about 18 mm in height and 70 mm in diameter, while some tests were performed in large-size samples with a diameter of 150 mm and about 33 mm in height to meet ASTM (2019) requirements regarding grain size and specimen height. The data available in the data depot of DesignSafe is the raw data (without any post-processing or filtering) for all the experiments presented in Chapters 5 and 6.

B.2.1 Tested soils

CV-DSS tests were performed using seven coarse-grained soils (Figure B.2) with different median grain sizes (D_{50}) and coefficients of uniformity (C_u). Soils 100A, 100B, 100C, and 100D are uniform coarse-grained soils with different D_{50} values that were sourced from the same natural alluvial deposit (Sturm 2019), and were combined to form soil mixtures with different C_u's: 50AB (i.e., 50% 100A, 50% 100B by mass), 33ABC, and 25ABCD soils. Given their common geological origin, these soils are expected to isolate the effect of grain size and gradation on the monotonic and cyclic response of coarse-grained soils. Physical and index properties of these soils are summarized in Table B.4, and more details regarding their index characterization are available in Sturm (2019)

B.2.2 Testing procedure

Specimens with relative densities (D_R) between 35 and 80% were prepared via air pluviation, which consisted of pouring dry sand from a constant height into the specimen container. Looser specimens (D_R = 25-35%) were prepared following a procedure similar to Method B of ASTM D4254 (2016) for performing minimum dry density tests. After applying a vertical stress of 25 kPa, specimens were subjected to a series of pre-conditioning strain-controlled drained cycles with an amplitude of 0.045% shear strain and a frequency of 0.1 Hz to improve the compliance between the top porous ridged disc and specimens (Humire et al. 2022). Based on a series of preliminary tests presented in Humire et al. (2021), it was found that the application of 50 pre-conditioning drained cycles was appropriate for this testing program to ensure a full engagement of the top platen while avoiding significant changes in the soil response. After pre-conditioning, all samples were consolidated under a vertical stress of 100 kPa. For tests under sloping ground conditions, the samples were subjected to constant-stress (drained) monotonic shearing with a shear strain rate of 50% per hour to apply the target static shear bias (α). Finally, samples were subjected either to a constant-volume monotonic shearing with a shear strain rate of 50% per hour until 25% shear strain was achieved, or a constant-volume stress-controlled cyclic shearing with a loading frequency of 0.05 Hz. Since the equivalent undrained conditions are imposed by maintaining a constant height during shearing, all tests presented herein were performed on dry specimens.

B.2.3 Summary of tests

The testing programs presented in Chapters 5 and 6 included 10 monotonic and 86 cyclic CV-DSS tests of 70 mm in diameter, and 28 cyclic CV-DSS tests of 150 mm in diameter. Those tests are summarized in Tables B.5 and B.6, which include the effective overburden stress (σ'_{vo}), cyclic stress ratio (CSR), static shear stress ratio (α), relative density (D_R) after consolidation, and the number of loading cycles (N_{cyc}) to achieve a single amplitude shear strain (γ_{SA}) of 3% for each test. All tests in Tables B.5 and B.6 are available in DesignSafe as *.txt files with the following columns: (1) shear strain in %, (2) shear stress in kPa, (3) effective overburden stress in kPa, and (4) vertical strain in %.

B.3 References

ASTM International. 2016. *Standard Test Methods for Minimum Index Density and Unit Weight of Soils and Calculation of Relative Density*. ASTM D4254-16. West Conshohocken, PA: ASTM International, approved March 1, 2016. https://doi.org/10.1520/D4254-16

ASTM International. 2019. *Standard Test Method for Consolidated Undrained Cyclic Direct Simple Shear Test under Constant Volume with Load Control or Displacement Control*. ASTM D8296-19. West Conshohocken, PA: ASTM International, approved November 1, 2019. https://doi.org/10.1520/D8296-19

Carey, T. J., Stone, N., and Kutter, B. L. 2020. Grain Size Analysis and Maximum and Minimum Dry Density Testing of Ottawa F-65 Sand for LEAP-UCD-2017. In *Model Tests and*

Numerical Simulations of Liquefaction and Lateral Spreading, edited by B. L. Kutter, M. T. Manzari, and M. Zeghal, 31–44. Cham, Switzerland: Springer. https://doi.org/10.1007/978-3-030-22818-7

Humire, F., Lee, M., Ziotopoulou, K., Gomez, M. G., and DeJong, J. T. 2022. Development and evaluation of pre-conditioning protocols for sand specimens in constant-volume cyclic direct simple shear tests. *Geotechnical Testing Journal* (under review).

Humire, F., Ziotopoulou, K., and DeJong, J. T. 2021. Evaluating shear strain accumulation of sands exhibiting cyclic mobility behavior. In *Proceedings of 20th International Conference on Soil Mechanics and Geotechnical Engineering (ICSMGE), Sydney, Australia*.

Parra Bastidas, A. M. 2016. *Ottawa F-65 Sand Characterization*. PhD dissertation, University of California, Davis.

Sturm, A. P. 2019. *On the Liquefaction Potential of Gravelly Soils: Characterization, Triggering and Performance*. PhD dissertation, University of California, Davis.

B.4 Tables and figures

Table B.1. Properties of Ottawa F-65 sand (Carey et al. 2020): maximum and minimum void ratio (e_{max} and e_{min}), largest grain size in smallest 10% of grains by mass (D_{10}), median grain size (D_{50}), coefficient of uniformity (C_u), and coefficient of curvature (C_c).

Soil Name	e_{max}	e_{min}	D_{10} (mm)	D_{50} (mm)	C_u	C_c
Ottawa F-65	0.778	0.508	0.15	0.20	1.47	0.88

Table B.2. Summary of constant-volume (equivalent undrained) cyclic DSS tests performed under uniform loading (UL) conditions and presented in Chapter 4.

Name in Chapter 4	File name in DesignSafe	D_R (%)	σ'_{vo} (kPa)	τ_{cyc} (kPa)
UL-01	190725-1250_DSSc_Trial21	37.7	100	10
UL-02	190830-1330_DSSc_FH_A20	38.7	100	10
UL-03	190731-1723_DSSc_FH_A03	48.0	100	15
UL-04	190730-1100_DSSc_FH_A01	59.7	100	10
UL-05	190822-1730_DSSc_FH_A15	61.3	100	12
UL-06	190814-1206_DSSc_FH_A10	58.7	100	15
UL-07	190826-1331_DSSc_FH_A17	56.0	100	18
UL-08	190731-1126_DSSc_FH_A02	63.0	100	15
UL-09	190805-1242_DSSc_FH_A04	64.3	100	15
UL-10	190904-1513_DSSc_FH_A21	75.2	100	15
UL-11	190808-1600_DSSc_FH_A05	76.4	100	15
UL-12	190911-1230_DSSc_FH_A22	76.9	100	20
UL-13	190916-1510_DSSc_FH_A25	77.5	100	20
UL-14	190808-1936_DSSc_FH_A06	79.0	100	20
UL-15	200618_0846_DSSc_FH_A38	37.5	50	7.5
UL-16	200626_0840_DSSc_FH_A45	42.1	50	7.5
UL-17	200620_1500_DSSc_FH_A40	50.6	50	7.5
UL-18	200609_1350_DSSc_FH_A34	56.0	50	10
UL-19	200617_0912_DSSc_FH_A37	60.1	50	10
UL-20	200608_1036_DSSc_FH_A33	63.4	50	7.5
UL-21	200624_0949_DSSc_FH_A43	66.3	50	7
UL-22	200612_1430_DSSc_FH_A36	69.6	50	8.5
UL-23	200622_0950_DSSc_FH_A41	79.6	50	10
UL-24	190819-1200_DSSc_FH_A13	42.3	400	60
UL-25	200620_1145_DSSc_FH_A39	52.4	400	40
UL-26	190823-1215_DSSc_FH_A16	55.4	400	40

UL-27	190815-1641_DSSc_FH_A11	60.4	400	60
UL-28	190827-1150_DSSc_FH_A18	64.9	400	34
UL-29	190822-1200_DSSc_FH_A14	66.2	400	60
UL-30	200623_0950_DSSc_FH_A42	70.4	400	60
UL-31	191206-1720_DSSc_FH_A32	78.5	400	80

Table B.3. Summary of constant-volume (equivalent undrained) cyclic DSS tests performed under irregular loading (IL) conditions and presented in Chapter 4.

Name in Chapter 4	File name in DesignSafe	D_R (%)	σ'_{vo} (kPa)	$\tau_{cyc,1}$ (kPa)	$\tau_{cyc,2}$ (kPa)	$\tau_{cyc,3}$ (kPa)
IL-01	190816-1656_DSSc_FH_A12	61.5	100	15	7.5	3.75
IL-02	200625_0854_DSSc_FH_A44	64.4	100	15	5	10
IL-03	200720_1720_DSSc_FH_A46	66.6	100	12	6	12
IL-04	200722_1730_DSSc_FH_A48	68.0	100	16	8	12

Table B.4. Properties of the coarse-grained soils with varying gradations presented in Chapters 5 and 6 (Sturm 2019): maximum and minimum void ratio (e_{max} and e_{min}), largest grain size in smallest 10% of grains by mass (D_{10}), median grain size (D_{50}), coefficient of uniformity (C_u), and coefficient of curvature (C_c).

Soil Name	e_{max}	e_{min}	D_{10} (mm)	D_{50} (mm)	C_u	C_c
100A	0.881	0.579	0.12	0.18	1.68	1.02
100B	0.835	0.524	0.31	0.51	1.80	1.04
100C	0.839	0.557	0.91	1.31	1.54	1.04
100D	0.812	0.54	1.79	2.58	1.53	1.00
50AB	0.753	0.468	0.13	0.29	2.82	0.76
33ABC	0.622	0.397	0.15	0.51	4.41	0.68
25ABCD	0.544	0.303	0.16	0.80	7.44	0.67

Table B.5. Summary of the 70 mm constant-volume (equivalent undrained) cyclic DSS tests presented in Chapters 5 and 6.

File name in DesignSafe	Soil	Type of Test	σ'_{vo} (kPa)	CSR	α	D_R (%)	N_{cyc} to γ_{SA}=3%
201029_1716_DSSmu_RR_100A_12	100A	Monotonic Undrained	100	-	0	40.5	-
210718_0946_DSSmu_FH_100A_27	100A	Monotonic Undrained	100	-	0.1	44.1	-
210717_0915_DSSmu_FH_100A_24	100A	Monotonic Undrained	100	-	0.2	42.7	-
210717_1308_DSSmu_FH_100A_26	100A	Monotonic Undrained	100	-	0.35	43.9	-
210710_1311_DSSmu_FH_100A_23	100A	Monotonic Undrained	100	-	0.5	46.4	-
210616_0926_DSSc_FH_100A_50	100A	Cyclic Undrained	100	0.10	0	27.0	1.7
200915_1034_DSSc_RR_100A_21_v2	100A	Cyclic Undrained	100	0.08	0	42.2	14.6
210327_1120_DSSc_FH_100A_37	100A	Cyclic Undrained	100	0.12	0	42.5	2.1
200915_1228_DSSc_RR_100A_22	100A	Cyclic Undrained	100	0.10	0	42.9	5.6
200915_1439_DSSc_RR_100A_23	100A	Cyclic Undrained	100	0.15	0	45.3	0.7
210710_1510_DSSc_FH_100A_55	100A	Cyclic Undrained + Post-Cyclic Monotonic	100	0.12	0	58.1	3.1
201111_1341_DSSc_FH_100A_34	100A	Cyclic Undrained	100	0.15	0	58.5	2.2
200908_1346_DSSc_FH_100A_14	100A	Cyclic Undrained	100	0.15	0	59.7	3.1
200826_1523_DSSc_RR_100A_05	100A	Cyclic Undrained	100	0.15	0	62.7	4.7
210509_1445_DSSc_RR_100A_47	100A	Cyclic Undrained	100	0.18	0	63.3	1.6
200826_1003_DSSc_FH_100A_04	100A	Cyclic Undrained	100	0.10	0	64.7	24.1
200903_1140_DSSc_RR_100A_12	100A	Cyclic Undrained	100	0.10	0	66.0	20.7
200903_1615_DSSc_RR_100A_13	100A	Cyclic Undrained	100	0.13	0	66.4	10.6
200901_1131_DSSc_FH_100A_08	100A	Cyclic Undrained	100	0.13	0	71.4	11.1
201006_1223_DSSc_RR_100A_25	100A	Cyclic Undrained	100	0.15	0	77.0	6.1
201006_0933_DSSc_RR_100A_24	100A	Cyclic Undrained	100	0.12	0	80.0	14.7
201006_1657_DSSc_RR_100A_26	100A	Cyclic Undrained	100	0.10	0	80.4	38.7
210330_1618_DSSc_FH_100A_40_v2	100A	Cyclic Undrained	100	0.05	0.05	41.6	55.2
210401_0921_DSSc_FH_100A_43	100A	Cyclic Undrained	100	0.08	0.05	42.6	8.2
210327_1350_DSSc_FH_100A_38	100A	Cyclic Undrained	100	0.10	0.05	41.7	1.3

Table B.5. Summary of the 70 mm constant-volume (equivalent undrained) cyclic DSS tests presented in Chapters 5 and 6 (cont.).

File name in DesignSafe	Soil	Type of Test	σ'_{vo} (kPa)	CSR	α	D_R (%)	N_{cyc} to γ_{SA}=3%
210710_0940_DSSc_FH_100A_54	100A	Cyclic Undrained (w/ Irregular Loading)	100	0.08 - 0.04 - 0.08	0.05	44.1	7.9
210402_1056_DSSc_FH_100A_46_v2	100A	Cyclic Undrained	100	0.04	0.1	44.0	498.2
210331_1055_DSSc_RR_100A_41	100A	Cyclic Undrained	100	0.05	0.1	35.5	8.3
210709_1542_DSSc_FH_100A_52	100A	Cyclic Undrained	100	0.06	0.1	44.6	6.1
210510_0838_DSSc_FH_100A_48	100A	Cyclic Undrained (w/ Irregular Loading)	100	0.10 - 0.05 - 0.10	0.1	42.8	0.2
210402_0841_DSSc_RR_100A_45	100A	Cyclic Undrained	100	0.015	0.2	39.8	57.3
210401_1125_DSSc_FH_100A_44	100A	Cyclic Undrained	100	0.02	0.2	44.3	9.1
210709_1733_DSSc_FH_100A_53	100A	Cyclic Undrained	100	0.024	0.2	39.8	1.3
210331_1647_DSSc_FH_100A_42	100A	Cyclic Undrained	100	0.05	0.2	42.0	0.2
210616_1334_DSSc_FH_100B_14	100B	Cyclic Undrained	100	0.10	0	40.6	5.6
200929_0952_DSSc_RR_100B_04	100B	Cyclic Undrained	100	0.06	0	44.7	121.1
200929_1309_DSSc_RR_100B_05	100B	Cyclic Undrained	100	0.08	0	46.2	55.1
201005_1130_DSSc_FH_100B_07_V2	100B	Cyclic Undrained	100	0.10	0	46.2	10.1
200929_1513_DSSc_RR_100B_06	100B	Cyclic Undrained	100	0.12	0	47.4	5.6
201005_1345_DSSc_FH_100B_08	100B	Cyclic Undrained	100	0.15	0	47.6	1.2
201005_1627_DSSc_FH_100B_09	100B	Cyclic Undrained	100	0.15	0	62.4	2.7
200928_1705_DSSc_FH_100B_03	100B	Cyclic Undrained	100	0.08	0	62.6	29.6
200928_1506_DSSc_FH_100B_02	100B	Cyclic Undrained	100	0.10	0	63.6	8.6
200928_1115_DSSc_FH_100B_01	100B	Cyclic Undrained	100	0.13	0	64.3	6.6
201007_1022_DSSc_FH_100B_10	100B	Cyclic Undrained	100	0.12	0	77.5	8.6
201007_1245_DSSc_FH_100B_11_v2	100B	Cyclic Undrained	100	0.15	0	81.4	5.3
201007_1720_DSSc_FH_100B_12	100B	Cyclic Undrained	100	0.20	0	81.9	2.6
210325_1318_DSSc_FH_100C_19	100C	Cyclic Undrained	100	0.1	0	32.0	2.1
210616_1139_DSSc_KZ_100C_25	100C	Cyclic Undrained	100	0.06	0	41.6	21.6
210614_1458_DSSc_KZ_100C_23	100C	Cyclic Undrained	100	0.07	0	43.3	10.1

Table B.5. Summary of the 70 mm constant-volume (equivalent undrained) cyclic DSS tests presented in Chapters 5 and 6 (cont.).

File name in DesignSafe	Soil	Type of Test	σ'_{vo} (kPa)	CSR	α	D_R (%)	N_{cyc} to γ_{SA}=3%
210614_1137_DSSc_FH_100C_22	100C	Cyclic Undrained	100	0.1	0	44.0	3.6
210615_1155_DSSc_KZ_100C_24	100C	Cyclic Undrained	100	0.12	0	45.3	0.8
210712_1045_DSSc_FH_100C_27	100C	Cyclic Undrained + Post-Cyclic Monotonic	100	0.12	0	56.5	1.2
210711_1212_DSSc_FH_100C_26	100C	Cyclic Undrained	100	0.12	0	64.8	2.2
200916_1038_DSSc_RR_100C_16	100C	Cyclic Undrained	100	0.08	0	66.1	12.1
200916_1319_DSSc_RR_100C_17	100C	Cyclic Undrained	100	0.1	0	66.2	4.2
200916_1523_DSSc_RR_100C_18	100C	Cyclic Undrained	100	0.06	0	66.3	31.6
201002_1215_DSSc_RR_50AB_08	50AB	Cyclic Undrained	100	0.13	0	38.6	0.8
200930_1150_DSSc_FH_50AB_01	50AB	Cyclic Undrained	100	0.10	0	40.9	3.7
210616_1510_DSSc_KZ_50AB_13	50AB	Cyclic Undrained	100	0.07	0	43.2	33.6
201002_0955_DSSc_RR_50AB_07	50AB	Cyclic Undrained	100	0.08	0	48.4	20.2
200930_1527_DSSc_FH_50AB_02	50AB	Cyclic Undrained	100	0.08	0	49.3	17.1
200930_1730_DSSc_FH_50AB_03	50AB	Cyclic Undrained	100	0.12	0	51.5	4.6
201001_0952_DSSc_RR_50AB_04	50AB	Cyclic Undrained	100	0.13	0	58.0	5.6
201001_1146_DSSc_RR_50AB_05	50AB	Cyclic Undrained	100	0.10	0	58.2	12.2
201001_1400_DSSc_RR_50AB_06	50AB	Cyclic Undrained	100	0.08	0	60.4	38.7
201008_1012_DSSc_RR_50AB_09	50AB	Cyclic Undrained	100	0.13	0	74.6	11.7
201008_1340_DSSc_RR_50AB_10	50AB	Cyclic Undrained	100	0.15	0	77.3	8.7
201008_1552_DSSc_RR_50AB_11	50AB	Cyclic Undrained	100	0.20	0	79.5	3.7
210223_1156_DSSmu_RR_33ABC_11	33ABC	Monotonic Undrained	100	-	0	44.2	-
210718_1334_DSSmu_FH_33ABC_47	33ABC	Monotonic Undrained	100	-	0.1	40.9	-
210712_1246_DSSmu_FH_33ABC_40	33ABC	Monotonic Undrained	100	-	0.2	44.6	-
210718_1135_DSSmu_FH_33ABC_46	33ABC	Monotonic Undrained	100	-	0.35	43.1	-
210712_1604_DSSmu_FH_33ABC_41	33ABC	Monotonic Undrained	100	-	0.5	45.8	-
210709_1125_DSSc_FH_33ABC_38	33ABC	Cyclic Undrained	100	0.10	0	25.0	1.7

Table B.5. Summary of the 70 mm constant-volume (equivalent undrained) cyclic DSS tests presented in Chapters 5 and 6 (cont.).

File name in DesignSafe	**Soil**	**Type of Test**	**σ'_{vo} (kPa)**	**CSR**	**α**	**D_R (%)**	**N_{cyc} to γ_{SA}=3%**
210223_1748_DSSc_FH_33ABC_12	33ABC	Cyclic Undrained	100	0.07	0	34.8	8.2
210224_0947_DSSc_FH_33ABC_13	33ABC	Cyclic Undrained	100	0.10	0	37.6	3.1
210224_1206_DSSc_FH_33ABC_14	33ABC	Cyclic Undrained	100	0.14	0	46.0	0.8
210224_1508_DSSc_RR_33ABC_15	33ABC	Cyclic Undrained	100	0.06	0	45.8	55.1
210325_0950_DSSc_FH_33ABC_16	33ABC	Cyclic Undrained	100	0.10	0	48.2	4.1
200911_1211_DSSc_FH_33ABC_01	33ABC	Cyclic Undrained	100	0.15	0	65.3	1.1
200914_1445_DSSc_FH_33ABC_05	33ABC	Cyclic Undrained	100	0.08	0	59.0	11.6
200914_1830_DSSc_FH_33ABC_06	33ABC	Cyclic Undrained	100	0.10	0	57.5	5.2
210711_1005_DSSc_FH_33ABC_39	33ABC	Cyclic Undrained + Post-Cyclic Monotonic	100	0.12	0	57.3	2.1
210511_1111_DSSc_FH_33ABC_26	33ABC	Cyclic Undrained	100	0.05	0.05	39.2	40.2
210511_1547_DSSc_FH_33ABC_28	33ABC	Cyclic Undrained	100	0.06	0.05	37.0	18
210511_1658_DSSc_FH_33ABC_29	33ABC	Cyclic Undrained	100	0.075	0.05	41.4	8.2
210716_1631_DSSc_FH_33ABC_44	33ABC	Cyclic Undrained (w/ Irregular Loading)	100	0.08 - 0.04 - 0.08	0.05	48.3	7.4
210510_1223_DSSc_FH_33ABC_21	33ABC	Cyclic Undrained	100	0.05	0.1	42.4	51.2
210511_0924_DSSc_FH_33ABC_25	33ABC	Cyclic Undrained	100	0.06	0.1	40.0	4.2
210716_1158_DSSc_FH_33ABC_42	33ABC	Cyclic Undrained	100	0.065	0.1	46.5	1.3
210716_1447_DSSc_FH_33ABC_43	33ABC	Cyclic Undrained (w/ Irregular Loading)	100	0.10 - 0.05 - 0.10	0.1	42.8	0.2
210510_1813_DSSc_FH_33ABC_24	33ABC	Cyclic Undrained	100	0.02	0.2	42.7	175.2
210716_1811_DSSc_FH_33ABC_45	33ABC	Cyclic Undrained	100	0.025	0.2	40.0	5.3
210511_1822_DSSc_FH_33ABC_30	33ABC	Cyclic Undrained	100	0.03	0.2	42.0	6.3
210511_1322_DSSc_FH_33ABC_27_v2	33ABC	Cyclic Undrained	100	0.035	0.2	41.2	0.4

Table B.6. Summary of the 150 mm constant-volume (equivalent undrained) cyclic DSS tests presented in Chapter 5.

File name in DesignSafe	**Soil**	**Type of Test**	**σ'_{vo} (kPa)**	**CSR**	**α**	**D_R (%)**	**N_{cyc} to γ_{SA}=3%**
210318_1528_DSSc_RR_100A_150_27	100A	Cyclic Undrained	100	0.10	0	33.7	5.7
200923_1500_DSSc_FH_100A_150_03	100A	Cyclic Undrained	100	0.15	0	42.6	3.1
210118_1050_DSSc_FH_100A_150_19	100A	Cyclic Undrained	100	0.10	0	42.9	18.1
210121_1809_DSSc_RR_100A_150_22	100A	Cyclic Undrained	100	0.08	0	45.8	52.1
200921_0829_DSSc_FH_100A_150_01	100A	Cyclic Undrained	100	0.10	0	61.4	19.2
201118_1807_DSSc_FH_100A_150_17	100A	Cyclic Undrained	100	0.15	0	55.3	4.2
210715_1052_DSSc_FH_100A_150_29	100A	Cyclic Undrained	100	0.10	0	61.2	20.1
210516_1951_DSSc_RR_100A_150_28	100A	Cyclic Undrained	100	0.18	0	68.1	5.2
201119_1153_DSSc_RR_100A_150_18	100A	Cyclic Undrained	100	0.13	0	70.9	16.7
201116_1636_DSSc_FH_100A_150_15	100A	Cyclic Undrained	100	0.15	0	64.6	7.2
201120_1224_DSSc_FH_100D_150_01	100D	Cyclic Undrained	100	0.10	0	48.7	6.6
201217_0952_DSSc_FH_100D_150_07	100D	Cyclic Undrained	100	0.10	0	33.9	4.1
201218_1557_DSSc_RR_100D_150_08	100D	Cyclic Undrained	100	0.07	0	46.9	31.2
201219_1100_DSSc_FH_100D_150_09	100D	Cyclic Undrained	100	0.15	0	34.1	1.1
201221_1104_DSSc_RR_100D_150_10	100D	Cyclic Undrained	100	0.15	0	34.5	0.8
210111_1350_DSSc_FH_100D_150_11	100D	Cyclic Undrained	100	0.15	0	41.2	1.1
210112_1016_DSSc_RR_100D_150_12	100D	Cyclic Undrained	100	0.07	0	38.4	27.6
210129_1044_DSSc_RR_100D_150_16	100D	Cyclic Undrained	100	0.15	0	63.6	1.7
210201_1019_DSSc_FH_100D_150_17	100D	Cyclic Undrained	100	0.10	0	61.0	6.6
210205_1009_DSSc_RR_100D_150_20v2	100D	Cyclic Undrained	100	0.08	0	60.4	14.6
201202_1450_DSSc_RR_25ABCD_150_02	25ABCD	Cyclic Undrained	100	0.1	0	56.4	8.2
201203_1145_DSSc_FH_25ABCD_150_03	25ABCD	Cyclic Undrained	100	0.1	0	57.2	10.1
210712_1815_DSSc_FH_25ABCD_150_19	25ABCD	Cyclic Undrained	100	0.07	0	56.3	26.2
201205_1118_DSSc_FH_25ABCD_150_05	25ABCD	Cyclic Undrained	100	0.1	0	40.9	5.1
201207_1200_DSSc_RR_25ABCD_150_06	25ABCD	Cyclic Undrained	100	0.07	0	39.2	18.1
201210_1042_DSSc_FH_25ABCD_150_09	25ABCD	Cyclic Undrained	100	0.15	0	40.7	1.7
210309_1215_DSSc_RR_25ABCD_150_17	25ABCD	Cyclic Undrained	100	0.1	0	29.5	4.7
210312_1106_DSSc_FH_25ABCD_150_18	25ABCD	Cyclic Undrained	100	0.07	0	17.7	17.6

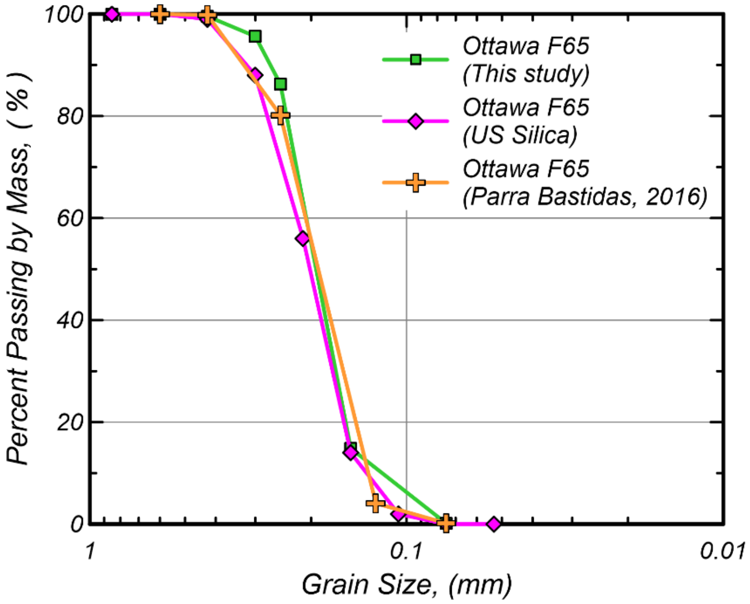

Figure B.1. Grain size distributions of Ottawa F-65 sand.

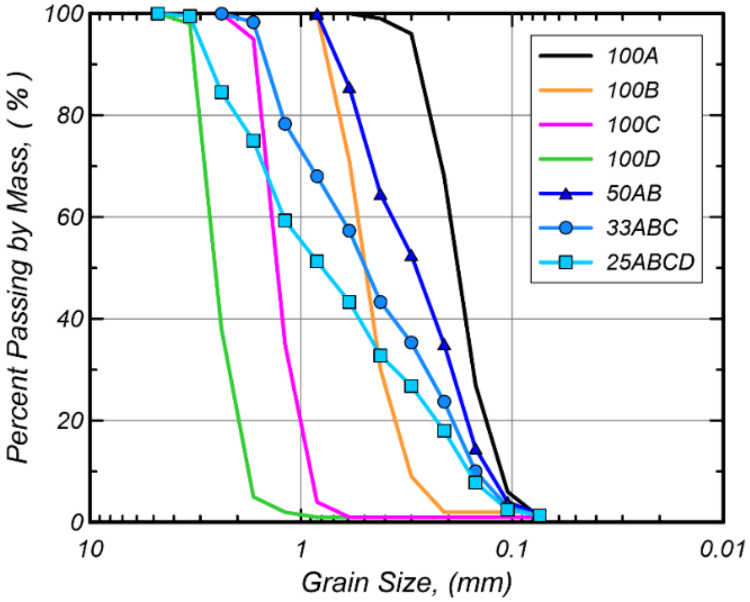

Figure B.2. Grain size distributions of the soil mixtures presented in Chapters 5 and 6.